THE DYNAMIC ROLE OF RIDGES IN A β–PLANE CHANNEL

Towards understanding the dynamics of large scale circulation in the Southern Ocean

by

Liping Wang

M.S. Institute of Atmospheric Physics, Academia Sinica
(1987)

Submitted in partial fulfillment of the
requirements for the degree of

DOCTOR OF PHILOSOPHY

at the

MASSACHUSETTS INSTITUTE OF TECHNOLOGY

and the

WOODS HOLE OCEANOGRAPHIC INSTITUTION

July 1993

Signature of Author ....
Joint Program in Physical Oceanography
Massachusetts Institute of Technology
Woods Hole Oceanographic Institution
July 30, 1993

Certified by ....
Rui Xin Huang
Associate Scientist
Thesis Supervisor

Accepted by ....
Lawrence Pratt
Chairman, Joint Committee for Physical Oceanography
Massachusetts Institute of Technology
Woods Hole Oceanographic Institution

THE DYNAMIC ROLE OF RIDGES IN A β-PLANE CHANNEL
Towards understanding the dynamics of large scale circulation in the Southern Ocean

by

Liping Wang

Submitted in partial fulfillment of the requirements for the degree of
Doctor of Philosophy at the Massachusetts Institute of Technology
and the Woods Hole Oceanographic Institution
July 30, 1993

Abstract

In this thesis, the dynamic role of bottom topography in a β-plane channel is systematically studied in both linear homogeneous and stratified layer models in the presence of either wind stress (Chapters 2, 3, 4, and 6) or buoyancy forcing (Chapter 5). In these studies, the structure of the geostrophic contour plays a fundamental role, and the role of bottom topography is looked at from two different angles. It is shown that blocking all the geostrophic contours leads to two different physical processes in which bottom topographic form drag is generated (Chapters 2, 3 and 4) and enables geostrophic flow in a β-plane channel to support a net cross-channel volume transport (Chapters 5 and 6). It is demonstrated that by blocking all the geostrophic contours in the presence of a sufficiently high ridge, the dynamics of both source-sink and wind driven circulations in a β-plane is similar to that in a closed basin.

First, wind-driven circulation in the inviscid limit is discussed in a linear barotropic channel model in the presence of a bottom ridge. There is a critical height of the ridge, above which all geostrophic contours in the channel are blocked. In the subcritical case, the Sverdrupian balance does not apply and there is no solution in the inviscid limit. In the supercritical case, however, the Sverdrupian balance applies. The form drag is generated through two different physical processes: the through-channel recirculating flow and the Sverdrupian gyre flow. These processes are fundamentally different from the nonlinear Rossby wave drag generation. In this linear model, the presence of a supercritical high ridge is essential in the inviscid limit. With this form drag generation determined, an explicit form for the zonal transport in the channel is obtained, which shows what model parameters determine the through-channel transport. In addition, the model demonstrates that most of the potential vorticity dissipation occurs at the northern boundary where the ridge intersects.

The result from the homogeneous channel model in Chapter 2 is then extended to a model whose geometry consists of a zonal channel and two partial meridional barriers along each boundary at the same longitude. Both the model transport and especially the model circulation are significantly affected by the presence of the two meridional barriers. The presence of the northern barrier always leads to a decrease in the transport. The presence of the southern barrier, however, increases the transport for a narrow ridge. The northern barrier only has a localized influence on the circulation pattern, while the southern barrier has a global influence in the channel.

Then a multi-layer Q-G model is constructed by assuming that potential vorticity in all subsurface layers is homogenized. The circulation is made up of baroclinic and the barotropic part. The barotropic part is same as that in a corresponding barotropic model, and is solely determined by the wind stress, while the baroclinic part is not directly related to the wind stress. It is determined by the potential vorticity homogenization and lateral boundary conditions. The presence of the stratification does not affect the bottom topographic form drag generation. The interfacial form drag is generated by the stationary eddies. Corresponding to the circulation structure, the zonal through-channel transport associated with the barotropic circulation is determined by the wind stress and bottom topography. The other part associated with the baroclinic circulation, however, is not directly related to the wind stress and it is determined by the background stratification.

Based upon the discussion on the geostrophic contour, a simple barotropic model of abyssal circulation in a circumpolar ocean basin is constructed. The presence of a supercritically high ridge is both necessary and sufficient for geostrophic flow in a $\beta-$plane channel to support a net cross-channel volume flux. In the presence of a sufficiently high ridge, the classical Stommel & Arons theory applies here, but with significant modifications. The major novelty is that a through-channel recirculation is generated. Both its strength and direction depend critically upon the model parameters. Then, a schematic picture of the abyssal circulation in a rather idealized Southern Ocean is obtained. The most significant feature is the narrow current along the northern boundary of the circumpolar basin, which feeds the deep western boundary currents of the Indian Ocean and Pacific Ocean and connects all the oceanic basins in the Southern Ocean.

Finally, the question of how the northward surface Ekman transport out of the circumpolar ocean is returned is discussed in a two-layer model with an infinitesimally thin surface Ekman layer on top of a homogeneous layer of water in a rather idealized Southern Ocean basin. First, the case with a single subtropical ocean basin is discussed. In the case with a sufficiently high ridge connecting the Antarctic and the meridional barrier, an explicit solution is found. The surface Ekman layer sucks water from the lower layer in the circumpolar basin. This same amount of water flows northward as the surface Ekman drift. It downwells in the subtropical gyre, and is carried to the western boundary layer. From there, the same amount of water flows southward as a western boundary current across the inter-gyre boundary between the circumpolar ocean and the subtropical gyre along the west coast to the southern boundary of the meridional barrier. Then, the same amount of water is carried southward and feeds the water loss to the surface Ekman layer due to the Ekman sucking in the interior circumpolar ocean. The case with multiple subtropical ocean basins such as the Southern Ocean is also discussed. It is demonstrated that the surface Ekman drift drives a strong inter-basin water mass exchange.

Thesis Supervisor:
Dr. Rui Xin Huang, Associate Scientist
Woods Hole Oceanographic Institution

Acknowledgments

I have had the good fortune to have worked with many different people during my time in the Joint Program. Looking back, I feel what I have learnt most is patience and persistence. My advisor, Xin Huang, let me work on my own and make my own mistakes. I thank him for sharing his ideas and enthusiasm about the dynamics of the ocean circulation. What I have learnt most from him is never giving up. Joe Pedlosky helped me gain confidence when I was in the difficult time of changing my thesis topic. I learnt from him what is the agony and frustration of taking on a big problem "in the dark". His persistent push has made my stay here more productive than I originally thought. Carl Wunsch taught me how to think critically and how to look at both model and observational results, and their relationship. Pointed questioning by Harry Bryden, Glenn Flierl and Jim Luyten has helped me very much throughout the whole process of my thesis work.

I would like to thank Larry Pratt for serving as my advisor in the first summer when I just came here from China, and Jim Luyten for serving as my advisor in the first year. Over the years, I have had many discussions with other faculty members and students of the MIT/WHOI Joint Program. Among them, I talked with Mike McCartney on the dynamics of the Southern Ocean circulation, Bruce Warren on deep circulation of the world ocean, John Marshall and Sarah Gille for many discussions on the Antarctic Circumpolar Current. I also had interesting discussions with Kirk Bryan, Arnold Gordon and Worth Nowlin on the subject of Southern Ocean circulation. I would like to thank Profs. Qing-cun Zeng and Ronghui Huang for introducing me into this fascinating field of physical oceanography. I would also like to thank my fellow Joint Program students for teaching me a lot of things in addition to physical oceanography. I thank Huai-min Zhang for letting me using his PC, Barbara Gaffron for helping me with my thesis writing.

Most of all, I thank my parents for their love and encouragement. I thank my wife, Yan Lou, for her support and understanding throughout the years, and for her giving birth to my lovely son, Peter, who has added lots of happiness to my time in the Joint Program.

This thesis was supported by National Science Foundation through grant OCE OCE90-17158. Part of the numerical simulation was performed at NCAR's supercomputer, and was supported by SCD/NCAR.

Contents

Chapter 1

Introduction

Among the world oceans, the Antarctic circumpolar ocean is the only one which is not blocked meridionally. It serves to connect the Indian, Pacific and Atlantic Oceans. Through this circumpolar ocean the other three oceans communicate with each other in terms of heat, fresh water and other properties, *e.g.*, Gordon (1986) and Rintoul (1988). Most early data came from commercial exploration of the Southern Ocean. Only recently has more systematic and scientifically oriented exploration of the Southern Ocean taken place resulting in the comprehensive atlas of the Southern Ocean by Gordon *et al.* (1982). A comprehensive and informative history of the Antarctic circumpolar ocean is given by Deacon (1984).

The Antarctic Circumpolar Ocean has long been recognized as a transitional zone between surface waters with antarctic and subantarctic characteristics (Meinardus, 1923). More recent studies, *e.g.*, Gordon *et al.* (1977), showed that this transitional zone further branches into several narrow frontal zones, mainly the subantarctic and polar fronts, as shown in Fig.1.1. Associated with this transitional zone flows the largest eastward current in the world, the **Antarctic Circumpolar Current**. Fig.1.2 shows the geostrophic current at the sea surface referenced to 1000dba. It is about 1800km wide except at Drake

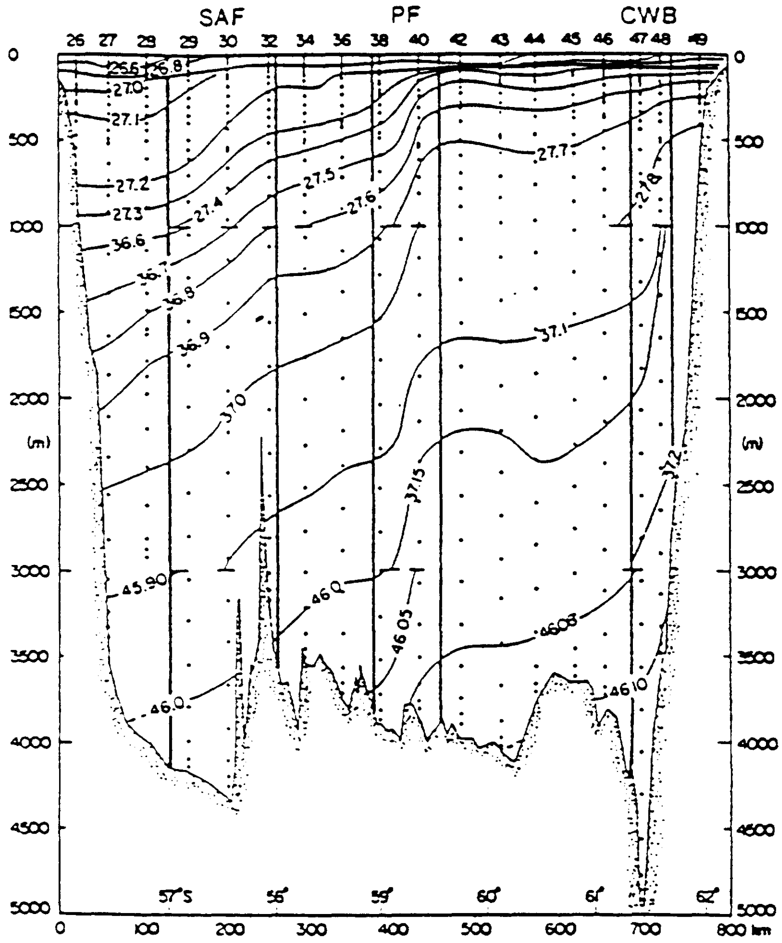

Figure 1.1: Potential density anomaly in vertical section across Drake Passage as observed on R/V *Thompson* during 1976, adapted from Nowlin & Clifford (1982). SAF refers to Subantarctic Front, PF the Polar Front and CWB the Continental Water Boundary.

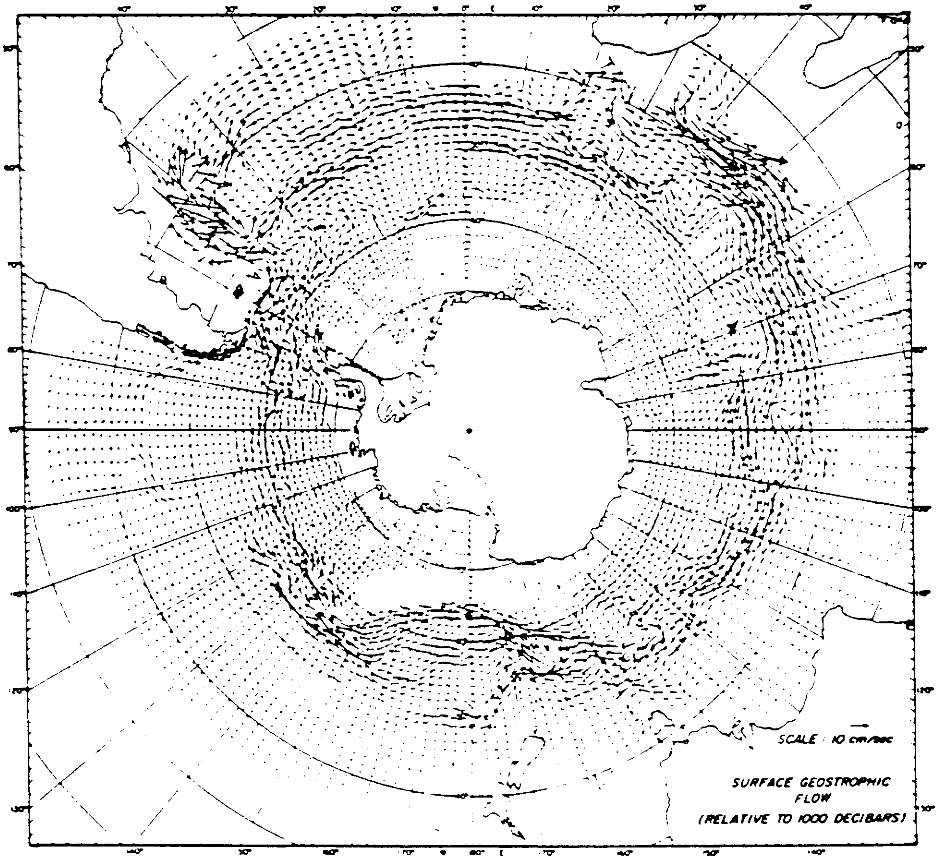

Figure 1.2: Geostrophic current at the sea surface relative to 1000dba from historical data. The current component is evaluated from 1° latitude by 2° longitude grid point values from Gordon *et al.* (1978).

Passage and extends all the way to the ocean floor as indicated by the strong and deep reaching baroclinicity shown in Fig. 1.1.

Similar to gyre circulation in subtropical oceans, the Antarctic Circumpolar Current (hereafter referred to as ACC) has been generally thought to be driven principally by surface wind stress shown in Fig. 1.3, although the relative importance of wind versus thermohaline forcing has not been clearly understood. The problem unique to the circumpolar ocean is how the eastward wind stress input is balanced. Three basic explanations have been proposed in the fifties and sixties. They are: form drag due to bottom topography (Munk and Palmen, 1951); non-zonal dynamics (Stommel, 1957); and the water discharged from the Antarctic (Barcilon, 1966). Very little attention has been given to the overall vorticity balance, *e.g.*, Baker (1982). Despite all these effort and some more recent modeling works, *e.g.*, Wolff *et. al.* (1991) and Klinck (1991), as Nowlin and Klinck (1986) pointed out in their summary of the scientific level of our understanding of the dynamics of the circumpolar ocean as of 1985, the important issue regarding both the momentum and vorticity balances is still unclear. The most fundamental question here is what parameters in the circumpolar ocean determine the zonal transport of the ACC.

1.1 Observational background.

The most fundamental dynamic property of the circumpolar ocean is the zonal transport of the ACC. Realistic estimate of its zonal transport is often used as an observational check on circulation models (Johnson and Bryden, 1989). Early estimates of the ACC transport varied wildly because they required the selection of a reference level using dynamic calculation. As is clearly shown in Fig. 1.1, the geostrophic shear in the ACC extends practically to the bottom. Any choice of a reference level would bias the zonal transport and result in a westward flow below the reference level. The determination of the ACC transport is also complicated by the fact that it is practically impossible to separate the ACC from adjacent

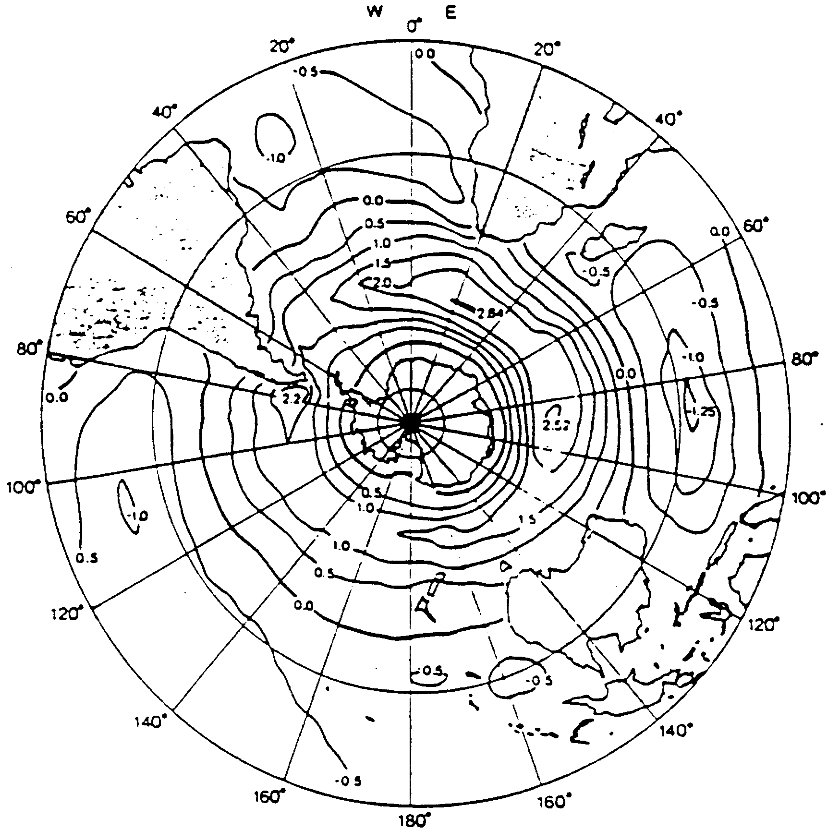

Figure 1.3: Annual mean eastward wind stress (units of $0.1N/m^2$) from Nowlin & Klinck (1986).

currents associated with subtropical gyres in the open ocean except at Drake Passage. So far all estimates of the ACC transport have been done within Drake Passage. This would lead to the question, how representative is the ACC transport calculated within Drake Passage of the entire ACC?

The first estimates of the ACC transport from direct measurement were made at Drake Passage in 1969 (Reid and Nowlin, 1971) and 1970 (Foster, 1972). These two independent estimates gave $237Sv$ and $-15Sv$, respectively. Understandably, these results provoked further field observations. The reason for the wildly different results was later identified as the poor determination of the reference level velocity in the calculation. Using a much better data base, geostrophic transport through Drake Passage relative to 3000dba for seven crossings made from 1975 to 1980 was shown to be fairly stable with an average of $103Sv$ and a standard deviation of $13Sv$ (Whitworth *et al.*, 1982). A major objective of the International Southern Ocean Studies (ISOS) program was to obtain a year long record of ACC transport at Drake Passage. Several estimates emerged from this program: $110 - 139Sv$ (Nowlin *et al.*, 1977), $139 \pm 36Sv$ (Bryden & Pillsbury, 1977) and $127 \pm 14Sv$ (Fandry & Pillsbury, 1979). Among these three estimates agreement was rather good. The eastward flowing ACC is not uniformly distributed latitudinally in the circumpolar ocean. Most of the ACC transport seems to be associated with two current cores separated by a transitional zone. Through the thermal wind relation, these two cores are associated with two density fronts: the subantarctic front and the polar front. Fig. 1.1 shows a vertical section of the density anomaly at Drake Passage. A salient feature of this figure is that the baroclinicity extends practically to the bottom. The fronts are rather narrow, 50 km or less at Drake Passage (Nowlin and Clifford, 1982), and about 100 km in the open ocean (Nowlin & Klinck, 1986). There are studies, *e.g.*, Gordon *et al.* (1978) and Hoffman (1985), which suggest that the Subantarctic Front and Polar Front are circumpolar in extent.

The final ISOS transport product at Drake Passage was a time series from January 1979 to January 1980. Results analyzed by Whitworth & Peterson (1985) are shown here in

Fig. 1.4. The net transport above $2500m$, shown in the top panel of Fig. 1.4, is $125 \pm 10Sv$. The bottom panel shows the geostrophic transport in the upper $2500m$ relative to $2500dba$. The variation in this part clearly has a lower frequency than the total. Pressure records from $500m$ depth on both sides of Drake Passage during $1977 - 1978$ were obtained, which showed a strong semiannual signal (Wearn and Baker, 1980). Attempts have been made to relate the observed variability of zonal transport in Drake Passage to that of the wind stress over the Southern Ocean. Years of effort to correlate the variabilities of the zonal transport and wind stress have proved equally difficult as the attempts to explain the low and high index cycle of the mid-latitude westerlies in the atmosphere (Lindzen, 1986). Wearn & Baker (1980) analyzed a 3-year time series of transport at Drake Passage inferred from the bottom pressure measurement on both sides of Drake Passage. They found a high correlation with the circumpolar-averaged zonal component of wind stress over the latitude band $40°S - 60°S$. Chelton (1982), however, pointed out that the results were suspect on statistical background: the apparent high correlation could be due to existence of energetic, narrow-band semi-annual variability in both time series.

One of the most distinct features of the circulation in the Antarctic circumpolar ocean is that the influence of bottom topography on the circulation is much stronger than that in subtropical gyres. This is demonstrated in two respects. First, the route of the major part of the ACC is steered by bottom topographic features in the circumpolar ocean shown in Fig. 1.5. Second, the influence of the topographic feature around Drake Passage and any others in the circumpolar oceans seems to be quite different. Crossing Drake Passage, the major part of the ACC shifts more than 10 degrees northward while in other place it more or less follows the bathymetry or more precisely local geostrophic contours (Gordon *et al.*, 1978). This clearly indicates that the topographic features around Drake Passage presumably has a far different role in determining the ACC compared to any other topography there.

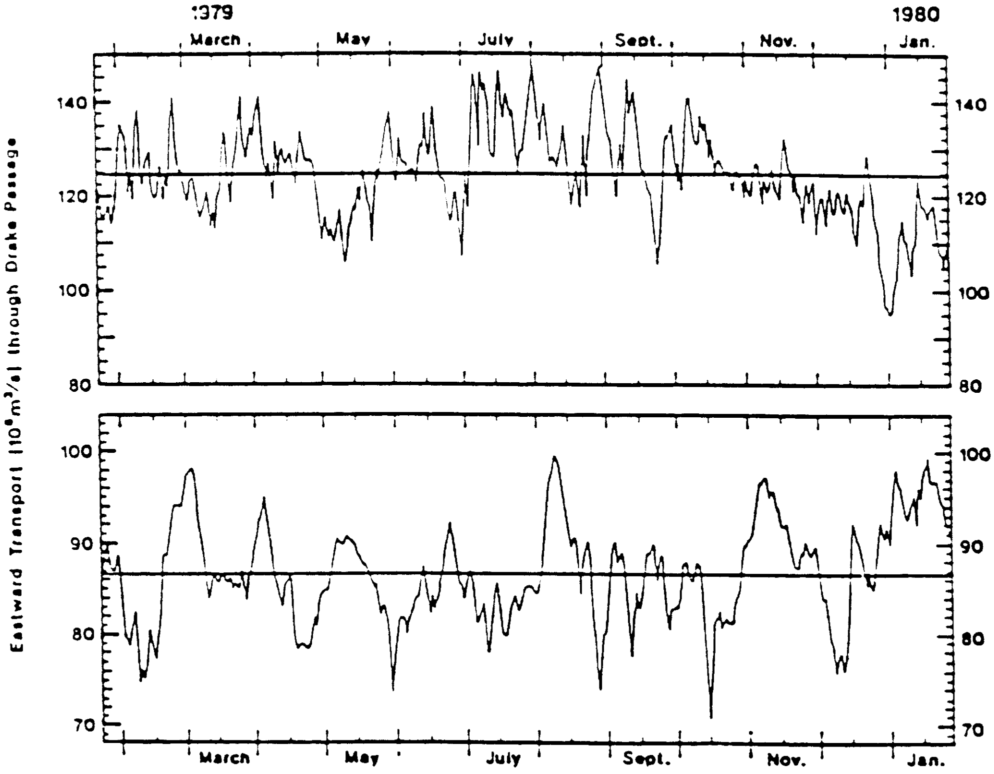

Figure 1.4: Transport time series at Drake Passage in $10^6 m^3/s$ from Whitworth & Peterson (1985). The top panel is the net transport while the lower panel is the geostrophic transport in upper 2500dba.

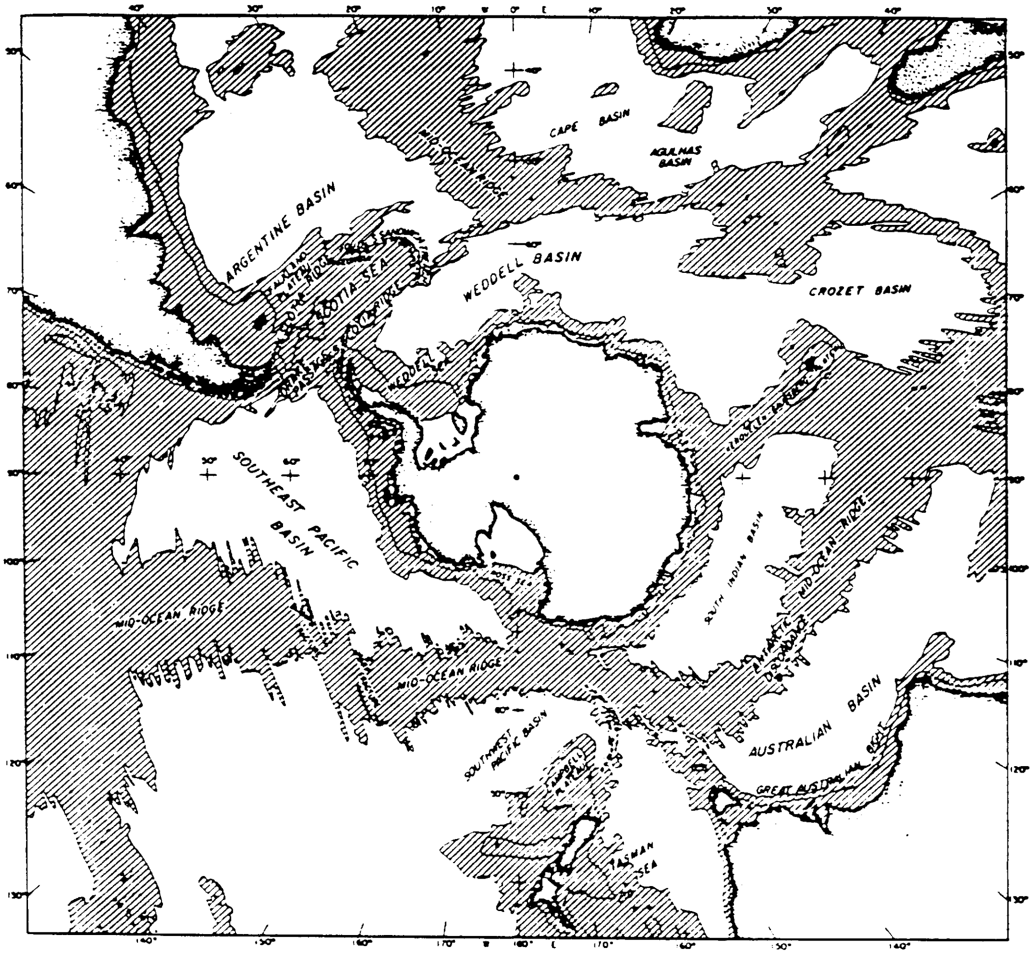

Figure 1.5: Southern Ocean bathymetry from Gordon *et al.* (1978). Depth less than 4000m is hatched.

In addition to the strong ACC, the Antarctic region supplies the World Ocean with its Antarctic Bottom Water, formed around the Antarctic Continent (Warren, 1981). This bottom water formation must be compensated in the upper layer. In the deep layer, the Antarctic Bottom Water could manage to flow northward across the circumpolar ocean as deep western boundary currents against various ocean ridges. In the upper layer, how the water is compensated is unclear. Since a strong meridional density gradient is associated with the ACC as shown in Fig.1.1, a natural density barrier is created. Thus, in the upper layer both sides of the ACC is isolated. Such isolating effect would presumably tend to increase the density gradient across the ACC due to the air-sea heat exchange. This has a profound influence on the baroclinic structure of the ACC. Using a 3-dimensional ocean general circulation model, Cox (1989) found that if Drake Passage is closed, then in the South Atlantic there is a strong meridional cell against South America driven by the buoyancy forcing. In the presence of the gap near Drake Passage, however, the strength of the meridional cell greatly reduces and splits into two cells with the stronger narrow cell lying to the south of the gap. The presence of the ACC, which is generally thought to be driven principally by wind-stress, would further strengthen this isolation of the extreme Southern Ocean from the rest of the World Ocean.

Another related important issue regarding the water mass balance in the circumpolar ocean is how the surface northward Ekman drift, which could be as large as $30Sv$ (Trenberth *et al.*, 1990), is returned. Warren (1990) and Toggweiler & Samuels (1992) argued that on those isopycnal surfaces above the topographic features around Drake Passage there can not be any net geostrophic flow across the circumpolar ocean. Thus, Toggweiler & Samuels (1992) tied the return of the northward surface Ekman drift in the circumpolar ocean with the North Atlantic Deep Water formation. The point is that this North Atlantic Deep Water is deep enough to cross the circumpolar ocean as a regular deep western boundary current against the topographic features around Drake Passage. Nevertheless, this explanation seems to be unable to account for the difference between the North Atlantic Deep Water formation of about $20Sv$ (Warren, 1981) and the surface northward Ekman drift of about $30Sv$ (Trenberth *et al.*, 1990) in the circumpolar ocean, without even mentioning that some of the North Atlantic Deep Water flows to the Indian and Pacific Oceans.

1.2 Dynamical modeling background

The most fundamental issue regarding the ACC is to find a dynamic balance that allows for the observed surface wind stress as a driving force while maintaining a reasonable transport. Transport is the most basic variable used to test the applicability of any models. By the end of 1940's, the groundwork to understand the barotropic structure of the wind-driven gyre circulation in closed basins was laid by Sverdrup (1947), Stommel (1948) and Munk (1950). The natural step adopted by Hidaka and Tsuchiya (1953) was to apply the basic idea of these theories to the circumpolar ocean. In their model, a constant wind stress was applied as the driving force to a $\beta-$plane channel with a flat bottom; lateral and vertical viscous effects provided the dissipation. Their model predicted a transport which was about an order of magnitude larger than the observed value $134Sv$ (Nowlin and Klinck, 1986) with a reasonable choice for the frictional process. Reducing the transport to a reasonable value would require an uncomfortably large eddy frictional coefficient, which would imply (Wolff et al., 1991) a meridional momentum transport of the order of $0.1m^2/s^2$. This is at least an order of magnitude larger than the observed value $10^{-2} \sim 10^{-3}m^2/s^2$ (Bryden and Heath, 1985). This dilemma was later confirmed by McWilliams *et al.* (1978). They developed an eddy-resolving 3-layer Q-G model of the wind-driven circulation in a $\beta-$plane channel. Vigorous eddies due to baroclinic instability developed in the flow. The equivalent eddy viscosity calculated from the model was nearly equal to the value used by Hidaka and Tsuchiya (1953) to get a realistic value for the transport. These results clearly suggested that the basic dynamics adequate in a closed basin can not be directly applied to the circumpolar ocean, and something fundamentally important must have been missing in these models. As a result, three major mechanisms have been advanced to explain the basic dynamics of the ACC.

The *first* one was introduced by Munk and Palmen (1951). They realized that neither the lateral friction nor bottom friction is large enough to balance wind stress. Instead, they proposed that the bottom topographic form drag might be an efficient candidate to balance the wind stress. It is now thought the only proper mechanism to balance the wind stress input, *e.g.*, Johnson and Bryden (1989), Wolff *et al.* (1991). Though continental barriers are absent, yet there are significant submarine ridges to build up a net zonal pressure gradient. They can enable the ultimate transfer of horizontal momentum into the solid earth. This has two implications. First, the ACC must reach the bottom topography. Second, the wind stress is not zonally uniformly transferred down into the bottom. The difficulty with this mechanism is how the bottom topographic form drag is generated and how the wind stress at the surface gets transported down to the bottom in the presence of stratification. The estimation by Wang (1993b), which is not presented here, shows that the form drag due to the nonlinear Rossby wave radiation resulting from flow over topography discussed by people such as McCartney (1975) is too small. This presumably suggests that some other mechanism must account for the major bottom topographic form drag generation in the circumpolar ocean.

The *second* one was proposed by Stommel (1957). From an observational point of view, Stommel was the first to find that the ACC does not flow in a zonal channel at all but that only a narrow band of latitude is not blocked by land barrier. Even this narrow band is blocked by bottom topography that comes within $1000m$ of the surface. Stommel argued that most of the flow is *Sverdrup-like.* Furthermore, he maintained that viscous dissipation takes place in the western boundary currents that exist along land barriers, with the principal dissipation occurring downstream of Drake Passage along South America. Stommel's argument is essentially about the potential vorticity balance associated with the ACC.

The *third* one was put forward by Barcilon (1966, 1967). He showed that the discharge of water from the Antarctic continent can drive a substantial westward flow, thus reducing the eastward zonal transport. However, Nowlin and Klinck (1986) argued that realistically this discharge is too weak to exert any significant effect on the dynamics of the ACC.

Wyrtki (1960) made a detailed Sverdrupian transport calculation for the Southern Ocean using his best estimate for the *meridional* structure of the zonal wind stress at that time. The transport was integrated from the western coast of South America, where meridional structure of the flow across Drake Passage was *prescribed.* The calculated circulation was consistent with the large scale circulation in the Southern Ocean as it was understood then. Obviously, this calculation was a diagnostic calculation which itself could not determine the transport of the ACC. It did not address the dynamic balance within Drake Passage. Baker (1982) made a similar Sverdrupian calculation using a much improved data base. His calculation basically supported Wytki's (1960) calculation.

The first wind-driven transport theory of the ACC was put forward by Kamenkovich (1962) as a combination of barotropic and Ekman flow. No stratification was included, but smooth bottom topography was allowed. Vertical friction was used to balance the wind stress. His model predicted a reasonable transport. However, the assumptions that there is no blocked geostrophic contour and the surface Ekman drift be balanced by a opposite bottom Ekman flow makes it difficult to tell whether his theory is relevant to the ACC. Gill (1968) realized Stommel's (1957) hypothesis in its dynamic detail except with a flat bottom. It was Stommel's basin model (1948) with a recirculating gap. Although his results did show the dynamic importance of the meridional boundaries on the flow in the Southern Ocean, without bottom topography it still required a uncomfortably large bottom friction or lateral friction to get a reasonable ACC transport. Schulman (1970) presented a numerical version of Gill's model including the effect of nonlinearity and bottom topographies. His model results showed that the topographic ridge in Drake Passage had far stronger influence on the ACC than any topographic features in the open ocean. This numerical results suggested that the dynamic balance in Drake Passage might be far different from that in the open ocean, which seemed to be consistent with the observational study such as Gordon *et al.* (1978). A numerical investigation about the interaction of stratification and bottom topography was carried out by Gill and Bryan (1971) by using an eight-level primitive equation model. Two forms were considered for the gap through which recirculation passes: with and without a topographic ridge in the gap. The interesting result of their work was that as they added the topographic ridge, the transport increased rather than decreasing as Munk and Palmen (1951) suggested. They ascribed this to the thermal forcing induced by the presence of the topographic ridge.

Johnson and Bryden (1989) made a diagnostic study of the baroclinic structure of the ACC. Their model incorporated the width of the ACC, the strong eddy process in the region parameterized in terms of large scale characteristics, and the deep penetration of a baroclinically unstable velocity field. Assuming that downward eddy transfer of momentum was predominantly by *transient eddies*, they predicted a reasonable zonal transport. McWilliams *et al.* (1978) described a set of eddy-resolving numerical experiments for a wind driven channel flow over topography. In sharp contrast to the conventional thought of down-gradient diffusion of momentum, their model showed that lateral Reynolds stresses exerted by eddies on the mean flow tended to transfer momentum into the center of the eastward current and thus concentrate the jet. Their model predicted several narrow jets, which might have some implications for the observed multi cores of the ACC. Wolff *et al.* (1991) extended McWilliams *et al.*'s (1978) work to a two-layer eddy-resolving Q-G model. The principal dynamic balance emerging from the model results supported Munk and Palmen's (1951) concept — momentum input by wind stress is transported downward to the deep ocean, where it is further put into the solid earth via the topographic form drag. However, their model results showed that the interfacial form drag is mainly generated by the standing topographic eddies, rather than by the transient eddies as Johnson

& Bryden (1989) assumed. Treguier & McWilliams (1990) reached a similar conclusion in their numerical study on the ACC.

1.3 Overview of thesis

Despite all the effort, the central question as to **what parameters in the Southern Ocean determine the zonal transport of the ACC** is still unanswered. To respond to this question we have to understand the role of bottom topography as previous studies clearly showed us that bottom topography must play an essential role in the overall dynamics of the Southern Ocean circulation. The central question can be answered from two different angles. From the point view of momentum balance the question is really how bottom topographic form drag is generated which is needed to balance the momentum input by the wind stress. How the zonal transport is tied to the bottom topographic form-drag generation is of key importance. In the presence of stratification another question naturally arises as to how the interfacial form drag is generated. From the point view of mass balance in the circumpolar ocean, the westerly wind stress drives the surface northward Ekman flux on the order of about $30Sv$ out of the circumpolar zone. For the large scale circulation it is generally thought that geostrophy applies. In a channel with a flat bottom it is quite clear that geostrophic flow can not carry any net meridional volume flux. Now, how is the northward surface Ekman drift returned? Can geostrophic flow in a channel carry a net cross-channel volume flux?

1.3.1 Model assumptions

The realistic bottom topography and coastal line shape, as shown in Fig.1.5, are too complicated to be included in any simple model. Throughout this thesis, the realistic circumpolar ocean is idealized as either a $\beta-$plane channel (Chapters 2, 4 and 5) or $\beta-$plane channel with simple partial meridional barriers (Chapters 3, 5 and 6). The bottom topography is idealized as simple ridges. Most of the time only a single ridge is considered, for the sake of obtaining a simple explicit solution. It is by no means an attempt to simulate the realistic large scale circulation in the Southern Ocean, but rather to try to understand the physical process behind those complicated Southern Ocean circulations. In Chapters 2, 3 and 4, the dynamic role of bottom topography is discussed from the point of view of momentum balance in the circumpolar ocean. In Chapters 5 and 6, the dynamic role of of bottom topography is discussed from the point of view of water mass balance in the Southern Ocean. The discussions throughout this thesis are carried out with the assumption of *inviscid limit* for the sake of achieving solutions of explicit form. For the large scale wind-driven circulation in a closed basin an important parameter is $U/\beta L^2 \ll 1$, where U and L are the characteristic velocity and length. Thus, the inertial processes are ignored in the theories on the gyre circulation such as those of Rhines & Young (1982b) and Luyten, Pedlosky & Stommel (1983). For the large scale circulation in the circumpolar zone with $U \sim 10cm/s$ and $L \sim 500km$, we have

$$\frac{U}{\beta L^2} \sim 0.04 \ll 1.$$

Another way to look at this is by comparing the meridional momentum flux with the wind stress. Bryden & Heath (1985) concluded from observational data that the meridional momentum flux is about an order of magnitude smaller than the mean wind stress input. Thus, in the discussions through-out this thesis all inertial processes will be ignored. Within the various frontal structure with $U \sim 50cm/s$ and $L \sim 100km$, however, $U/\beta L^2 > 1$. Thus frontal structure is left out throughout this thesis. Furthermore, as a first step towards understanding the large scale circulation in the Southern Ocean, we will ignore the variabilities of the circulation throughout the thesis.

1.3.2 Synopsis of thesis

In Chapter 2 we study the wind-driven circulation in a linear barotropic channel model in the presence of a bottom ridge. There is a critical height of the ridge, above which all geostrophic contours in the channel are blocked. In the subcritical case, the Sverdrupian balance does not apply and there is no solution in the inviscid limit. In the supercritical case, however, the Sverdrupian balance applies. The form drag is generated through two different physical processes: the through-channel recirculating flow and the Sverdrupian gyre flow. These processes are fundamentally different from the nonlinear Rossby wave drag generation. In this linear model, the presence of a supercritically high ridge is essential in the inviscid limit. The form-drag is generated regardless of the flow direction. With this form drag generation determined, an explicit form for the zonal transport in the channel is obtained, which clearly shows what model parameters determine the through-channel transport. In addition, the model demonstrates that most of the potential vorticity dissipation occurs at the northern boundary where the ridge is located.

In Chapter 3, the results from the homogeneous channel model in Chapter 2 are then extended to a model whose geometry consists of a zonal channel and two partial meridional barriers along each boundary at the same longitude. Both the model transport and especially the model circulation are significantly affected by the presence of the two meridional barriers. The relation between the transport and model parameters is more complicated. The presence of the northern barrier always leads to a decrease in the transport. The presence of the southern barrier, however, increases the transport for a narrow ridge. In terms of the circulation structure, the presence of a southern barrier has a far more profound influence than that of a northern one. The northern barrier only has a localized influence (confined over the ridge) on the circulation pattern, while the southern barrier has a global influence in the channel.

In Chapter 4, the influence of stratification is discussed. A multi-layer Q-G model is constructed by assuming that potential vorticity in all sub-surface layers is homogenized, which is presumably achieved by those transient eddies resulting from baroclinic instability, not explicitly included. It is shown that the circulation is made up of the baroclinic part and the barotropic part, which is same as that in a corresponding barotropic model. The wind stress only determines the barotropic component, while the baroclinic part is not directly related to the wind stress. The potential vorticity homogenization and the lateral boundary conditions together determine the baroclinic component. The presence of the stratification does not affect the bottom topographic form drag generation discussed in the corresponding barotropic model. The interfacial form drag is generated by the stationary perturbations. Corresponding to the circulation structure, the zonal through-channel transport associated with the barotropic circulation is determined by the wind stress and bottom topography. The other part associated with the baroclinic circulation, however, is not directly related to the wind stress and it is determined by the background stratification. The presence of stratification increases the zonal transport.

In Chapter 5, based upon the discussion on the geostrophic contour, a simple barotropic model of abyssal circulation in a circumpolar ocean basin is constructed. The presence of a supercritically high ridge is both *necessary* and *sufficient* for geostrophic flow in a $\beta-$plane channel to support a net cross-channel volume flux. In the presence of a sufficiently high ridge, the classical Stommel & Arons theory applies here, but with significant modifications. The major novelty is that a through-channel recirculation is generated. Both its strength and direction depend critically upon the model parameters. Then, a schematic picture of the abyssal circulation in a rather idealized Southern Ocean is obtained. The most significant feature is the narrow current along the northern boundary of the circumpolar basin. It feeds the deep western boundary currents of the Indian Ocean and Pacific Ocean and serves to connect all the oceanic basins in the Southern Ocean.

Then, in Chapter 6 the question of what is the fate of the northward surface Ekman transport out of the circumpolar zone is discussed in a two-layer model with an infinitesimally thin surface Ekman layer on top of a homogeneous layer of water in a rather idealized Southern Ocean basin. First, the case with a single subtropical ocean basin is discussed. In the case with a sufficiently high ridge connecting the Antarctic and the meridional barrier, an explicit solution is found. The surface Ekman layer sucks water from the lower layer in the circumpolar basin. This same amount of water flows northward as the surface Ekman drift, and downwells to the lower layer in the subtropical gyre, where it is carried to the western boundary layer. From the western boundary layer of the subtropical gyre, the same amount of water flows southward as a western boundary current across the inter-gyre boundary between the circumpolar ocean and the subtropical gyre along the west coast to the southern boundary of the meridional barrier. From there, the same amount of water is carried southward by the wind-driven Sverdrupian gyre circulation and feeds the water loss to the surface Ekman layer due to the Ekman sucking in the interior circumpolar ocean. Then, the case with multiple subtropical ocean basins such as the Southern Ocean is discussed. It is demonstrated that the surface Ekman drift drives a strong inter-basin water mass exchange.

It should be pointed out that due to the assumption of the inviscid limit, internal discontinuities of streamfunctions is one of the major features in the circulation. The internal current is presumably vulnerable to the presence of small but finite dissipation. It is not very clear to us at this time how much of and to what degree the circulation obtained in the inviscid limit will change when finite friction is introduced into the model. A parallel numerical calculation with finite friction is very desirable in testing the robustness of the solution, especially that of the multi-layer model, in the invicsid limit.

In summary, the dynamic role of bottom topography in the potential vorticity, momentum and mass balances in a $\beta-$plane channel is discussed. *It will be shown that by blocking all geostrophic contours, the dynamics of both wind and source-sink driven circulation in a $\beta-$plane channel is somewhat similar to that in a closed basin which we are familiar with.* The physical process through which bottom topographic form drag is generated is discussed in Chapter 2. The influence of partial meridional barriers on the wind-driven circulation is discussed in Chapter 3. The influence of stratification is discussed in Chapter 4. A simple model for the abyssal circulations will be presented in Chapter 5. The water mass balance associated with the wind-driven circulation is discussed in Chapter 6. We conclude this thesis with summary and discussion about the relevance of the results from this thesis to the realistic large scale circulations in the Southern Ocean in Chapter 7.

Chapter 2

Wind-driven circulation in a β–plane channel, Part I: A linear homogeneous channel model

2.1 Introduction

Ever since the pioneering work of Sverdrup (1947), Stommel (1948) and Munk (1950), almost all theories about large scale wind-driven circulations have been focused upon the gyre circulations within closed basins, such as the North Atlantic. The backbone of all these theories is Sverdrup dynamics, which is essentially a theory of potential vorticity. Within the framework of this theory, it is generally assumed that gyre-scale circulations within closed basins can be divided into two parts in which different dynamic processes prevail. The first part is the so-called Sverdrup interior where friction and inertial effects are not important. The second part is the western boundary region where the interior southward Sverdrup flow is returned northward. Within this western boundary region, higher order dynamics such as bottom friction (Stommel, 1948), lateral diffusion (Munk, 1950) and inertial effects (Charney, 1955) neglected in the Sverdrup interior are of essential importance. These theories have been quite successful in explaining many important observed features in large scale gyre circulations. See Huang (1991) for a review of the latest developments in the theories of large scale wind-driven circulations.

Despite much success in explaining wind-driven gyre circulations in closed basins, the dynamic features of the Antarctic Circumpolar Current are poorly understood. Different from basins with meridional boundaries, the Antarctic Circumpolar region between $56^{o}S$ and $62^{o}S$ is the only zonally unbounded region in the world oceans. Here the westerlies continuously put eastward momentum and negative potential vorticity into the eastward-flowing ACC (Nowlin and Klinck, 1986). Unlike the gyre circulation, here both the momentum balance and potential vorticity balance play vital roles in determining the structure of the ACC. The essence of the Sverdrup theory is the presence of an eastern boundary which blocks all the geostrophic contours and gives rise to a single solution by integrating from the eastern boundary. Since there are no meridional barriers in the Antarctic Circumpolar Ocean, it is not clear whether Sverdrup dynamics can apply.

The most fundamental issue regarding the ACC is to find a dynamic balance which allows for observed surface wind stress as a driving force while maintaining reasonable transport values. Transport is a key variable to test the applicability of models to the ACC. Early on, Munk and Palmen (1951) suggested that topographic form drag could provide the retarding force necessary to balance the wind stress. Stommel (1957) first observed, which is now apparent from the Gordon *et al.* atlas (1982), that the ACC does not flow along latitude circles at all. In fact only a narrow band of latitude is not blocked by land barriers and even this band is semi-blocked by bottom topography that comes within 1000m of the surface. Stommel maintained that most of the flow is Sverdrupian-like, since a pressure difference is allowed to build up across continental boundaries. He further argued that dissipation take place mainly in the western boundary currents present along the land barriers, with the principal dissipation occurring downstream of the Drake Passage along South America.

Wang (1993a) (hereafter referred to as W93) has carried out a series of studies on wind-driven circulation in a $\beta-$plane channel, mostly through the approach of numerical integration for the viscous cases with or without inertial effects. These studies show that a topographic ridge and isolated topography have fundamentally different dynamic influences on the wind-driven circulation. This suggests to us that the topography near Drake Passage might play a far different role than any others in the Circumpolar Ocean. To see this, we consider the following linear barotropic potential vorticity equation in the case with a uniform wind stress

$$J\left(\psi, \beta y + \frac{f_0}{H}\right) = -\kappa \nabla^2 \psi, \tag{1.1}$$

where conventional notations (see Pedlosky, 1987) have been used, and f_0, H, h and κ represent the mean Coriolis parameter in the $\beta-$plane channel whose width is D, the mean total water depth, the bottom topography and the bottom frictional coefficient, respectively. In this simple linear model, the geostrophic contours are determined by

$$q = \beta y + \frac{f_0}{H} h(x, y).$$

In the case with isolated topography, no geostrophic contour is blocked due to the presence of the topography. In the inviscid limit, there is a free mode to the linear model with

$$\psi_f = Q\left(\beta y + \frac{f_0}{H} h\right),$$

where Q could be any function. However, in the presence of a ridge, such as $h = h(x)$, some geostrophic contours will be blocked by the lateral boundaries. There is a critical height

$$h_c = \frac{\beta D}{|f_0|} H,$$

above which, namely

$$max\{h(x)\} > h_c,$$

all geostrophic contours in the channel are blocked by the lateral boundaries due to the presence of the ridge. In this case, there is no free solution to the linear model in the inviscid limit. Any motions have to be externally forced. Actually, Bryan & Cox (1972) already pointed out the importance of the geostrophic contour blocking in their numerical simulation of the world ocean circulations. The numerical calculations in W93 suggest that in the case with $h_0 > h_c$, the total through-channel transport converges to a finite value as κ diminishes. This implies that a linear model possesses a basic dynamic balance in the inviscid limit. The calculations also indicate that the zonal transport in the channel tends to increase as the width of the ridge increases and decreases as the ridge height increases. The numerical calculations, however, could not provide a clearer picture beyond these points due to its own limitation. Then, the fundamental questions still remain to be answered as to what and how model parameters determine the zonal transport in the channel.

The first theory about the through-channel transport involving bottom topography was proposed by Kamenkovich (1962). He made the assumption that there were no blocked geostrophic contours, which in his model coincide with the streamlines to the lowest order. Given the situation in the Drake Passage, this is clearly not justified. He showed that the interior transport along the curves of constant f/H is proportional to the integral of the wind stress component along f/H contours. Johnson and Hill (1975) extended Kamenkovich's model (1962) into a 3-D homogeneous ocean with the additional assumption that the surface Ekman transport balances the bottom Ekman transport. The model result is about the same as that of Kamenkovich's. Given the situation around Drake Passage, obviously, we have to modify the assumption that no geostrophic contour is blocked. Davey (1980) presented a quasi-linear theory for rotating flow over topography in periodic channel. His model had a weak and uniform forcing for small bottom friction and again isolated bottom topography was used.

In this chapter, the Circumpolar Ocean is idealized as a simple homogeneous zonal β−plane channel, isolated from the rest of the world ocean. There has been observational evidence (Johnson & Bryden, 1989) that suggests that the momentum exchange between the ACC and its adjacent oceans is negligible compared with the momentum input from the wind stress. The focus of our study is on a linear barotropic model of the wind-driven circulation in a zonal β−plane channel in the inviscid limit. The discussions for a β−plane channel in the presence of partial meridional barriers will be presented in Chapter 3. The influence of stratification will be discussed in Chapter 4. The most fundamental question we want to pursue is what and how model parameters control the zonal transport in the channel. To analyze the dynamics of the circulation, several idealized prototypes will be studied. We will begin our analyses with a f−plane channel model forced by a uniform wind stress in Section 2, because it is very simple, yet physically rather illuminating. Afterwards we will discuss the circulation in a β−plane channel forced by a uniform wind stress in Section 3. The dynamic effect of the wind stress curl on the transport will be discussed in Section 4. Special attention will be paid to topographic form drag generation via the wind stress curl forcing. Finally, Section 5 closes this chapter with some discussions about the results and the relevance of the model results to the Antarctic Circumpolar Current.

2.2 An f−plane model with a uniform wind stress

Assuming a uniform wind stress with $\tau_x = constant$ and $\tau_y = 0$, for an f−plane channel the potential vorticity equation (1.1) reduces to

$$J\left(\psi, \frac{f_0}{H}h\right) = -\kappa\nabla^2\psi, \tag{2.1}$$

with boundary conditions

$$\psi|_{y=0} = 0; \qquad \psi|_{y=D} = \psi_0. \tag{2.2}$$

ψ_0 is determined through the momentum balance

$$f_0 h \overline{\frac{\partial \psi}{\partial x}}^{xy} - \kappa \frac{H}{D} \psi_0 + \frac{\tau_x}{\rho_0} = 0, \tag{2.3}$$

obtained by multiplying the zonal momentum equation by $H - h$, integrating over the whole channel and using the quasi-geostrophic approximation. In (2.3), $-xy$ is defined as

$$\overline{Z}^{xy} \equiv \frac{1}{LD} \int_0^L \int_0^D Z \, dx dy,$$

where L is the length of the channel. First, consider a simple case with

$$h(x,y) = \begin{cases} h_0 (1 - |\frac{L/2 - x}{x_0}|) & \text{if } |L/2 - x| \leq x_0; \\ 0 & \text{otherwise.} \end{cases} \tag{2.4}$$

The channel is divided into three different dynamic regions, A, B and C, shown in Fig. 2.1. On this $f-$plane channel, the potential vorticity is

$$q = \frac{f_0}{H} h + f_0,$$

i.e., the topographic vortex stretching term plus a constant planetary vorticity. For any isolated topographic features in the $f-$plane channel, geostrophic contours coincide with isobaths and thus close themselves. Any ridge in the form of (2.4) with $h_0 > 0$, however, would block all the geostrophic contours over the ridge, as is shown in Fig. 2.1. In fact, the critical height for the ridge like (2.4) is

$$h_c = 0.$$

So any ridge with $h_0 > 0$ would block all the geostrophic contours over the ridge; Fig. 2.1 is just one such example.

In region A, the potential vorticity is uniform and fluid particles are allowed to move without any external potential vorticity forcing. In regions B and C, fluid particles are free to move along isobaths. Any cross-isobath movement, however, has to be associated with strong vorticity generation through the bottom frictional process, as is obvious from (2.1). Consider how a fluid particle, P, shown in Fig. 2.1, crosses the ridge. In region A, its

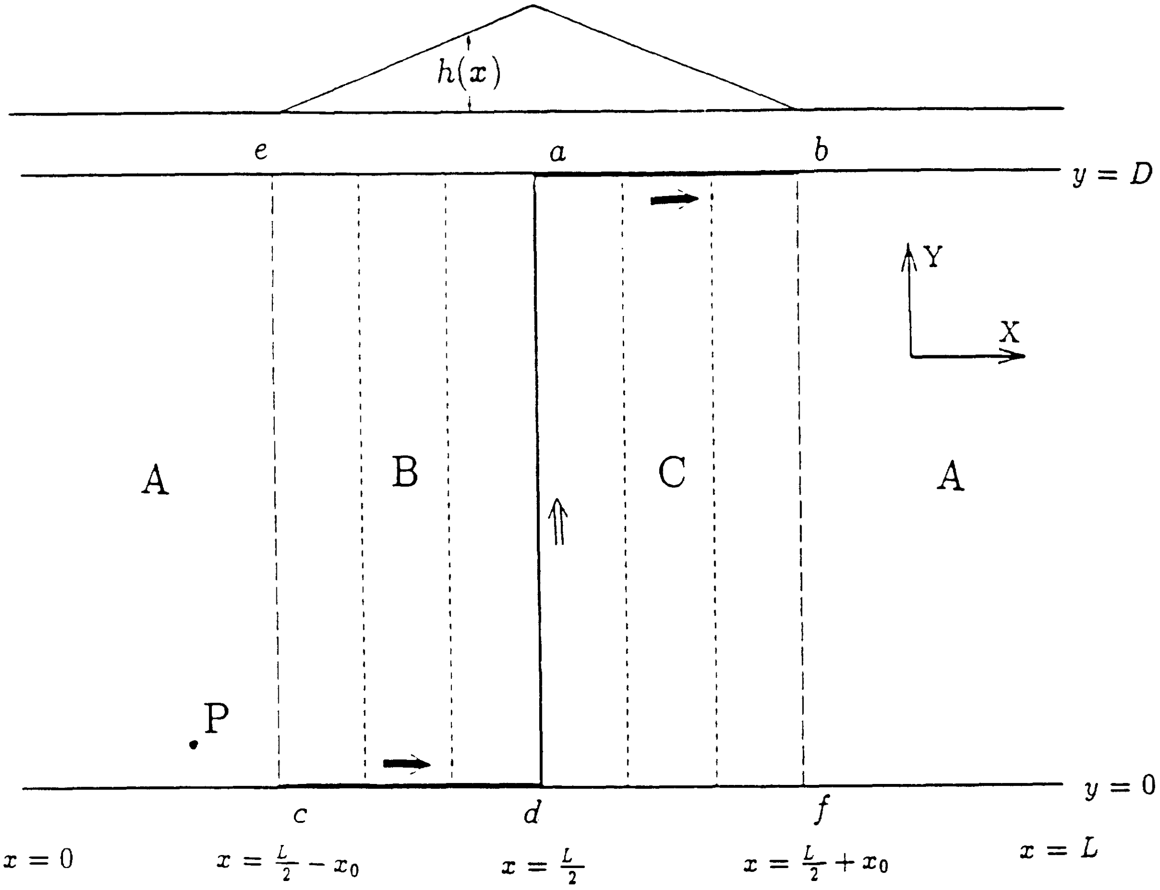

Figure 2.1: A schematic view of the domain of the circulation driven by a uniform wind stress in an f−plane channel over the ridge. On top is the profile of the ridge. The dashed lines over the ridge are the geostrophic contours. The solid arrows represent boundary layer currents, the open arrow represents the internal current along a geostrophic contour.

potential vorticity is f_0. When P crosses $x = L/2 - x_0$ and enters B, its potential vorticity changes to $f_0(1 + h/H)$. Thus, there must be a source of negative vorticity. In this model, it can only come from the frictional torque produced by the bottom friction within some narrow boundary layers. In fact, a narrow southern boundary layer current over region B along segment $c - d$ fits the vorticity requirement because the strong frictional force near the southern boundary and the weak frictional force off the boundary creates the necessary vorticity source for a boundary current. On the other hand, any strong zonal current away from the southern boundary can not meet the vorticity requirement because on the southern side of such a current there is positive vorticity generation due to the cyclonic velocity shear. Similarly, there is a northern boundary layer along segment $a - b$ over the region C. Accordingly, there is no boundary current possible along segment $e - a$ and $d - f$. So, compared to Stommel's classical model (1948) for a wind-driven circulation in a closed basin, $e - a$ and $d - f$ are the two equivalent eastern boundaries, while $a - b$ and $c - d$ are the two equivalent western boundaries with the background potential vorticity decreasing (increasing) over region B (C) eastward.

Once the equivalent eastern and western boundaries are identified, it is rather straightforward to find the solution in the inviscid limit. This is true for any arbitrary ridges. In the inviscid limit the governing equation for both regions B and C except the two equivalent western boundaries is

$$J\left(\psi, \frac{f_0}{H}h\right) = 0.$$

Introducing characteristic variable s such that

$$\frac{dx}{ds} = \frac{f_0}{H}\frac{\partial h}{\partial y}, \tag{2.5}$$

$$\frac{dy}{ds} = -\frac{f_0}{H}\frac{\partial h}{\partial x}, \tag{2.6}$$

the potential vorticity equation reduces to

$$\frac{d\psi}{ds} = 0. \tag{2.7}$$

The boundary condition for region B, at the equivalent eastern boundary $e - a$, is

$$\begin{aligned} y|_{s=0} &= D, \\ \psi|_{s=0} &= \psi_0. \end{aligned}$$

Thus the solution is

$$\psi|_B = \psi_0, \tag{2.8}$$

except within the equivalent western boundary layer along segment $c - d$. This is true for any arbitrary ridge. Similarly, the boundary condition for region C, at the equivalent eastern boundary $d - f$, is

$$\begin{aligned} y|_{s=0} &= 0, \\ \psi|_{s=0} &= 0. \end{aligned}$$

Thus the solution is

$$\psi|_C = 0, \tag{2.9}$$

except within the equivalent western boundary layer along segment $a - b$. Along $c - d$, the governing equation for the boundary layer current is

$$\frac{\partial \psi}{\partial y} = -\delta \frac{\partial^2 \psi}{\partial y^2},$$

where

$$\delta = \kappa/\alpha \ll D$$

with $\alpha = -(f_0/H)(\partial h_0/\partial x) = -f_0 h_0/H x_0$ as the topographic β. δ is the Stommel boundary layer thickness along $c - d$. The boundary layer solution is

$$\psi = \psi_0(1 - e^{-y/\delta}), \tag{2.10}$$

except right near the corner points $x = L/2 - x_0$ and $x = L/2$. Similarly, along segment $a - b$ except $x = L/2$ and $x = L/2 + x_0$, the boundary layer structure is

$$\psi = \psi_0 e^{-(D-y)/\delta}. \tag{2.11}$$

This completes the solution over the ridge. Between B and C is a discontinuity of streamfunction with

$$\Delta\psi|_{C-B} \;=\; -\psi_0, \tag{2.12}$$

which represents the internal jet connecting the two equivalent western boundary currents along segments $a-b$ and $c-d$.

With this solution over the ridge, the topographic form drag can be easily calculated. The total form drag generated in the channel is

$$\tau_{total} \;\equiv\; -\rho_0 \iint f_0\psi\frac{\partial h}{\partial x}dxdy \;=\; \rho_0(H\psi_0)\Delta q D,$$

where $\Delta q \;\equiv\; -f_0h_0/H$. Thus, in the inviscid limit, the total form drag is linearly proportional to the zonal transport, $-H\psi_0$, in the channel, the width of the channel D, and the strength of the potential vorticity barrier $\Delta q \;=\; -f_0h_0/H$ imposed by the ridge. It is linearly related to the relative height of the ridge with respect to the mean depth of the water in the channel and the Earth's rotation rate. This linear topographic form-drag generation is fundamentally different from that due to the downstream nonlinear Rossby wave radiation in inertial models discussed by Johnson (1977). In an inertial model on an $f-$plane, there is no topographic form drag generation. While in this linear barotropic Q-G model in the inviscid limit, although isolated topographic features can not generate form drag, ridges which block all geostrophic contours can lead to topographic form drag generations. The form-drag is generated regardless of the flow direction in the channel, and it is always against the flow.

From the total form drag, the channel-averaged form drag is

$$\tau_D \;\equiv\; \rho_0 f_0 \overline{h\frac{\partial\psi}{\partial x}}^{xy} \;=\; -\rho_0\frac{f_0h_0\psi_0}{L}. \tag{2.13}$$

Balancing the form drag and the wind stress input, one obtains the transport and a simple relation between the model parameters and the zonal transport in the channel in the inviscid limit

$$T_r \equiv -H\psi_0 = \frac{\tau_0 H L}{\rho_0 |f_0| h_0}. \tag{2.14}$$

According to (2.14), the relation between the model parameters and the zonal transport in the channel is rather simple in the inviscid limit. First of all, this simple formula shows that the width of the channel has no effect on the total transport, which is fundamentally different from the frictionally controlled case with a flat bottom such as that discussed by Hidaka & Tsuchiya (1953) and the β−plane case to be discussed later. This can be understood in the following way. By averaging the x-momentum equation along the southern boundary and using $v|_{y=0} = 0$, we obtain a momentum constraint at $y = 0$

$$\kappa \overline{u|_{y=0}}^x = \frac{\tau_0}{H\rho_0}. \tag{2.15}$$

It indicates that at the southern boundary, the wind stress is balanced purely by the bottom frictional drag. This is also true at the northern boundary. As $\kappa \to 0$, the boundary layer current along segment $c - d$ converges into a very strong narrow jet with characteristic thickness $\delta \ll D$. Thus, the channel width D has no direct influence on either the boundary layer thickness or the structure of the solution in the inviscid limit. Using (2.10) one has

$$\overline{u|_{y=0}}^x = \frac{f_0 h_0}{H} \cdot \frac{\psi_0}{\kappa L}, \tag{2.16}$$

which is independent of both D and x_0. Substituting (2.16) into (2.15) still leads to (2.14). Second, the transport is proportional to L, the length of the channel. This is simply because the total wind stress input along each latitude is proportional to L while the total form drag is independent of the length of the channel. Lastly, the width of the ridge has no effect on the transport so long as it is finite because either the form drag generation or (2.16) is independent of the width of the ridge.

Equation (2.14) can be rewritten as

$$T_r = \frac{\tau_0 L/\rho_0}{\Delta q},$$

where $\Delta q = -f_0 h_0/H$. Thus, the transport is inversely proportional to the strength of the background potential vorticity barrier Δq, introduced by the presence of the ridge and determined by the ridge height. From the potential vorticity balance, Δq represents the net amount of potential vorticity each fluid particle has to exchange with the bottom in order to cross the ridge. In this sense, the problem is really potential vorticity controlled in the inviscid limit. Δq measures *the degree to which the ridge impedes the through-channel flow.* Thus, we introduce a parameter, **potential vorticity resistance**, as

$$P_c = \Delta q,$$

for a single ridge. In the case with a flat bottom, there is no potential vorticity resistance, and the zonal transport in the channel goes to infinity in the inviscid limit. Similarly, for isolated bottom topography with no blocked geostrophic contours, no potential vorticity resistance is introduced either, so the transport still goes to infinity in the inviscid limit. P_c depends upon three model parameters, namely, f_0, the Coriolis parameter, H, depth of the water, and the ridge height, h_0. In the barotropic model, the bottom topography affects the whole water column uniformly, so it is not surprising to see that the model transport is very sensitive to the ridge height, especially when h_0 is low.

So far, only the circulation structure over the ridge has been discussed. In the interior away from the ridge, region A in Fig. 2.1, the governing equation is

$$\frac{\partial^2\psi}{\partial x^2} + \frac{\partial^2\psi}{\partial y^2} = 0.$$

The boundary conditions at $y = 0, D$ are

$$\psi|_{y=0} = 0; \qquad \psi|_{y=D} = \psi_0,$$

while those at $x = L/2 - x_0$ and $x = L/2 + x_0$ are

$$\psi|_{x=L/2-x_0} = \psi_0 \quad for \quad y \neq 0,$$
$$\psi|_{x=L/2+x_0} = 0 \quad for \quad y \neq D;$$

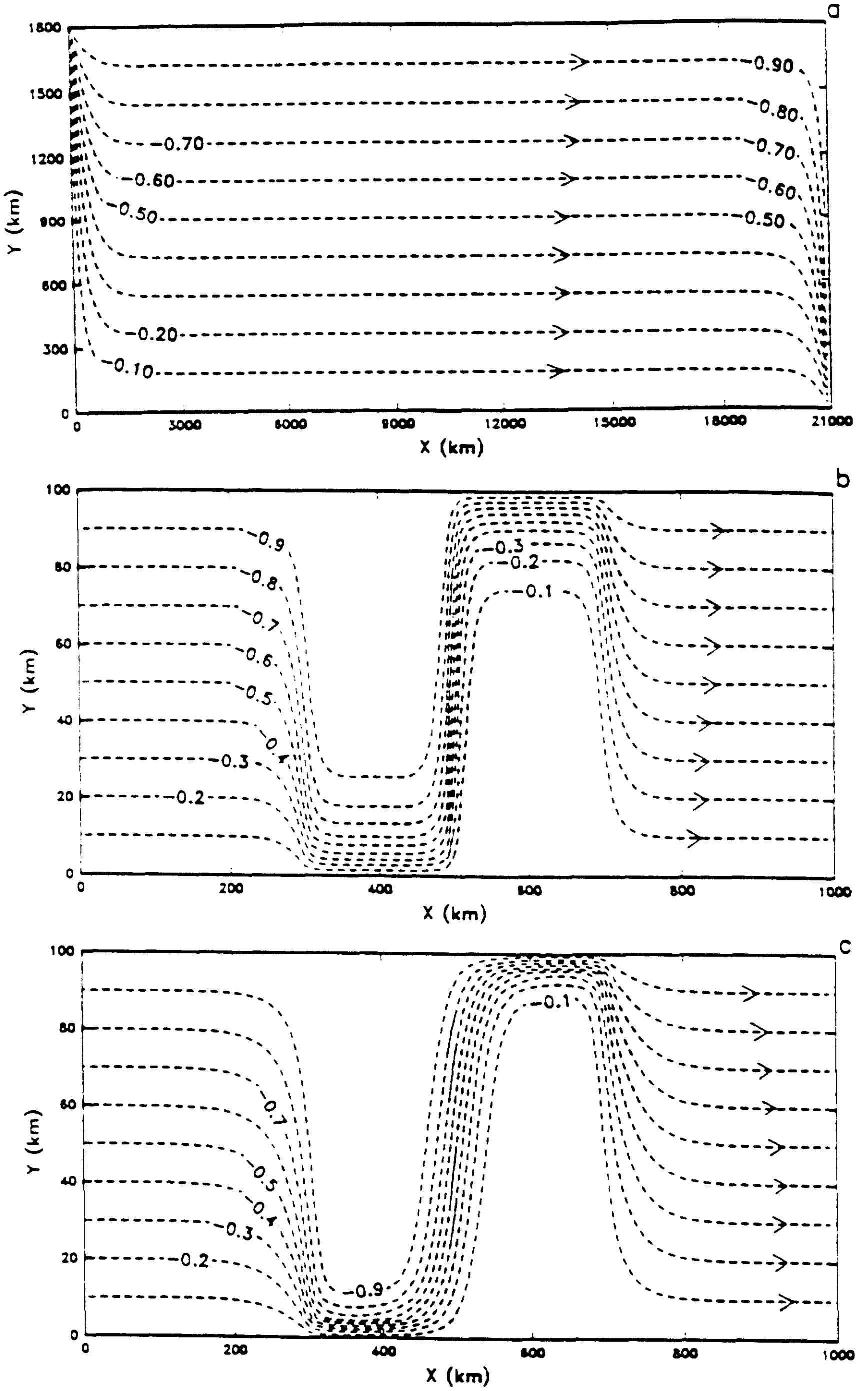

Figure 2.2: (a) The normalized streamfunction in the interior away from the ridge in the inviscid limit with $L = 24000km$, $D = 1800km$ and $x_0 = 1500km$, the corresponding circulation over the ridge shown in Fig. 2.1. (b) The normalized streamfunctions of the wind-driven circulation in the f−plane channel, for a case with a ridge in the form of (2.4), $\tau_0 = 0.08N/m^2$, $L = 1000km$, $D = 100km$, $x_0 = 200km$, $h_0 = 60m$ and small but finite friction $\kappa = 5 \times 10^{-8}/s$. Note here that in order to resolve the boundary layer currents, a much smaller model domain is used. (c) Same as (b) but for a case with a Gaussian ridge.

see the appendix for a detailed discussion. Fig. 2.2(a) shows the normalized interior streamfunction in the inviscid limit with $x_0 = 1500km$. It is driven by a source at the upper left corner and a sink at the lower right corner. This figure together with the circulation over the ridge sketched in Fig. 2.1 completes the wind-driven circulation in the $f-$plane channel in the inviscid limit.

In the inviscid limit, along segment $d-a$ over the ridge is a strong internal jet whose width is zero. In the presence of a small but finite κ, its width is finite. The leading terms in the potential vorticity balance are

$$\alpha\frac{\partial\psi}{\partial y} = \kappa\frac{\partial^2\psi}{\partial x^2}.$$

A scale analysis of this equation would give the thickness of the internal boundary layer as

$$\delta_x \sim \sqrt{\delta D}.$$

It is quite different from the Stommel boundary layers. Numerical integration of the model (2.1) and (2.2) is employed to find the solution for a small but finite κ. Fig. 2.2(b) shows the normalized streamfunction for a topographic feature in the form of (2.4) with $h_0 = 60m$ and $\kappa = 5 \times 10^{-8}$. In order to resolve the boundary layers whose scales are $\delta \sim 5km$ and $\delta_x \sim 23km$, a much smaller model domain is chosen with $D = 100km$, $L = 1000km$ and $x_0 = 200km$. The model resolution is $\Delta x = 10km$ and $\Delta y = 5km$. Both the internal boundary layer over the ridge and the two Stommel boundary layers along the two equivalent western boundaries are well resolved. Corresponding to the inviscid solution, there are a southern and a northern boundary layer over the ridge, which are joined by an internal boundary current on the top of the ridge. About $100km$ (the width of the channel) away from the ridge, is a uniform interior flow. Although the discussion so far has been only for the case with linear profile like (2.4), the same approach and argument apply to cases with arbitrary profile. One example is shown in Fig. 2.2(c) with same model setting, except that $h(x)$ has a Gaussian shape. Because α now changes with x, so does the boundary layer thickness. And noticeably, $\alpha \to 0$ as $x \to 0$. So for finite

κ, there is substantial east-west tilting of the internal jet joining the two boundary layer jets. But as $\kappa \rightarrow 0$, the internal jet will and should converge to line $x = L/2$.

Finally, let us consider a case in which the topography consists of a series of isolated ridges such as that shown in (2.4) with corresponding height $\{h_{*i}\}$ $(i = 1, \cdots, N)$. Following the same argument as that for the case of a single ridge, each ridge produces a potential vorticity resistance with strength

$$P_{cj} = -f_0 \frac{h_{*j}}{H}.$$

The total potential vorticity resistance introduced by the presence of the series of isolated ridges is then

$$P_c = \sum_j P_{cj},$$

which is again independent of the width of the ridges. The presence of any additional isolated bottom topographic features makes no contribution to the total potential vorticity resistance. Correspondingly, the through-channel transport is

$$T_r = \frac{\tau_0 L/\rho_0}{P_c}. \tag{2.17}$$

It is rather interesting to see that formally the relation among the total wind stress forcing $\tau_0 L$ along each latitude, the model transport T_r and the potential vorticity resistance P_c is strikingly similar to Ohm's law in the elementary theory of electricity.

2.3 A β−plane model with a uniform wind stress

We discussed the wind-driven circulation in a f−plane channel forced by a uniform wind stress. In the presence of a potential vorticity barrier introduced by a ridge, for example, the through-channel transport of the wind-driven circulation is potential vorticity controlled in the inviscid limit. In a β−plane channel, the presence of the β−effect tends to

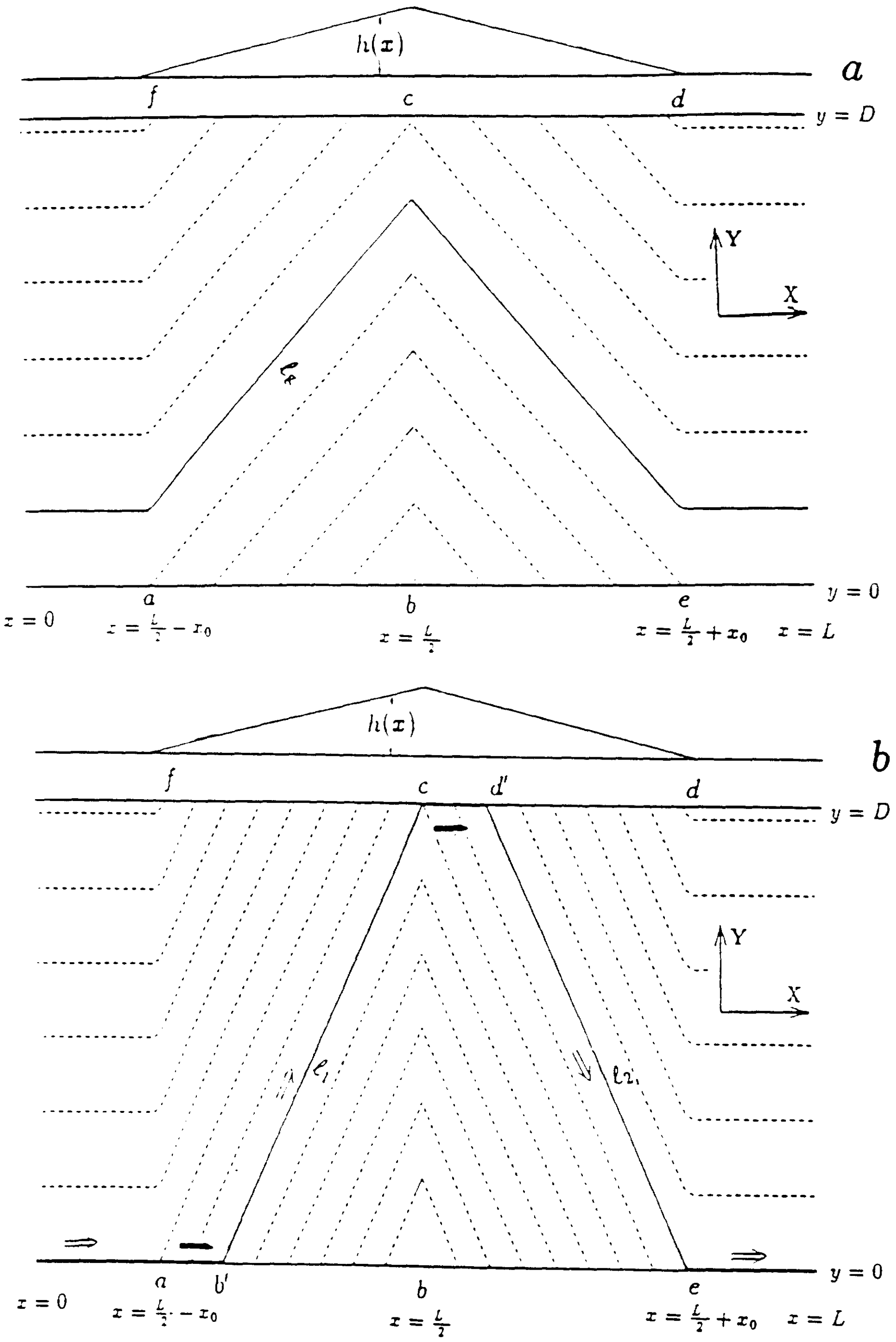

Figure 2.3: (a) The geostrophic contour structure in the channel for the subcritical case $h_0 < h_c$, dashed lines are the geostrophic contours. On top is the profile of the ridge. (b) The geostrophic contour structure for the supercritical state with $h_0 > h_c$, dashed lines are the geostrophic contours. The solid arrows represent boundary layer currents, the open arrows represent the internal currents along a geostrophic contour.

steer geostrophic contours across the ridge without being blocked by the lateral boundaries, as is shown in Fig. 2.3(a). Now the focus of this section is how the presence of the β-effect will change the potential vorticity resistance, and thus the through-channel transport in the inviscid limit. A simpler case forced by a uniform wind stress is discussed first. The case with a nonuniform wind stress will be studied in the next section.

The governing equation in the β-plane channel is

$$J\left(\psi, \beta y + \frac{f_0}{H}h\right) = -\kappa \nabla^2 \psi, \tag{3.1}$$

with the boundary condition

$$\psi|_{y=0} = 0; \qquad \psi|_{y=D} = \psi_0. \tag{3.2}$$

Again, ψ_0 is determined through the momentum balance (2.3), and h is defined in (2.4). In the f-plane channel model, there is no potential vorticity gradient in the absence of ridges. In the presence of the β-effect, however, geostrophic contours defined as

$$\beta y + f_0 \frac{h}{H} = constant,$$

are simply zonal lines in the absence of any topography. In the presence of a ridge, geostrophic contours are deflected over the ridge, and some of the geostrophic contours are blocked by the southern or northern boundaries over the ridge, as is shown in Fig. 2.3(a). If $h_0 < h_c$, then all those geostrophic contours

$$\beta y + \frac{f_0}{H}h = \beta y_0,$$

with $0 \le y \le D(1 - h_0/h_c)$ are not blocked. ℓ_g in Fig. 2.3(a) is just one such unblocked geostrophic contour. Here

$$h_c \equiv \frac{\beta D}{|f_0|}H,$$

is the critical height of the ridge. $h_0 < h_c$ is the subcritical state. Those nonblocked geostrophic contours provide the free passage for the through-channel flow. Along these nonblocked geostrophic contours, there is a free mode to the linear model (3.1) with

$$\psi_f = Q\left(\beta y + f_0 \frac{h}{H}\right),$$

where Q could be any function. In this case, the presence of the ridge does not introduce any potential vorticity barrier in the channel, and along these nonblocked geostrophic contours, any forcing could lead to a strong linear resonance depending upon the frictional processes. And the solution is unbounded in the inviscid limit.

If $h_0 > h_c$, the model is in a supercritical state in which all geostrophic contours in the channel are blocked either by the southern or the northern boundary as is shown in Fig. 2.3(b). Correspondingly, there are neither free passages nor free modes in the channel. To cross the ridge, the minimum amount of potential vorticity a fluid particle has to exchange with the bottom is

$$P_c = |f_0|\frac{h_0}{H} - \beta D. \tag{3.3}$$

Parallel to the case on an $f-$plane, P_c is defined as the potential vorticity resistance introduced by the the ridge on the $\beta-$plane. Obviously, the strength of the potential vorticity resistance depends upon the supercriticality of the ridge, $\Delta h_c \equiv h_0 - h_c$, because

$$P_c = \frac{|f_0|}{H}\Delta h_c.$$

Note that $h_c = 0$ on the $f-$plane, so in the $f-$plane channel with the presence of any ridges, there is always a potential vorticity resistance and the wind-driven circulation is always supercritical. In this sense, Δh_c is actually the effective height of a ridge on the $\beta-$plane. At the critical state or in the subcritical state with $h_0 \leq h_c$, $P_c = 0$ and there is no potential vorticity resistance.

As discussed in Section 2, in the supercritical state with a uniform wind stress, no cross-geostrophic contour flow is allowed unless there is a strong potential vorticity generation through the bottom friction. Similar to the $f-$plane case, an equivalent western boundary layer is and is only allowed to develop along the segments $a-b$ and $c-d$, shown in Fig. 2.3(b). Different from the $f-$plane case, even in the interior away from the ridge, there is a potential vorticity gradient due to the presence of the $\beta-$effect. Away from the two possible equivalent western boundaries, any flow must follow geostrophic contours. Therefore, the flow joining the two boundary layer currents along $a-b$ and $c-d$ has to flow along a geostrophic contour, ℓ_1, defined as

$$y = \frac{\alpha}{\beta}\left(x - \frac{L}{2}\right) + D. \tag{3.4}$$

ℓ_1 intersects the northern boundary at point c $(L/2, D)$ and the southern boundary at point b' $(L/2 - x_0 + x_*, 0)$, where

$$x_* = x_0 - \frac{\beta}{\alpha}D = x_0\frac{\Delta h_c}{h_0}.$$

It actually measures the supercriticality of the ridge height. Along $b'-b$ there is no boundary current. Otherwise, it has no place to go. b' turns out to be a corner point where the current in the boundary layer $a-b'$ changes its direction and flows along ℓ_1. c is another corner point where the current changes its direction again and flows along the northern boundary. Now the question is where this northern boundary current terminates. There is a geostrophic contour ℓ_2, defined as

$$y = \frac{\alpha}{\beta}\left(\frac{L}{2} + x_0 - x\right). \tag{3.5}$$

ℓ_2 intersects the southern boundary at point e $(L/2 + x_0, 0)$ and the northern boundary at point d' $(L/2 + x_*, D)$. The requirement of no flow across geostrophic contours forces the current in the interior away from the ridge to flow along the southern boundary, otherwise streamlines would intersect the equivalent eastern boundary along $f-c$. Correspondingly, over the ridge with $L/2 < x < L/2 + x_0$, the current has to flow along ℓ_2. Therefore the northern boundary layer terminates at point d'. Thus we have constructed a loop of current as shown in Fig. 2.3(b), consisting of a southern boundary current in regions

$0 < x < L/2 - (x_0 - x_*)$ and $L/2 + x_0 < x < L$ and a northern boundary current in the region $L/2 < x < L/2 + x_*$. Over the ridge, the current flows along ℓ_1 in region $L/2 - (x_0 - x_*) < x < L/2$ and along ℓ_2 in region $L/2 < x < L/2 + x_*$. Currents along segments $a - b'$ and $c - d'$ are equivalent western boundary currents. While along ℓ_1, ℓ_2 and the southern boundary, the current flows as an internal boundary layer current in the inviscid limit.

Another way to find the solution is by directly introducing a characteristic variable s defined as

$$\frac{dx}{ds} = \frac{\partial q}{\partial y}, \tag{3.6}$$

$$\frac{dy}{ds} = -\frac{\partial q}{\partial x}, \tag{3.7}$$

then the potential vorticity equation reduces to

$$\frac{d\psi}{ds} = 0, \tag{3.8}$$

away from the two equivalent western boundaries along segments $a - b$ and $c - d$, shown in Fig. 2.4. The geostrophic contours, short dashed lines in Fig. 2.4, serve as the characteristics. Starting the characteristic integration from the two equivalent eastern boundaries $f - c$ and $b - e$ with

$$\psi|_{f-c} = \psi_0,$$

$$\psi|_{b-e} = 0,$$

one obtains the interior solution

$$\psi = \psi_0 \quad for \ \ region \ \ A, B, C$$

$$\psi = 0 \quad for \ \ region \ \ D, E.$$

Accordingly, there are discontinuities of streamfunction along ℓ_1 with

$$\Delta\psi|_{E-A} = -\psi_0,$$

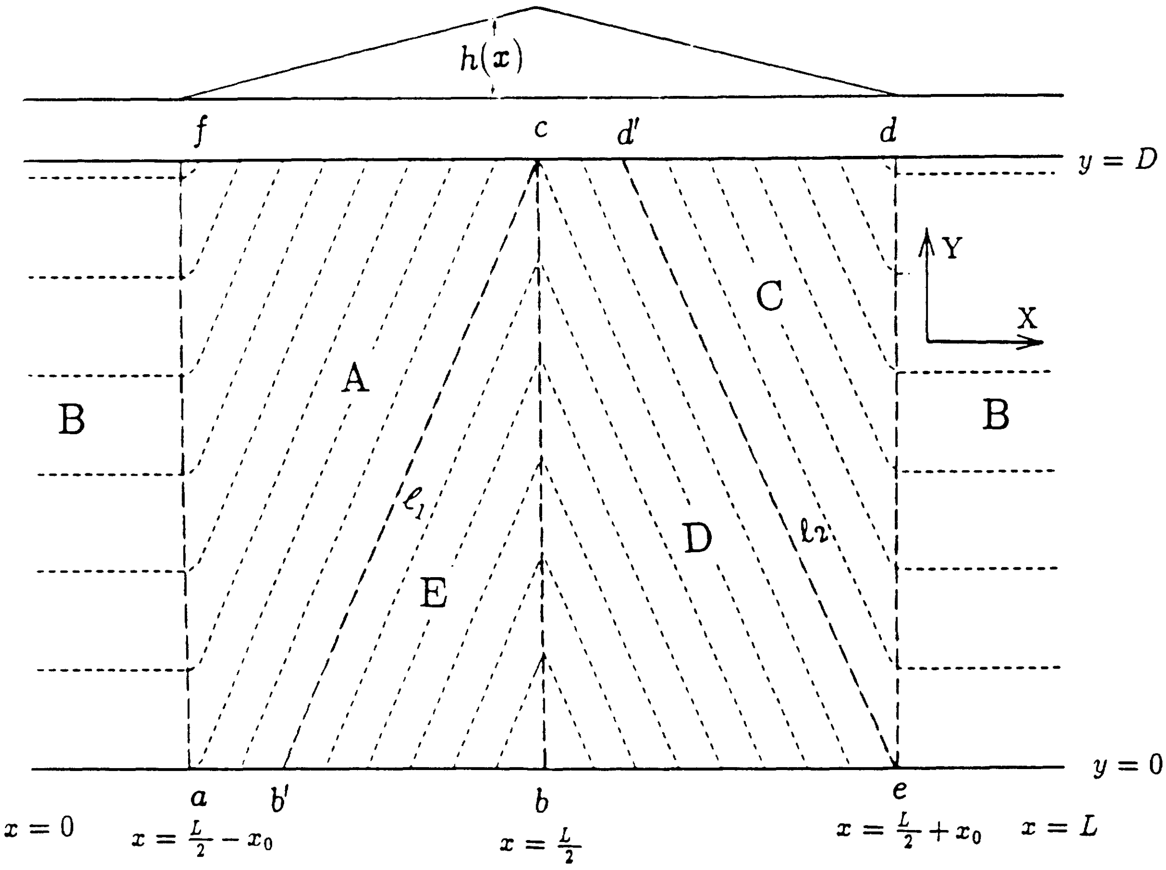

Figure 2.4: A schematic view of the model domain for the characteristic integration in a β−plane. On top is the profile of the ridge. The domain is divided into subdomains A, B, C, D and E bounded by heavy dashed lines. The short dashed lines are the geostrophic contours.

along ℓ_2 with

$$\Delta\psi|_{C-D} \;=\; \psi_0,$$

and along the southern boundary with

$$\Delta\psi|_{y=0} \;=\; \psi_0.$$

These discontinuities of streamfunction represent the internal currents over the ridge and along the southern boundary.

This simple analytical solution gives rise to a straightforward calculation of the topographic form drag. In comparison, a form drag calculation in the case with any finite κ would require knowledge of the detailed structure of the wind-driven current over the ridge. With the above discussion we have

$$\begin{aligned} \tau_D &\equiv \rho_0 f_0 \overline{h\frac{\partial\psi}{\partial x}}^{xy} \\ &= -\frac{\rho_0 f_0 \psi_0}{DL}\int_0^L\int_0^D \left\{\delta\left[y-\frac{\alpha}{\beta}(x-x_e)-D\right]-\delta\left[y-\frac{\alpha}{\beta}(x_0-x)\right]\right\} h(x)dxdy, \end{aligned}$$

in the inviscid limit. This integration is straightforward and the result is

$$\tau_D \;=\; -\frac{\rho_0 f_0 \psi_0 h_0}{L}\left(1-\frac{h_c}{h_0}\right). \tag{3.9}$$

Obviously, the topographic form-drag generation in this linear barotropic Q-G channel model is quite different from that in the inertial models discussed by Johnson (1977). In the inertial model, any topography, whether it blocks any geostrophic contours or not, would lead to a form-drag generation, although the blocking of the linear geostrophic contours does enhance the wave drag generation (W93). In this linear model, however, only supercritical high ridges can lead to form-drag generation in the inviscid limit. It puts a rather strong restriction on the bottom topography with which linear form-drag can be generated in the inviscid limit. Furthermore, this linear form-drag generation can occur only in a channel with **finite** width, while in inertial models, the nonlinear form-drag generation can occur on an infinite β−plane (Johnson, 1977). On the f−plane, however, it can occur in a channel and the channel's width does not matter. Of course, for finite κ, any topography can lead to a linear form drag generation. Another fundamental difference is that in the inertial model, only eastward flow can lead to a form-drag generation, while westward flow can not. In this linear model, however, form-drag is generated regardless of the flow directions. Similar to that in the $f-$plane model, the form-drag is always against the flow, even in the case with a westward flow. It is rather easy to see that the form drag generated in the $f-$plane model is stronger than that in the $\beta-$plane model comparing the flow pattern in Fig. 2.1 and Fig. 2.3(b) for same model parameters noting $\tau_D \propto \overline{h\partial\psi/\partial x}^{xy}$. Actually, for a given ψ_0 and model parameters, the form drag generation reaches its maximum in the $f-$plane channel model, noting $h_c = 0$ in (3.9) for the $f-$plane case.

Balancing the topographic form drag with the wind stress input in (2.3) determines ψ_0, which gives the zonal transport in the channel as

$$T_{r0} = \frac{\tau_0 L/\rho_0}{|f_0|\frac{h_0}{H} - \beta D}. \tag{3.10}$$

In the calculations carried out by Gill & Bryan (1971), the earth's rotation rate used was only one tenth of the real rotation rate. (3.10) suggests that the model could have overestimated the through-channel transport by about 10 times. Actually, one can get (3.10) from the boundary condition (2.15). On the $f-$plane the length of the boundary layer at the southern boundary is x_0, the half width of the ridge. On the $\beta-$plane, however, the actual length of the boundary layer at the southern boundary is $x_* = \frac{\Delta h_c}{h_0} x_0$. The boundary layer current structure along $a - b'$ is similar to that of the $f-$plane model discussed in the preceding section. Thus with (2.10), one can have

$$\overline{u}^x|_{y=0} = \frac{|\alpha|\psi_0 x_*}{\kappa L}. \tag{3.11}$$

Substituting this into (2.15) gives rise to (3.10) again. Obviously, as $\beta \to 0$, (3.10) approaches (2.14). This is because as $\beta \to 0$, $\Delta h_c \to 0$, thus $x_* \to x_0$ and (3.11) approaches (2.16). It is worth noting that although as $\beta \to 0$ the transport in the $\beta-$plane model approaches that in the $f-$plane model, the circulation pattern in the $\beta-$plane model shown in Fig. 2.3(b), however, does not approach that in $f-$plane model shown in Figs. 2.1 and 2.2(a).

The relationship of transport versus model parameters for the $f-$plane and $\beta-$plane are quite similar, as is apparent by comparing (2.14) and (3.10). The discussion in section 2 applies to the $\beta-$plane model, except for the extra βD term in the denominator of (3.10). In the $f-$plane model, the transport is independent of the channel width, D. The reason is that in the $f-$plane, the total potential vorticity resistance is solely determined by the ridge. In the $\beta-$plane model, although the ridge does introduce the same amount of potential vorticity resistance, $|f_0|\frac{h_0}{H}$, yet the $\beta-$effect tends to steer the geostrophic contours across the ridge without being blocked by the two lateral boundaries as shown in Fig. 2.3(a). As a result, the potential vorticity resistance is reduced. Therefore, the transport in the $\beta-$plane channel is always larger than its counterpart in an $f-$plane channel. The weakening effect of β on the potential vorticity resistance is measured by βD, the amount of planetary vorticity a cross-channel fluid particle would have to change. It is solely determined by the width of the channel, D. This β-effect is stronger in a wider channel than a narrower channel, since

$$P_c = |f_0|\frac{h_0}{H} - \beta D = |f_0|\frac{\Delta h_c}{H}.$$

In the subcritical state with $\Delta h_c < 0$, the β-effect overpowers the potential vorticity resistance introduced by the ridge, and there is no net potential vorticity resistance. Only in the supercritical state with $\Delta h_c > 0$ does the potential vorticity resistance introduced by the ridge overpower the β steering effect, resulting in a net potential vorticity resistance. In the supercritical state, the strength of the net potential vorticity resistance decreases with increasing channel width. Thus, in the $\beta-$plane, the transport increases with increasing channel width. This is the only difference between the $f-$plane results and the $\beta-$plane results in terms of the relationship between the transport and the model parameters.

Comparing Fig. 2.1 with Fig. 2.3(b), one can see that the length of the boundary layer at the southern boundary for the $f-$plane model is x_0, while that for the $\beta-$plane model is x_*. This gives rise to the difference between (3.11) and (2.16). The ratio between the $\beta-$plane one and the $f-$plane one is $\Delta h_c/h_0$ with the former always smaller than the latter for the same ψ_0. To satisfy (2.15), ψ_0 thus the transport in the $\beta-$plane channel is always larger than that in the corresponding $f-$plane channel. The ratio between them is just $\Delta h_c/h_0$. Another perspective from which to explain the difference is to check the flow pattern over the ridge which critically determines the form drag generation. It is easy to see that the flow pattern over the ridge in the $f-$plane channel model shown in Fig. 2.1 is more efficient than that shown in Fig. 2.3(b) in terms of generating form drag for the same set of model parameters and ψ_0 noting $\tau_D \propto \overline{h\partial\psi\partial x}$. To balance the same wind stress leads to a larger $|\psi_0|$, thus a larger zonal transport in the $\beta-$plane model than in the $f-$plane model. It is worth noting that because $\Delta h_c/h_0$ increases as either h_0 increases or D decreases, the zonal transport difference between the $f-$plane model and the $\beta-$plane model shrinks as either h_0 increases or D decreases. In the limit with $D \rightarrow 0$, (3.10) approaches (2.14), because $h_c \rightarrow 0$ thus $x_* \rightarrow x_0$ noting (3.11) and (2.16).

Consider a model problem with parameters chosen as $\tau_0 = 0.08N/m^2$, $\rho_0 = 1.03g/cm^3$, $L = 2.4 \times 10^7 km$, $D = 1.8 \times 10^6 km$, $H = 5km$, $f_0 = -2\omega \sin\theta^0$ and $\beta = 2\omega\cos\theta^0/a$ with $\theta = 60^0 S$ and $a = 6.37 \times 10^6 km$, then the transport is $86Sv$ for the $f-$plane model, and $1504Sv$ for the $\beta-$plane model for a ridge with $h_0 = 865m$, close to the corresponding critical height $h_c = 815.7m$ in the $\beta-$plane channel. This transport value in the $\beta-$plane model is an order of magnitude larger than the observed value. In the next section we will show that in the presence of a nonuniform wind stress (in the Circumpolar Ocean the wind stress is indeed not uniform), potential vorticity input will make a large contribution to the form drag generation. This will change zonal transport in the channel substantially.

Suppose we now have a series of ridges, represented as $\{h^j(x)\}$ with $j = 1,\cdots,m$. Each one is in the form of (2.4). Among these ridges,

$$h_0^j > h_c \qquad (j = 1,\cdots,m_0),$$

while

$$h_0^j \;\le\; h_c \qquad (j = m_0 + 1, \cdots, m),$$

where h_0^j is the ridge height. Then, the total potential vorticity resistance introduced by this series of topographic features is

$$P_c^* \;=\; \sum_{j=1}^{m_0} \left(|f_0| \frac{h_0^j}{H} - \beta D \right). \tag{3.12}$$

Ridges with subcritical height do not contribute to the total potential vorticity resistance. And the corresponding through-channel transport is

$$T_{r0}^* = \frac{\tau_0 L / \rho_0}{P_c^*}. \tag{3.13}$$

The presence of those ridges lower than the critical height, h_c, has no influence on the transport **in the inviscid limit**. The effect of these low ridges is merely to deflect the flow passage slightly.

It is quite straightforward to extend the above discussions to a general bottom topography, and the final result is still (3.13). In the real Circumpolar Ocean, besides the ridge near Drake Passage, there are three other major ridges. They are the Kerguelen Plateau in the southern Indian Ocean, the southeast Indian Ridge south of Australia, and the Pacific Antarctic Ridge. The local meridional scales of these ridges are very large, so are their corresponding local βD's. Their presence most probably introduces no net potential vorticity resistance because they are very likely locally subcritical. Therefore, in the case with uniform wind stress forcing, their presence most likely does not change the wind-driven transport through the channel. It is solely determined by the ridge around Drake Passage, as was suggested by Stommel (1957). At the longitudes of Drake Passage the channel is very narrow, thus tending to introduce a strong potential vorticity resistance. It is worth noting that observational studies, such as Gordon *et al.* (1978), have shown that the transport of the ACC is mainly concentrated within two narrow frontal zones, which are presumably caused by the baroclinic process. By coincidence, the model circulation forced by a uniform wind stress even in this simple barotropic model is also concentrated within a narrow zone. In the Circumpolar Ocean, the wind stress forcing is not uniform, then what difference will the presence of an external potential vorticity input cause?

2.4 A β−plane model with a non-uniform wind stress

In the discussions above the influence of the external potential vorticity input through the wind stress curl has been ignored. The numerical experiments by W93 showed that the form drag generation due to the external potential vorticity input is comparable with the mean wind stress input. The numerical experiments with finite κ also suggested that in the supercritical state the Sverdrup balance holds in the interior away from topography. Due to the limitation of the numerical experiments, however, it is not quite clear whether this is true in the subcritical state close to the critical state. Now we are going to demonstrate that in the inviscid limit the Sverdrup relation is bound to fail in the subcritical state even if it is close to the critical state.

For simplicity, we decompose ψ as

$$\psi = \psi^u + \psi^c, \tag{4.1}$$

where ψ^u is governed by equations (3.1) and (3.2), and thus carries all the zonal transport in the channel; while ψ^c satisfies

$$J\left(\psi^c, \beta y + f_0 \frac{h}{H}\right) = w_e - \kappa \nabla^2 \psi^c, \tag{4.2}$$

with boundary conditions

$$\psi^c|_{y=0,D} = 0, \tag{4.3}$$

ψ^c is driven by the potential vorticity input w_e and does not carry any net zonal transport. The total transport, represented by ψ_0, is still determined by (2.3). In the following discussion, the wind stress is assumed to be

$$\tau = -\tau_0 cos\frac{\pi}{D}y + \varepsilon\tau_0, \tag{4.4}$$

which bears some similarity to the zonally averaged one (Nowlin & Klinck, 1986) if ε, a constant coefficient, is close to 1. Correspondingly, one has

$$w_e = w_0 sin\frac{\pi}{D}y,$$

with $w_0 = -\pi\tau_0/\rho_0 HD$.

From mass balance, the net flow across any geostrophic contour, ℓ_g, shown in Fig. 2.3(a), for example, has to be zero, *i.e.*,

$$\int_{\ell_g} v_n dl = 0, \tag{4.5}$$

where n denotes the local unit normal vector of ℓ_g. Suppose ℓ_g closes itself as shown in Fig. 2.3(a), *i.e.*, it is not blocked. If the Sverdrup balance holds everywhere along ℓ_g, *i.e.*,

$$J\left(\psi^c, \beta y + \frac{f_0}{H}h\right)|_{\ell_g} = w_e,$$

then, v_n is always larger or less than zero depending upon how we choose n noting $w_e < 0$, and

$$\int_{\ell_g} v_n dl \neq 0.$$

This clearly violates the mass conservation statement (4.5). Thus, the Sverdrup relation must fail somewhere along ℓ_g. This is similar to the case with a sufficiently high bottom topography in a closed basin discussed by Pedlosky (1987). In the supercritical state, however, all geostrophic contours are blocked, each geostrophic contour intersects the boundaries twice. Boundary layer structure could develop at one end, through which the interior (here it means away from the boundary layer) Sverdrup flow is returned and mass conservation is satisfied. This is can be seen from Fig. 2.4, where $a - b$ and $c - d$ are the two equivalent western boundaries and $b - e$ and $f - c$ are the two equivalent eastern boundaries. In terms of the potential vorticity balance, the subcritical state poses no potential resistance, there is free flow passage in the channel and there is no solution along those unblocked geostrophic contours in the inviscid limit. Dynamically, this is quite similar to a closed basin on a $f-$plane discussed by Stommel (1948). The supercritical state poses a potential vorticity control and there is no free flow passage in the channel. In this case there is a solution in the inviscid limit. Dynamically, this is quite similar to that in a closed basin on a $\beta-$plane where, in the presence of meridional barriers, the $\beta-$effect poses a potential vorticity resistance in the basin in the sense that any meridional flow has to be externally forced in the classical Stommel model (1948).

Now let us look at the circulation driven by the surface Ekman pumping and satisfying (4.3). Fig. 2.4 shows the model domain in the supercritical state. The heavy dashed lines divide the whole domain into 5 small domains, labeled A, B, C, D and E, for the convenience of characteristic integration. Away from the two equivalent western boundary layers, the governing equation reduces to the Sverdrup balance

$$J\left(\psi^c, \beta y + f_0 \frac{h}{H}\right) = w_e.$$

Introducing a characteristic variable s such that

$$\frac{dx}{ds} = \frac{\partial q}{\partial y}, \tag{4.6}$$

$$\frac{dy}{ds} = -\frac{\partial q}{\partial x}, \tag{4.7}$$

then the potential vorticity equation reduces to

$$\frac{d\psi^c}{ds} = w_e. \tag{4.8}$$

In this way, the geostrophic contours $\beta y + f_0 \frac{h}{H} = constant$ serve as the characteristics in this model.

In region A, the initial conditions for the characteristic equations (4.6), (4.7) and (4.8) are

$$x|_{s=0} = x_s,$$

$$
\begin{aligned}
y|_{s=0} &= D, \\
\psi^c|_{s=0} &= 0,
\end{aligned}
$$

and the solution is

$$
\psi^c|_A = -\frac{w_0 D}{\alpha\pi}\left(1+cos\frac{\pi}{D}y\right).
$$

In region B, the governing equation becomes

$$
\beta\frac{\partial\psi^c}{\partial x} = w_e,
$$

with the boundary condition

$$
\psi^c|_{x=L/2-x_0} = -\frac{w_0 D}{\alpha\pi}\left(1+cos\frac{\pi}{D}y\right),
$$

and the solution is

$$
\begin{aligned}
\psi^c|_B &= -\frac{w_0 D}{\alpha\pi}\left(1+cos\frac{\pi}{D}y\right)+\frac{w_0}{\beta}(x-L/2+x_0)\,sin\frac{\pi}{D}y, \quad for \quad 0<x<L/2-x_0; \\
\psi^c|_B &= -\frac{w_0 D}{\alpha\pi}\left(1+cos\frac{\pi}{D}y\right)+\frac{w_0}{\beta}\left(x+x_0-\frac{3}{2}L\right)sin\frac{\pi}{D}y, \quad for \quad L/2+x_0<x<L.
\end{aligned}
$$

In region C, the initial condition for the characteristic equations (4.6), (4.7) and (4.8) are

$$
\begin{aligned}
x|_{s=0} &= L/2+x_0, \\
y|_{s=0} &= y_s, \\
\psi^c|_{s=0} &= -\frac{w_0 D}{\alpha\pi}\left(1+cos\frac{\pi}{D}y_s\right) + \frac{w_0}{\beta}(2x_0-L)sin\frac{\pi}{D}y_s,
\end{aligned}
$$

and the solution is

$$
\begin{aligned}
\psi^c|_C = &-\frac{w_0 D}{\alpha\pi}\left\{1+cos\frac{\pi}{D}\left[y-\frac{\alpha}{\beta}(L/2+x_0-x)\right]\right\} \\
&+\frac{w_0}{\beta}(2x_0-L)sin\frac{\pi}{D}\left[y-\frac{\alpha}{\beta}(L/2+x_0-x)\right] \\
&-\frac{w_0 D}{\alpha\pi}\left\{cos\frac{\pi}{D}\left[y-\frac{\alpha}{\beta}(L/2+x_0-x)\right]-cos\frac{\pi}{D}y\right\}.
\end{aligned}
$$

In region D, the initial conditions for the characteristic equations (4.6), (4.7) and (4.8) are

$$\begin{aligned} x|_{s=0} &= x_s, \\ y|_{s=0} &= 0, \\ \psi^c|_{s=0} &= 0, \end{aligned}$$

and the solution is

$$\psi^c|_D = -\frac{w_0 D}{\alpha\pi}\left(1 - cos\frac{\pi}{D}y\right).$$

In region E, the initial conditions for the characteristic equations (4.6), (4.7) and (4.8) are

$$\begin{aligned} x|_{s=0} &= L/2, \\ y|_{s=0} &= y_s, \\ \psi^c|_{s=0} &= -\frac{w_0 D}{\alpha\pi}\left(1 - cos\frac{\pi}{D}y_s\right), \end{aligned}$$

and the solution is

$$\begin{aligned} \psi^c|_E &= -\frac{w_0 D}{\alpha\pi}\left\{1 - cos\frac{\pi}{D}\left[y - \frac{\alpha}{\beta}(x - L/2)\right]\right\} \\ &+ \frac{w_0 D}{\alpha\pi}\left\{cos\frac{\pi}{D}\left[y - \frac{\alpha}{\beta}(x - L/2)\right] - cos\frac{\pi}{D}y\right\}. \end{aligned}$$

Obviously, along both segments $a - b$ and $c - d$, equivalent western boundary layers are needed to close the circulation. The circulation ψ^c is shown in Fig. 2.5 for a chosen model parameter set. Notice that flow in regions A and D is purely zonal. The explanation is as follows. Differentiating (4.2) with respect to x and noting $\partial w_e/\partial x = 0$, one can have an equation for $v^c = \partial\psi^c/\partial x$ such as

$$J\left(v^c, \beta y + f_0\frac{h}{H}\right) = -\kappa\nabla^2 v^c.$$

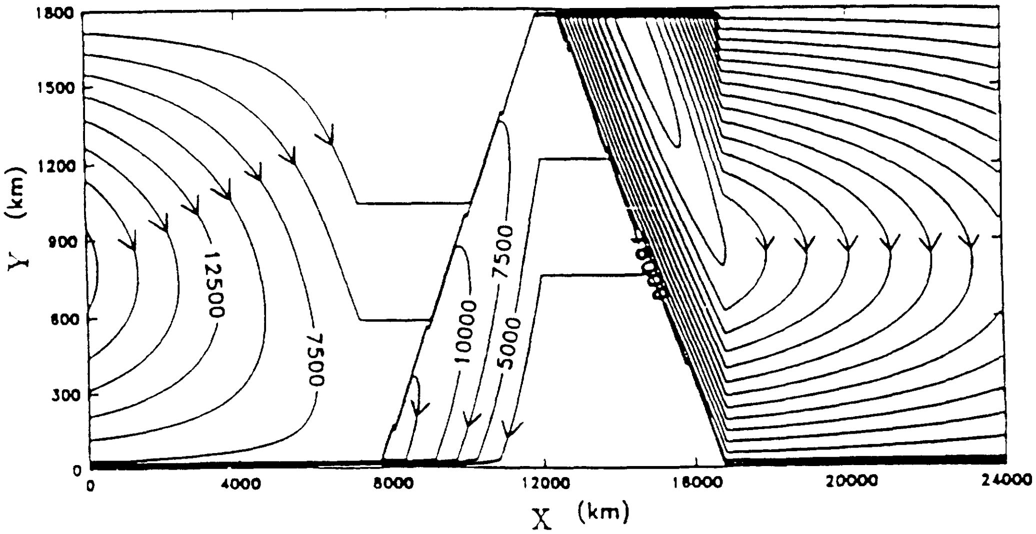

Figure 2.5: The streamfunction (m^2/s) of the external potential vorticity input-driven circulations in the $\beta-$plane channel. The model parameters are chosen as $L = 24000km$, $D = 1800km$, $x_0 = 4800km$ and $\tau_0 = 0.08N/m^2$.

The boundary condition for region A is that $v = 0$ at $y = D$, the equivalent eastern boundary for A. Then, based upon the characteristics and the same discussion for ψ^c, one has

$$v^c|_A = 0.$$

Obviously, the same is true for that in region D. There are discontinuities at the boundaries between regions A and E and regions C and D with

$$\Delta\psi^c|_{E-A} = \Delta\psi^c|_{C-D} = -\frac{2w_0 D}{\alpha\pi}.$$

Thus, in addition to the two equivalent western boundary layer currents at the northern and southern boundaries, there are three internal currents along geostrophic contours. They are along ℓ_1 between regions A and E, ℓ_2 between regions C and D, and ℓ_3 along the southern boundary in the interior away from the ridge, shown in Fig. 2.5. The volume transports of these three internal jets are all equal to

$$T_{rin} = \frac{2\tau_0 x_0 H}{\rho_0 |f_0| h_0}.$$

The scenario is quite similar to the case in a closed basin discussed by Cessi & Pedlosky (1986), and the physical mechanism for the presence of the discontinuities is similar to that outlined there. For a wind stress in the form (4.4) with model parameters chosen as $\tau_0 = 0.08N/m^2$, $\rho_0 = 1.03g/cm^3$, $L = 2.4 \times 10^7 km$, $D = 1.8 \times 10^6 km$, $H = 5km$, $f_0 = -2\omega sin\theta^0$ and $\beta = 2\omega cos\theta^0/a$ with $\theta = 60^0 S$ and $a = 6.37 \times 10^6 km$

$$T_{rin} = 8.5Sv, \tag{4.9}$$

for $x_0 = 1200km$ and $h_0 = 865m$. With the same model parameters, the meridional Sverdrup volume transport in the interior basin for a narrow ridge is roughly

$$T_{Sv} = \frac{Hw_0}{\beta}(L - 2x_0) = -257Sv, \tag{4.10}$$

which is much stronger than the volume flux of the internal currents along ℓ_1, ℓ_2 and the southern boundary.

The channel-averaged topographic form drag due to ψ^c is

$$\tau_D^{\psi^c} \equiv \frac{\rho_0 f_0}{LD}\iint h\frac{\partial\psi^c}{\partial x}dxdy = \frac{\rho_0 f_0}{LD}\left(\int_A+\int_B+\int_C+\int_D+\int_E+\int_{\ell_1}+\int_{\ell_2}\right)h\frac{\partial\psi^c}{\partial x}dxdy.$$

Using the streamfunctions listed above, one has

$$\begin{aligned}
\tau_D^A &= \tau_D^B = \tau_D^D = 0, \\
\tau_D^C &= -2(x_0/L)\tau_0\left[-(\frac{\Delta x}{x_0}-\frac{2}{\pi^2}\frac{\Delta x}{x_0}) + \frac{L-2x_0}{2x_0}\right], \\
\tau_D^E &= 2(x_0/L)\tau_0(1-\frac{\Delta x}{x_0}+\frac{2}{\pi^2}\frac{\Delta x}{x_0}), \\
\tau_D^{\ell_1} &= -2(x_0/L)\tau_0(1-\frac{h_c}{2h_0}), \\
\tau_D^{\ell_2} &= -2(x_0/L)\tau_0\frac{h_c}{2h_0}.
\end{aligned}$$

Thus the channel-averaged topographic form drag generated by the external potential vorticity input is

$$\tau_D^{\psi^c} = -\tau_0\left(1-\frac{2x_0}{L}\right). \tag{4.11}$$

This form drag generation is fundamentally different from both the nonlinear Rossby wave drag generation discussed by Johnson (1977) and the linear form-drag generation discussed in the preceding sections. In those cases, there is no external potential vorticity input, and the form drag generation is closely related to the zonal transport within the channel. In this case, however, the form drag generation is directly related to the external potential vorticity input via the wind stress curl. The external forcing determines the magnitude of the form-drag generation. But as is obvious from the discussions above, the mean wind stress, $\overline{\tau_x}^{xy}$, does not affect this form drag generation. In fact, only the meridional shear of the wind stress, $\partial\tau_x/\partial y$, contributes to the form drag generation. So this form drag could either be against the mean wind stress if $\varepsilon > 0$, or enhance the mean wind stress forcing if $\varepsilon < 0$. Furthermore, this form drag could either be stronger or weaker in magnitude than the mean wind stress $\overline{\tau_x}^{xy}$ depending upon both the wind stress profile and the model parameters.

The form drag generated by the through-channel flow, ψ^u, as discussed in the preceding section, is

$$\tau_D^{\psi^u} = \frac{\rho_0 f_0 \psi_0 h_0}{L}\left(1 - \frac{h_c}{h_0}\right). \tag{4.12}$$

If $\varepsilon = 1$ in (4.4), then the mean wind stress is τ_0, and one has

$$-1 < \frac{\tau_D^{\psi^c}}{\tau_0} \leq 0.$$

First of all, the topographic form drag generated by the Sverdrup flow, ψ^c, is always against the mean wind stress, $\overline{\tau_x}^{xy} = \tau_0$, and smaller in magnitude noting (4.4). Thus, it always decelerates the eastward through-channel flow driven by the mean wind stress. Second, its magnitude decreases with increasing width of the ridge. This is different from that due to the through-channel flow, ψ^u. Suppose we choose wind stress of the form

$$\tau_x = \tau_0\left[1 - R(x, x_0) cos\pi y/D\right],$$

with

$$R(x, x_0) = \begin{cases} 0 & \text{if } h = 0; \\ 1 & \text{if } h \neq 0. \end{cases}$$

Then, using a similar procedure to that used to find ψ^c we can find the corresponding streamfunction. With the streamfunction one has

$$\tau_D^{\psi^c} = 0,$$

and in this case the Sverdrup flow does not produce any topographic form drag. This demonstrates the importance of the meridional flow within the basin driven by the vorticity input in generating the topographic form drag. This also explains why there is a factor of $L - 2x_0$ in (4.11). Actually from (4.11), $\tau_D^{\psi^c} = 0$ if $x_0 = L/2$, *i.e.*, if the ridge extends to the whole channel. $\tau_D^{\psi^c}$ could be very strong for a narrow ridge. For a ridge with $x_0 = L/20$, one has

$$\tau_D^{\psi^c} = -0.9\tau_0.$$

So, for a narrow ridge, most of the mean wind stress input is balanced by the topographic form drag generated by the Sverdrup flow. Third, the form drag generation, $\tau_D^{\psi^*}$ in (4.12), via the through-channel flow critically depends upon the supercriticality of the ridge height. The form drag $\tau_D^{\psi^c}$, however, does not depend upon the supercriticality of the ridge height, so long as the $h_0 > h_c$. This is also rather different from the nonlinear Rossby wave drag generation discussed in Johnson (1977) where the form drag depends upon the topographic height. Fourth, similar to the form drag generation in the $f-$plane model, $\tau_D^{\psi^c}$ does not depend upon the the width of the channel.

For a wind stress in the form of (4.4) with $\varepsilon = 1$, the momentum balance

$$\tau_D^{\psi^*} + \tau_D^{\psi^c} + \overline{\tau_x^{xy}} = 0,$$

leads to the total zonal transport

$$T_r = \frac{\tau_0 2x_0/\rho_0}{|f_0|\frac{h_0}{H} - \beta D} = T_{r0}\cdot\frac{2x_0}{L}. \tag{4.13}$$

Consequently, one obtains a constraint

$$0 < T_r \leq T_{r0}.$$

The ratio between T_r and T_{r0} is

$$R_T = \frac{2x_0}{L}.$$

So the presence of the external potential vorticity input through the wind stress curl reduces transport by as much as $1 - R_T$ percent. As $x_0 \rightarrow 0$, $R_T \rightarrow 0$.

Different from the case with a uniform wind stress, the transport now does depend linearly upon the width of the ridge, x_0, due to $\tau_D^{\psi^c}$ generation by the wind-driven Sverdrup flow. For a ridge with $x_0 = 1200km$ and the rest of the model parameters chosen as those in obtaining (4.9) and (4.10), $R_T = 0.1$, and correspondingly, $T_r \approx 150Sv$ for $h_0 = 865m$. It reduces to about $47.8Sv$ if $h_0 = 1000m$. The total zonal transport increases linearly as the width of the ridge, x_0, increases, which is because $\tau_D^{\psi^c}$ decreases linearly with increasing width of the ridge. As is shown Fig. 2.6, the total zonal transport in the channel decreases inversely and linearly as the ridge height increases. It is not surprising that the model transport is so sensitive to the topographic parameters, given that a barotropic model is used. In a baroclinic model, the result should be much less sensitive to the topographic parameters.

With T_r and T_{rin}, the total volume transport of the internal current along the geostrophic contour ℓ_1 is

$$T_{\ell_1} = T_r\left(1 + \frac{\Delta h_c}{h_0}\right),$$

which always flows northward and larger than the transport of the through-channel flow. However, the total volume transport of the internal current along the geostrophic contour ℓ_2 is

$$T_{\ell_2} = -T_r\left(1 - \frac{\Delta h_c}{h_0}\right),$$

which also always flows southward but is smaller than the transport of the through-channel flow. It will be shown in Chapter 3 that this not always true in the presence of a partial meridional barrier in the channel. For $\Delta h_c \ll h_0$, one has $T_{rin} \ll T_r$. The volume flux ratio between the Sverdrup flow in the interior basin away from the ridge and the through-channel flow is

$$\frac{T_{Sv}}{T_r} = \pi\frac{L}{2x_0}\frac{\Delta h_c}{h_c},$$

which is linearly and inversely linearly proportional to the h_0 and x_0, respectively. For the model parameters chosen in obtaining (4.9) and (4.10), one has

$$\frac{T_{Sv}}{T_r} \sim 1.8, \tag{4.14}$$

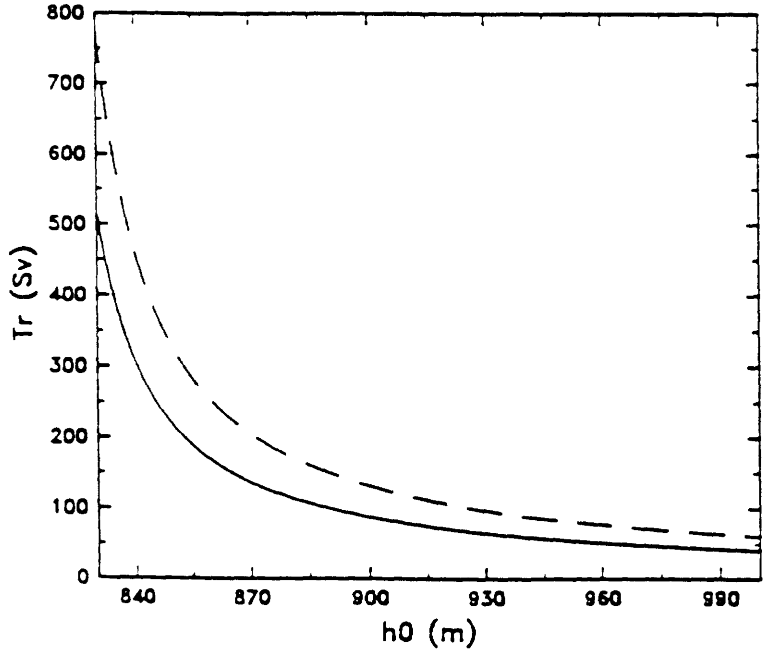

Figure 2.6: T_r versus h_0 for $x_0 = 1200km$ (solid line) and $x_0 = 1800km$ (dashed line). The model parameters were chosen as $L = 24000km$, $D = 1800km$, $\tau_0 = 0.08N/m^2$, $\rho_0 = 1.03g/cm^3$, $H = 5km$ and $\theta_0 = 60^0S$.

for $h_0 = 865m$ and $x_0 = 1200km$; the zonal transport in the channel is only about half the Sverdrup transport.

If a wind stress is of the form

$$\tau_x = -\tau_0 cos\frac{\pi}{D}y,$$

i.e., $\varepsilon = 0$ in (4.4), then $\overline{\tau_x}^{xy} = 0$, and the corresponding through-channel transport is

$$T_r = -T_{r0}\left(1 - \frac{2x_0}{L}\right). \tag{4.15}$$

So in the case with a narrow ridge with $x_0 \ll L$, $T_r \sim -T_{r0}$, a very strong westward through-channel transport is produced through form drag generated via the external potential vorticity input. Only in the special case with $x_0 = L/2$ or if the form

$$\tau_x = -\tau_0 R(x, x_0) cos\frac{\pi y}{D}$$

is chosen, can the through-channel transport vanish. This is rather different from the case in a closed basin, where the mean wind stress does not have any direct effect on the lowest order solution.

The discussions above can be easily extended to cases with multiple ridges. But unlike the case forced by a uniform wind stress, a ridge with $h_0 < h_c$ affects the Sverdrup flow and thus changes the topographic form drag due to the Sverdrup flow. Otherwise, the wind-driven circulation is similar to the case with a single ridge. In this section we have only discussed the case with ridges in the form of (2.4), the same method is applicable to a general topography so long as there are no closed geostrophic contours. But we may not be able to get such a neat, explicit form as (4.13) for the zonal transport in the channel.

2.5 Conclusion and discussion

Simple linear barotropic models are proposed for the wind-driven circulations in both $f-$plane and $\beta-$plane channels. In an $f-$plane channel forced by a uniform wind stress, a ridge with non-zero height is always in a supercritical state, and a solution in the inviscid limit always exists. The zonal transport in the channel can be written in a very simple and explicit form (2.14). It is determined by the wind stress, the length of the channel, the Coriolis parameter, the depth of the channel, and the height of the ridge. The width of the ridge has no effect on the transport. A parameter called potential vorticity resistance is introduced to quantify *the degree to which the ridge impedes the through-channel flow.* It is defined as

$$P_c \equiv |f_0|\frac{h_0}{H},$$

for a single ridge in the form of (2.4). From the potential vorticity balance, P_c represents the minimum amount of potential vorticity a fluid particle has to exchange with its environment in order to cross the ridge. Using P_c, the transport can be written

$$T_r = \frac{\tau_0 L/\rho_0}{P_c}.$$

So the transport decreases with increasing P_c, similar to Ohm's law in the elementary theory of electricity. For the case with multiple ridges, the total potential vorticity resistance is the sum of each individual's. Isolated topographic features, which can not block the geostrophic contours, impose no potential vorticity control on the flow.

In the case with a $\beta-$plane channel forced by a uniform wind stress, the $\beta-$effect tends to steer the through-channel flow over the ridge. This effect contributes $-\beta D$ to the potential vorticity resistance, so

$$P_c \equiv |f_0|\frac{h_0}{H} - \beta D = |f_0|\frac{\Delta h_c}{H}.$$

Notice that only a supercritical ridge with Δh_c, the effective height of the ridge, positive, can control the through-channel flow. With redefined P_c, the expression for the transport is same as that for the $f-$plane cases. In the cases with multiple ridges, P_c is the sum of the contributions from all supercritical ridges. Ridges with subcritical or critical height do not affect the transport in the inviscid limit. In the cases with uniform wind stress, the volume transport in the $f-$plane channel is always smaller than that in the corresponding $\beta-$plane channel.

In the presence of a nonuniform wind stress, however, the vorticity-driven flow will also contribute to the topographic form drag generation. Again, only in the supercritical state, can a solution for the vorticity-driven flow be found. It is the classical Sverdrup flow (Stommel, 1948) with some modifications. In this case, the external potential vorticity input is mostly dissipated within the two equivalent western boundary layers, especially the northern one. The corresponding form drag generation depends upon the width of the ridge with respect to the length of the channel. But it does not depend upon the supercriticality of the ridge height. For a narrow ridge with $x_0 \ll L$, this form drag is comparable to the mean wind stress. Compared with the case forced by a uniform wind stress, one fundamental change is that the zonal transport in the channel does not depend upon the length of the channel any more, instead it depends linearly upon the width of the ridge. In the case with only external potential vorticity input, a westward flow can be generated and its through-channel transport depends upon the width of the ridge. For a narrow ridge, the westward transport can be very strong.

It has been demonstrated that the linear topographic form drag generation in the inviscid limit is fundamentally different from the nonlinear Rossby wave drag generation in an inertial model. Here, unlike the inertial model, not all topography can lead to form drag generation. In the simple case discussed in sections 2 and 3, the linear form-drag is directly related to the potential vorticity resistance introduced by the presence of the ridge. In the inertial model such as Johnson's (1977), form-drag generation is possible only for an eastward flow. In this linear model in the inviscid limit, however, form-drag generation is possible regardless of the flow direction. The only similarity is that in both cases, the form-drag is against the flow. In the case with external potential vorticity input, via the wind stress curl discussed in section 4, however, the form drag generation is directly related to the forcing. The other difference is that in this latter case, the form-drag is not related to the height of the ridge, so long as the height is in the supercritical range.

Although we began the discussions in this chapter with the intention of applying the results to the Antarctic Circumpolar Current, the circulation pattern shown in Fig. 2.5 looks like anything but the real ACC (Gordon *et al.*, 1982). Then one naturally wonders why this is the case. First of all, from the discussions in the preceding sections, one should notice that the geostrophic contour structure, critically determined by the bottom topography in a $\beta-$plane channel, determines the circulation pattern in the model. Obviously, the topographic features in the Circumpolar Ocean are both far more complicated than and different from the simple ridge chosen in the model for the convenience of getting a neat and simple relation between the model transport and parameters. This presumably would lead to a far different circulation pattern. Second, in this chapter, the discussions proceed with the assumption of an inviscid limit. In the presence of finite friction, those internal boundary layer currents have finite widths and the circulations will change accordingly. Lastly, as is shown by Nowlin & Klinck (1986), strong frontal structure is one of the most significant features in the Circumpolar Ocean, but it is absent from our simple barotropic Q-G model used here. The presence of these frontal structures must have a profound influence on the wind-driven circulation.

Despite all simplifications and the associated limitations of our model, we believe that some of the model results are robust regardless of the model's assumptions. First of all, the geostrophic contour blocking is critical in determining the wind-driven circulation in the periodic channel regardless of the model and topography geometry. Our analysis indicates that the topography near Drake Passage, as Stommel (1957) speculated, plays a central role in determining the wind-driven circulation in the Circumpolar Ocean, while other topographic features most likely play only a secondary role. Second, the physical processes through which the topographic form drag is generated are closely related to the momentum balance in the Circumpolar Ocean, especially the importance of the external potential vorticity input through the wind stress curl. This physical process is far different from the better known and studied nonlinear Rossby wave drag generation, discussed by Johnson (1977) for an example. Third, as the model suggests, the external potential vorticity input from the wind stress is mostly dissipated around the tip of the South American continent. As we will see in Chapter 4, the presence of stratification will not change these three conclusions. Lastly, the model results have important implications for numerical simulation of the wind-driven circulation in the Circumpolar Ocean, such as the FRAM model (1991). The model indicates that the topographic form drag generation is closely related to both the meridional and zonal structure of the wind stress. In addition, the zonal volume transport is also linearly proportional to the mean wind stress. This implies that to simulate the wind-driven circulation in the Circumpolar Ocean requires rather high quality of the wind stress observations over the Circumpolar Ocean.

Appendix A

Is there a boundary layer along $e - c$ or $b - f$ in Fig. 2.1?

If there is a boundary layer along $e - c$, then one has

$$\lim_{\kappa \to 0} \psi_0^*(y;\kappa) \neq \psi_0,$$

where $\psi_0^*(y;\kappa) = \psi|_{x=L/2-x_0}(y,\kappa)$. From the solution in Section 2 we know that in the interior of region B

$$\psi = \psi_0.$$

Then, near $e - c$ over region B there must be a boundary layer. The governing equation to the lowest order is

$$\alpha \frac{\partial \psi}{\partial y} = -\kappa \frac{\partial^2 \psi}{\partial x^2}, \tag{A.1}$$

Noting the boundary condition, a scale analysis of (A.1) gives

$$\frac{\partial \psi}{\partial x}|_{x=L/2-x_0^+} \to \infty \tag{A.2}$$

as $\kappa \to 0$ in the inviscid limit unless

$$\psi_0^* \to \psi_0,$$

as $\kappa \to 0$. On the other hand, in region A the governing equation is

$$\frac{\partial^2\psi}{\partial x^2} + \frac{\partial^2\psi}{\partial y^2} = 0. \tag{A.3}$$

and its boundary condition is

$$\psi|_{y=0} = 0 \qquad \psi|_{y=D} = \psi_0,$$

and the two lateral boundary conditions at $x = L/2 \pm x_0$. In region A, ψ is a well behaved harmonic function given that the boundary conditions are continuous functions. So as $\kappa \to 0$

$$\frac{\partial\psi}{\partial x}|_{x=L/2-x_0^-} \to \phi_0(y), \tag{A.4}$$

from theory on elliptic equations, where $\phi_0(y)$ is some finite function. Thus as $\kappa \to 0$, discontinuity arises across $x = L/2 - x_0$ in $\frac{\partial\psi}{\partial x}$. From the governing equation (2.1), it is easy to see that both ψ and $\frac{\partial\psi}{\partial x}$ should be continuous by integrating (2.1) across $x = L/2 - x_0$. Thus there is a contradiction. To remove this contradiction, we must have

$$\psi_0^* \to \psi_0,$$

as $\kappa \to 0$ in the inviscid limit. The discussion for the case along $x = L/2 + x_0$ is similar. Therefore, there is no boundary layer structure along either $e - c$ over region B or $b - f$ over region C.

Appendix B

The influence of finite bottom friction on the loop of currents

Similar to the corresponding f−plane model, the characteristic thickness of the two equivalent western boundary layers along segments $c - d'$ and $a - b'$ in Fig. 2.3(b) is

$$\delta \sim \kappa/\alpha. \tag{B.1}$$

Within the internal current along the southern boundary in the region $0 \leq x \leq L/2 - x_0$ and $L/2 + x_0 \leq x \leq L$, the governing equation becomes

$$\beta \frac{\partial \psi}{\partial x} \sim -\kappa \frac{\partial^2 \psi}{\partial y^2}.$$

It is a typical diffusive equation. Noting the minus sign, the width of the current gets wider and wider further westward from the eastern end, point a in Fig. 2.3(b), of the southern equivalent western boundary layer, which can be viewed as a point sink in the inviscid limit. At point e of Fig. 2.3(b) just downstream of the ridge, the characteristic thickness is

$$\delta_y \sim \sqrt{(L - 2x_0)\delta_S}, \tag{B.2}$$

where $\delta_S = \kappa/\beta$ is the classical Stommel boundary layer thickness. For the internal current along geostrophic contour ℓ_1 in Fig. 2.3(b) both the two ends are equivalent western boundary layers, which in the inviscid limit can be viewed as a point source and a point sink. With the coordinate transformation such as

$$X = \alpha y + \beta x,$$
$$Y = \beta y - \alpha x,$$

the governing equation (4.1) becomes

$$\sqrt{\alpha^2 + \beta^2} \frac{\partial \psi}{\partial X} = -\kappa \left(\frac{\partial^2 \psi}{\partial X^2} + \frac{\partial^2 \psi}{\partial Y^2} \right).$$

Thus, similar to that for δ_y, the characteristic thickness of the internal current along ℓ_1 is

$$\delta_1 \sim \sqrt{\delta' L'}, \tag{B.3}$$

where $\delta' = \kappa/\sqrt{\alpha^2 + \beta^2}$ and L', $= \sqrt{D^2 + h_c^2 x_0^2 / h_0^2}$, is the length of ℓ_1. With similar discussion, the characteristic thickness of the internal current along ℓ_2 is

$$\delta_2 \sim \delta_1, \tag{B.4}$$

noting its eastern end is the western end of the internal current along the southern boundary. All these characteristic thicknesses are functions of the half width of the ridge, x_0. For a model parameters chosen as as those before with $\kappa = 10^{-7}s^{-1}$, $h_0 = 900m$, and a narrow ridge with $x_0 = 1.2 \times 10^6 m$, both $\delta \sim 5km \ll D$ and $\delta_1 = \delta_2 =\sim 70km \ll D$, thus the equivalent western boundary layer currents and the internal current along ℓ_j are quite narrow with respect to the channel width. They will keep their identities as intense narrow jets even in the presence of a finite bottom friction. On the other hand, $\delta_y \sim 430km$, which is quite wide with respect to the channel width. Apparently if we decrease κ, the thicknesses of the loop of currents will decrease. Fig. 2.7 shows the numerical solution for the cases with uniform wind stress (a) and the wind stress curl-driven Sverdrupian gyre circulation (b) for a small but finite bottom friction. In order to properly resolve the various boundary layer structure, a much smaller domain is used in the calculation. As shown in the figure, the gyre circulation is rather close to the inviscid solution while the mean wind stress driven circulation is substantially different from that in the inviscid limit for the bottom frictional coefficient used. The ratio between the numerical and the analytical solutions for the form drag generated by the Sverdrupian gyre is 0.33, while it is only 0.075 for that generated by the through-channel recirculating flow. Obviously for $\kappa = 10^{-7}s^{-1}$ which corresponds to a spin-down time of about 120 days, the circulation pattern, and the form drag in particular, are quite different from those obtained in the inviscid limit. The situation is substantially better for the case with the f-plane model. For the f-plane model, the ratio is about 0.7 for the through-channel recirculaing flow for $\kappa = 2 \times 10^{-8}s^{-1}$. If we carry out further calculations with even smaller bottom frictional coefficient, the circulation will be closer to that obtained in the inviscid limit. But a frictional coefficient much smaller than what is thought to be reasonable has to be used. Thus, we conclude that the solution obtained in the inviscid limit is rather sensitive to the presence of frictional processes in the realistic situation.

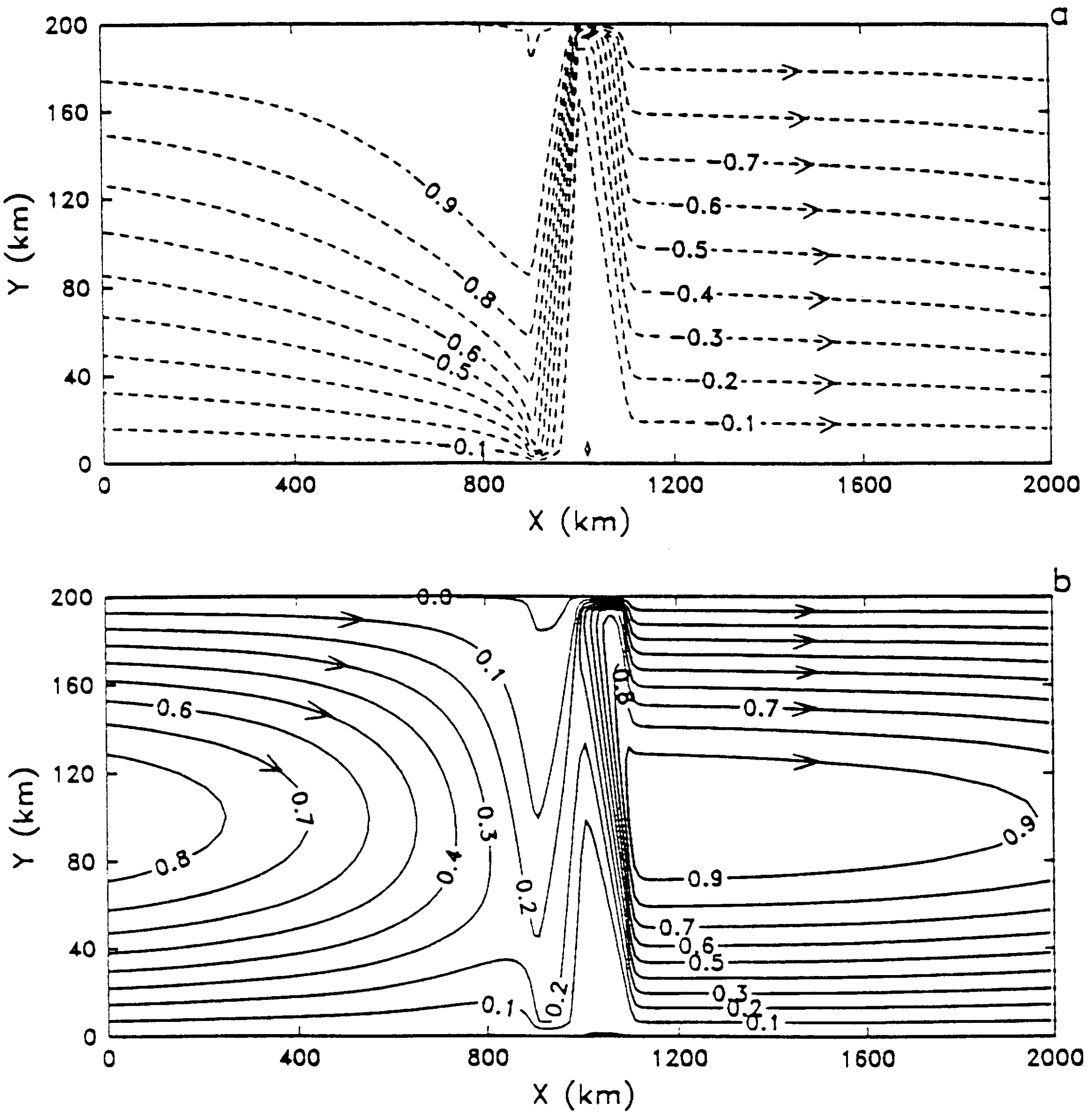

Figure 2.7: The normalized streamfunction forced by uniform wind stress (a) and wind stress curl (b). The model parameters are $L = 2000km$, $D = 200km$, $\tau_0 = 0.08N/m^2$, $H = 5km$ and $\theta_0 = 60^0S$, $x_0 = 100km$, $h_0 = 110m$ and $\kappa = 10^{-7}s^{-1}$.

Chapter 3

Wind-driven circulation in a β-plane channel, Part II: A linear homogeneous channel model with partial meridional barriers

3.1 Introduction

In Chapter 2, wind-driven circulation in an idealized homogeneous channel model was discussed with the aim of trying to explain the wind-driven circulations in the circumpolar ocean. The simple model clearly showed what and how the model parameters determine the circulation structure, and especially the through-channel transport. In the supercritical case, it revealed how and where the dissipation of the potential vorticity occurs, and how the linear topographic form drag is generated. It emphasized the fundamental role of the bottom ridge which can block the geostrophic contours in the channel. In the supercritical state, dynamically speaking, the wind-driven circulation in the channel is similar to those in a closed basin discussed in the classical Stommel model (1948) in terms of potential vorticity balance. The novelty is the momentum balance in the channel. As is clear from Gordon *et al.* (1982) atlas, the geometry of the circumpolar ocean is far different from a zonal channel, notably the narrowness around the Drake Passage due to the presence of both the South American continent and the Antarctic peninsula. As Stommel (1957) pointed out, both the bottom topography and the coastal geometry could be important in determining both the transport and the circulation in the circumpolar ocean. Gill (1968) put forward a simple barotropic model which emphasized the role of the coastal geometry but ignored the role of the bottom topography. His model did show that the geometry of the coastal line has some influence on both the transport and the circulation in the circumpolar ocean. His results, however, apparently showed the necessity of introducing bottom topography into the model in order to get a reasonable transport.

The results from Chapter 2 clearly show us the topographic control on both the through-channel transport and the circulation in a linear homogeneous zonal channel model. Nevertheless, the circulation in the channel is far from the observed circulation in the circumpolar ocean due to the various simplifications. It is the purpose of this chapter to combine the discussions in Chapter 2 and Gill's (1968) together by including two partial meridional barriers in the channel model to see what role partial meridional barriers may play in determining the wind-driven circulation in the channel. As Gill (1968) did, these two meridional barriers are meant to represent crudely the dynamic role of the South American continent and the Antarctic peninsula in determining the transport and the circulation structure in the circumpolar ocean as is shown in Gordon *et al.* atlas (1982). It is hoped that the presence of the partial meridional barriers would make the wind-driven circulation in the channel closer to the observed than that discussed in Chapter 2.

Following the discussions in Chapter 2, the circumpolar ocean is idealized here as a simple zonal channel with two partial meridional barriers, isolated from the rest of the World Oceans. Again a linear homogeneous Q-G model is used. This chapter is organized in the following way. In Section 2 we will discuss the case with a uniform wind stress, mainly how the geostrophic contour determines the current structure in the channel and how the form drag is generated in the channel with the presence of the two partial meridional barriers. In Section 3 we will discuss the case with a nonuniform wind stress, mainly how the presence of the two partial meridional barriers affects the Sverdrupian flow, and the associated form drag generation. Section 4 closes this chapter with some discussion about the results and especially the relevance of the model results to the wind-driven circulation in the realistic circumpolar ocean. This chapter is mainly devoted to addressing the question: what dynamic role can partial meridional barriers play in determining wind-driven circulations in a homogeneous channel model?

3.2 A $\beta-$plane model with a uniform wind stress

Assuming that $\tau_x = \tau_0 = constant$ and $\tau_y = 0$, then with the conventional notations (Pedlosky, 1987), the quasi-geostrophic potential vorticity equation for a linear homogeneous model is

$$J\left(\psi, \beta y + \frac{f_0}{H}h\right) \;=\; -\kappa\nabla^2\psi, \tag{2.1}$$

where f_0, H, h and κ represent the mean Coriolis parameter in the $\beta-$plane channel, the mean total water depth, the bottom topography, and the bottom frictional coefficient, respectively. The width and length of the channel are D and L, respectively. The boundary conditions are

$$\psi \;=\; \psi_0 \quad \text{along the northern boundary;} \tag{2.2}$$

$$\psi \;=\; 0 \quad \text{along the southern boundary.} \tag{2.3}$$

The tips of the two meridional barriers are y_1 and y_2. A schematic view of the model domain is shown in Fig. 3.1. In this linear homogeneous model ψ_0 is determined through the momentum balance

$$\rho_0 f_0 h\overline{\frac{\partial\psi}{\partial x}}^x \;-\; \kappa\rho_0\overline{u}^x H \;+\; \tau_0 \;=\; 0 \qquad y_1 < y < y_2, \tag{2.4}$$

where $\overline{}^x$ is defined as

$$\overline{Z}^x \;\equiv\; \frac{1}{L}\int_0^L Z\,dx.$$

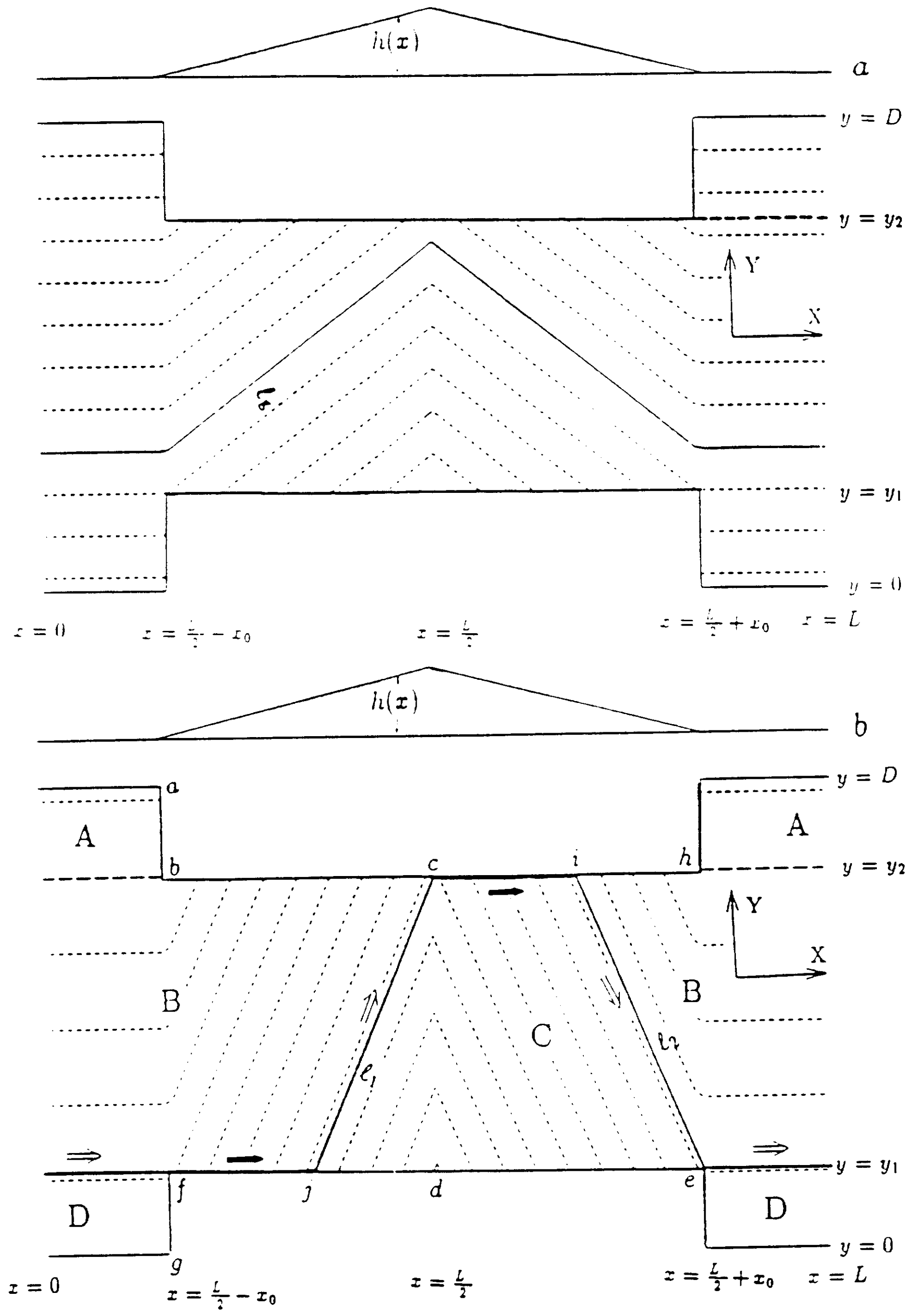

Figure 3.1: The geostrophic contours in the channel. On the top is the profile of the ridge. The short dashed lines represent the geostrophic contours. (a) The subcritical case. (b) The supercritical case. The long dashed and the thick solid lines represent the boundaries between different subdomains. The solid arrows together with the thick solid lines represent the equivalent western boundary layer current, while the non-solid arrows together with the thick solid lines represent the internal current along a geostrophic contour.

Equation (2.4) is obtained by multiplying the linear x-momentum equation with $H - h$, integrating over a latitude circle and using the quasi-geostrophic approximation. It is worth noting that in this linear model, there is no meridional momentum exchange between region $y_1 < y < y_2$ and regions $0 \le y \le y_1$ or $y_2 \le y \le D$. The momentum input at each latitude within the region with $y_1 < y < y_2$ has to be balanced by the form drag generated at the latitude together with the corresponding frictional drag. The momentum balance for the region with either $0 \le y \le y_1$ or $y_2 \le y \le D$ is similar to that in a closed basin.

As is discussed in Chapter 2, isolated topographic features are of no interest to us in the inviscid limit. In the following discussions only ridge-like topography will be discussed. First, let us consider a simple ridge in the form of

$$h(x,y) = \begin{cases} h_0(1 - |\frac{L/2-x}{x_0}|) & \text{if } |L/2 - x| \le x_0; \\ 0 & \text{otherwise.} \end{cases} \tag{2.5}$$

Considering the situation around Drake Passage, the topography and the two partial meridional barriers are located at the same longitudes. In the absence of any topographic features, the geostrophic contours defined as

$$q = \beta y + \frac{f_0}{H} h = constant$$

are simply zonal lines. Those in region $y_1 < y < y_2$ close themselves, while the rest are blocked by the two partial meridional barriers. In the presence of a ridge in the form of (2.4), however, some of the geostrophic contours with $y_1 < y < y_2$ will be blocked by the coastal boundaries as shown in Fig. 3.1(a). Nevertheless, if the ridge is not high enough such that $h_0 < h_c$, where

$$h_c \equiv \frac{\beta(y_2 - y_1)}{|f_0|} H,$$

then not all geostrophic contours are blocked. Those geostrophic contours

$$\beta y + \frac{f_0}{H} h(x) = \beta y_0,$$

with $y_1 < y_0 < \Delta y(1 - h_0/h_c)$ are not blocked by the lateral boundaries. $\Delta y = y_2 - y_1$. ℓ_g is just one of these unblocked geostrophic contour. These nonblocked geostrophic contours provide free passage for the through-channel recirculating flow in the inviscid limit, which would lead to linear resonance in the presence of wind stress. However, if the ridge is high enough such that $h_0 > h_c$, then all geostrophic contours in the channel are blocked by the coastal boundaries. In this case, any motion in the channel has to be externally forced. Fig. 3.1(b) shows the geostrophic contour structure in the channel in one supercritical state. Thus, h_c will be called the critical ridge height, and $h_0 > (<) h_c$ will called the supercritical (subcritical) state. In the absence of any partial meridional barriers, the critical ridge height is

$$h_{0c} \equiv \frac{\beta D}{|f_0|} H,$$

in the same $\beta-$plane channel. The presence of the two partial meridional barriers obviously lowers the critical height. And in the case with $h_c < h_0 < h_{0c}$ all geostrophic contours in the channel are blocked in the presence of the barriers, while for the same ridges not all geostrophic contours in the channel are blocked in the absence of the barriers. Thus, for a ridge with $h_c < h_0 < h_{0c}$, the presence of the two partial meridional barriers makes a critical difference. Furthermore, in a purely $\beta-$plane channel, the supercritical state is present only in a channel with finite width D. In the presence of the meridional barriers, however, the width of the ridge does not matter so long as the gap between the two barriers is finite.

With the same analysis as that in Chapter 2, the equivalent eastern boundaries are $a-b$, $b-c$, $d-e$ and $f-g$, as shown in Fig. 3.1(b), while the rest of the lateral boundaries where geostrophic contours intersect are the corresponding equivalent western boundaries. Accordingly, the model domain is divided into four dynamically different subdomains, A, B, C and D. Then, in the area away from the equivalent western boundaries, the potential vorticity equation reduces to

$$J\left(\psi, \beta y + \frac{f_0}{H} h\right) = 0,$$

in the inviscid limit. Let us introduce a characteristic variable s such that

$$\frac{dx}{ds} = \frac{\partial q}{\partial y}, \tag{2.6}$$

$$\frac{dy}{ds} = -\frac{\partial q}{\partial x}, \tag{2.7}$$

and the potential vorticity equation reduces to

$$\frac{d\psi}{ds} = 0. \tag{2.8}$$

In this way, the geostrophic contours serve as the characteristics for the model. We start the integration of (2.6), (2.7) and (2.8) in each subdomain from its corresponding equivalent eastern boundaries with

$$\begin{aligned} \psi|_{a-b} &= \psi|_{b-c} = \psi_0, \\ \psi|_{d-e} &= \psi|_{f-g} = 0. \end{aligned}$$

Then, the solution is

$$\begin{aligned} \psi &= \psi_0 \quad \text{for } regions \;\; A, B; \\ \psi &= 0, \quad \text{for } regions \;\; C, D, \end{aligned}$$

except within the equivalent western boundaries along segments $f - j$ and $c - i$ where boundary layer currents are needed to close the circulation. Along geostrophic contour $y = y_1$ in the regions with $0 \leq x < L/2 - x_0$ and $L/2 + x_0 < x \leq L$ there is a discontinuity of the streamfunction with

$$\Delta\psi|_{y_1} = \psi_0,$$

which, as an internal current, represents the model current in the inviscid limit. Between regions B and C along geostrophic contour ℓ_1, defined as

$$y = y_2 - \frac{\alpha}{\beta}(L/2 - x),$$

where $\alpha = -f_0 h_0 / x_0 H$ is the topographic β, is a second internal current with

$$\Delta\psi|_{\ell_1} \ = \ -\psi_0.$$

Between regions C and B along geostrophic contour ℓ_2, defined as

$$y = y_1 \ + \ \frac{\alpha}{\beta}(L/2 + x_0 - x),$$

is a third internal current with

$$\Delta\psi|_{B-C} \ = \ -\psi_0.$$

They are similar to the internal currents discussed in Chapter 2. Along $f - j$ and $c - i$ are two equivalent western boundary layer currents which connect the internal currents. Thus, a loop of currents as shown in Fig. 3.1(b) is present, which is forced by the uniform wind stress.

The circulation structure in Fig. 3.1(b) gives rise to a straightforward calculation of the topographic form drag

$$\tau_D \equiv \rho_0 f_0 \overline{h\frac{\partial\psi}{\partial x}}^{x} \ = \ -\frac{\rho_0 f_0 \psi_0 h_0}{L}\left(1 - \frac{h_c}{h_0}\right) \qquad y_1 < y < y_2.$$

It is worth noting that τ_D here is uniform within region $y_1 < y < y_2$, just like the wind stress input. Otherwise, meridional momentum exchange would be required and the linear assumption would not be valid. The discussion about the form drag generation is similar to that in Chapter 2. The presence of the two partial meridional barriers enhances the form drag generation for the same model parameters and ψ_0. First, noting that as the gap between the barriers approaches zero, one has

$$\lim_{y_1 \to y_2} h_c \ = \ 0,$$

thus, the maximum form drag in this $\beta-$plane channel is

$$\tau_D^{max} \ = \ \lim_{y_1 \to y_2} \ = \ -\frac{\rho_0 f_0 \psi_0 h_0}{L},$$

which is the form drag generated in a corresponding $f-$plane channel model discussed in Appendix A. Apparently, in an $f-$plane model, both the channel width and length of the gap between the barriers do not affect the form drag generation. Second, unlike that discussed in Chapter 2, the width of the channel has no influence on the form drag generation in this $\beta-$plane model, and it can be generated on an infinite $\beta-$plane so long as $h_0 > h_c$. However, in the absence of the barriers, form drag can be generated only in a $\beta-$plane model with finite width because $h_{0c} \to \infty$ as $D \to \infty$. Balancing the topographic form drag with the wind stress in (2.4) determines ψ_0, which gives rise to the following simple formula for the through-channel volume transport

$$T_{r0} = \frac{\tau_0 L/\rho_0}{P_c}, \tag{2.9}$$

where P_c is the potential vorticity resistance in this model, defined as

$$P_c = |f_0|\frac{h_0}{H} - \beta(y_2 - y_1). \tag{2.10}$$

Obviously, the presence of the two meridional barriers reduces the steering effect of the $\beta-$effect on the geostrophic contours over the ridge, thus increasing the potential vorticity resistance in the channel.

The presence of the two partial meridional barriers has two effects. First, it alters the circulation structure. The presence of the southern meridional barrier moves the position of the current from the southern boundary to $y = y_1$, and now it appears as a mid-ocean jet along $y = y_1$. Second, it always reduces the through-channel transport. The relation between the transport and the model parameters is similar to that in the purely zonal channel model. The only difference is that in this model, the transport is related to the width of the opening between the two meridional barriers, $\Delta y = y_2 - y_1$, rather than to the width of the channel, D. This can be explained in the following way. Noting $\frac{\partial\psi}{\partial x}|_{y=y_1} = 0$, the zonal mean momentum balance at $y = y_1$ is

$$\kappa\overline{u}^x = \frac{\tau_0}{\rho_0 H}, \tag{2.11}$$

i.e., the wind stress at $y = y_1$ is purely balanced by bottom frictional drag. The structure of the equivalent western boundary current along $f - j$ is

$$\psi = \psi_0(1 - e^{-(y-y_1)/\delta}),$$

where $\delta = \kappa/\alpha$ is the characteristic thickness of the equivalent western boundary. Apparently, the structure of this boundary current is independent of both the width, D, of the channel and the distance between the two meridional barriers, Δy. The zonal length of this boundary current

$$\Delta x = x_0 \frac{h_0 - h_c}{h_0} \tag{2.12}$$

however, depends upon Δy but not upon D. Δx actually measures the supercriticality, $h_0 - h_c$, of the ridge height. With this, as $\kappa \to 0$, one has

$$\kappa \overline{u}^x|_{y=y_1} = -\psi_0 \frac{P_c}{HL},$$

which is independent of D. Putting this equation into (2.11) one has (2.9).

The transport ratio for the cases with and without partial meridional barriers is

$$\epsilon = \frac{h_0/h_{0c} - 1}{h_0/h_{0c} - \Delta y/D},$$

if $h_0 > h_{0c}$, the critical ridge height in the absence of any partial meridional barriers. Apparently, one always has

$$1 - h_{0c}/h_0 < \epsilon < 1,$$

as shown in Fig. 3.2. If $\Delta y/D < (2 - h_0/h_{0c})$, $\epsilon < 1/2$. Thus, meridional barriers with a narrow opening between, *i.e.*, small Δy, could lower the transport substantially. The influence declines as the ridge height increases, as shown in Fig. 3.2. Finally, one interesting observation is that *in the inviscid limit* as $\Delta y \to 0$ one has

$$T_{r0} \to \frac{\tau_0 L/\rho_0}{|f_0|\frac{h_0}{H}}.$$

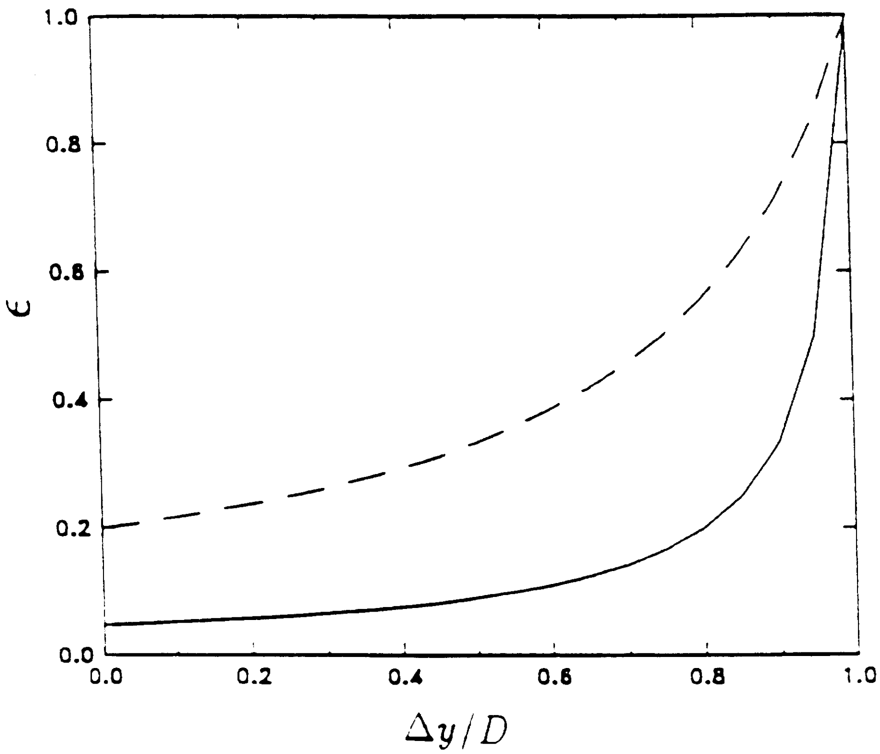

Figure 3.2: Transport ratio ϵ versus $\Delta y/D$. The solid line represents $h_0/h_c = 1.05$ while the dashed is for $h_0/h_c = 1.25$.

It is actually the result of an $f-$plane model, discussed in the appendix. The reason is that as $\kappa \to 0$, in the gap between the two meridional barriers, the boundary layer currents along segments $f-j$ and $c-i$ converge to the boundaries at $f-j$ and $c-i$. They are independent of the width of the gap. Furthermore, as $\Delta y \to 0$, $\Delta x \to x_0$ noting (2.12). Thus, the transport approaches that of the corresponding $f-$plane model results.

Now let's see how the presence of an additional ridge down stream would affect both the circulation and through-channel transport. The bottom topography now is

$$\begin{aligned} h(x,y) &= \begin{cases} h_1(1-|\frac{L_1-x}{x_1}|) & \text{if } |L_1-x| \leq x_1 \\ 0 & \text{otherwise} \end{cases} \\ &+ \begin{cases} h_2(1-|\frac{L_2-x}{x_2}|) & \text{if } |L_2-x| \leq x_2; \\ 0 & \text{otherwise,} \end{cases} \end{aligned}$$

which consists of two isolated ridges with $x_1+x_2 < L_2-L_1$. The supercriticality of the first ridge height $h_1 > h_c$ is still assumed. Around the second ridge, there are no meridional barriers. The presence of the additional ridge changes the geostrophic contour structure within the area over the ridge. The dashed lines in Fig. 3.3 (a), (b) and (c) show the geostrophic contours of the three cases with $h_2 \leq h_{*c}$, $h_{*c} < h_2 \leq h_{0c}$ and $h_2 > h_{0c}$, respectively, where

$$h_{*c} = \frac{\beta(D-y_1)}{|f_0|}H.$$

In all three figures, ℓ_1 and ℓ_2 over the first ridge are defined similar to those in Fig. 3.1(b). The difference among these three cases is that the geostrophic contour

$$\beta y + \frac{f_0}{H}h(x) = \beta y_1,$$

crosses the ridge at $x = L_2$ in Fig. 3.3(a). In Fig. 3.3(b), it does not cross the ridge at $x = L_2$ but not all of the geostrophic contours to its south are blocked by the northern boundary over the area of the additional ridge, while in Fig. 3.3(c), all geostrophic contours in the channel are blocked by either the northern or southern boundary over the area of the second ridge.

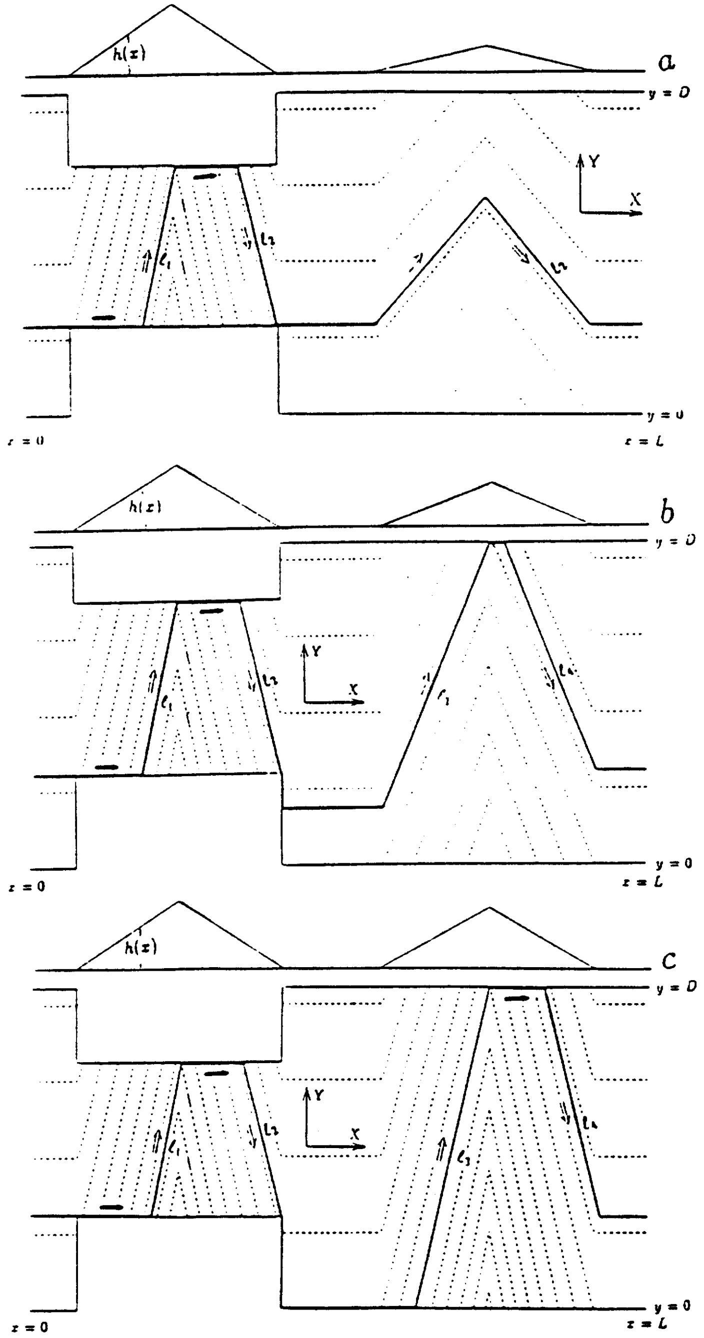

Figure 3.3: Similar to Fig. 3.1 but with the presence of an additional ridge. (a) with $h_2 \leq \beta(D-y_1)H/|f_0|$; (b) with $\beta(D-y_1)H/|f_0| < h_2 \leq \beta DH/|f_0|$; (c) with $h_2 > \beta DH/|f_0|$.

Knowing the geostrophic contour structure, one can determine the various equivalent dynamic western and eastern boundaries similar to the previous case. The circulation structure can be easily obtained by employing the same characteristic method as that for the previous case with a single ridge. Around the first ridge, the circulation is the same as that discussed in the previous case in the absence of the second ridge. In Fig. 3.3(a), the additional ridge has only a local influence. The passage of the otherwise purely zonal internal jet between $x = L_2 - x_2$ and $x = L_2 + x_2$ is displaced northward over the additional ridge. It flows along the geostrophic contour ℓ_2, defined as

$$\beta y + \frac{f_0}{H} h(x)|_{\ell_2} \;=\; \beta y_1.$$

This circulation pattern indicates that the presence of the additional ridge at $x = L_2$ with $h_2 \leq h_{*c}$ has no contribution to the topographic form-drag generation, and the potential vorticity resistance is not increased either. The through-channel transport remains the same as in (2.9).

In Fig. 3.3(b), the additional ridge is within the range $h_{*c} < h_2 < h_{0c}$. The geostrophic contour

$$\beta y + \frac{f_0}{H} h(x) = \beta y_1$$

is blocked by the northern boundary over the second ridge. In order to cross the second ridge, downstream of the first ridge, the internal current has to flow along the geostrophic contour ℓ_3, defined as

$$\beta y + \frac{f_0}{H} h(x)|_{\ell_3} \;=\; \beta D + \frac{f_0}{H} h_2.$$

This current crosses geostrophic contours along the northern boundary between $L_2 < x < L_2 + x_*$ as an equivalent western boundary current, where x_* satisfies

$$x_* \;=\; x_2 \left(1 - \frac{h_{*c}}{h_2}\right).$$

Afterwards, it flows along the geostrophic contour ℓ_4, defined as

$$\beta y + \frac{f_0}{H} h(x)|_{\ell_4} \;=\; \beta y_1,$$

all the way to the western edge of the southern meridional barrier. Between ℓ_2 and ℓ_3, the current has to flow along the eastern edge of the southern meridional barrier between $y = y_0$ and $y = y_1$ as a regular western boundary current. The southern end of this western boundary current, y_0, satisfies

$$y_0 = D\left(1 - \frac{h_2}{h_{0c}}\right).$$

Unlike the case in Fig. 3.3(a), the presence of the second ridge with $h_{*c} < h_2$ has a global effect because the circulation pattern upstream of the second ridge is affected. Furthermore, the form-drag generation is enhanced by the presence of the second ridge, and with the circulation pattern shown in Fig. 3.3(b), one has

$$\tau_D = -\frac{\rho_0 f_0 \psi_0 h_1}{L}\left(1 - \frac{h_c}{h_1}\right) - \frac{\rho_0 f_0 \psi_0 h_2}{L}\left(1 - \frac{h_{*c}}{h_2}\right).$$

It is obvious to see that were there no southern meridional barrier, the second ridge with $h_{*c} < h_2 < h_{0c}$ could not lead to any contribution to the total topographic form drag generation. The presence of the southern meridional barrier leads to the blocking of the critical geostrophic contour

$$\beta y + \frac{f_0}{H}h(x) = \beta y_1,$$

which results in the form drag generation through the second ridge even though $h_2 < h_{0c}$. Unlike the case shown in Fig. 3.3(a), even though $h_1 < h_c$, still all the geostrophic contours within the channel are blocked by the lateral boundaries and there is form drag generation. Given the form drag, the through-channel transport can be easily obtained. It is the same as (2.9) only with the potential vorticity resistance modified here as

$$P_c \equiv -f_0\frac{h_1}{H} - \beta(y_2 - y_1) - f_0\frac{h_2}{H} - \beta(D - y_1). \tag{2.13}$$

The presence of the second ridge introduces an additional amount of potential vorticity resistance $-f_0 h_2/H - \beta(D - y_1)$. Apparently, the presence of the second ridge lowers the through-channel transport. Again the width of the second ridge does not affect the transport. As $y_2 \to y_1$, the transport is still the same as (2.9), except that P_c is now equal to $|f_0|\frac{h_1}{H} + |f_0|\frac{h_2}{H} - \beta(D - y_1)$. This transport does not converge to the result of the corresponding $f-$plane model because of the additional ridge. The transport for a corresponding $f-$plane model is similar as (2.9), but the potential vorticity resistance is

$$P_{0c} = -f_0\frac{h_1}{H} - f_0\frac{h_2}{H}.$$

In Fig. 3.3(c), unlike either 3(a) or 3(b), no geostrophic contours can go over the second ridge with $h_2 > h_{0c}$. In order to cross the second ridge, the current has to cross geostrophic contours along the southern boundary between $x = L_0 - x_2$ and $x = L_0 - x_2 + x_{**}$ as an equivalent western boundary current, where x_{**} satisfies

$$x_{**} = x_2\left(1 - \frac{h_{0c}}{h_2}\right).$$

Then, it flows along the geostrophic contour ℓ_3, defined as

$$y = D - \frac{f_0 h_2}{\beta x_2 H}(x - L_2).$$

Between ℓ_2 and point $(L_2 - x_2, 0)$ it first flows along the eastern edge of the southern meridional barrier as a regular western boundary current until it reaches the southern boundary. Afterwards, it flows along the southern boundary. The rest is similar to that shown Fig. 3.3(b). The discussion about the relation between the transport and the model parameters are the same as that for the case shown in Fig. 3.3(b) and is not repeated here. It is worth noting that like Fig. 3.3(b), the additional ridge has a global influence on the circulation structure. In both cases, the influence is upstream of the second ridge, while downstream there is no influence.

It is quite straightforward to extend the above discussions to a general bottom topography and coastal geometry, so long as there are no closed geostrophic contours. The three cases above demonstrate that in a very wide channel with a narrow gap between two meridional barriers, which corresponds to that in Fig. 3.3(b) with $h_{*c} > h_2$ and

$h_c < h_1$, only topographic features between the barriers are important in determining the circulation, while other topographic features can only alter the flow passage. This presumably has important implication for the wind-driven circulation in the circumpolar ocean. Because Drake Passage is much narrower than the gap south of either Australia or South Africa, the critical height for the ridge around Drake Passage is much lower than any others in the circumpolar ocean. This implies that the topography around the Drake Passage could be in the supercritical range while the others are most likely not. This indicates that the bottom topography around the Drake Passage plays a fundamental role in determining the circulation in the circumpolar ocean, while others most likely play only a secondary role should the wind stress be uniform. In this sense, the Drake Passage is a choke point in the overall dynamics of the wind-driven circulation in the circumpolar ocean. For a uniform wind stress with model parameters chosen as $\tau_0 = 0.08N/m^2$, $\rho_0 = 1.03 \times 10^3 kg/m^3$, $L = 2.4 \times 10^4 km$, $D = 1.8 \times 10^3 km$, $H = 5km$, $x_0 = 1200km$, $f_0 = -2\omega \sin\theta^0$ and $\beta = 2\omega\cos\theta^0/a$ with $\theta = 60^0 S$ and $a = 6.37 \times 10^3 km$, $h_c = 408m$ and $T_r = 412Sv$ for $h_0 = 587m$, which is in the subcritical range if there are no meridional barriers.

3.3 A $\beta-$plane model with a non-uniform wind stress

In the preceding section, we have discussed the case with a uniform wind stress forcing. The influence of the two partial meridional barriers is quite clear and straightforward, and result is qualitatively similar to the corresponding case in the absence of any barriers discussed in Chapter 2. The discussion in Chapter 2 also showed that the wind stress curl could lead to a strong topographic form drag generation against the mean wind stress. In this section, we want to see how the presence of the two partial meridional barriers would affect that result and the Sverdrupian circulation in the channel.

The governing equation is now

$$J\left(\psi, \beta y + f_0 \frac{h}{H}\right) = w_e - \kappa \nabla^2 \psi,$$

with the boundary conditions (2.2) and (2.3). Again ψ_0 is determined through (2.4) with τ_0 replaced by $\overline{\tau_x}^x$, even though $\overline{\tau_x}^x$ is now a function of y. The discussion in Chapter 2 showed that in the case with a subcritical ridge, the Sverdrupian balance does not apply and there is no finite solution in the inviscid limit. In the case with a supercritical ridge, however, the Sverdrupian balance applies in the $\beta-$plane channel, even though there are no east or west coasts. The discussion is similar in this channel model with the presence of the two partial meridional barriers, it is thus not to be repeated here. In the case with a supercritical ridge, the potential vorticity equation reduces to

$$J(\psi, q) = w_e, \tag{3.1}$$

except within the various equivalent western boundary layers, see Fig. 3.4. Introducing characteristic variable s defined in (2.6) and (2.7), then one has

$$\frac{d\psi}{ds} = w_e. \tag{3.2}$$

For the convenience of characteristic integration, the model domain is divided into subdomains A, B, C, D, E, F and G, as shown in Fig. 3.4. The wind stress is chosen as

$$\tau_x = \tau_0 \left(1 - \varepsilon \cos \frac{\pi}{D} y\right) \tag{3.3}$$

and $\tau_y = 0$. $\varepsilon = 0, 1$. $\varepsilon = 0$ means uniform wind stress. Then, correspondingly

$$w_e = w_0 \sin \frac{\pi}{D} y,$$

where $w_0 = -\varepsilon \pi \tau_0 / \rho_0 H D$.

In regions A and G, the governing equation becomes

$$\beta \frac{\partial \psi}{\partial x} = w_e,$$

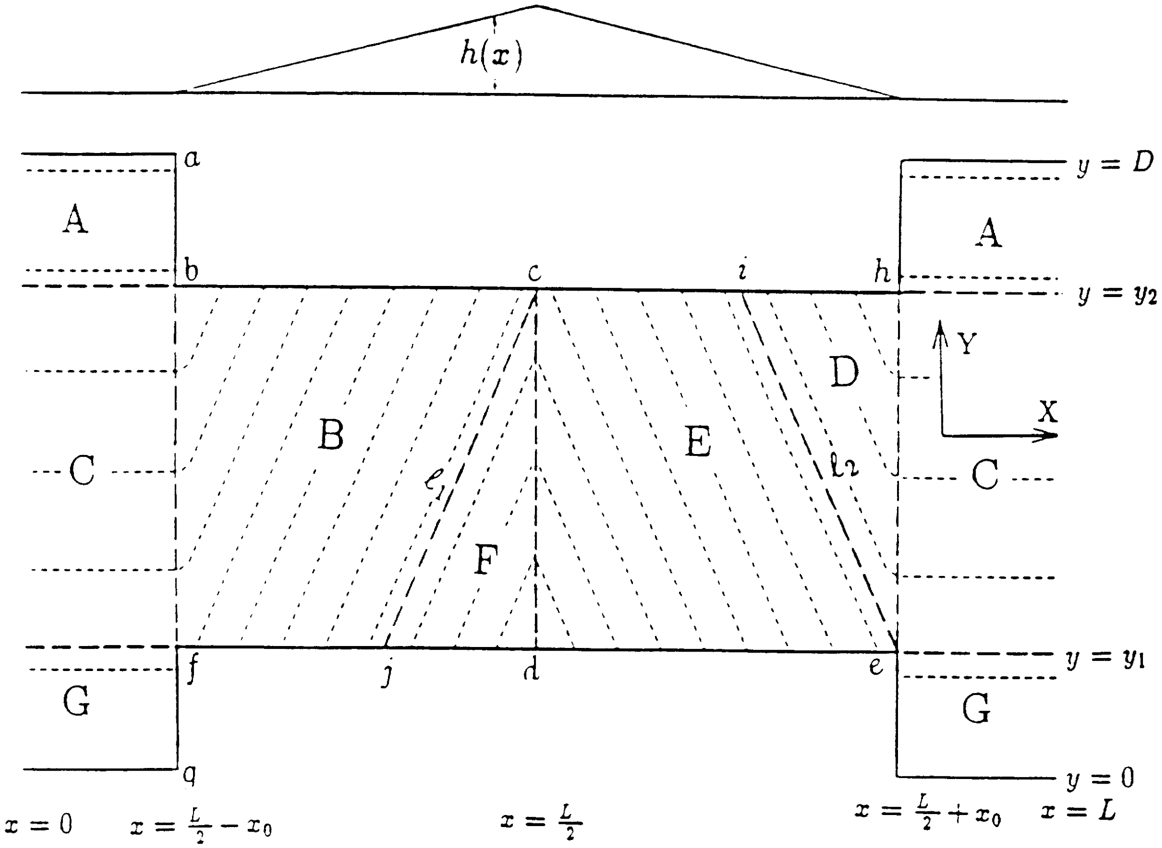

Figure 3.4: A schematic view of the domain of the circulation driven by a non-uniform wind stress in a β−plane channel with two partial meridional barriers. The short dashed lines represent the geostrophic contours, while the long dashed line represent the boundaries between different subdomains. On top is the profile of the ridge.

with the boundary condition

$$\psi|_{x=L/2-x_0} = \psi_0$$

for region A, and

$$\psi|_{x=L/2-x_0} = 0$$

for region G. The solution is

$$\begin{aligned}
\psi|_A &= \psi_0 + \frac{w_0}{\beta}(x - L/2 + x_0)\sin\frac{\pi}{D}y \quad \text{for} \quad 0 \le x \le L/2 - x_0, \\
&= \psi_0 + \frac{w_0}{\beta}\left(x - \frac{3}{2}L + x_0\right)\sin\frac{\pi}{D}y \quad \text{for} \quad L/2 - x_0 \le x \le L; \\
\psi|_G &= \frac{w_0}{\beta}(x - L/2 + x_0)\sin\frac{\pi}{D}y \quad \text{for} \quad 0 \le x \le L/2 - x_0, \\
&= \frac{w_0}{\beta}\left(x - \frac{3}{2}L + x_0\right)\sin\frac{\pi}{D}y \quad \text{for} \quad L/2 + x_0 \le x \le L.
\end{aligned}$$

In region B, the initial conditions for the characteristic equations (2.6), (2.7) and (3.2) are

$$\begin{aligned}
x|_{s=0} &= x_s, \\
y|_{s=0} &= y_2, \\
\psi|_{s=0} &= \psi_0.
\end{aligned}$$

The solution is

$$\psi|_B = \psi_0 - \frac{T_c}{2}\left(\cos\frac{\pi}{D}y_2 - \cos\frac{\pi}{D}y\right),$$

where

$$T_c = -\frac{2w_0D}{\alpha\pi}.$$

In region C, the governing equation reduces to

$$\beta\frac{\partial\psi}{\partial x} = w_e,$$

with the boundary condition

$$\psi|_{x=L/2-x_0} = \psi_0 - \frac{T_c}{2}\left(\cos\frac{\pi}{D}y_2 - \cos\frac{\pi}{D}y\right),$$

The solution is

$$\begin{aligned}
\psi|_C &= \psi_0 - \frac{T_c}{2}\left(\cos\frac{\pi}{D}y_2 - \cos\frac{\pi}{D}y\right) + \frac{w_0}{\beta}(x - L/2 + x_0)\sin\frac{\pi}{D}y \\
&\qquad\qquad \text{for} \quad 0 \le x \le L/2 - x_0; \\
&= \psi_0 - \frac{T_c}{2}\left(\cos\frac{\pi}{D}y_2 - \cos\frac{\pi}{D}y\right) + \frac{w_0}{\beta}(x - \frac{3}{2}L + x_0)\sin\frac{\pi}{D}y \\
&\qquad\qquad \text{for} \quad L/2 - x_0 \le x \le L.
\end{aligned}$$

In region D, the initial conditions for the characteristic equations (2.6), (2.7) and (3.2) are

$$\begin{aligned}
x|_{s=0} &= L/2 + x_0, \\
y|_{s=0} &= y_s, \\
\psi|_{s=0} &= \psi_0 - \frac{T_c}{2}\left(\cos\frac{\pi}{D}y_2 - \cos\frac{\pi}{D}y_s\right) + \frac{w_0}{\beta}(2x_0 - L)\sin\frac{\pi}{D}y_s.
\end{aligned}$$

The solution is

$$\begin{aligned}
\psi|_D = \psi_0 &- \frac{T_c}{2}\left\{\cos\frac{\pi}{D}y_2 - \cos\frac{\pi}{D}\left[y - \frac{\alpha}{\beta}(L/2 + x_0 - x)\right]\right\} \\
&+ \frac{w_0}{\beta}(2x_0 - L)\sin\frac{\pi}{D}\left[y - \frac{\alpha}{\beta}(L/2 + x_0 - x)\right] \\
&+ \frac{T_c}{2}\left\{\cos\frac{\pi}{D}\left[y - \frac{\alpha}{\beta}(L/2 + x_0 - x)\right] - \cos\frac{\pi}{D}y\right\}.
\end{aligned}$$

In region E, the initial conditions for the characteristic equations (2.6), (2.7) and (3.2) are

$$\begin{aligned}
x|_{s=0} &= x_s, \\
y|_{s=0} &= 0, \\
\psi|_{s=0} &= y_1.
\end{aligned}$$

The solution is

$$\psi|_E = \frac{T_c}{2}\left(\cos\frac{\pi}{D}y_1 - \cos\frac{\pi}{D}y\right).$$

In region F, the initial conditions for the characteristic equations (2.6), (2.7) and (3.2) are

$$\begin{aligned} x|_{s=0} &= L/2, \\ y|_{s=0} &= y_s, \\ \psi|_{s=0} &= \frac{T_c}{2}\left(\cos\frac{\pi}{D}y_1 - \cos\frac{\pi}{D}y_s\right). \end{aligned}$$

The solution is

$$\begin{aligned} \psi|_F = & \frac{T_c}{2}\left\{\cos\frac{\pi}{D}y_1 - \cos\frac{\pi}{D}\left[y + \frac{\alpha}{\beta}(L/2 - x)\right]\right\} \\ - & \frac{T_c}{2}\left\{\cos\frac{\pi}{D}\left[y + \frac{\alpha}{\beta}(L/2 - x)\right] - \cos\frac{\pi}{D}y\right\}. \end{aligned}$$

Similar to the case with a uniform wind stress, there are three internal currents represented by discontinuities of streamfunction. Along geostrophic contour ℓ_1, the discontinuity of the streamfunction is

$$\Delta\psi|_{\ell_1} = -\psi_0 + \frac{T_c}{2}\left(\cos\frac{\pi}{D}y_1 - \cos\frac{\pi}{D}y_2\right), \tag{3.4}$$

which indicates a northward flow if $\psi_0 < 0$, *i.e.*, there is an eastward through-channel flow. Similarly, along geostrophic contour ℓ_2, the discontinuity of the streamfunction is

$$\Delta\psi|_{\ell_2} = \psi_0 + \frac{T_c}{2}\left(\cos\frac{\pi}{D}y_1 - \cos\frac{\pi}{D}y_2\right) + \frac{w_0}{\beta}(2x_0 - L)\sin\frac{\pi}{D}y_1, \tag{3.5}$$

which indicates a southward (northward) flow if it is negative (positive). Along geostrophic contour $y = y_1$, the discontinuity of the streamfunction is

$$\Delta\psi|_{y_1} = \psi_0 + \frac{T_c}{2}\left(\cos\frac{\pi}{D}y_1 - \cos\frac{\pi}{D}y_2\right), \tag{3.6}$$

which generally indicates an eastward flow if $\psi_0 < 0$. Obviously, if $\varepsilon = 0$, *i.e.*, the wind stress is uniform, the solution degenerates to the solution discussed in the preceding section. And if $y_1 = 0$ and $y_2 = D$, the above solutions reduce to the purely zonal channel model case discussed in Chapter 2. Figs. 3.5, 3.6, 3.8 and Fig. 3.10 show four examples of the wind-driven circulation for different y_1 and y_2 to be discussed later in greater detail.

With the above solution the calculation of the topographic form drag is straightforward albeit tedious, and one has

$$\begin{aligned}\tau_D/\rho_0 &= P_c H\psi_0/L + \tau_0 \cos\frac{\pi}{D}y \\ -\tau_0 \Bigg[(1-2x_0/L)\cos\frac{\pi}{D}y_1 &+ \frac{x_0}{L}(1-h_c/h_0)\left(\cos\frac{\pi}{D}y_1 + \cos\frac{\pi}{D}y_2\right) + \\ &\frac{D}{\pi\Delta y}\frac{h_c}{h_0}\frac{2x_0}{L}(\sin\frac{\pi}{D}y_2 - \sin\frac{\pi}{D}y_1)\Bigg].\end{aligned}$$

The form drag τ_D depends upon y through the second term. Nevertheless, it has the same dependence on y as the wind stress. Otherwise a meridional momentum exchange would be required, and our linear model here would not be appropriate. The first terms, as discussed in section 2, represented the linear form drag generation by the through-channel recirculating flow carrying all the through-channel volume transport, while the other terms together represent the linear form-drag generation via the Sverdrupian flow driven by the wind stress curl, in accordance with discussions in Chapter 2. These two form-drag generation processes are independent of each other in our linear model.

In Fig. 3.6 with $y_1 = 0$ and $y_2 < D$, the form drag generated through the Sverdrupian flow is

$$\begin{aligned}\tau_{D2} &= \tau_0\cos\frac{\pi}{D}y - (1-2x_0/L)\tau_0 - \\ \tau_0\frac{x_0}{L}(1-h_c/h_0)\left(1+\cos\frac{\pi}{D}y_2\right) &- \tau_0\frac{D}{\pi\Delta y}\frac{h_c}{h_0}\frac{2x_0}{L}\sin\frac{\pi}{D}y_2,\end{aligned}$$

and one always has

$$\tau_{D2} \le \tau_{D1},$$

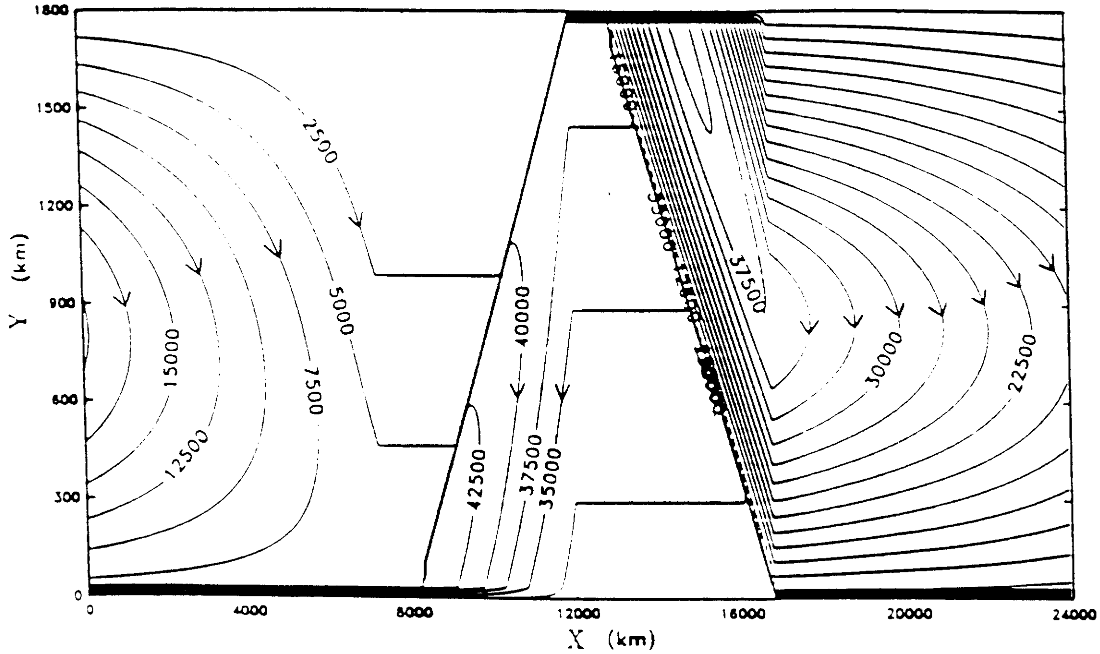

Figure 3.5: The streamfunction (m^2/s) for the case with a purely zonal channel. The model parameters are $H = 5000m$, $D = 1800km$, $L = 24000km$, $x_0 = 4800km$, $h_0 = 1000m$, $\theta = 60°S$, $\tau_0 = 0.08N/m^2$.

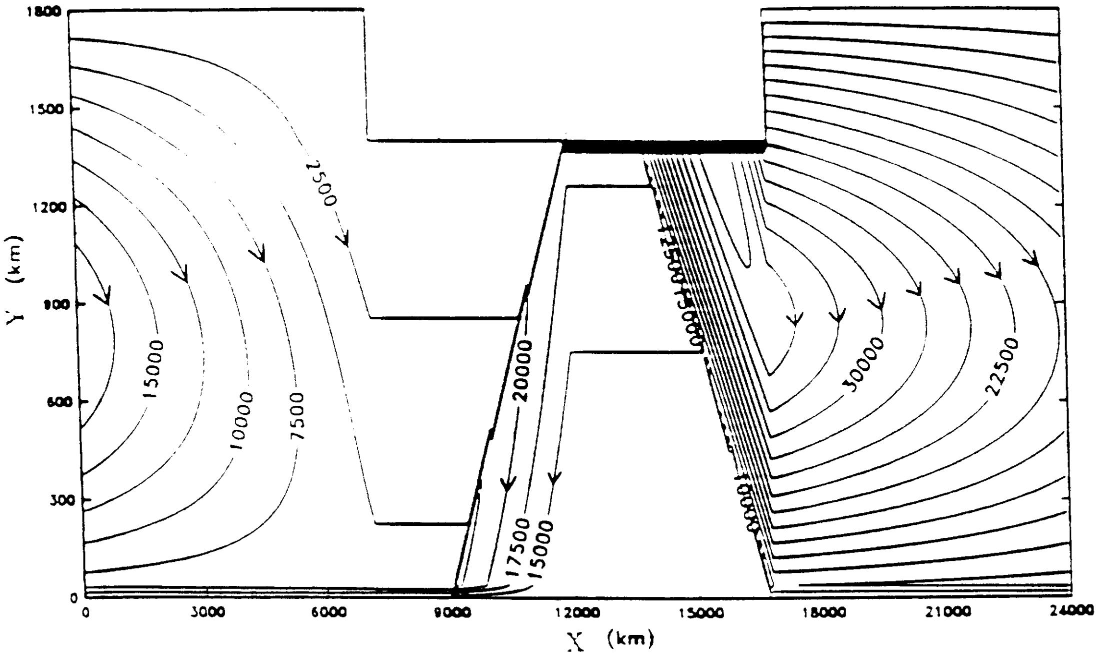

Figure 3.6: Similar to Fig. 3.5 except $y_1 = 0$ and $y_2 = 1400km$.

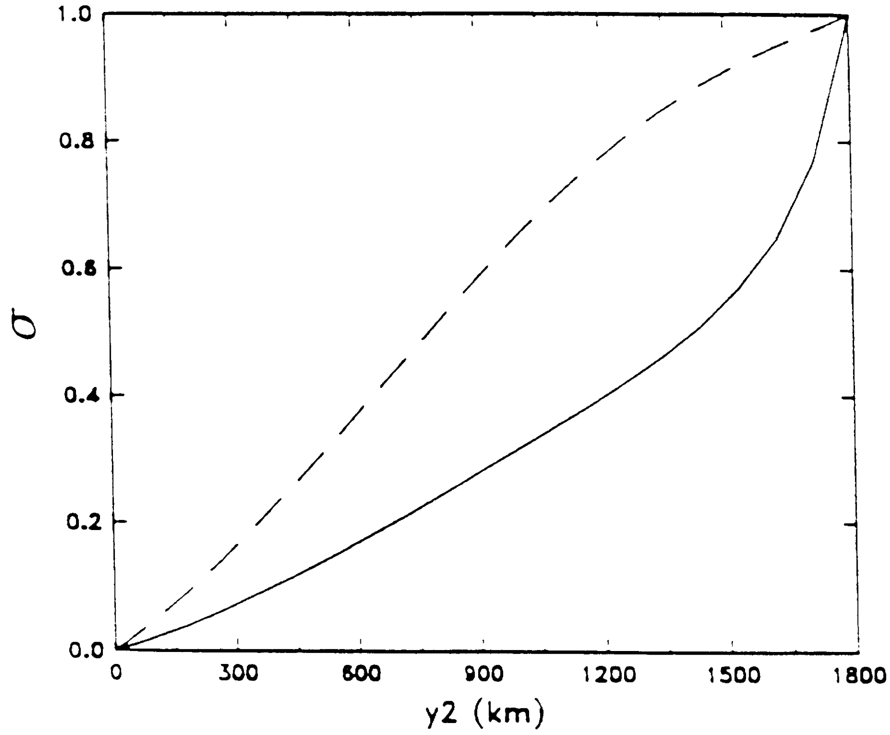

Figure 3.7: σ versus y_2, the solid line for $h_0 = 900m$ and the dashed line for $h_0 = 1100m$. The other model parameters are similar to those in Fig. 3.5.

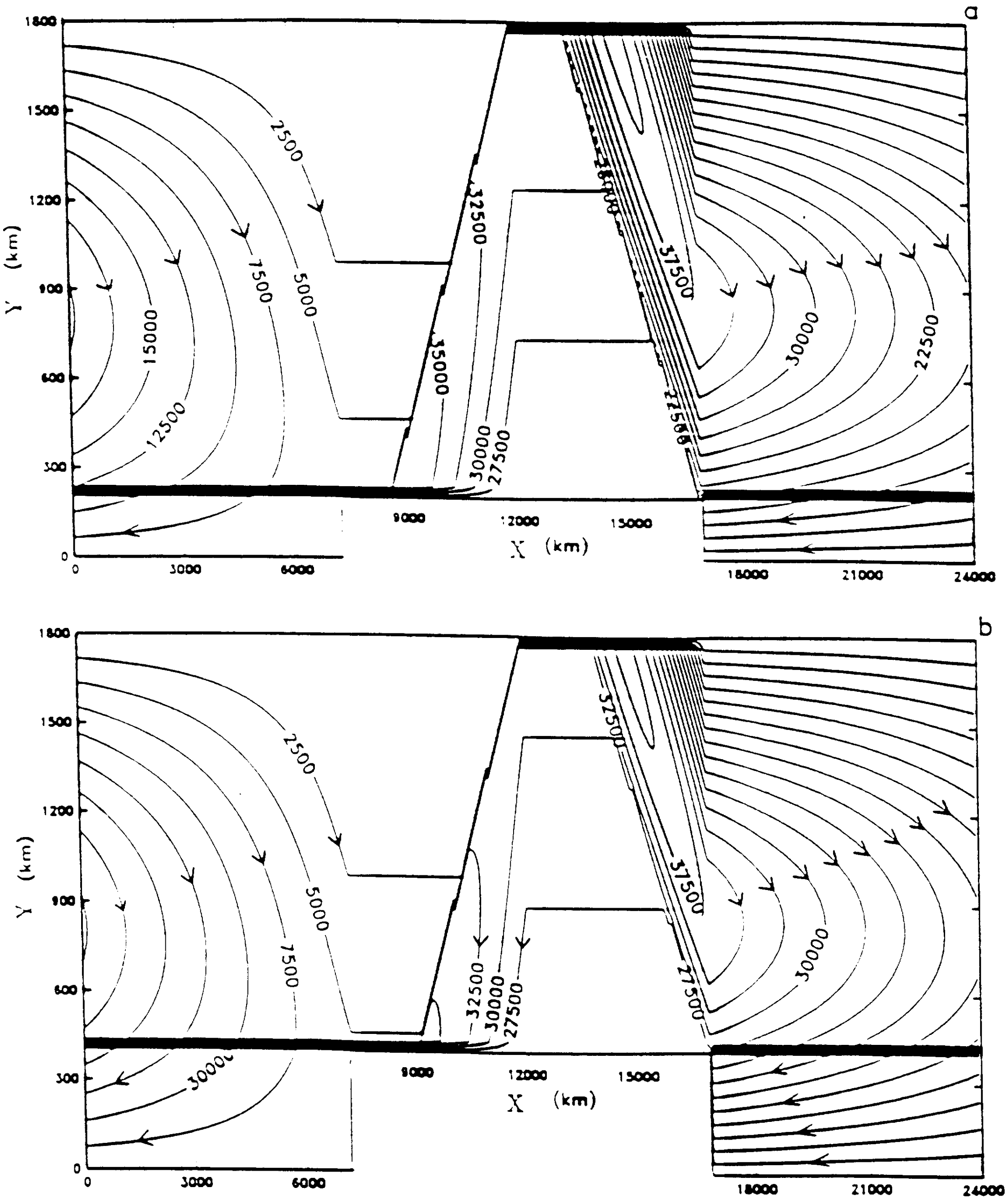

Figure 3.8: Similar to Fig. 3.5 except $y_1 = 160km$ (a) and $y_1 = 400km$ (b).

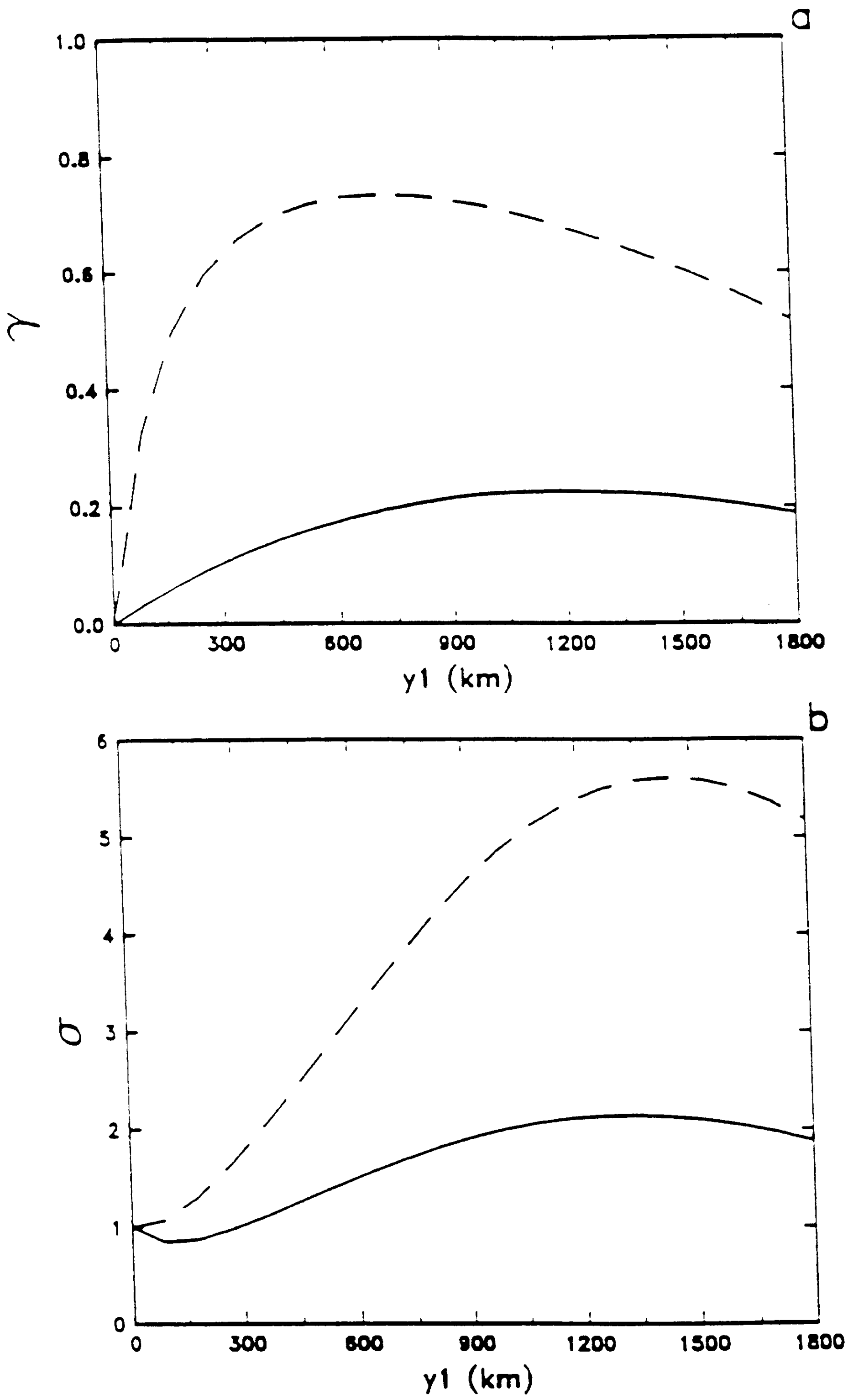

Figure 3.9: (a) γ versus y_1 for $x_0 = 1200km$, the solid line for $h_0 = 900m$ and the dashed line for $h_0 = 1100m$, (b) Same as (a) but σ versus y_1 with $x_0 = 1200km$. The other model parameters are similar to those in Fig. 3.5.

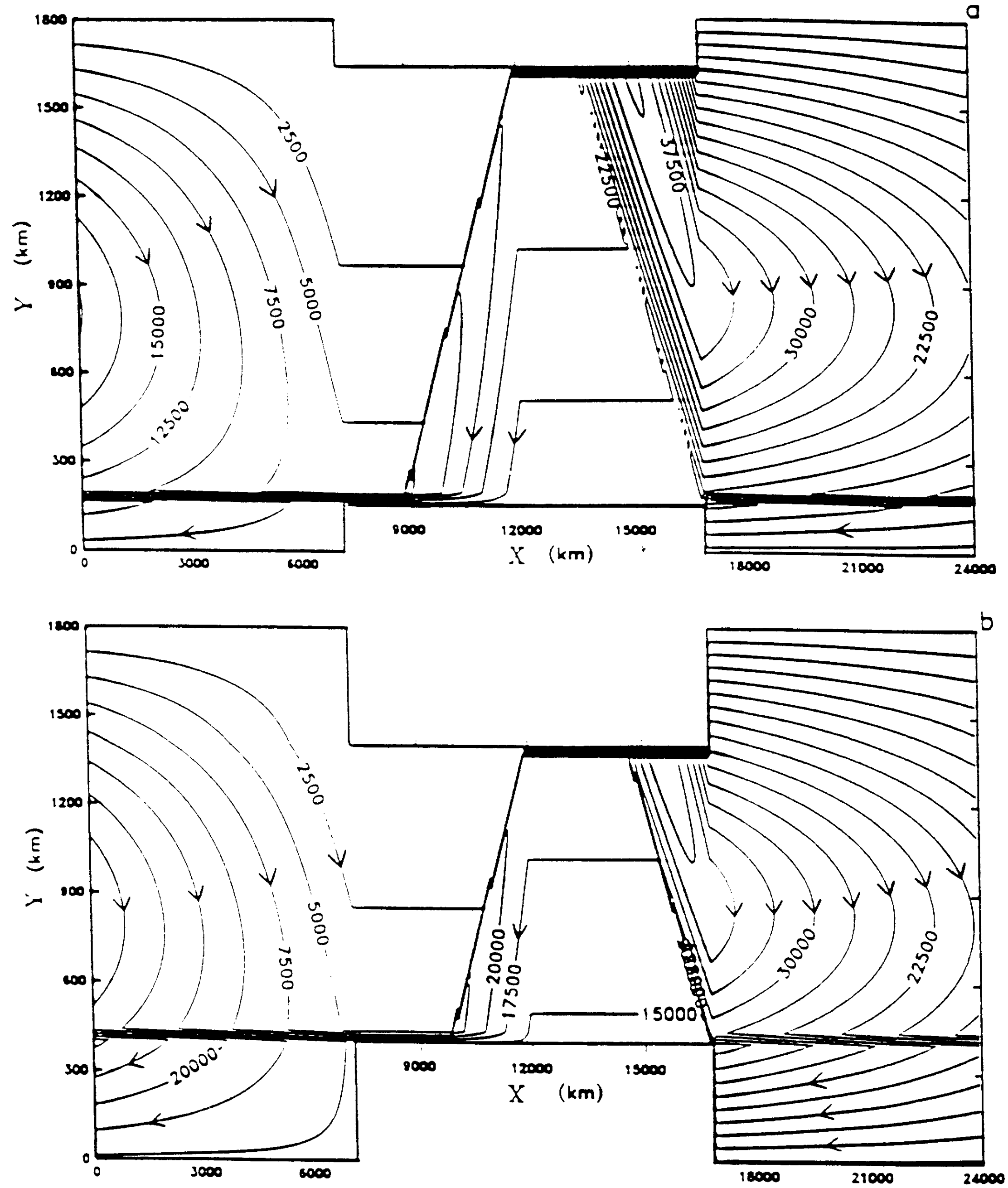

Figure 3.10: Similar to Fig. 3.5 except $y_1 = 160km$ (a), and $y_1 = 400km$ (b).

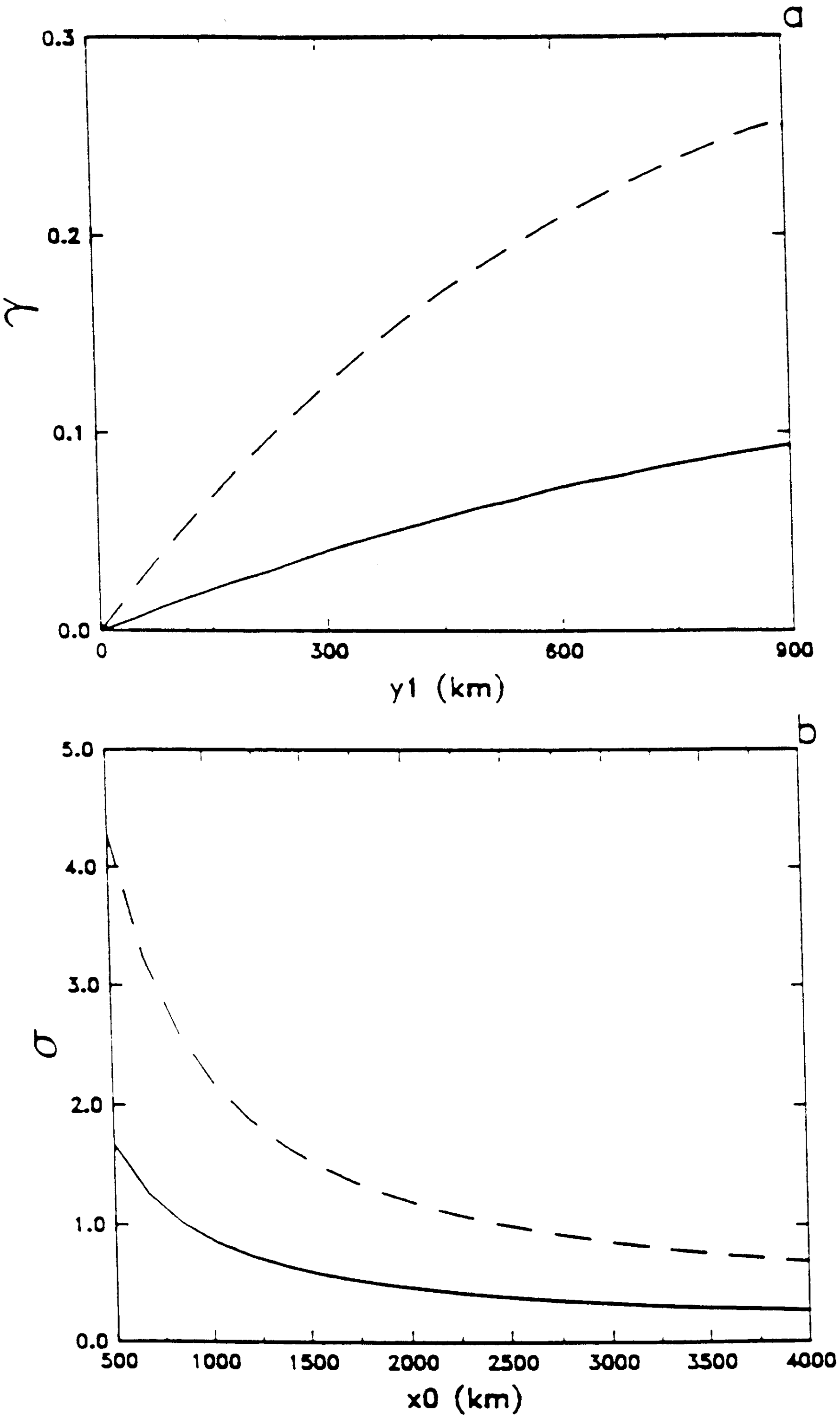

Figure 3.11: (a) Similar to Fig. 9(a) except for the cases with symmetric barriers. (b) σ versus x_0 with $y_1 = D/3$. The solid line is for $h_0 = 900m$ and the dashed line for $h_0 = 1100m$.

where τ_{D1}, defined as

$$\tau_{D1} \equiv \tau_0 \cos\frac{\pi}{D}y - (1 - 2x_0/L)\tau_0,$$

is the form drag generated by the Sverdrupian flow in the purely zonal channel model. So the presence of the northern barrier always enhances the linear form drag generation via the Sverdrupian circulation against the zonal mean wind stress. The reason is the following. Similar to Fig. 3.5, all the southward Sverdrupian flow within the interior basin away from the ridge shown in Fig. 3.6 is returned northward in region D, noting Fig. 3.4. This northward flow contributes to generate form drag against the mean wind stress, noting (2.4). Unlike that show in Fig. 3.5, not all the southward Sverdrupian flow in the interior in Fig. 3.6 goes through region D except within the northern equivalent western boundary layer (comparing Fig. 3.4 and Fig. 3.6). This southward Sverdrupian flow contributes to generate form drag which enhances the zonal mean wind stress, noting (2.4). Thus the presence of the northern barrier results in a larger form-drag generation against the zonal mean wind stress via the Sverdrupian circulation.

In Fig. 3.8 with $y_1 > 0$ and $y_2 = D$, the form drag generated through the Sverdrupian flow is

$$\begin{aligned}\tau_{D3} = {} & \tau_0 \cos\frac{\pi}{D}y - (1 - 2x_0/L)\tau_0 \cos\frac{\pi}{D}y_1 + \\ & \tau_0\frac{x_0}{L}(1 - h_c/h_0)\left(1 - \cos\frac{\pi}{D}y_1\right) + \tau_0\frac{D}{\pi\Delta y}\frac{h_c}{h_0}\frac{2x_0}{L}\sin\frac{\pi}{D}y_1,\end{aligned}$$

and one always has

$$\tau_{D3} \geq \tau_{D1}.$$

So the presence of the southern barrier always weakens the linear form drag generation via the Sverdrupian circulation, because the presence of the southern barrier shrinks region D, compared with that in Fig. 3.5. Noting (2.4), this would reduce the effective $h(x)$ in generating the form drag due to the Sverdrupian flow. Besides, the presence of the southern barrier weakens the northward return flow of the Sverdrupian flow over the ridge in region D, this also reduces the form drag generation. Thus, the presence of the southern barrier results in a weaker form drag compared with that in the purely zonal channel.

In the presence of both the southern and northern barriers, the above two opposite effects will compete with each other. In general with $y_2 \leq D/2$ or $D - y_2 \geq y_1$, the second effect tends to dominate. For the simple case with $y_2 = D - y_1$, one has

$$\tau_{D4} \;=\; \tau_0 \cos\frac{\pi}{D}y \;-\; (1 - 2x_0/L)\tau_0 \cos\frac{\pi}{D}y_1.$$

Obviously, the second effect discussed above prevails, and one always has

$$\tau_{D4} \;\geq\; \tau_{D1}.$$

Similar to case 3, In this case, the form drag generated by the Sverdrupian flow is always smaller than that in the corresponding purely zonal channel model.

Balancing the wind stress τ_x with the topographic form drag τ_D in (2.4) determines ψ_0, and leads to the following through-channel transport

$$T_r \;=\; T_{r0}\left[1 \;-\; (1 - 2x_0/L)\cos\frac{\pi}{D}y_1 \;-\; \frac{x_0}{L}\left(1 - \frac{h_c}{h_0}\right)\left(\cos\frac{\pi}{D}y_1 + \cos\frac{\pi}{D}y_2\right) \;-\; \frac{D}{\pi\Delta y}\frac{h_c}{h_0}\frac{2x_0}{L}\left(\sin\frac{\pi}{D}y_2 - \sin\frac{\pi}{D}y_1\right)\right]. \tag{3.7}$$

With the transport formula above one can discuss several special cases according to the positions of the tips of the two partial meridional barriers.

(1) $y_1 = 0$ **and** $y_2 = D$.

In this case, the solution reduces to the simple case discussed in Part I with

$$T_{r1} \;=\; \frac{\tau_0 2x_0/\rho_0}{|f_0|\frac{h_0}{H} - \beta D}. \tag{3.8}$$

So, the case discussed in Chapter 2 is only the simplest special case. In this case, regions A and G in Fig. 3.4 disappear. The circulation pattern is shown in Fig. 3.5.

The circulation within the channel can generally be divided into 4 different components. The major one is the Sverdrupian gyre over regions C and D, noting Fig. 3.4.

The equivalent western boundary layer of this gyre circulation is along segment $i - h$ along the northern boundary. The rough estimate of the gyre's volume flux for the case with a narrow ridge $x_0 \ll L$ is

$$T_{Sv} \sim \frac{H w_0 L}{\beta}. \tag{3.9}$$

The second gyre lies over the ridge in region E and F. This mini-gyre can be further divided into two parts, the outer and the inner part. For the outer part, in region E, it is purely zonal. The equivalent western boundary layers are along segment $j - d$ along the southern boundary and along segment $c - i$ along the northern boundary. In the meridional direction, it is closed by the internal currents along ℓ_1 and ℓ_2. The inner part of this gyre lies only over region F. The corresponding equivalent western boundary is along segment $j - d$ along the southern boundary. It is closed by the internal current along ℓ_1. The volume flux, HT_c, of this mini-gyre is generally much smaller than that of the first one for $x_0 \ll L$. Both gyres are singly connected. The other two parts are the two through-channel recirculating flows, whose volume fluxes combine to make the total through-channel transport. Unlike the two gyre circulations, these later two through-channel recirculating flows are not singly connected. The major one flows along the southern boundary, ℓ_1 and ℓ_2, as an internal boundary current, while along segments $f - j$ and $c - i$ it flows as an equivalent western boundary current. The volume flux of this branch is $T_{r1} - HT_c$. The second one is weaker, and it flows to the north of the major Sverdrupian gyre in region C. Over region B, it is purely zonal flow, and represented by $\psi|_B$. It flows along ℓ_1 as an internal current and crosses the ridge as an equivalent western boundary current along segment $c - h$.

(2) $y_1 = 0$ and $y_2 < D$.

In this case, the transport reduces to

$$T_{r2} = \frac{\tau_0 2x_0/\rho_0}{|f_0|\frac{h_0}{H} - \beta y_2}\left[1 - \frac{1}{2}\left(1 - \frac{h_c}{h_0}\right)\left(1 + \cos\frac{\pi}{D}y_2\right) - \frac{Dh_c}{\pi \Delta y h_0}\sin\frac{\pi}{D}y_2\right]. \tag{3.10}$$

Thus in the presence of only a partial northern barrier, one always has

$$T_{r2} < T_{r1}.$$

Unlike case 1, in this case the transport is related to both the ridge width and the length of the channel, besides it is also related to the length of the northern barrier. The presence of the northern barrier always leads to a lower through-channel transport. This is because the presence of the northern barrier leads to both a larger potential vorticity resistance and stronger form-drag generation against the zonal mean wind stress via the Sverdrupian flow. Both effects contribute to lower the through-channel transport. The circulation pattern is shown in Fig. 3.6.

As $y_2 \to 0$, *i.e.*, the gap between the northern barrier and the southern boundary is very small, we have

$$T_{r2} \to 0.$$

Here it is assumed that $\kappa \to 0$ such that $\delta \ll y_2$ still holds. This is quite intuitive. As $y_2 \to 0$, the wind stress between $0 < y < y_2$, $\overline{\tau_x}^y \to 0$. This transport is also the result of a similar $\beta-$plane model with $y_2 \to 0$ discussed in the preceding section forced by a uniform wind stress $\overline{\tau_x}^y \to 0$. As we have discussed in the preceding section, as the channel width goes to zero, the $\beta-$steering effect on the geostrophic contours over the ridge vanishes, and the $\beta-$plane result degenerates to the $f-$plane result. Fig. 3.7 shows $\sigma \equiv T_{r2}/T_{r1}$ versus y_2 for $h_0 = 900m$ (solid line) and for $h_0 = 1100m$ (dashed line). It monotonically increases from 0 at $y_2 \to 0$ to 1 at $y_2 = D$, and increases with increasing ridge height. It is worth noting that T_{r2}/T_{r1} is independent of x_0.

The circulation pattern shown in Fig. 3.6 is basically similar to that shown in Fig. 3.5. The only difference is that the major Sverdrupian gyre now lies over region A, C and D, and the corresponding equivalent western boundaries are now along segment $i-h$ along the northern boundary and at the western boundary of the northern barrier, *i.e.*, the eastern edge of the southern barrier. The rough estimate of the volume flux of this Sverdrupian gyre for a narrow ridge is still given by (3.9). The presence of the northern barrier weakens volume fluxes of both branches of the through-channel recirculating flows.

It is interesting to note that as $y_2 \to 0$, the through-channel recirculating flows vanish and the circulation in the channel approaches the regular Sverdrupian gyre in a closed basin.

(3) $y_2 = D$ and $y_1 > 0$.

In this case, the transport reduces to

$$T_{r3} = \frac{\tau_0 L/\rho_0}{|f_0|\frac{h_0}{H} - \beta(D - y_1)} \left[1 - \frac{L - 2x_0}{L} \cos\frac{\pi}{D}y_1 + \right.$$
$$\left. \frac{x_0}{L}(1 - h_c/h_0)\left(1 - \cos\frac{\pi}{D}y_1\right) + \frac{2x_0}{L}\frac{D}{\pi\Delta y}\frac{h_c}{h_0}\sin\frac{\pi}{D}y_1\right]. \tag{3.11}$$

This case is more complicated than case 2. Although the presence of the southern barrier always leads to a larger potential vorticity resistance, it also leads to a weaker form-drag generation via the Sverdrupian flow, compared with case 1. So, the transport can be either larger or smaller than that in case 1. The corresponding circulation pattern is shown in Fig. 3.8.

As $y_1 \to D$, we have

$$T_{r3} \to \frac{2\tau_0 L/\rho_0}{|f_0|\frac{h_0}{H}}.$$

Here it is assumed that $\kappa \to 0$ such that $\delta \ll D - y_1$ still holds. Again, it is the result in a $f-$plane model discussed in Appendix A if a uniform wind stress $\tau_x = 2\tau_0$ were applied, because between $y_1 < y < D$, $\overline{\tau_x}^y \to 2\tau_0$. What is different from case 2 is that although in both cases $\Delta y \to 0$, the through-channel transport in case 2 vanishes while it does not vanish in case 3. If

$$\frac{2x_0}{L} < \gamma,$$

where

$$\gamma = \frac{1 - \cos\frac{\pi}{D}y_1}{\frac{\Delta P_c}{P_{c0}} + \left(1 - \cos\frac{\pi}{D}y_1\right) - \frac{1}{2}(1 - h_c/h_0)\left(1 - \cos\frac{\pi}{D}y_1\right) - \frac{D}{\pi\Delta y}\frac{h_c}{h_0}\sin\frac{\pi}{D}y_1},$$

one has

$$T_{r3} > T_{r1},$$

where $P_{c0} = -f_0 h_0/H - \beta D$ and $\Delta P_c = \beta y_1$. In this case, the decrease of the form-drag generation via the Sverdrupian circulation due to the presence of the southern barrier overpowers the increase in potential vorticity resistance. And the presence of the southern barrier leads to an increase, rather than decrease, in through-channel transport. Otherwise, the opposite happens and the presence of the southern barrier leads to a decrease in the through channel transport. As is shown in Fig. 3.9(a), γ first increases from 0 as y_1 increases from zero, then it decreases. Only for a rather wide ridge can the presence of the southern barrier lower the transport. Fig. 3.9(b) shows $\sigma = T_{r3}/T_{r1}$ for $x_0 = 1200km$. It indicates that for both cases with $h_0 = 900m$ (solid line) and $h_0 = 1100m$ (dashed line), the presence of the southern barrier leads to a substantial increase in the through-channel transport, except for a very small y_1.

The detailed structure of the circulation patterns in the presence of the southern barrier, as shown in Fig. 3.8(a) for $y_1 = 160km$ and (b) for $y_1 = 400km$, is quite different from that shown in Fig. 3.6. The difference between Fig. 3.8(a) and (b) is that in (a),

$$\Delta\psi|_{\ell_2} < -\frac{T_c}{2}\left(1 + \cos\frac{\pi}{D}y_1\right),$$

the internal current along ℓ_2 continuously flows southward; while in (b)

$$\Delta\psi|_{\ell_2} > 0,$$

the internal current along ℓ_2 flows northward, noting Fig. 3.4. The above two criteria can be met by adjusting either the length of the southern barrier, y_1, or the ridge height, h_0. In both (a) and (b), the major Sverdrupian gyre downstream of the ridge discussed in case 1 and case 2 breaks down into two gyres. The rough estimate of volume flux of the northern Sverdrupian gyre, whose boundary is the outer most singly connected closed streamline to the north of $y = y_1$, for a narrow ridge is now

$$T_{Sv}^n \sim \frac{Hw_0}{\beta}(L - 2x_0)\left(1 - \sin\frac{\pi}{D}y_1\right), \tag{3.12}$$

while that of the southern one is

$$T_{Sv}^s \sim \frac{Hw_0}{\beta}(L - 2x_0)\sin\frac{\pi}{D}y_1. \tag{3.13}$$

In (a), the southern Sverdrupian gyre with $y \leq y_1$ is isolated from the circulation to the north. Similar to case 1, the through-channel is still divided into two parts. Nevertheless, the volume flux of the internal current along ℓ_2 is now weakened roughly by $\frac{w_0}{\beta}H(2x_0 - L)sin\frac{\pi}{D}y_1$, and this part is carried out through the flow to north of the northern Sverdrupian gyre. This branch of the through channel flow embraces the northern Sverdrupian gyre. The rest of the circulation is similar to that in case 1.

In case (b), the circulation is much more complicated. (If $y_1 > D/2$, the northern Sverdrupian gyre completely disappears.) The southern Sverdrupian gyre is not totally isolated from the rest of the circulation. The volume flux of its western boundary current is (3.13). Part of this western boundary current with volume flux

$$T_{sw} = H\left[\psi_0 - \frac{T_c}{2}\left(1 + \cos\frac{\pi}{D}y_1\right)\right].$$

is returned via the internal current along $y = y_1$. The rest with volume flux $T_{nw} = T^s_{Sv} - T_{sw}$ flows northward along ℓ_2 and splits into two parts. One part with volume flux $H\frac{T_c}{2}(1 + \cos\frac{\pi}{D}y_1)$ flows westward over region E to region F until it reaches the southern boundary along $j - d$. There it converges to an equivalent western boundary current. Afterwards, it flows northward along ℓ_1 and eastward along the northern boundary. It joins the other branch, which flows directly northward along ℓ_2, at point i (see Fig. 3.4) at the northern boundary. Then, they return southward as the flow to the immediate north of the northern Sverdrupian gyre. The through-channel recirculating flow in region B is similar to that in case 1. What is different is that unlike case 1 or (a), it does not split at point i. It flows eastward to the north of the return flow for the southern Sverdrupian gyre. Obviously, the circulation pattern of (b) is closer to the "observed" circulation in the circumpolar ocean. Therefore, in terms of changing circulation structure, the southern barrier has a far more fundamental influence than the northern barrier, especially when it is sufficiently long. Furthermore, the influence of the northern barrier is localized around the northern barrier, while that of southern one is global in that circulation structure in the whole channel is affected.

(4) $y_2 = D - y_1$.

In this case, the transport reduces to

$$T_{r4} = \frac{\tau_0 L/\rho_0}{|f_0|\frac{h_0}{H} - \beta(D - 2y_1)} \left[1 - (1 - 2x_0/L)\cos\frac{\pi}{D}y_1\right]. \tag{3.14}$$

For this case with symmetric barriers, the relation between the transport and the model parameter is quite simple. The weakening effect of the southern barrier on the form-drag generation via the Sverdrupian circulation prevails over the enhancing effect of the northern barrier. The form-drag generation via the Sverdrupian circulation is always weaker than that in case 1. Nevertheless, the presence of the symmetric barriers also raises the potential vorticity resistance. Thus, the situation is similar to that in case 3, and the transport can be either larger or smaller than that in case 1. The corresponding circulation pattern is shown in Fig. 3.10.

Similar to the preceding cases, as $y_1 \to D/2$, we have

$$T_{r4} \to \frac{\tau_0 L/\rho_0}{|f_0|\frac{h_0}{H}},$$

Here it is assumed that $\kappa \to 0$ such that $\delta \ll y_2 - y_1$ still holds. Again, it is the result in the corresponding $f-$plane channel if a uniform wind stress $\tau_x = \tau_0$ were used, because between $y_1 < y < y_2$, $\overline{\tau_x}^y \to \tau_0$. And,

$$\sigma = \frac{T_{r4}}{T_{r1}} \begin{cases} < 1 & \text{if } \frac{2x_0}{L} > \gamma; \\ = 1 & \text{if } \frac{2x_0}{L} = \gamma; \\ > 1 & \text{if } \frac{2x_0}{L} < \gamma, \end{cases}$$

where

$$\gamma = \frac{1 - \cos\frac{\pi}{D}y_1}{\left(1 - \cos\frac{\pi}{D}y_1\right) + \frac{\Delta P_c}{P_{c0}}},$$

where $P_{c0} = |f_0|\frac{h_0}{H} - \beta D$ and $\Delta P_c = 2\beta y_1$. As is shown in Fig. 3.11(a), γ (the dashed line for $h_0 = 1100m$ and the solid line for $h_0 = 900m$) increases with increasing y_1, *i.e.*, decreasing gap between the two barriers, and increasing height of the ridge. This is slightly different from those shown in Fig. 3.9(a). Above the line, the increase in the potential vorticity resistance prevails over the decrease in the form-drag generation through the Sverdrupian circulation, and the presence of the two barriers lowers the transport, while below the line the opposite happens. Fig. 3.11(b) shows σ versus x_0 (the dashed line for $h_0 = 1100m$ and the solid line for $h_0 = 900m$) for $y_1 = D/3$. For a narrow ridge, the presence of symmetric barriers substantially enhances the through-channel transport, while for a wide ridge, the opposite happens. Fig. 3.10(a) shows the circulation patterns for short symmetric barriers with $y_1 = 160km$, while (b) shows that for a long symmetric barriers with $y_1 = 400km$. The discussion is quite similar to that of case 3, and is not repeated here. For a wind stress in the form (3.3) with model parameters chosen as $\tau_0 = 0.08N/m^2$, $\rho_0 = 1.03 \times 10^3 kg/m^3$, $L = 2.4 \times 10^4 km$, $D = 1.8 \times 10^3 km$, $H = 5km$, $x_0 = 1200km$, $f_0 = -2\omega \sin\theta$ and $\beta = 2\omega\cos\theta/a$ with $\theta = 60^0 S$ and $a = 6.37 \times 10^3 km$, $T_{r4} = 150Sv$ for $h_0 = 587m$, which would be in the subcritical range if there were no meridional barriers. For these model parameters, $2x_0/L > \gamma$, thus the presence of the symmetric partial meridional barriers substantially lowers the through-channel transport.

In the preceding section we have discussed the case with an additional ridge downstream of the first ridge. We could proceed with a similar discussion in the presence of another additional ridge. The discussion is rather tedious, yet yields no new physics. Therefore, the results are not presented here.

3.4 Conclusion and discussion.

In this chapter, the discussions in Chapter 2 have been generalized into a more general situation in an otherwise purely zonal channel with two partial meridional barriers at each side of the channel at the same longitude. The presence of the two meridional barriers has significant influence on both the through-channel transport and especially the circulation structure in the channel. The meridional barriers increase the potential vorticity resistance introduced by the ridge. Nevertheless, it can either enhance or weaken the topographic form drag generation via the Sverdrupian flow forced by the wind stress curl, depending upon the lengths of the two barriers and the ridge width in the gap. It demonstrates that both the bottom topography discussed in Chapter 2 and the coastline shape discussed by Gill (1968) are important in determining the wind-driven circulation in a $\beta-$plane channel.

In the case with a uniform wind stress, compared with the case discussed in Chapter 2, the presence of any partial meridional barriers always reduces the transport due to the increase in the potential vorticity resistance, thus, a stronger form drag generation. In the case with a non-uniform wind stress, the transport can either go up or go down, depending upon the lengths of the two meridional barriers. In the case with only a northern barrier, the form drag generation by the Sverdrupian flow is enhanced, in addition to the increase in the potential vorticity resistance. Thus, the through-channel transport is substantially reduced compared with the case without any meridional barriers. The presence of a southern barrier, however, always raises the transport for a narrow ridge despite the increase in the potential vorticity resistance. Only for a rather wide ridge can the transport be reduced. In the presence of two symmetric meridional barriers at each side of the channel, the transport decreases for a wide ridge, but increases for a narrow ridge, compared with that in the case with a purely zonal channel. In all cases, most of the dissipation of the potential vorticity occurs along segment $c - h$ at the northern boundary and the eastern edge of the northern barrier (Fig. 3.4).

The presence of the meridional barriers not only changes the through-channel transport, but also very significantly changes the circulation patterns in particular. Relatively speaking, the presence of the southern barrier has a far more profound influence on the circulation structure than that of the northern barrier. The presence of the northern barrier has only a local influence on the circulation structure within the area covered by the northern barrier. However, the presence of the southern barrier has a global influence on all the circulation structure within the channel, especially when the length of the southern barrier is sufficiently long. In this case, there is no southward internal current over the eastern portion of the ridge. Instead, an additional northward internal current over the eastern portion of ridge emerges. The through-channel recirculating flow is entirely to the north of the northern Sverdrupian gyre, and the corresponding circulation pattern is closer to the observed surface circulation in the circumpolar ocean shown in Gordon *et al.* atlas (1982).

This model again demonstrates the importance of both the geostrophic contour structure and the topographic form drag generation via the Sverdrupian flow forced by the wind stress curl. The discussions in this chapter combine the Gill model (1968) and the purely zonal channel model discussed in Chapter 2. It realized Stommel's (1957) hypothesis in its dynamic detail in a rather idealized simple linear barotropic model. In their review article, Nowlin & Klinck (1986) emphasized that two fundamental questions with regard to the large scale dynamics of the wind-driven circulation in the circumpolar ocean need to be answered. These two questions are how the momentum input via the wind stress and the potential vorticity input via the wind stress curl are balanced in the circumpolar ocean. So, to some extent, the discussions in this chapter and Chapter 2 answered those two question in a rather idealized situation. Furthermore, this model suggests that both the coastline geometry and bottom topography around Drake Passage play a fundamental role in determining the wind-driven circulation in the circumpolar ocean, while all other topography most likely plays only a secondary role.

Although the discussions in Chapter 2 have been generalized into a more general geometry in this chapter, which is presumably closer to the realistic circumpolar ocean, the circulation pattern in the *inviscid limit* shown in Fig. 3.10(b) is still far from the observed surface circulation in the circumpolar ocean (Gordon *et al.*, 1982). The reasons for this are similar to those discussed in Chapter 2. First of all, a rather idealized bottom topography and coastline geometry are used in the model. Second, the buoyancy forcing and stratification are both ignored here. As we will see in Chapter 4, stratification has a profound influence on both the circulation structure and zonal through-channel transport.

Third, frontal structure, one of the most significant features of the large scale circulation in the circumpolar ocean, is absent from the model. Lastly, an inviscid limit is assumed in the model. Otherwise, the internal current along $y = y_1$ in Fig. 3.10(b) would be a far wider one, as explained by Wang (1993a) and would be counterbalanced by the westward Sverdrupian flow in the channel. In spite of all the drastic simplification in setting up the model, it is believed that the essential part of the model results has important implications in the much more complicated real circumpolar ocean. First of all, both the coastline and bottom topography play fundamental roles in determining the wind-driven circulation in the circumpolar ocean. Second, the physical processes through which form drag is generated is closely relevant to the momentum balance in the circumpolar ocean. Third, most of the potential vorticity input from the wind stress curl is dissipated around the tip of the South American continent, especially the eastern portion. As we will see in the next chapter, the presence of stratification will not change these conclusions. From a practical point of view, the model result suggests that to simulate the wind-driven circulation in the Southern Ocean requires a good data set on both mean and horizontal structure of the wind stress over the Southern Ocean.

Appendix

Wind-driven circulation in an $f-$plane model

Assuming a uniform zonal wind stress with $\tau_x = \tau_0 = constant$, and $\tau_y = 0$, for an $f-$plane channel shown in Fig. 3.12, the potential vorticity equation (2.1) reduces to

$$J\left(\psi, \frac{f_0}{H}h\right) = -\kappa\nabla^2\psi,$$

with the same boundary conditions (2.2) and (2.3) and same constraint (2.4) for ψ_0. With same discussion as in Chapter 2, segments $a-b$ and $e-f$ are the two equivalent eastern boundaries, while $b-c$ and $d-e$ are the two equivalent western boundaries. Using the same characteristic method, one can find that

$$\psi = \psi_0 \quad \text{for} \quad region \;\; B,$$

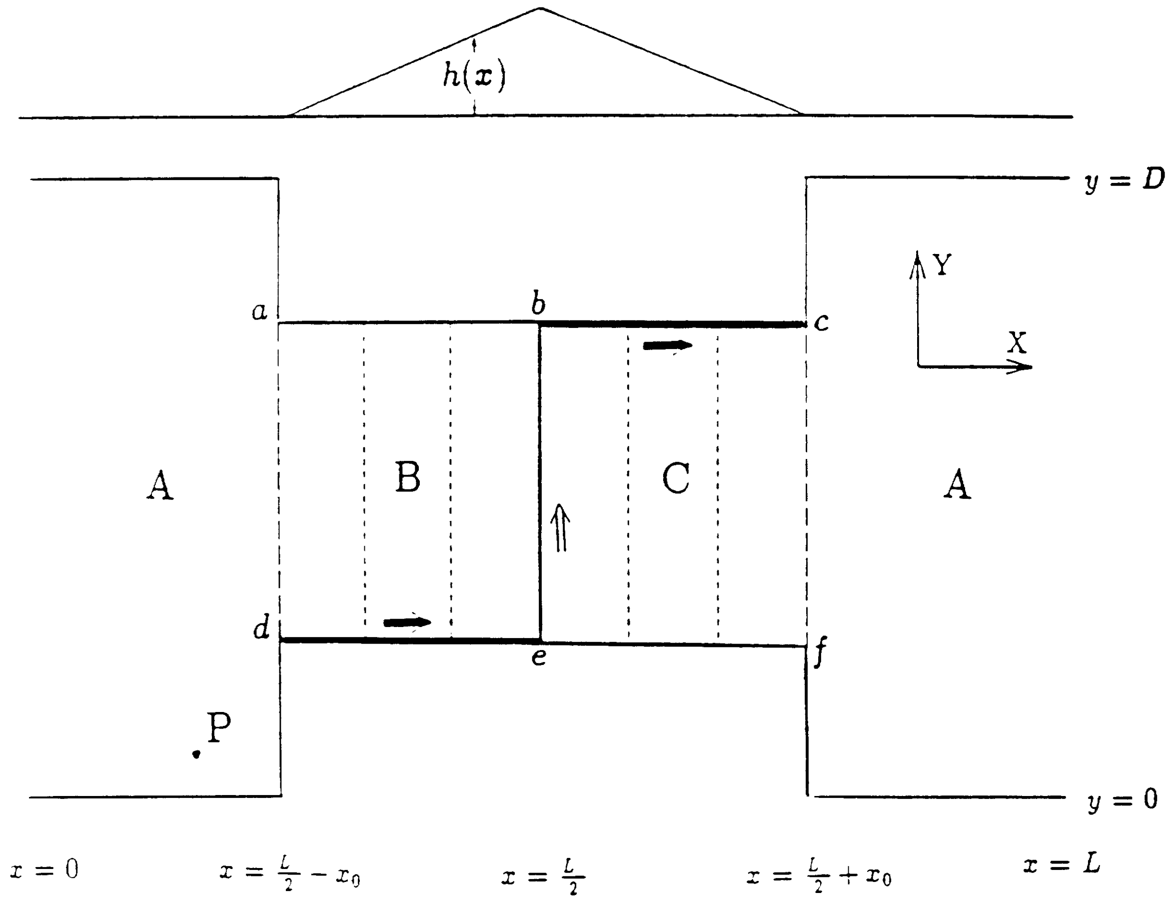

Figure 3.12: A schematic view of the domain of the circulation driven by a uniform wind stress in a f−plane channel over the ridge. On top is the profile of the ridge. The dashed lines over the ridge are the geostrophic contours. The solid arrow represents boundary layer current, the non-solid arrow represents the internal current along a geostrophic contour.

$$\psi = 0 \quad \text{for} \quad region\ C.$$

Along $d-e$ and $b-c$ are two western boundary currents. Along $b-e$ is a discontinuity of streamfunction with

$$\Delta\psi|_{C-B} = -\psi_0,$$

which connects the two equivalent western boundary currents as an internal current. Correspondingly, the topographic form drag is

$$\tau_D = -\frac{\rho_0 f_0 \psi_0 h_0}{L}.$$

This form drag generation is independent of y_1, y_2 and D. Balancing the form drag with the wind stress, one obtains (2.9) with the potential vorticity resistance now defined as

$$P_c \equiv -f_0 \frac{h_0}{H},$$

which is independent of y_1, y_2 and D. Another way to determine the transport is using (2.11). Similarly, one has

$$\kappa\overline{u^x} = -\psi_0 \frac{P_c}{HL}.$$

Note here the length of the two equivalent western boundaries is x_0 rather than Δx as in the $\beta-$plane case. In the interior away from the ridge, the circulation, similar to that discussed in Chapter 2, can be thought of as being driven by a source at point c and a sink at point d. Thus, the presence of the two partial meridional barriers does not have any influence on both the zonal transport and the circulation over the ridge.

Chapter 4

Wind-driven circulation in a β–plane channel, Part III: A multi-layer model

4.1 Introduction

Wind-driven circulations in a β–plane channel were discussed in Chapters 2 and 3 in a linear homogeneous model. It was shown that geostrophic contour blocking plays an essential role in generating topographic form drag and determining the circulation in the inviscid limit. The circulation can generally be divided into two parts: the two equivalent western boundary layers where friction is of vital importance and the rest where friction is negligible and the Sverdrupian balance appears to hold. The model clearly demonstrated how the bottom topographic form drag is generated, where the potential vorticity input is dissipated, and what model parameters determine the zonal transport. One of the major shortcomings of the model is its assumption of homogeneity thus lack of vertical structure. In a homogeneous model, the bottom topography affects the whole water column from bottom to top uniformly. This could change significantly in the presence of stratification.

Generally speaking, in the presence of stratification the problem becomes much more difficult, because it brings in a strong nonlinearity associated with the large interfacial displacement. The difficulty associated with the gyre circulation in a closed basin was demonstrated by Rooth *et al.* (1978) and Rhines & Young (1982a, RYa hereafter). Ignoring any nonlinearity including the interfacial vortex stretching in a two-layer Q-G model, Smith & Fandry (1978) extended Johnson & Hill's (1975) linear homogeneous model into its two-layer version. They found that both the upper and lower layer flows tend to follow the linear barotropic geostrophic contour f/H because in their model there were strong interfacial frictional coupling and no blocked geostrophic contour. However, neglecting the nonlinearity associated with the interfacial stretching is not appropriate for large scale wind-driven circulation in the circumpolar ocean given the large vertical displacement of isopycnal surfaces shown in Fig. 1.1. The parallel case in a closed basin was discussed by RYa. They demonstrated that interfacial vortex stretching plays a vital role in the wind-driven circulation in a closed basin. Wind-driven circulations in a two-layer $\beta-$plane channel model including the nonlinear interfacial stretching have been generally studied through direct numerical simulations, *e.g.*, McWilliams *et al.* (1978), Treguier & McWilliams (1990), and Wolff *et al.* (1991). Their model's results generally point out the different influence of isolated topography and ridges. Eddy-resolving numerical simulations by Wolf-Gladrow *et al.* (1991) indicate that the potential vorticity gradient in each layer is far different from the planetary vorticity gradient. Nevertheless, the fundamental question of what model parameters determine the zonal through-channel transport remains unclear. In a two-layer model, in addition to the question of how the bottom topographic form drag is generated, another question naturally comes up as to how the interfacial form drag is generated which is needed to transport momentum input downward from the surface layer due to the wind stress. A major controversy arises with respect to this latter question. All three eddy-resolving numerical model studies mentioned above pointed out that the interfacial form drag is generated mostly through the stationary eddies in the presence of large scale bottom topographic features. Johnson & Bryden (1989) and Marshall *et al.* (1993) argued otherwise that the interfacial form drag is generated mostly through transient eddies resulting from baroclinic instability.

The purpose of this chapter is to address the central question of what model parameters determine the zonal transport in the presence of stratification. To answer this question we have to answer two other questions first: how the presence of stratification affects the bottom topographic form-drag generation discussed in Chapter 2 and how the interfacial form drag is generated. Similar to Chapter 2, a zonal channel model will be used, and the *inertial effects* will be ignored but the nonlinearity associated with the interfacial vortex stretching will be retained. By doing so, meridional momentum exchange between different latitudes is excluded. Thus momentum input at each latitude has to be locally balanced in a way similar to that in the corresponding linear barotropic model. The central assumption in the model is that the transient eddies, while not explicitly included in the model, would nevertheless homogenize the potential vorticities in each sub-surface layer away from possible boundary layers following the discussion by Rhines & Young (1982b, RYb hereafter). This assumption of potential vorticity homogenization is consistent with the potential vorticity map obtained by Wolf-Gladrow *et al.* (1991) in their Q-G eddy-resolving numerical simulation. The major difference is that in the β−plane channel there is no shadow zone similar to that in a closed basin. The parallel case for the mid-latitude atmosphere is discussed by Lindzen (1993).

The discussion is organized as follows. The wind-driven circulation in a two-layer model will be discussed in Section 2. We will first discuss the case forced by uniform wind stress, then the case forced by nonuniform wind stress. There are three important points we want to make. First, stratification does not have any direct influence on the way bottom topographic form drag is generated, and it is identical to that in the corresponding barotropic model. Second, stationary eddies are capable of transporting momentum downward. In fact, the interfacial form drag generation in the model is entirely due to the stationary eddies. Third, the wind stress curl leads to both large interfacial and bottom topographic form-drag generation in the case with a narrow ridge. Then, in Section 3 a corresponding three-layer model will be discussed. It demonstrates that increased vertical resolution does not affect the results from the two-layer model. Section 4 closes this chapter with discussions. This chapter demonstrates that the total transport is composed of two parts. The first which we call the barotropic part is identical to that in the corresponding barotropic model discussed in Chapter 2 and is determined by the wind stress and model parameters associated with the ridge. The second part, the baroclinic part, is due entirely to the presence of the stratification. Thus, the presence of the stratification enhances the zonal transport in the channel.

4.2 A two-layer model

In Chapter 2, the circulations driven by both uniform and non-uniform wind stress were discussed. Unlike the case in a closed basin, the uniform wind stress could drive a strong loop of currents in the $\beta-$plane channel. In the inviscid limit the circulation is confined within the loop of currents which has vanishingly small width. A non-uniform wind stress, however, drives a loop of currents and a Sverdrupian gyre circulation and the zonal transport is much reduced in the case with a narrow ridge. In this section, let us see how the presence of stratification would change the circulation structure in the simplest layer model, *i.e.*, a two-layer model.

Assuming wind stress is $\tau_x = \tau_x(y)$, $\tau_y = 0$ and following conventional notations, the potential vorticity equations for the upper and lower layer are (Pedlosky, 1987)

$$J(\psi_1, q_1) = \frac{f_0}{H_1} w_e - \kappa H_1 \nabla^2 (\psi_1 - \psi_2), \tag{2.1}$$

$$J(\psi_2, q_2) = \kappa H_1 \nabla^2 (\psi_1 - \psi_2) - \kappa_0 H_1 \nabla^2 \psi_2, \tag{2.2}$$

respectively with

$$\begin{aligned} q_1 &= \beta y + F(\psi_2 - \psi_1), \\ q_2 &= \beta y + F(\psi_1 - \psi_2) + \frac{f_0}{H_1} h, \\ F &= f_0^2 / g' H_1. \end{aligned}$$

f_0 is the reference Coriolis parameter in the channel. $g' = g(\rho_2 - \rho_1)/\rho_0$ is the reduced gravity with ρ_j as the density in jth layer, and ρ_0 is the reference density. Each layer has the same depth $H_1 = H/2$, where H is the total depth. Following RYb, ψ_i and q_i are time-mean flow quantities. The nonlinear inertial effect is assumed unimportant. The interfacial friction, κ, presumably represents the net effect of the transient eddy process, for which RYb gave a detailed discussion. κ_0 is the bottom frictional coefficient, which represents the ultimate dissipation in this two-layer model. h is the bottom topography, which for simplicity is chosen as

$$h(x,y) \;=\; \begin{cases} h_0(1 - |\frac{L/2-x}{x_0}|) & \text{if } |L/2 - x| \;\leq\; x_0; \\ 0 & \text{otherwise,} \end{cases} \tag{2.3}$$

where L is the length of the channel. The boundary conditions are

$$\psi_1|_{y=0} \;=\; 0; \qquad \psi_1|_{y=D} \;=\; \psi_{10}, \tag{2.4}$$

$$\psi_2|_{y=0} \;=\; 0; \qquad \psi_2|_{y=D} \;=\; \psi_{20}. \tag{2.5}$$

ψ_{i0} are determined through the momentum balance

$$\frac{f_0^2}{g'}\overline{\psi_2\frac{\partial\psi_1}{\partial x}}^x + \kappa H_1\left(\overline{\frac{\partial\psi_1}{\partial y}}^x - \overline{\frac{\partial\psi_2}{\partial y}}^x\right) + \frac{\tau_x}{\rho_0} \;=\; 0, \tag{2.6}$$

$$\frac{f_0^2}{g'}\overline{\psi_1\frac{\partial\psi_2}{\partial x}}^x + f_0\overline{h\frac{\partial\psi_2}{\partial x}}^x - \kappa H_1\left(\overline{\frac{\partial\psi_1}{\partial y}}^x - \overline{\frac{\partial\psi_2}{\partial y}}^x\right) + \kappa_0 H_1\overline{\frac{\partial\psi_2}{\partial y}}^x \;=\; 0. \tag{2.7}$$

The first equation is obtained by multiplying the upper layer zonal momentum equation by its thickness, integrating over the whole channel and using the quasi-geostrophic approximation. The second equation is obtained in a similar way. In the above, $\overline{}^x$ is defined as

$$\overline{Z}^x \;\equiv\; \frac{1}{L}\int_0^L Z\,dx.$$

Because the inertial effect is neglected, there is no meridional momentum exchange and (2.6) and (2.7) have to be satisfied at each latitude except along the two lateral boundaries. In (2.6) the first term represents the interfacial form drag, while the second term represents the interfacial frictional drag. These physical processes together account for the total downward momentum transport from the surface layer to the bottom layer. In (2.7) the first and third terms are identical to those in (2.6) with a different sign. The second term represents the bottom topographic form drag and the fourth term represents the bottom frictional drag. In the absence of bottom topography, one apparent solution is

$$\begin{aligned} u_1 &= (1+\kappa_0/\kappa)\frac{2\tau_x}{\rho_0\kappa_0 H}, \\ u_2 &= \frac{2\tau_x}{\rho_0\kappa_0 H}. \end{aligned}$$

In this solution, there is neither interfacial nor bottom topographic form drag and the frictional process determines the solution. This is essentially the dilemma experienced by Hidaka & Tsuchiya (1953). If we choose "reasonable" value for $\kappa = \kappa_0 = 10^{-7}s^{-1}$, corresponding to a damping time scale of about 120 days, then

$$u_1 \ - \ u_2 \ = \ 31cm/s,$$

for $\tau_x = 0.08N/m^2$ and $H = 5km$. However, the critical shear for baroclinic instability is (Pedlosky, 1987)

$$\Delta U \ = \ \beta g' H / 2f_0^2 \ = \ 2.7cm/s,$$

for $g' = 1.5cm/s$. Apparently, the frictionally determined flow in the absence of bottom topography is well baroclinically unstable which could lead to the development of large transient eddies as demonstrated by McWilliams *et al.* (1978) in a much more elaborate numerical model. In the presence of bottom topography, the circulation could be entirely different as discussed in Chapter 2. In the following discussion we will always assume that the wind stress is strong enough such that the corresponding wind-driven flow in the case with a flat bottom is baroclinically unstable.

Consider a spin-up process of this two-layer model. Once the wind stress is switched on, the flow in the channel will grow first in the upper layer. As the shear becomes large enough, baroclinic instability will emerge, which will result in strong transient eddies. These transient eddies will transport momentum from the surface layer to the lower layer to be balanced by the bottom topographic form drag. At the same time these eddies drive a circulation in the lower layer which is not directly forced by the wind stress. See Rhines & Holland (1979) for an insightful discussion of the role of these transient baroclinic eddies. In this initial spin-up process, the downward transport of momentum from the surface to bottom layer is carried out predominantly by those transient eddies. Once this spin-up process is completed and the system settles down to a statistical equilibrium, it is assumed that the potential vorticity in the lower layer will be homogenized presumably by those transient eddies originating from baroclinic instability except within ***possible boundary layers***. See RYb for a detailed discussion for a closed basin. Actually, there are both observational and numerical evidences, as discussed by Marshall *et al.* (1993), which seems to suggest that the potential vorticity in those non-outcropped isopycnal surfaces in the circumpolar region is indeed very homogeneous. It is worth pointing out that in the mid-latitude atmosphere the potential vorticity on isentropic surfaces is also found to be rather uniform as discussed by Lindzen (1993). Assuming that the potential vorticity in the lower layer is homogenized away from possible boundary layers, we have

$$\psi_1 = \psi_2 + \frac{1}{F}\left(q_{20} - \beta y - \frac{f_0}{H_1}h\right), \tag{2.8}$$

where q_{20} is the uniform potential vorticity in the lower layer. The zonal mean baroclinic shear is a uniform westerly shear flow with $\overline{u_1}^x - \overline{u_2}^x = g'H_1\beta/f_0^2$, which is just the threshold shear for the onset of baroclinic instability in a two-layer model. It is very important to notice that this shear is not directly related to the wind stress, but rather is determined solely by the background stratification presumably set by the global thermohaline process.

Equation (2.8) immediately implies that, within the segments $f - d$ and $a - e$ where the ridge intersects the northern and southern boundaries (see Fig. 2.3), the potential vorticity in the lower layer is not homogenized. In those areas, the frictional process will be important just like the western boundary layer in a closed basin (Young & Rhines, 1982). It is *assumed* that there are always suitable boundary layers which can close the circulation in a way similar to Luyten *et al.* (1983). See Appendix A for a more detailed discussion about these boundary layer dynamics. Away from those areas that have vanishingly small area in the inviscid limit, the potential vorticity in the lower layer is assumed homogenized. It is rather easy to see that (2.8) automatically satisfies the momentum balance (2.7) in the inviscid limit by multiplying (2.8) with $\partial\psi_2/\partial x$ and integrating around the channel. Therefore, the momentum balance is now the bottom topographic form drag balancing the wind stress

$$f_0 \overline{h\frac{\partial\psi_2}{\partial x}}^{x} + \frac{\tau_x}{\rho_0} = 0,$$

except along the two lateral boundaries. Noting (2.8), (2.1)+(2.2) yields

$$J\left(\psi_2, \beta y + \frac{f_0}{H}h\right) = \frac{f_0}{H}w_e + \frac{g'}{2f_0}J(h, \beta y)$$

away from the two segments $f - d$ and $a - e$. If we put

$$\psi_2 = \psi_B - \frac{\beta}{F}y, \tag{2.9}$$

then

$$J\left(\psi_B, \beta y + \frac{f_0}{H}h\right) = \frac{f_0}{H}w_e. \tag{2.10}$$

Quite remarkably this governing equation of ψ_B is identical to the governing equation in the corresponding linear barotropic model, and the linear geostrophic contours $\beta y + \frac{f_0}{H}h =$ *constant* of the corresponding barotropic model discussed in Chapter 2 again serves as the characteristics for the governing equation of ψ_B in this two-layer baroclinic model. Fig. 2.3 shows one example of the geostrophic contour structure in the supercritical state. Notice that they are all blocked by the lateral boundaries in the segments $f - d$ and $a - e$. In the barotropic model this equation is valid except the two equivalent western boundaries, segments $c - d$ and $a - b$. In this two layer model, however, the above equation breaks down within entire segments $f - d$ along the northern boundary and $a - e$ along the southern boundary. The general solution to the above equation is

$$\psi_B = \psi_b + G\left(\beta y + \frac{f_0}{H}h\right),$$

where ψ_b, a forced circulation, is the solution of the corresponding linear barotropic model discussed in Chapter 2. The second part is a free solution and G could be any function. Noting that the potential vorticity in the lower layer is assumed homogenized, this ψ_B satisfies (2.2) to the lowest order away from the two segments $f-d$ and $a-e$. In the corresponding linear barotropic model, the geostrophic contour blocking along the two equivalent eastern boundaries automatically removes the free solution and only the forced solution, *i.e.*, the first part, is left. In this two-layer model, the situation is subtler and such a mechanism does not work because (2.10) is not valid along segments $b-e$ and $f-c$. Nevertheless, as we discussed in Appendix A, to the *lowest order* segments $f-c$ and $b-e$ (see Fig. 4.1), which are the two equivalent eastern boundaries in the corresponding barotropic model, can not support any boundary layer structure. Any non-zero G would require lowest order boundary layer structures within both $f-c$ and $b-e$. Such lowest order boundary layers along $b-e$ and $f-c$, however, do not exist. Therefore, one must have

$$G = 0,$$

to the lowest order. This uniquely determines the wind-driven circulation in β-plane channel. For the convenience of the following discussions, we will first take up the circulation forced by uniform wind stress, then we will discuss the circulation forced by nonuniform wind stress.

4.2.1 A case with uniform wind stress

If $\tau_x = \tau_0 = constant$, the governing equation (2.10) for ψ_B reduces to

$$J\left(\psi_B, \beta y + \frac{f_0}{H} h\right) = 0$$

with the boundary condition

$$\begin{aligned} \psi_B|_{y=0} &= 0, \\ \psi_B|_{y=D} &= \psi_{b0}, \end{aligned}$$

where $\psi_{b0} = \psi_{20} - \beta D/F$ to be determined later by momentum balance. With the discussions above, ψ_B is just the barotropic circulation discussed in Chapter 2, and one has

$$\begin{aligned}\psi_B &= \psi_{b0} \quad for\ region\ A, B, C,\\ \psi_B &= 0 \quad for\ region\ D, E,\end{aligned}$$

except along segments $a-b$ and $c-d$, where are boundary layer structures according to the discussions in Appendix A. Thus the streamfunction in the lower layer is

$$\psi_2 = \psi_B - \frac{\beta}{F}y, \tag{2.11}$$

and streamfunction in the upper layer is

$$\psi_1 = \psi_B - 2\frac{\beta}{F}y - \frac{g'}{f_0}h. \tag{2.12}$$

$q_{20} = 0$ is chosen noting the condition along the southern boundary away from the ridge area. The interface between the two layers is

$$h_2 = H_1 + h + \frac{\beta H_1}{f_0}y. \tag{2.13}$$

So, besides the zonally uniform meridional tilting, the interfacial profile is exactly the same as that of the bottom ridge. To look at the circulation structure (2.11) and (2.12), the circulation can be decomposed into two parts: the barotropic part

$$\psi_j^b = \psi_B, \tag{2.14}$$

and the baroclinic part

$$\psi_1^c = -2\frac{\beta}{F}y - \frac{g'}{f_0}h, \tag{2.15}$$

$$\psi_2^c = -\frac{\beta}{F}y \tag{2.16}$$

for the convenience of the physical explanation. In Appendix B, a two-layer uniform baroclinic zonal flow over a ridge on a β−plane is considered. It is shown there that if the lower flow satisfies $U_2 = \beta/F$, then there is no response in the lower layer and all the response is trapped within the upper layer regardless of the flow in the upper layer. In the present two-layer model of wind-driven circulation, to satisfy that condition, the lower layer flow in the baroclinic part is just (2.16). In this way, the interfacial form drag is guaranteed to be equal to the bottom form drag and carries momentum downward from the surface layer to the bottom layer where it is balanced by the bottom topographic form drag. Thus this process determines the flow in the lower layer. As is assumed, the potential vorticity in the lower layer is homogenized which is presumably carried out by transient eddies, thus in order for this baroclinic flow (ψ_1^c, ψ_2^c) to be marginally stable baroclinically, the shear has to be

$$u_1^c - u_2^c = \frac{\beta}{F}.$$

This process determines the baroclinic shear structure. These two physical processes above determine the baroclinic structure (ψ_1^c, ψ_2^c) of the wind-driven circulation in the channel.

Similar to the barotropic model, in both layers there are discontinuities of streamfunctions along ℓ_1 with

$$\Delta\psi_1|_{E-A} = \Delta\psi_2|_{E-A} = -\psi_{b0},$$

along ℓ_2 with

$$\Delta\psi_1|_{C-D} = \Delta\psi_2|_{C-D} = \psi_{b0},$$

and along the southern boundary with

$$\Delta\psi_1|_{y=0} = \Delta\psi_2|_{y=0} = \psi_{b0}.$$

These discontinuities of streamfunctions represent the barotropic internal currents over the ridge and along the southern boundary. These loops of internal currents do not change with depth, and we will see that it is similar in the three layer-model to be discussed in the next section.

With the circulation structure discussed above, the bottom topographic form drag can be easily calculated as

$$\tau_D = \rho_0 f_0 \overline{h\frac{\partial \psi_2}{\partial x}}^x = -\frac{\rho_0 f_0 \psi_{b0} h_0}{L}(1 - h_c/h_0), \tag{2.17}$$

where

$$h_c = \frac{\beta D}{|f_0|}H$$

is the critical ridge height in the corresponding linear barotropic model, which can block all the geostrophic contours in the $\beta-$ plane channel. In this form-drag generation process in the lower layer, only the ψ_B component makes a direct contribution, while the other part associated with the baroclinic circulation does not. It is quite clear that the form-drag generation in this stratified two-layer model is similar to that in the corresponding barotropic model, and the presence of stratification apparently has no direct influence.

The momentum input from the wind stress in the upper layer is transported down to the second layer by the interfacial form drag

$$\tau_I = \rho_0 \overline{\frac{f_0^2}{g'}\psi_2 \frac{\partial \psi_1}{\partial x}}^x = -\frac{\rho_0 f_0 \psi_{b0} h_0}{L}(1 - h_c/h_0).$$

This interfacial form drag generation is due to the correlation between the barotropic flow ψ_B and the baroclinic flow (ψ_1^c, ψ_2^c). It is only related to the barotropic through-channel transport represented by ψ_{b0} and is independent of the zonal transport associated with the baroclinic circulation. It is also related to the ridge height and the channel width because h_c is related to the D. In this two-layer model the interfacial form drag is entirely due to the stationary eddies, which is not inconsistent with the results from the two-layer eddy-resolving numerical model such as that of Wolf-Gladrow *et al.* (1991) and the FRAM model results (Stevens & Ichenko, 1992).

Balancing the interfacial form drag and the wind stress to determine ψ_{b0}, one obtains the transport and a simple relation between the model parameter and the zonal transport in each layer

$$\begin{aligned} T_{r1} &= \frac{\tau_0 L H_1/\rho_0}{|f_0|h_0 - \beta D H} + 2DH_1\frac{\beta}{F}, \\ T_{r2} &= \frac{\tau_0 L H_1/\rho_0}{|f_0|h_0 - \beta D H} + DH_1\frac{\beta}{F}. \end{aligned}$$

In each layer, the first part is due to the loop of barotropic currents. Its relationship with model parameters was discussed in Chapter 2. The second part is due entirely to the presence of the stratification. Apparently, the stratification enhances the zonal through-channel transport, which is consistent with the numerical model results of Bryan & Cox (1972) and Cox (1989). This part is very sensitive to the choice of the background stratification. Nevertheless, it is independent of any parameter associated with the ridge. The total zonal transport in the channel is then

$$T_r = \frac{\tau_0 L H/\rho_0}{|f_0|h_0 - \beta D H} + 3g'DH_1^2\beta/f_0^2. \tag{2.18}$$

So, given the stratification, the baroclinic transport is solely determined by the width of the channel and is not directly related to the wind stress. The barotropic transport is the same as that of the corresponding barotropic model and is determined by the wind stress.

Figs. 4.1(a) and (b) show the normalized streamfunctions in the upper and lower layer, while (c) shows the interface between the two layers. It is worth noting that the solution obtained does not apply within the two segments $f-d$ and $a-e$ except within the segments $f-c$ and $b-e$ for the lower layer. As we discuss in Appendix A, boundary layer structures have to be appended, thus, in Fig. 4.1 the contours in those areas are only schematic. Unlike the corresponding barotropic model, in this two-layer model, besides the loop of currents, there are uniform eastward flows in both layers. Moreover there is a strong stationary eddy represented by $-g'h/f_0$ in (2.12) in the upper layer over the ridge. It plays a fundamental role in generating the interfacial form drag. The circulation structure in both layers is much richer than its corresponding barotropic model. Fig. 4.1(c) shows that away from the ridge the interface uniformly tilts southward, and rises up over the ridge. It reaches its maximum height over the ridge. From the results of $\beta-$plane model, it is

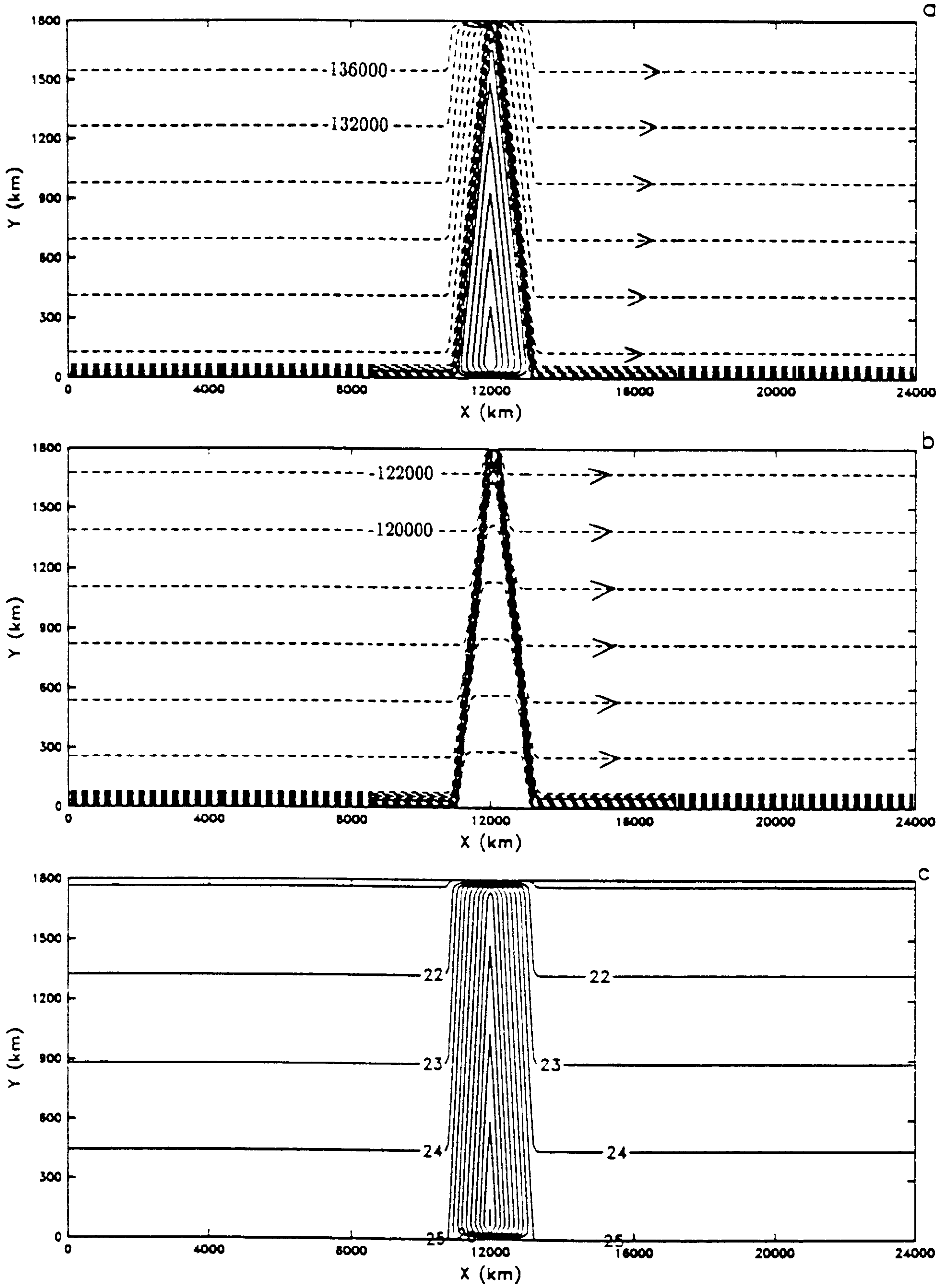

Figure 4.1: The normalized streamfunctions of uniform wind stress-driven circulations ((a) for the surface layer, (b) for the bottom layer) and the corresponding interface (c) in the β−plane channel with model parameters chosen as $L = 24000km$, $D = 1800km$, $H = 5km$, $x_0 = 2000km$, $h_0 = 950m$ and $\Delta\rho/\rho_0 = 4 \times 10^{-4}$, $H_1 = 2.5km$, $f_0 = -2\omega sin\theta^0$ and $\beta = 2\omega cos\theta^0/a$ with $\theta = 60^0 S$ and $a = 6.37 \times 10^6 km$, $\rho_0 = 1.03g/cm^3$ and $\tau_0 = 0.08N/m^2$.

quite interesting to see that in a corresponding f-plane model with $\beta = 0$, the presence of the stratification does not have any influence on the zonal transport. The circulation in the baroclinic model is the same as that in the corresponding barotropic model except that there is a stationary eddy in the upper layer over the ridge.

Suppose we now have a series of ridges, represented as $\{h^j(x)\}$ with $j = 1, \cdots, m$. Each one is in the form of (2.4). Among these ridges,

$$h_0^j \; > \; h_c \qquad (j = 1, \cdots, m_0),$$

while

$$h_0^j \; \leq \; h_c \qquad (j = m_0 + 1, \cdots, m),$$

where h_0^j is the ridge height. Then, following the discussion in Chapter 2, the total potential vorticity resistance introduced by this series of topographic features is

$$P_c \; = \; \sum_{j=1}^{m_0} \left(|f_0| \frac{h_0^j}{H} - \beta D \right).$$

Ridges with subcritical height do not contribute to the total potential vorticity resistance. And the corresponding through-channel transport is

$$T_r^* = \frac{\tau_0 L / \rho_0}{P_c} \; + \; 3g' D H_1^2 \beta / f_0^2. \tag{2.19}$$

The presence of those ridges lower than the critical height, h_c, has no influence on the transport *in the inviscid limit.* The effect of these low ridges is merely to deflect the flow passage of the loop of currents slightly, and the baroclinic circulation is not affected.

It is quite straightforward to extend the above discussions to a general bottom topography, and the final result is still (2.19). In the realistic circumpolar ocean, in addition to the ridge near Drake Passage, there are three other major ridges. They are the Kerguelen Plateau in the southern Indian Ocean, the southeast Indian Ridge south of Australia, and the Pacific Antarctic Ridge. The local meridional scales of these ridges are very large, so are their corresponding local βD. They are most probably locally subcritical, thus their presence introduces no net potential vorticity resistance. Therefore, in the case with uniform wind stress forcing, their presence most likely does not change the wind-driven barotropic through-channel transport. It is solely determined by the ridge around Drake Passage. Near Drake Passage the channel is very narrow, thus tending to introduce a strong bottom topographic and interfacial form-drag generation, and circulation is most likely only determined by parameters associated with this topographic feature.

4.2.2 A case with non-uniform wind stress

In the above discussion the influence of the wind stress curl was ignored. In the corresponding barotropic model, the wind stress curl leads to a very significant amount of bottom topographic form drag generation in the case with a narrow ridge. Now let us see how that works in the presence of stratification. In the following discussion the wind stress is chosen as

$$\tau_x = \tau_0 \left(1 - cos\frac{\pi}{D}y\right),$$

and $\tau_y = 0$, which is somewhat similar to the zonally averaged observed one in the circumpolar zone as shown by Nowlin & Klinck (1986). From discussion in Chapter 2, we conclude that the Sverdrupian balance only applies to the case with a supercritical ridge. And the solution to (2.10) is

$$\psi_B|_A = \psi_{b0} - \frac{w_0 D}{\alpha\pi}\left(1 + cos\frac{\pi}{D}y\right),$$

$$\begin{aligned}
\psi_B|_B &= \psi_{b0} - \frac{w_0 D}{\alpha\pi}\left(1 + cos\frac{\pi}{D}y\right) + \frac{w_0}{\beta}(x - L/2 + x_0) sin\frac{\pi}{D}y, \quad for \quad 0 < x < L/2 - x_0, \\
\psi_B|_B &= \psi_{b0} - \frac{w_0 D}{\alpha\pi}\left(1 + cos\frac{\pi}{D}y\right) + \frac{w_0}{\beta}(x + x_0 - \frac{3}{2}L) sin\frac{\pi}{D}y, \quad for \quad L/2 + x_0 < x < L,
\end{aligned}$$

$$\psi_B|_C = \psi_{b0} - \frac{w_0 D}{\alpha\pi}\left\{1 + cos\frac{\pi}{D}\left[y - \frac{\alpha}{\beta}(L/2 + x_0 - x)\right]\right\} +$$

$$\frac{w_0}{\beta}(2x_0 - L)sin\frac{\pi}{D}\left[y - \frac{\alpha}{\beta}(L/2 + x_0 - x)\right] -$$
$$\frac{w_0 D}{\alpha\pi}\left\{cos\frac{\pi}{D}\left[y - \frac{\alpha}{\beta}(L/2 + x_0 - x)\right] - cos\frac{\pi}{D}y\right\},$$

$$\psi_B|_D = -\frac{w_0 D}{\alpha\pi}\left(1 - cos\frac{\pi}{D}y\right),$$

$$\psi_B|_E = -\frac{w_0 D}{\alpha\pi}\left\{1 - cos\frac{\pi}{D}\left[y - \frac{\alpha}{\beta}(x - L/2)\right]\right\} +$$
$$\frac{w_0 D}{\alpha\pi}\left\{cos\frac{\pi}{D}\left[y - \frac{\alpha}{\beta}(x - L/2)\right] - cos\frac{\pi}{D}y\right\}.$$

where $w_0 = -\pi\tau_0/\rho_0 HD$. Therefore, the wind-driven circulation in this two-layer model is

$$\psi_1 = \psi_B - 2\frac{\beta}{F}y - \frac{g'}{f_0}h, \tag{2.20}$$
$$\psi_2 = \psi_B - \frac{\beta}{F}y. \tag{2.21}$$

Although the presence of wind stress curl changes the barotropic component of the circulation, the baroclinic part is not affected. The reason is that the baroclinic part of the circulation is again determined by the two physical processes: maintaining the neutral baroclinic instability and keeping the interface in the same shape as that of the bottom except the zonally uniform meridional tilting such that the interfacial form drag equals the bottom topographic form drag. Apparently, these two physical processes are not affected by the presence of the wind stress curl. The wind stress change can only induce corresponding change in the barotropic component.

Similar to the circulation forced by uniform wind stress, there are discontinuities of barotropic streamfunction at the boundaries between regions A and E with

$$\Delta\psi_1|_{E-A} = \Delta\psi_2|_{E-A} = -\psi_{b0} - \frac{2w_0 D}{\alpha\pi},$$

between regions C and D with

$$\Delta\psi_1|_{C-D} = \Delta\psi_2|_{C-D} = \psi_{b0} - \frac{2w_0 D}{\alpha\pi},$$

and along the southern boundary away from the ridge with

$$\Delta\psi_1|_{y=0} \;=\; \Delta\psi_2|_{y=0} \;=\; \psi_{b0} - \frac{2w_0 D}{\alpha\pi},$$

where $\alpha = |f_0|h_0/Hx_0$.

From the solution above, one can calculate the bottom topographic form drag as

$$\tau_D \;=\; \rho_0 f_0 \overline{h\frac{\partial\psi_2}{\partial x}}^{x} \;=\; -\frac{\rho_0 f_0 \psi_{b0} h_0}{L}(1 - h_c/h_0) - \tau_0(1 - 2x_0/L) + \tau_0 cos\frac{\pi}{D}y,$$

which is same as that in the corresponding barotropic model discussed in Chapter 2 and discussion about its generation and relation to model parameters is thus similar. The first part is due to the loop of the barotropic currents. The second and third part is directly due to the wind stress curl. Apparently, the presence of the stratification again does not have any direct influence on the two physical processes of bottom topographic form drag generation first discussed in Chapter 2 in the corresponding barotropic model. The interfacial form-drag is

$$\tau_I \;=\; \rho_0\frac{f_0^2}{g'}\overline{\psi_2\frac{\partial\psi_1}{\partial x}}^{x} \;=\; -\frac{\rho_0 f_0 \psi_{b0} h_0}{L}(1 - h_c/h_0) - \tau_0(1 - 2x_0/L) + \tau_0 cos\frac{\pi}{D}y.$$

This interfacial form-drag generation is due to the correlation between the barotropic flow ψ_B and the baroclinic flow (ψ_1^c, ψ_1^c). Similar to that in the case with a uniform wind stress, it is only related to the barotropic through-channel transport represented by ψ_{b0} and independent of the baroclinic transport. Apparently the wind stress curl significantly enhances the interfacial form-drag generation just as it does the bottom topographic form-drag generation in the case with a narrow ridge. Nevertheless, this part of the form drag is always weaker than the mean wind stress τ_0, and it is again due to the stationary non-zonal flow, which is the wind stress curl driven Sverdrupian gyre circulation together with the perturbation $-g'h/f_0$.

Balancing interfacial form drag and the wind stress to determine ψ_{b0}, one obtains the zonal transport in each layer

$$T_{r1} \;=\; \frac{\tau_0 2x_0 H_1/\rho_0}{|f_0|h_0 - \beta DH} \;+\; 2DH_1\beta/F,$$

$$T_{r2} = \frac{\tau_0 2x_0 H_1/\rho_0}{|f_0|h_0 - \beta DH} + DH_1\beta/F.$$

In each layer, the first part is due to the loop of barotropic currents discussed in Chapter 2. The second part is due to the presence of the stratification. The total transport in the channel is then

$$T_r = \frac{\tau_0 2x_0 H/\rho_0}{|f_0|h_0 - \beta DH} + 3g'DH_1^2\beta/f_0^2. \tag{2.22}$$

Apparently, although the presence of the wind stress curl enhances both the interfacial and bottom topographic form-drag generation leading to a smaller barotropic zonal transport, while the baroclinic part remains the same. In the next section we will show that this is also true in a three-layer model, actually it can be shown that this is true in any layered model. In the limit $\tau_0 \rightarrow 0$, the zonal transport in the channel would be purely the baroclinic part with

$$T_r \rightarrow 3g'DH_1^2\beta/f_0^2.$$

It is worth noting that this limit is achieved in the inviscid limit. For the case with subcritical ridges among which the case with a flat bottom discussed previously is the simplest, the corresponding transport is infinitely large in the inviscid limit! This is fundamentally different from that in a closed basin. In a closed basin, the eastern boundary automatically shuts off this part. In this channel model, however, there was no such eastern boundary. Therefore for a rather weak wind stress, the through-channel transport is mostly associated with the baroclinic circulation. Quite obviously, there is always a *finite friction* in the realistic circumpolar ocean, thus the above discussion only applies for a strong enough wind stress in the sense that the wind-driven flow is in the supercritical state for baroclinic instability in the absence of bottom topography. According to the rough estimation made previously, even if the wind stress is as weak as one tenth of the observed, the corresponding wind-driven flow in the absence of topography is still in the supercritical state for baroclinic instability.

For model parameters chosen as $\tau_0 = 0.08N/m^2$, $\rho_0 = 1.03g/cm^3$, $L = 2.4 \times 10^4 km$, $D = 1.8 \times 10^3 km$, $H = 5km$, $x_0 = 1200km$, $f_0 = -2\omega sin\theta^0$ and $\beta = 2\omega cos\theta^0/a$ with $\theta = 60^0 S$ and $a = 6.37 \times 10^3 km$

$$T_r = 148Sv, \tag{2.23}$$

for $h_0 = 950m$ and $\Delta\rho/\rho_0 = 4 \times 10^{-4}$, which corresponds to quite a large baroclinic Rossby deformation radius $\approx 24km$. Among them $53Sv$ is carried by the barotropic component ψ_B, the rest with $95Sv$ is carried out by the baroclinic component (ψ_1^c, ψ_2^c). The upper layer carries about $90Sv$, while the lower layer carries about $58Sv$. Apparently, for a higher ridge, both the barotropic transport and the transport in the lower layer will be smaller. Fig. 4.2 shows the total transport, the transport in the upper layer and that in the corresponding barotropic model, respectively. If

$$h_0 < h_* = h_c + 4F\tau_0 x_0/(3\rho_0|f_0|\beta D),$$

the zonal transport carried by the barotropic component ψ_B is larger than that by the baroclinic component (ψ_1^c, ψ_2^c). Otherwise, it is weaker than that by the baroclinic component. In the corresponding barotropic model, the through-channel transport is rather sensitive to the choice of ridge height. In this two layer model, however, for the range with $h_0 > h_*$ the transport is mostly determined by the baroclinic component (ψ_1^c, ψ_2^c), thus it is not so sensitive to choice of the ridge height as is shown in Fig. 4.2. With the same model parameters, the meridional Sverdrup volume transport in the interior basin away from the ridge is roughly

$$T_{Sv} \sim \frac{Hw_0}{\beta}(L - 2x_0) = -257Sv, \tag{2.24}$$

for a narrow ridge. Thus the meridional Sverdrupian volume transport is substantially higher than the zonal through-channel transport.

Figs. 4.3(a) and (b) show the streamfunction in the upper and lower layer, respectively. Noting that the zonal velocity associated with the baroclinic component in the

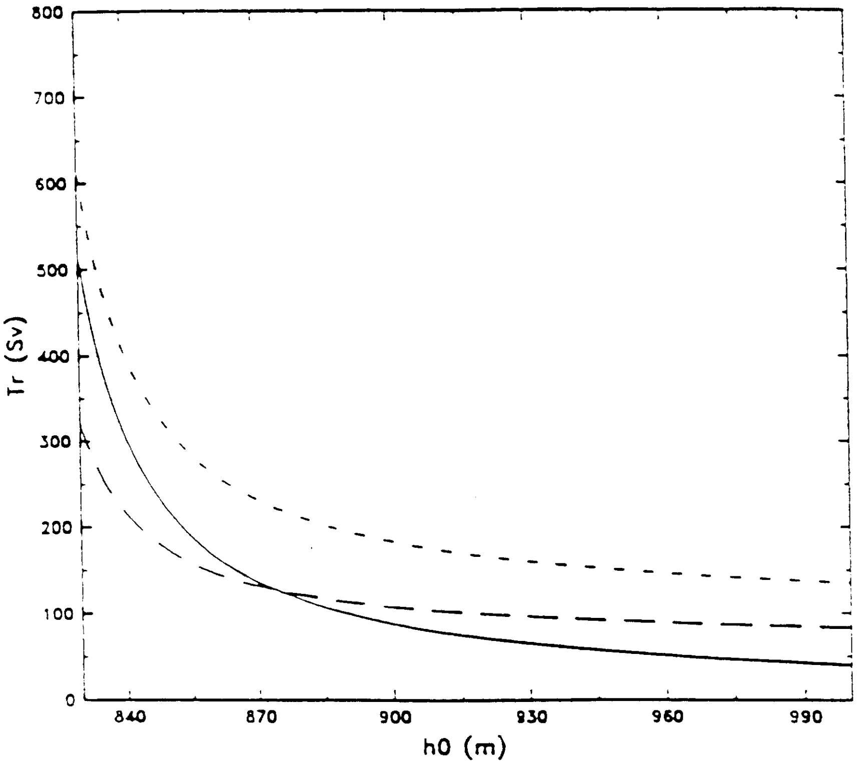

Figure 4.2: The zonal transport T_r versus h_0 in the case with a non-uniform wind stress. The ridge width is chosen as $x_0 = 1200km$, while the remaining parameters are similar to those used in Fig. 4.1. The short dashed line is the total transport, the long dashed line is the transport in the upper layer, and the solid line in the corresponding barotropic model.

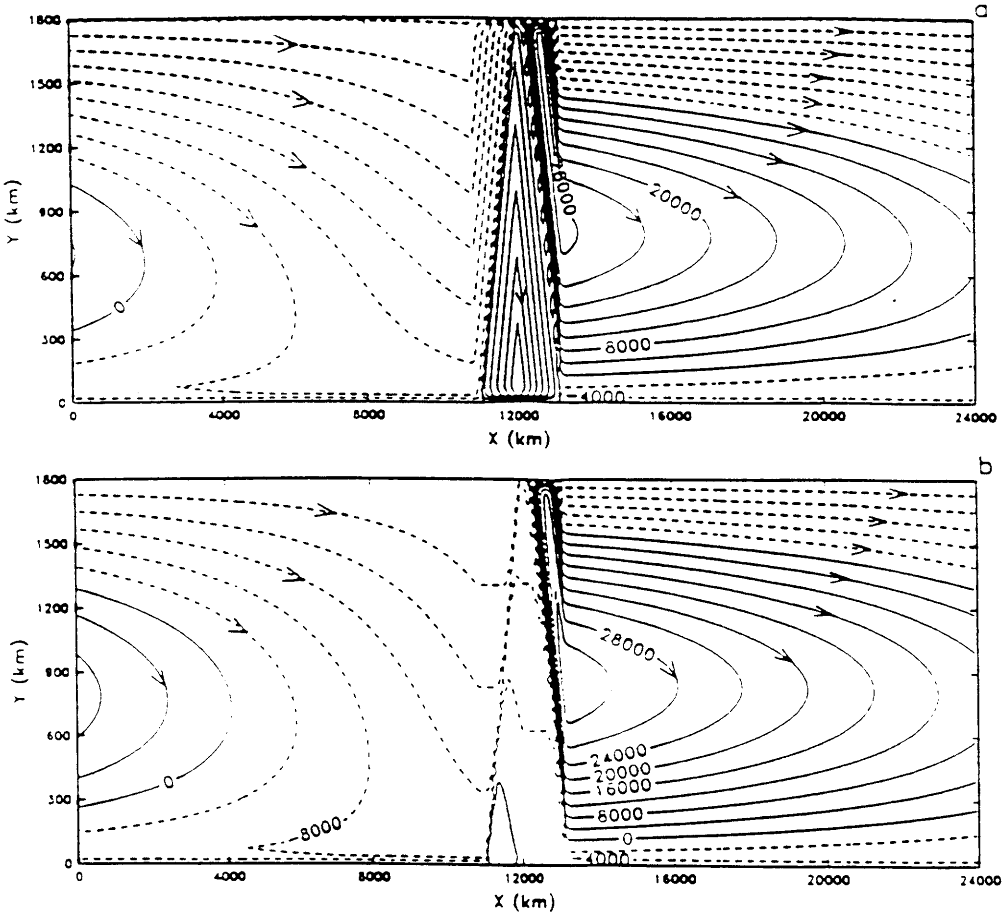

Figure 4.3: Same as Fig. 4.1(a) and (b) but for the case with a non-uniform wind stress.

upper layer is stronger than that in the lower layer, away from the ridge, the velocity vector in the lower layer rotates clockwise with respect to that in the upper layer. This is typical of the β−spiral in the wind-driven subpolar gyre. Although the Sverdrupian gyre circulation and the loop of currents which constitute of the barotropic component do not change with depth, the vertical shear in the baroclinic component renders the circulation structure in the upper layer rather different from that in the lower layer. The gyre circulation in the upper layer shrinks further to the southeast corner downstream of the ridge than that in the lower layer, compared with the corresponding barotropic situation. The structure of interface between the two layers is the same as that shown in Fig. 4.1(c). This is very different from that in a closed basin where associated with the subpolar gyre, the interface rises in the center of the gyre. In this β−plane channel, however, there is no such interface elevation because the Sverdrupian gyre circulation is barotropic, and does not lead to any associated interfacial elevation. The chief reasons are that here unlike the closed basin, there is no so-called eastern shadow zone associated with the wind-driven circulation, and the wind-driven circulation penetrates all the way to the bottom. Nevertheless, interfacial elevation does occur over the ridge due to the effect of the baroclinic flow over the ridge discussed in Appendix B.

4.3 A three-layer model

Despite its simplicity the two-layer model illustrates all the physical processes essential to the stratified wind-driven circulation in a β−plane channel:

(1) The circulation consists of two parts: the barotropic part and the baroclinic part. The barotropic part is the same as that in the corresponding barotropic model.

(2) The wind stress determines the barotropic component only.

(3) The requirement that potential vorticity in the subsurface layer be homogenized, except within possible boundary layers, determines the vertical shear of the baroclinic component except over the ridge.

(4) The inability of segments $f - c$ along the northern boundary and $b - e$ along the southern boundary to support any boundary layer structure to the lowest order determines the uniform zonal velocity of the baroclinic component in the lower layer.

(5) The presence of the stratification does not have any direct effect on the topographic form drag generation.

(6) The interfacial form drag is generated by the stationary eddies.

It would be interesting to extend the two-layer Q-G model results to a two-layer planetary geostrophic model which allows outcropping of the lower layer such as the Luyten *et al.* (1983) model. Instead, we want to discuss the wind-driven circulation more thoroughly by increasing the vertical resolution, and we want to show that the procedure discussed in the two-layer model is readily applicable to any layer models so long as the Q-G assumption is valid.

The simplest layer model with more vertical resolution is of course the three-layer model. A significant new feature is that the middle layer is not directly forced by the wind stress nor is it directly affected by the bottom topographic form drag. It merely acts as a messenger to pass the momentum from the surface layer to the bottom layer where it is balanced by the bottom topographic form drag. With standard notion, the Q-G potential vorticity equations are (Pedlosky, 1987)

$$J\left[\psi_1, \beta y + \frac{f_0^2}{g'H_1}(\psi_2 - \psi_1)\right] = \frac{f_0}{H_1} w_e, \tag{3.1}$$

$$J\left[\psi_2, \beta y + \frac{f_0^2}{g'H_2}(\psi_1 - \psi_2) + \frac{f_0^2}{g''H_2}(\psi_3 - \psi_2)\right] = 0, \tag{3.2}$$

$$J\left[\psi_3, \beta y + \frac{f_0^2}{g''H_3}(\psi_2 - \psi_3) + \frac{f_0}{H_3} h\right] = 0, \tag{3.3}$$

away from possible boundary layers within segments $f - d$ and $a - e$; see Appendix A for a detailed discussion. $g' = \frac{\rho_2 - \rho_1}{\rho_0} g$ and $g'' = \frac{\rho_3 - \rho_2}{\rho_0} g$, ρ_j is the density of layer j. The mean layer thicknesses of the three layers are H_1, H_2 and H_3, respectively. The bottom topography is still in the form of (2.3). The boundary conditions are

$$\psi_j|_{y=0} = 0; \quad \psi|_{y=D} = \psi_{j0}, \tag{3.4}$$

where $j = 1, 2, 3$. ψ_{j0} is determined through the momentum balance

$$\frac{f_0^2}{g'}\overline{\psi_2\frac{\partial\psi_1}{\partial x}}^x + \frac{\tau_x}{\rho_0} = 0, \tag{3.5}$$

$$\frac{f_0^2}{g'}\overline{\psi_1\frac{\partial\psi_2}{\partial x}}^x + \frac{f_0^2}{g''}\overline{\psi_3\frac{\partial\psi_2}{\partial x}}^x = 0, \tag{3.6}$$

$$\frac{f_0^2}{g''}\overline{\psi_2\frac{\partial\psi_3}{\partial x}}^x + f_0\overline{h\frac{\partial\psi_3}{\partial x}}^x = 0. \tag{3.7}$$

The first equation says that the wind stress input in the surface layer is transferred down to the middle layer by the interfacial form drag between the surface and middle layer

$$\tau_{I12} = \rho_0\frac{f_0^2}{g'}\overline{\psi_2\frac{\partial\psi_1}{\partial x}}^x .$$

In the middle layer, the momentum input from the surface layer is then transferred down to the bottom layer by the interfacial form drag between the middle and bottom layer

$$\tau_{I23} = \rho_0\frac{f_0^2}{g'}\overline{\psi_3\frac{\partial\psi_2}{\partial x}}^x .$$

In the bottom layer, the wind stress is ultimately balanced by the bottom topographic form drag

$$\tau_D = \rho_0 f_0\overline{h\frac{\partial\psi_3}{\partial x}}^x .$$

Assuming that the potential vorticities in both middle and bottom layers are homogenized away from possible boundary layers, as is suggested by Wolf-Gladrow *et al.*'s numerical simulation (1991), one has

$$\psi_1 = \psi_3 - \left[\frac{g''H_3}{f_0^2} + \frac{g'(H_2+H_3)}{f_0^2}\right]\beta y - \frac{g'+g''}{f_0}h, \tag{3.8}$$

$$\psi_2 = \psi_3 - \frac{g''H_3}{f_0^2}\beta y - \frac{g''}{f_0}h. \tag{3.9}$$

Without losing any generality, the potential vorticities in both the middle and bottom layers are chosen to be zero. Noting (3.7) and (3.8), the summation of (3.1), (3.2) and (3.3) yields

$$J\left(\psi_3, \beta y + \frac{f_0}{H}h\right) = \frac{f_0}{H}w_e + \frac{g'H_1 + g''(H_1+H_2)}{Hf_0}J(h, \beta y). \tag{3.10}$$

So, just like the two-layer model discussed in the preceding section, the linear barotropic geostrophic contours $\beta y + \frac{f_0}{H}h = constant$ of the corresponding barotropic model again serve as the characteristics for the governing equation of ψ_3 in this three-layer model. It is quite straightforward to demonstrate that this is true regardless of the number of layers so long as the Q-G assumption is valid and the potential vorticity homogenization is assumed for all sub-surface layers. In light of the discussions in section 2, the streamfunction in the bottom layer is

$$\psi_3 = \psi_B - \frac{g'H_1 + g''(H_1 + H_2)}{f_0^2}\beta y, \tag{3.11}$$

where ψ_B is the same as that in section 2.2. The streamfunctions in the surface and the middle layers are

$$\psi_1 = \psi_B - \frac{(g' + g'')H}{f_0^2}\beta y - \frac{g' + g''}{f_0}h, \tag{3.12}$$

$$\psi_2 = \psi_B - \frac{g'H_1 + g''H}{f_0^2}\beta y - \frac{g''}{f_0}h. \tag{3.13}$$

The interface between the surface and middle layers and that between the middle and bottom layers are

$$h_2 = H_2 + H_3 + h + \frac{\beta(H_2 + H_3)}{f_0}y, \tag{3.14}$$

$$h_3 = H_3 + h + \frac{\beta H_3}{f_0}y. \tag{3.15}$$

So, except for the zonally uniform meridional tilting, both interfacial profiles are exactly the same as that of the bottom ridge. And it can be shown that this is true regardless of the number of the layers. Following the discussions in section 2, the circulation can be decomposed into two parts: the barotropic part

$$\psi_j = \psi_B, \tag{3.16}$$

and the baroclinic part

$$\psi_1^c = -\frac{(g' + g'')H}{f_0^2}\beta y - \frac{g' + g''}{f_0}h, \tag{3.17}$$

$$\psi_2^c = -\frac{g'H_1 + g''H}{f_0^2}\beta y - \frac{g''}{f_0}h, \tag{3.18}$$

$$\psi_3^c = -\frac{g'H_1 + g''(H_1 + H_2)}{f_0^2}\beta y. \tag{3.19}$$

With discussion similar to the two-layer model, one can show that the requirement that the baroclinic part be baroclinically marginally stable and the response of the interface shape at each latitude be like that of the bottom ridge completely determines the baroclinic component of the circulation.

Similar to the two layer model, in all three layers there are discontinuities of streamfunctions at the boundaries between regions A and E with

$$\Delta\psi_1|_{E-A} = \Delta\psi_2|_{E-A} = \Delta\psi_3|_{E-A} = -\psi_{b0} - \frac{2w_0D}{\alpha\pi},$$

between regions C and D with

$$\Delta\psi_1|_{C-D} = \Delta\psi_2|_{C-D} = \Delta\psi_3|_{C-D} = -\psi_{b0} - \frac{2w_0D}{\alpha\pi},$$

and along the southern boundary away from the ridge with

$$\Delta\psi_1|_{y=0} = \Delta\psi_2|_{y=0} = \Delta\psi_3|_{y=0} = \psi_{b0} - \frac{2w_0D}{\alpha\pi}.$$

These discontinuities represent the internal barotropic currents over the ridge and along the southern boundary away from the ridge. This can be shown to be present in models with any number of layers.

With the streamfunctions in (3.11), one can compute the bottom topographic form drag as

$$\tau_D = \tau_{I12} = \tau_{I23} = -\frac{\rho_0 f_0 \psi_{b0} h_0}{L}(1 - h_c/h_0) - \tau_0(1 - 2x_0/L) + \tau_0 cos\frac{\pi}{D}y.$$

The bottom topographic form drag τ_D is same as that in the corresponding barotropic model, and the interfacial form drags τ_{I12} and τ_{I23} are the same as those in the two-layer model. The first term represents the form drag generation due to the loop of currents and the second and third terms are due to the wind stress curl. The presence of the stratification and finer vertical resolution appear to have no direct effect on the bottom topographic form-drag generation. Just like the two-layer model, the interfacial form-drag generation at both interfaces is due to the correlation between the barotropic component and the baroclinic component. It depends only upon the barotropic transport associated with ψ_{b0}. The zonally mean baroclinic flow does not contribute directly. Furthermore, the wind stress curl leads to a very significant interfacial form-drag generation just like that in the two-layer model.

Balancing the interfacial form drag and the wind stress determines ψ_{b0}, which gives rise to a simple formula for the zonal transport in each layer

$$\begin{aligned}
T_{r1} &= \frac{\tau_0 2x_0 H_1/\rho_0}{|f_0|h_0 - \beta DH} + \frac{(g' + g'')H}{f_0^2}\beta DH_1, \\
T_{r2} &= \frac{\tau_0 2x_0 H_2/\rho_0}{|f_0|h_0 - \beta DH} + \frac{g'H_1 + g''H}{f_0^2}\beta DH_2, \\
T_{r3} &= \frac{\tau_0 2x_0 H_3/\rho_0}{|f_0|h_0 - \beta DH} + \frac{g'H_1 + g''(H_1 + H_2)}{f_0^2}\beta DH_3.
\end{aligned}$$

In each layer, the first part is carried by the barotropic component. Its relation with the model parameters is similar to that in the corresponding barotropic model. The second part is carried by the baroclinic component due to the presence of the stratification. Similar to the two-layer model, the barotropic part is determined by the wind stress. The baroclinic part, however, is not directly related to the wind stress but is determined by the background stratification. The total zonal transport in the channel is

$$T_r = \frac{\tau_0 2x_0 H/\rho_0}{|f_0|h_0 - \beta DH} + [g'H_1(H + H_2 + H_3) + g''(H_1 + H_2)(H + H_3)]\beta D/f_0^2. \quad (3.20)$$

So the first part carried by the barotropic component is determined by the wind stress and topographic parameters. It is not affected by either stratification or finer vertical resolution. The second part is not directly related to either the wind stress or the topographic parameters. It is determined by the stratification, which is presumably set by thermohaline process, and the presence of background stratification leads to a stronger zonal through-channel transport. Apparently this second part is affected by the vertical resolution.

Figs. 4.4(a), (b) and (c) show the streamfunctions in the surface, middle and bottom layer, respectively. As is shown in (3.11), (3.12) and (3.13), the streamfunction in each layer is the barotropic circulation superimposed upon a uniform eastward flow away from the ridge, and this eastward flow increases from the bottom to the surface layer. Thus, visually the Sverdrupian gyre circulation is more compressed against the southeast corner downstream of the ridge from bottom to surface. Noting that the baroclinic zonal flow increases from the bottom to the surface layer, the velocity vector outside the ridge rotates clockwise from the surface to bottom, which is typical of a $\beta-$spiral in a subpolar gyre circulation. The interface elevations between the surface and middle layers and between the middle and bottom layers are similar to that shown in Fig. 4.1(c). Figs. 4.5(a) and (b) show the cross section of the interfacial height of the three layer model. In the meridional section away from the ridge, the interfaces slope downward northward. And the lower interface has a weaker slope than the upper interface in accordance with the thermal wind relation. As indicated by (3.12) and (3.13), both slopes are independent of strength of the stratification, *i.e.*, the density differences between different layers. In the zonal section, the shapes of both interfaces are identical to that of the bottom one. They are again independent of the stratification. Thus in each layer along any latitude, the situation looks similar to the corresponding barotropic model and the momentum balance in each layer is thus satisfied.

Similar to the two-layer model, the discussion in this section can be extended to any kind of bottom topography so long as there are no closed linear barotropic geostrophic contours. The results can be further extended to higher order layered models. The conclusion is still that the wind stress and bottom topography determine the barotropic part of the circulation, while the baroclinic circulation is not directly related to the wind stress. For a model with parameters chosen as $L = 24000km$, $D = 1800km$, $H = 5km$,

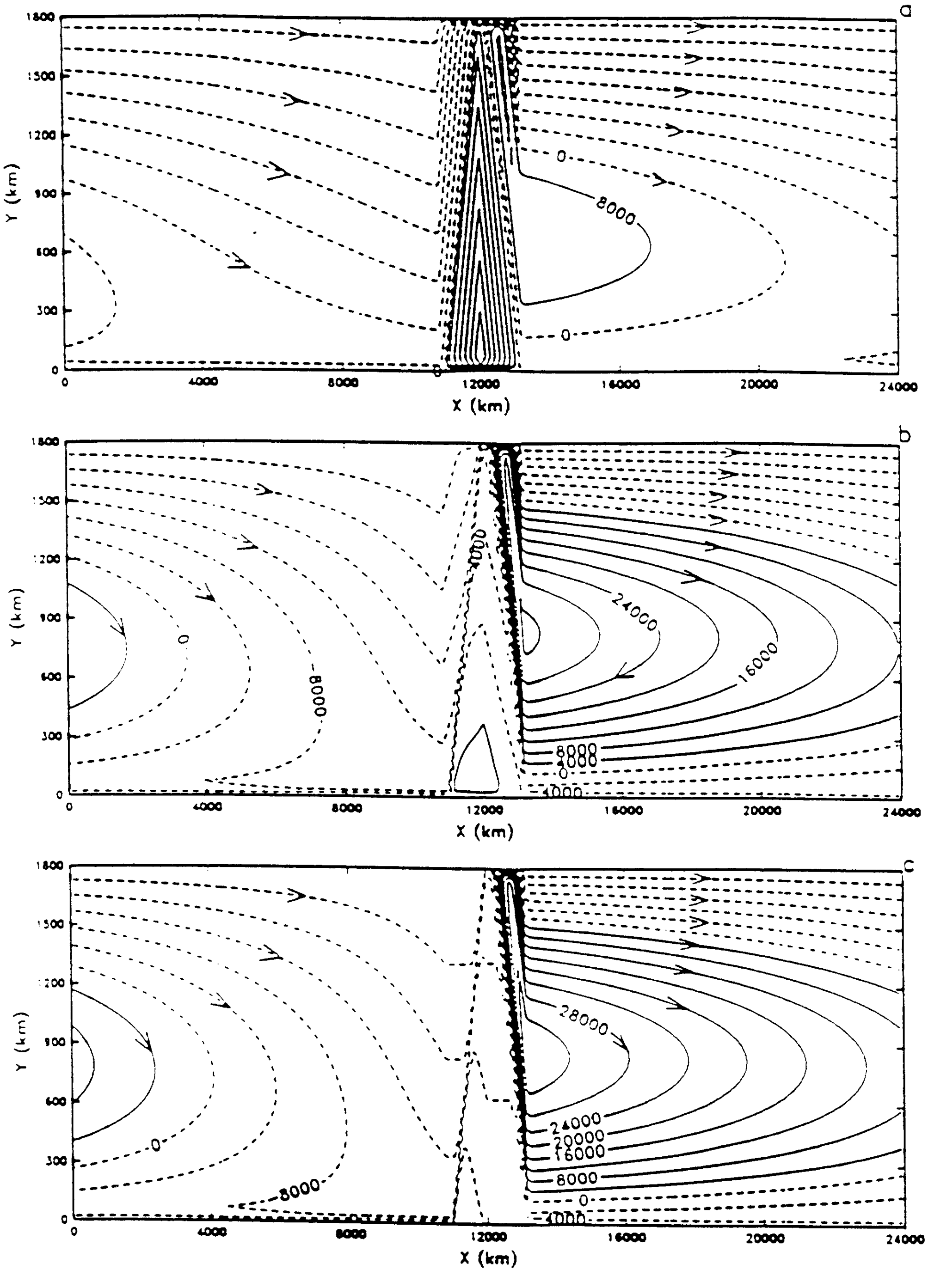

Figure 4.4: The normalized streamfunctions in the surface layer (a), middle layer (b) and bottom layer (c). The model parameters are chosen as $H_1 = 1000m$, $H_2 = 1000m$, $H_3 = 3000m$, $(\rho_2 - \rho_1)/\rho_0 = 3 \times 10^{-4}$, $(\rho_3 - \rho_2)/\rho_0 = 3 \times 10^{-4}$, while the rest are similar to those used in Fig. 4.2.

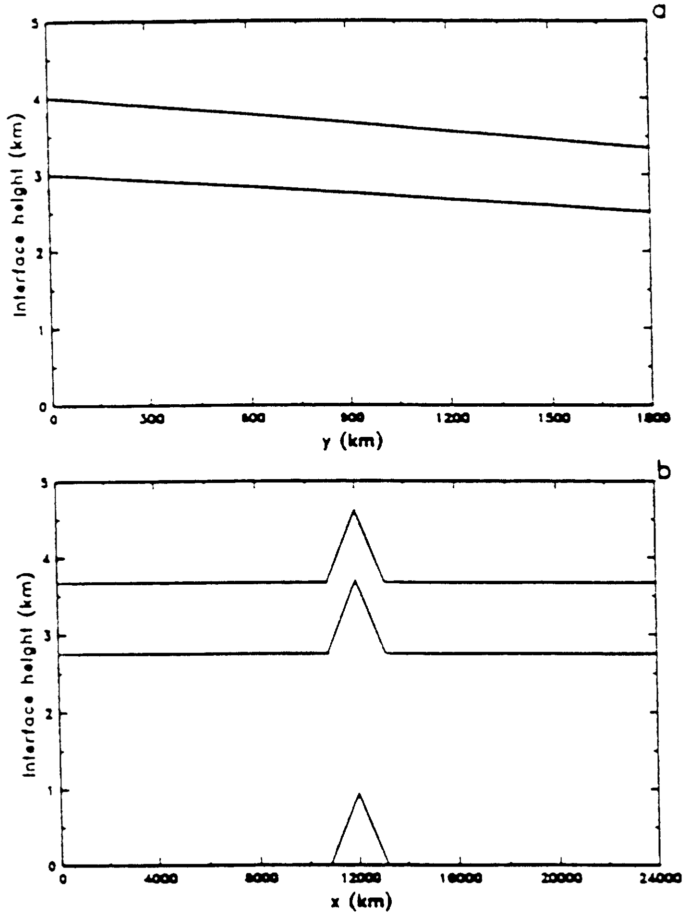

Figure 4.5: A meridional vertical section of the interfacial height away from the ridge (a) and a zonal vertical section of the interfacial height at $y = D/2$ (b). The bottom one in (b) is the profile of the bottom ridge. The model parameters are similar to those in Fig. 4.4.

$H_1 = 1000m$, $H_2 = 1000m$, $H_3 = 3000m$, $(\rho_2 - \rho_1)/\rho_0 = 8 \times 10^{-4}$, $(\rho_3 - \rho_2)/\rho_0 = 1 \times 10^{-4}$, $f_0 = -2\omega sin\theta$ and $\beta = 2\omega cos\theta/a$ with $\theta = 60^0 S$ and $a = 6.37 \times 10^6 km$, $\rho_0 = 1.03 g/cm^3$ and $\tau_0 = 0.08 N/m^2$, the total zonal transport is

$$T_r = 164Sv.$$

for $x_0 = 1200km$ and $h_0 = 950m$. Among them about $68Sv$ is in the upper layer, $26Sv$ is in the middle layer while the rest, $70Sv$, is in the bottom layer, thus quite a significant amount of zonal transport is carried by circulation below $2000m$ in the bottom layer. Apparently, the channel width to a large extent controls the zonal transport associated with the baroclinic part of the wind-driven circulation.

4.4 Conclusion and discussion

In this chapter, we have constructed a multi-layer Q-G model of the wind-driven circulation in a $\beta-$plane channel in the presence of a sufficiently high ridge. The central assumption is that potential vorticity in all sub-surface layers is fully homogenized except within possible boundary layers. The potential vorticity homogenization is presumably carried out by transient eddies, which are not explicitly included in the model. Similar to the corresponding linear barotropic model, geostrophic contour blocking is essential to the existence of a solution in the inviscid limit. The wind-driven circulation appears to be composed of a barotropic part and a baroclinic part. The barotropic part, identical to that in the corresponding barotropic model discussed in Chapter 2, is determined by the wind stress and the ridge parameters. The baroclinic part, however, is not directly related to the wind stress. It is determined by the requirement that the baroclinic flow be baroclinically marginally stable and the interfacial elevation between layers be in the same shape as the bottom ridge at each latitude in order that interfacial form-drag is equal to the bottom one. Due to the presence of the baroclinic flow, the wind-driven circulation exhibits a typical $\beta-$spiral structure in the vertical direction outside the ridge. And the Sverdrupian gyre is increasingly more compressed against the southeast corner downstream of the ridge from the bottom layer up to the surface.

It is shown that the presence of stratification does not have any direct influence on the bottom topographic form-drag generation. It is the same as its barotropic counterpart, and supercriticality of the ridge height is essential. In this multi-layer model, the interfacial form drag is generated by the stationary eddies. It is due to the correlation between the barotropic component and the baroclinic component, but the zonal mean baroclinic flow does not make direct contribution. Furthermore, the dependence of the interfacial form drag upon model parameters is similar to that of the bottom one. This appears to be generally true regardless of whether the potential vorticity in each sub-surface layer is fully homogenized or not so long as the inertial and frictional effects are weak enough. Take the three layer-model (3.1), (3.2) and (3.3) for example, generally in the middle and bottom layers one has

$$\begin{aligned}\beta y + \frac{f_0^2}{g' H_2}(\psi_1 - \psi_2) + \frac{f_0^2}{g'' H_2}(\psi_3 - \psi_2) &= R_2(\psi_2),\\ \beta y + \frac{f_0^2}{g'' H_3}(\psi_2 - \psi_3) + \frac{f_0}{H_3}h &= R_3(\psi_3)\end{aligned}$$

in the lowest order. R_2 and R_3 could be any reasonable functions. Multiply the first equation with $\partial\psi_2/\partial x$ and the second equation with $\partial\psi_3/\partial x$, then integrate them along a latitude, and one gets equation (3.6) and (3.7). There is no contradiction between our conclusion here and that arrived by Marshall *et al.* (1993) regarding the downward momentum transfer. Horizontal momentum is a 2-D vector. Marshall *et al.*'s (1993) conclusion only applies to that along a time mean Montgomery streamline, which is markedly different from a zonal line as indicated by the circulation structure obtained here.

In this multi-layer model, corresponding to circulation structure, the total zonal through-channel transport can be divided into two parts: the barotropic part and the baroclinic part. The first part is identical to that in the corresponding linear barotropic model. Thus, the wind stress, its meridional structure and the parameters associated with the bottom ridge determine the transport. The baroclinic part, however, is not directly related to the wind stress and its meridional structure. It is determined by the vertical stratification only. The stronger the stratification is, the larger the baroclinic transport. This result seems to be consistent with Olbers & Wubber (1991). To a large extent, this stratification is presumably determined by the global buoyancy-driven thermohaline circulation. Thus, the buoyancy forcing plays a fundamental role in determining the zonal transport and this process is not locally determined. To fully determine the zonal transport one has to understand the global thermohaline circulation first. This is fundamentally different from that in a closed basin. In a closed basin, the total meridional Sverdrupian transport is uniquely determined by the wind stress and is independent of the stratification (RYa, Luyten *et al.*, 1983), although the vertical structure is. In the present $\beta-$plane channel model, however, wind stress alone can not fully determine the total through-channel transport.

Although compared with its barotropic counterpart the circulation in the surface layer looks much closer to the observed large scale circulation in the circumpolar area shown by Gordon *et al.* (1978), the circulation pattern and interfacial elevation structure in particular still do not look like those of any observed corresponding isopycnal surface. This presumably implies that some important physics is still missing from this simple stratified Q-G model. First, in the discussion potential vorticity homogenization is assumed in sub-surface layers. Any departure from that assumption would induce interface distortion from the one obtained in the model. Second, as was discussed in Chapter 3 in the corresponding barotropic model, the presence of any partial meridional barriers could induce significant change in the barotropic wind-driven circulation in the channel. If partial meridional barriers were included in this multi-layer model, corresponding change would presumably occur. Third, the bottom is assumed to be an isothermal surface. As shown by Orsi *et al.* (1992), there is indeed intersection of isopycnal surface with the ocean bottom in the circumpolar ocean, although this intersection is much weaker than that at the sea surface. Fourth, the discussion is carried in the inviscid limit. It is not clear how a small but finite friction would change the picture obtained in this chapter. Fifth and most importantly, strong frontal structure is one of the most significant features in the circumpolar ocean (Nowlin & Klinck, 1986), but it is excluded from our present model by virtue of the model assumption. Its presence could have substantial influence on the three dimensional structure of the wind-driven circulation.

In spite of all the shortcomings, the model does highlight some of the important physics of the large scale wind-driven circulation in the circumpolar ocean. First of all, just as the corresponding barotropic model shows, the topography around Drake Passage plays a vital role in determining the wind-driven circulation in the circumpolar ocean regardless of the presence of stratification. It blocks all the linear barotropic geostrophic contours (Krapisky, personal communication), thus the topographic form drag is generated. The model suggests that the bottom topographic form-drag generation process is not directly influenced by the stratification, and the horizontal structure of the wind stress is of leading order importance. Second, the model suggests that the interfacial form drag needed to transport momentum down from surface to the bottom is probably mostly due to the stationary eddies. This presumably implies that one may be able to get most of the downward momentum flux from the conventional data base such as hydrographic sections. Whether the mechanism indeed operates in the realistic circumpolar ocean is apparently an open question. It would be very interesting to make an actual calculation using the currently available data in the circumpolar area. Lastly from the point of view of numerical modeling, the simple Q-G model suggests that to model correctly the zonal transport of the Antarctic Circumpolar Current, generally thought driven primarily by wind stress, one has to model the global thermohaline circulation correctly in order to determine the stratification.

Appendix A

Boundary layer structure within segments $f-d$ and $a-e$

In the following discussion we will assume that, within these boundary layers, $\kappa = \kappa_0$ for simplicity.

A.1 Boundary layer structure in the two layer model

A.1.1 Boundary layer structure within segment $f - c$

Adding (2.1) and (2.2) yields

$$\beta\left(\frac{\partial\psi_1}{\partial x} + \frac{\partial\psi_2}{\partial x}\right) + \alpha\frac{\partial\psi_2}{\partial y} = \frac{f_0}{H_1}w_e - \kappa_0\nabla^2\psi_2, \tag{A.1}$$

where $\alpha = -\frac{f_0}{H_1}\frac{\partial h}{\partial x}$ (> 0). Unless there is a shadow zone near $f - c$ similar to that in a closed basin such as that discussed by Young & Rhines (1982), the potential vorticity homogenization requires that there be a boundary layer structure along $f - c$ to the lowest order at least in one layer in order to satisfy the kinematic boundary conditions at $f - c$. The numerical results of Wolf-Gladrow *et al.* (1991) seem to indicate that there is no shadow zone structure in any sub-surface layers. If the characteristic thickness of the boundary layer is $1/\kappa$, then it is easy to see that there could not be any boundary layer in either the lower or the upper layer for the lowest order solution. Thus, the characteristic thickness of the boundary layer should be different from $1/\kappa$. Suppose it is $\varepsilon = 1/\sqrt{\kappa}$, and

$$Y = \frac{D - y}{\varepsilon} \tag{A.2}$$

$$\psi_j(x, y) = \psi_j^{(0)}(x, Y) + \varepsilon\psi_j^{(1)}(x, Y) + ..., \tag{A.3}$$

then from (A.1) the lowest order balance gives

$$\psi_2^{(0)} = \psi_{b0} - \beta D/F, \tag{A.4}$$

Noting $\psi_2|_{y=D}$. Therefore, the bottom layer can not support a boundary layer to the lowest order and there must be a boundary layer structure to the lowest order in the upper layer. The first order balance of (A.1) gives

$$\beta\frac{\partial\psi_1^{(0)}}{\partial x} - \alpha\frac{\partial\psi_2^{(1)}}{\partial Y} = 0. \tag{A.5}$$

The first order balance from (2.1) gives

$$\frac{\partial^2 \psi_1^{(0)}}{\partial Y^2} + \beta \frac{\partial \psi_1^{(0)}}{\partial x} + F\left(\frac{\partial \psi_1^{(0)}}{\partial Y}\frac{\partial \psi_2^{(1)}}{\partial x} - \frac{\partial \psi_1^{(0)}}{\partial x}\frac{\partial \psi_2^{(1)}}{\partial Y}\right) = 0. \tag{A.6}$$

(A.5) and (A.6) determine $\psi_1^{(0)}$ subject to the boundary conditions

$$\begin{aligned} \psi_1(0)|_{Y=0} &= \psi_{b0} - 2\beta D/F \\ \psi_1(0)|_{Y\to\infty} &\to \psi_{b0} - 2\beta D/F - g'h/f_0, \end{aligned}$$

noting $\psi_1|_{y=D}$ and ψ_1. In principle we can solve the above boundary value problem presumably through numerical methods and determine the boundary layer structure. If the above boundary value problem has no solution, then there must be a shadow zone near $f - c$ and the whole discussion in the present chapter has to be modified. But this is against Wolf-Gladrow *et al.*'s (1991) numerical simulation which seems to indicate that there is no shadow zone in any sub-surface layers. Therefore we conclude that the above boundary value problem has a solution and the discussion carried in this chapter is valid. The discussion about the situation along segment $b - e$ is similar.

A.1.2 Boundary layer structure within segment $c - d$

Unlike segment $f - c$, there is a boundary layer in each layer within segment $c - d$. Suppose $\varepsilon = 1/\kappa$, and

$$\begin{aligned} Y &= \frac{D-y}{\varepsilon} \\ \psi_j(x,y) &= \psi_j^{(0)}(x,Y) + \varepsilon\psi_j^{(1)}(x,Y) + ..., \end{aligned}$$

then the governing equations are

$$\frac{\partial^2 \psi_1^{(0)}}{\partial Y^2} + F\left(\frac{\partial \psi_1^{(0)}}{\partial Y}\frac{\partial \psi_2^{(0)}}{\partial x} - \frac{\partial \psi_1^{(0)}}{\partial x}\frac{\partial \psi_2^{(0)}}{\partial Y}\right) = 0, \tag{A.7}$$

$$\frac{\partial^2 \psi_2^{(0)}}{\partial Y^2} - \alpha\frac{\partial \psi_2^{(0)}}{\partial Y} = 0. \tag{A.8}$$

The corresponding boundary conditions are

$$\begin{aligned}\psi_1(0)|_{Y=0} &= \psi_{b0} - 2\beta D/F, \\ \psi_1(0)|_{Y\to\infty} &\to \psi_B(x, D) - 2\beta D/F - g'h/f_0, \\ \psi_2(0)|_{Y=0} &= \psi_{b0} - \beta D/F, \\ \psi_2(0)|_{Y\to\infty} &\to \psi_B(x, D) - \beta D/F,\end{aligned}$$

noting $\psi_j|_{y=D}$ and ψ_j. In principle we can solve the above boundary value problem numerically and determine the boundary layer structure. The discussion and conclusion for the situation within segment $a - b$ are similar.

A.2. Boundary layer structure in the three layer model

The discussion within both segments $c - d$ and $a - b$ are similar to that in the two layer model, and they can support a boundary layer with characteristic thickness $\sim 1/\kappa$ in each layer. Within segments $f - c$ and $b - e$ the discussion is slightly different but the conclusion is similar. Suppose $\varepsilon = 1/\sqrt{\kappa}$, and

$$\begin{aligned}Y &= \frac{D - y}{\varepsilon} \\ \psi_j &= \psi_j^{(0)} + \varepsilon\psi_j^{(1)} + ...,\end{aligned}$$

then we have

$$\psi_3^{(0)} = \psi_{b0} - \beta D/F, \tag{A.9}$$

noting $\psi_2|_{y=D}$. Therefore, the bottom layer can not support a boundary layer to the lowest order, and the first order balance gives

$$\beta\left(\frac{\partial\psi_1^{(0)}}{\partial x} + \frac{\partial\psi_2^{(0)}}{\partial x}\right) - \alpha\frac{\partial\psi_3^{(1)}}{\partial Y} = 0. \tag{A.10}$$

The first order balance from the equation resulting from adding the potential vorticity equations of the surface and middle layer gives

$$\frac{\partial^2\psi_2^{(0)}}{\partial Y^2} + \beta\frac{\partial(\psi_1^{(0)} + \psi_2^{(0)})}{\partial x} + F\left(\frac{\partial\psi_2^{(0)}}{\partial Y}\frac{\partial\psi_3^{(1)}}{\partial x} - \frac{\partial\psi_2^{(0)}}{\partial x}\frac{\partial\psi_3^{(1)}}{\partial Y}\right) = 0. \tag{A.11}$$

The lowest order balance of the surface layer gives

$$\frac{\partial\psi_1^{(0)}}{\partial Y}\frac{\partial\psi_2^{(0)}}{\partial x} - \frac{\partial\psi_1^{(0)}}{\partial x}\frac{\partial\psi_2^{(0)}}{\partial Y} = 0. \tag{A.12}$$

The boundary conditions are

$$\begin{aligned}
\psi_1^{(0)}|_{Y=0} &= \psi_{b0} - \left[\frac{g''H_3}{f_0^2} + \frac{g'(H_2+H_3)}{f_0^2}\right]\beta D,\\
\psi_1^{(0)}|_{Y\to\infty} &\to \psi_{b0} - \frac{g'+g''}{f_0}h - \left[\frac{g''H_3}{f_0^2} + \frac{g'(H_2+H_3)}{f_0^2}\right]\beta D,\\
\psi_2^{(0)}|_{Y=0} &= \psi_{b0} - \frac{g''H_3}{f_0^2}\beta D,\\
\psi_2^{(0)}|_{Y\to\infty} &\to \psi_{b0} - \frac{g''}{f_0}h - \frac{g''H_3}{f_0^2}\beta D,
\end{aligned}$$

noting $\psi_j|_{y=D}$ and ψ_j. (A.10), (A.11) and (A.12) together with the boundary conditions above make up the boundary value problem for ψ_1 and ψ_2, which in principle can be solved numerically. The discussions for any higher order layer model are similar to this three layer model.

In conclusion for any layer models, within segments $c-d$ and $a-b$, there is a boundary layer in each layer with characteristic thickness $\sim 1/\kappa$; within segments $f-c$ and $b-e$, there is a boundary layer in each layer except the bottom layer with characteristic thickness $\sim 1/\sqrt{\kappa}$ for the lowest order solution.

Appendix B

Large scale uniform flow over topography

The influence of bottom topography on oceanic flow is widespread, depending upon the characteristic time and horizontal scales of the flow, and the characteristic scale of the bottom topography. In the stratified ocean, this influence also depends upon the vertical stratification. Following Rhines (1983) and Haynes (1985), we choose here to discuss one particular model about the influence of large scale bottom topography on planetary scale slow baroclinic oceanic flow to highlight the physics behind the way how the zonal velocity associated with the baroclinic component in the two-layer model in the lower layer discussed section 2 is determined. We consider a two-layer model with baroclinic zonal flow U_1 and U_2, density ρ_1 and ρ_2, and equal depth H_1 on an open $\beta-$plane. It encounters a large scale mid-ocean ridge $h(x)$ in the form of (2.3). With standard notation, the governing equations for the steady motion are simply

$$J(\psi_1, q_1) = 0, \tag{B.1}$$

$$J(\psi_2, q_2) = 0. \tag{B.2}$$

Equations (B.1) and (B.2) simply state that in both layers potential vorticity is conserved following streamlines, or in other words, fluid particles flow along isolines of potential vorticity in both layers. q_j is without relative vorticity. The partial differential equations can now be simplified into the simple algebraic equations

$$q_1 = Q_1(\psi_1), \tag{B.3}$$

$$q_2 = Q_2(\psi_2). \tag{B.4}$$

The functional forms of Q_1 and Q_2 can be determined by tracing along streamlines until h vanishes. As noted by Rhines (1983), for this simplified problem, we can use an either upstream or a downstream condition to determine the functional forms of Q_1 and Q_2. Using an upstream condition of uniform zonal flow, we have

$$Q_1(\psi_1) = -\frac{\beta + F(U_1 - U_2)}{U_1}\psi_1, \tag{B.5}$$

$$Q_2(\psi_2) = -\frac{\beta - F(U_1 - U_2)}{U_2}\psi_2. \tag{B.6}$$

These equations readily show that in the presence of uniform zonal flow U_1 and U_2 with $U_1 > U_2$, the planetary vorticity gradient β in the upper layer is enhanced by the interfacial vortex stretching, while that in the lower layer is weakened by the interfacial vortex stretching. With the two equations above, the solution can be found by simply substituting equations (B.5) and (B.6) into equations (B.3) and (B.4), we have

$$\begin{aligned}
\psi_1 &= -U_1 y + \frac{F f_o h U_1}{\beta H_1}(\beta/U_2 - F - FU_1/U_2)^{-1}, \\
\psi_2 &= -U_2 y + \frac{f_o h U_1}{\beta H_1}(FU_2/U_1 - \beta/U_1)(\beta/U_2 - F - FU_1/U_2)^{-1}.
\end{aligned}$$

In the special case with

$$U_2 = \frac{\beta}{F}, \tag{B.7}$$

then

$$\psi_1 = -U_1 y - \frac{g'}{f_0} h, \tag{B.8}$$

$$\psi_2 = -U_2 y, \tag{B.9}$$

regardless of U_1. In this special case, there is no response in the lower layer; all the response is in the upper layer.

Chapter 5

A simple model of abyssal circulation in a circumpolar ocean

5.1 Introduction

In the preceding three chapters, the dynamic role of bottom topography in the momentum balance is discussed. It is shown that the supercriticality of bottom ridges is essential in both the bottom topographic and interfacial form drag generation. In this chapter and the next one we want to study the dynamic role of bottom topography in the mass balance in a $\beta-$plane channel. In this chapter the buoyancy-driven circulation is discussed, while in the next chapter the wind-driven circulation will be discussed.

In the World Oceans, there are several distinct source regions of deep water formation, such as that in the North Atlantic Ocean. Warren (1981) gave an excellent review of the deep water formation in the world oceans. In compensation for the deep water formation in small source regions, there is a general slow upward movement of deep water over the rest of the world oceans. Based upon this idea and with the assumption of planetary geostrophy for flow away from the western boundaries, Stommel and Arons developed a theoretical conceptual model for the abyssal circulation in both closed basins and global ocean basins (Stommel, 1958; Stommel *et al.*, 1958; Stommel & Arons, 1960a and b).

The model predicted intense western boundary currents in each closed basin. And this prediction was indeed, to some extent, confirmed by Swallow & Worthington (1957) in the North Atlantic and by observations in other closed basins.

The classical Stommel & Arons model has been extended in several different directions. Kuo & Veronis (1973) employed tracers as indicators for the interior sluggish poleward flow. In contrast to the Stommel & Arons model, Kawase (1987) introduced a Newtonian damping in the continuity equation in a linear two layer model. It replaces the prescribed sinks and sources in Stommel & Arons' model (1960a) (SA hereafter), so that the buoyancy forcing is crudely determined by the internal dynamics of the model. The model was spun up from rest, and gave a steady state that is quantitatively consistent with the simpler Stommel & Arons theory. In the spin-up process, both Rossby and coastal Kelvin waves play important roles in propagating information in the basin. Hautala & Riser (1989) extended the Stommel & Arons model by including wind forcing and geothermal forcing. Rhines (1989) and Straub & Rhines (1990) discussed the influences of stratification, bottom topography, and the nonlinear spin up of the model abyssal circulation. They showed the importance of the geometry of geostrophic contours and steepening of the nonlinear Rossby waves.

All the theories above are applicable only to closed basins with meridional boundaries, where conventional Sverdrup dynamics is generally thought to hold. In the circumpolar ocean, there are no meridional boundaries to support the western boundary current, which is essential for the Stommel & Arons theory of abyssal circulation in closed basins. In the circumpolar ocean, the conceptual difficulty is to identify a physical process through which net meridional water mass exchange is carried out. In an annulus channel with a uniformly distributed source along the inner boundary and a corresponding uniformly distributed sink along the outer boundary, it was demonstrated in both laboratory experiments and theoretical models that the source to sink flow is carried jointly by the surface and bottom Ekman flow, *e.g.*, Barcilon (1967) and Hide (1968). Associated with this meridional circulation is a strong westward through-channel flow. It was this flow pattern which prompted Barcilon (1967) to argue that the peripheral Antarctic water discharge could act as a retarding force to counterbalance the wind stress. Wright & Willmott (1992) essentially applied the abyssal circulation theory for a closed basin to a circumpolar ocean. They discussed the time evolution of isolated cooling events, which dynamically is rather similar to the evolution of $18°C$ water in a subtropical gyre discussed by Dewar (1987). Despite all these studies, fundamental questions are still left unanswered. For example, is the classical Stommel & Arons theory for closed basins applicable to a circumpolar ocean in the presence of a sufficiently high bottom ridge? How do bottom waters formed in Weddell Sea and Ross Sea (Warren, 1981) cross the channel? Can geostrophic flow in a $\beta-$plane channel support a net cross-channel volume transport?

The purpose of this chapter is to discuss the abyssal circulation in a circumpolar ocean, idealized here as an isolated zonal $\beta-$plane channel. As the first step, the discussions will be carried out in a simple barotropic model similar to that for the wind-driven circulation discussed in Chapters 2 and 3. In section 2, the barotropic model and properties of the corresponding geostrophic contours will be discussed. Then, in section 3, following Stommel *et al.* (1958), we consider simple cases forced only by a point source and sink in the channel placed at the same side of the channel. In section 4, a simple case forced only by a point source and sink in the channel placed on different sides of the channel will be discussed. Our intention is mainly to answer the last two questions and to demonstrate the novelty of the buoyancy-driven flow in a channel against that in a closed basin. We will also show the similarity between wind stress forcing and buoyancy forcing in terms of generating through-channel recirculations. In section 5, we are going to demonstrate that in the presence of a sufficiently high ridge, the classical SA model in closed basins is applicable to a circumpolar ocean, but with significant modifications. In section 6, a schematic picture of the abyssal circulation of an idealized Southern Ocean will be constructed. It is characterized by a strong inter-basin water exchange. Thus, the circumpolar part of the schematic picture of the global abyssal circulation, first proposed by Stommel (1958) is completed. We close this chapter with discussion in section 7.

5.2 The linear homogeneous model

Following SA, we consider a homogeneous ocean in a planetary β−plane channel. Away from boundary layers and following conventional notation, the planetary geostrophy is

$$
\begin{aligned}
-fv &= -g\frac{\partial\zeta}{\partial x}, && (2.1)\\
fu &= -g\frac{\partial\zeta}{\partial y}, && (2.2)
\end{aligned}
$$

where ζ is the deviation of the free surface from its mean. The linear mass conservation equation is

$$
\frac{\partial(H-h)u}{\partial x} + \frac{\partial(H-h)v}{\partial y} = -Q(x,y), \qquad (2.3)
$$

where Q denotes the source (< 0) and sink (> 0) prescribed at the surface in the spirit of Stommel & Arons. H and h represent the mean water depth and the bottom topography, respectively. For simplicity, $h(x,y)$ is chosen as

$$
h(x,y) = \begin{cases} h_0(1-|\frac{L/2-x}{x_0}|) & \text{if } |L/2-x| \le x_0; \\ 0 & \text{otherwise,} \end{cases} \qquad (2.4)
$$

where L and x_0 are the length of the channel and half width of the ridge, respectively. The above equations lead to the following linear potential vorticity equation

$$
J(\zeta,q) = \frac{q^2}{g}Q, \qquad (2.5)
$$

where q is the linear potential vorticity defined as

$$
q = \frac{f}{H-h}. \qquad (2.6)
$$

Similar to the linear Q-G model, in this linear planetary geostrophic model, the potential vorticity of each fluid particle is solely determined by its position, and $q = constant$ defines the geostrophic contours. Mass conservation (2.3) requires

$$\overline{(H-h)v}^{x} = -\int_0^y \overline{Q}^x dy', \tag{2.7}$$

where

$$\overline{Z}^x \equiv \frac{1}{L}\int_0^L Z\,dx.$$

In this equation, $L\overline{(H-h)v}^{x}$ represents the total net cross-channel geostrophic volume transport. In the absence of any bottom topography, it is quite clear from (2.1) that one always has

$$\overline{v}^x = 0$$

because of the periodicity for $\zeta(x,y)$. In this case, geostrophic flow can not support any net cross-channel volume transport. Any net cross-channel volume transport has to be carried out through other physical processes, such as the surface and bottom Ekman boundary layers discussed by Hide (1968). In the presence of bottom topography, however, even though we still have $\overline{v}^x = 0$, $\overline{(H-h)v}^{x}$ may not necessarily be zero. Thus, geostrophic flow in a circumpolar ocean may be able to support a net cross-channel volume flux, to be demonstrated later.

As the model stands as (2.5), the discussion in terms of the geostrophic contours in Chapter 2 holds equally well here for the buoyancy driven flow. Therefore, in this chapter we will follow the same approach developed there. For the wind-driven circulations, as are discussed in the preceding chapters, in the case with a very low ridge there is no solution in the inviscid limit. In the case with a sufficiently high ridge, however, there is a solution in the inviscid limit. In the planetary geostrophic model, in the absence of any topography, the geostrophic contours $q = constant$ are straight zonal lines. In the presence of a ridge in the form of (2.4), some of the geostrophic contours will strike either the southern or northern boundary. Nevertheless, for a sufficiently low ridge with $h_0 < h_c$, all of the geostrophic contours

$$q = \frac{fs + \beta y_0}{H},$$

with $0 \leq y_0 < DH(h_c - h_0)/h_c(H - h_0)$ will strike neither the southern nor the northern boundary: they close themselves. h_c is defined as

$$h_c = -\frac{\beta D}{fs}H,$$

and $f_S = f|_{y=0}$. Free solutions exist along the unblocked geostrophic contours in the inviscid limit. For a sufficiently high ridge with $h_0 > h_c$, however, all geostrophic contours in the channel are blocked by the lateral boundaries; Fig. 5.1 shows such an example. In this case, any movement in the channel has to be externally forced. Correspondingly, h_c is defined as the critical height, and the case with $h_0 > (<) h_c$ will be called the supercritical (subcritical) state. With discussion similar to that of the wind-driven circulation, segments $a-c$ (see Fig. 5.1) along the northern boundary and $h-j$ along the southern boundary are the two equivalent eastern boundaries. Segments $c-e$ along the northern boundary and $f-h$ along the southern boundary are the two equivalent western boundaries. This is true regardless of the ridge height. From what we learned from gyre dynamics (SA), $\zeta(x,y)$ has to be prescribed along the equivalent eastern boundaries. Without losing any generality, we can set the boundary condition along the northern equivalent eastern boundary $a-c$ as

$$\zeta(x,D)|_{a-c} \ = \ 0,$$

while the condition at the southern equivalent eastern boundary $h-j$ as

$$\zeta(x,0)|_{h-j} \ = \ \zeta_0.$$

This boundary condition can not be set arbitrarily and has to be determined through the mass balance (2.7). This completes the model for the source-sink-driven circulation in a $\beta-$plane channel.

Unlike the wind-driven circulation, we will show that for the cases with only point source and sink forcings, solutions in the inviscid limit may be possible even with a subcritically high ridge in some cases. Nevertheless, a supercritically high ridge is needed if a

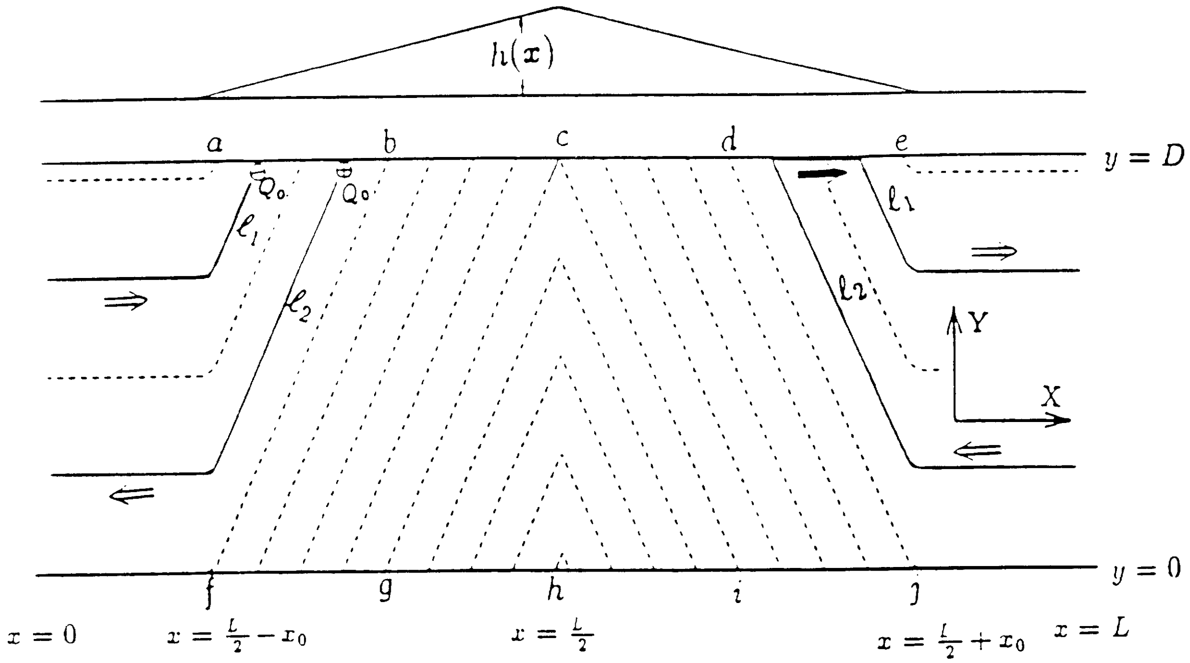

Figure 5.1: The circulation pattern driven by a pair of point source and sink at the northern boundary of the channel. *Case I*. On top is the profile of the ridge. Dashed lines are the geostrophic contours. Solid lines are the current route. Solid arrow represents equivalent western boundary current, while those open ones represent internal currents.

cross-channel volume flux is necessary. In section 3 we will present some interesting cases forced only by point sources and sinks placed at the northern boundary. In section 4 we will present a case forced by a point source and a point sink placed at different sides of the channel. These discussions by no means are intended to exhaust all possibilities, but rather they are meant to demonstrate both the dynamic difference and similarity between the classical SA model and the $\beta-$plane channel model. In the following discussions a supercritically high ridge will always be assumed.

5.3 Flow driven by a point source and a point sink at the northern boundary

It is assumed that the buoyancy forcing is in the form

$$Q(x,y) \;=\; -Q_0\delta(x-x_1)\delta(y-D) \;+\; Q_0\delta(x-x_2)\delta(y-D), \tag{3.1}$$

where $L/2 - x_0 \le x_2 < x_1 \le L/2$. They are both within the segment $a-c$. Away from the point source and sink and the two equivalent western boundaries, the potential vorticity equation (2.5) reduces to

$$J(\zeta, q) \;=\; 0.$$

Thus, any flow has to be along geostrophic contours in the interior. Cross $q-$contour flow is allowed only within the two equivalent western boundaries $c-e$ and $f-h$. In the supercritical state, the northern equivalent eastern boundary is divided by point b $(L/2 - x_c, D)$, where

$$x_c \;=\; x_0\frac{\Delta h_c}{h_0},$$

and $\Delta h_c = h_0 - h_c$, into two segments $a-b$ and $b-c$. x_c actually measures the supercriticality of the ridge height. The corresponding equivalent western boundary, $d-e$, for segment $a-b$ is within the northern equivalent western boundary. The corresponding equivalent western boundary, $f - g$, for segment $b - c$ is within the southern equivalent western boundary. Depending upon the location of the point forcing with respect to the critical point b, there are three different flow patterns. The essence of these discussions is that because the point source and point sink are placed at different geostrophic contours, the fluid from the point source to point sink has to cross $q-$contours. The real question is where is the cross $q-$contour flow.

Case I: $x_2 < x_1 < L/2 - x_c$

Both the point source and point sink are within segment $a - b$, so the only possible solution is shown in Fig. 5.1. The flow, with volume flux Q_0, starts from the source at (x_1, D) and moves along the geostrophic contour ℓ_2

$$q(x,y)|_{\ell_2} = \frac{f_N}{H - h(x_1)},$$

where $f_N = f|_{y=D}$, until it reaches the northern boundary again at point $(L - x_1, D)$ within the northern equivalent western boundary. Afterwards, the flow changes direction, crosses $q-$contours, and moves eastward until point $(L - x_2, D)$. At this point, it changes direction again, and moves along the geostrophic contour ℓ_1

$$q(x,y)|_{\ell_1} = \frac{f_N}{H - h(x_2)},$$

all the way to the point sink at (x_2, D). Dynamically, this solution is quite similar to that discussed by Stommel *et al.* (1958). It is easy to verify that there is no net cross-channel geostrophic volume flux, and the mass balance (2.7) is satisfied. Furthermore, there is a net westward volume flux Q_0 from the point source to the point sink, but there is no net eastward flux everywhere in the channel. A significant feature of this flow pattern is that the flow does not reach the southern boundary and there is no southern equivalent western boundary layer. All the cross $q-$contour flow occurs within the northern equivalent western boundary layer. A brief discussion about the influence of a finite and weak friction on this flow pattern is presented in the appendix.

Case II: $x_2 < L/2 - x_c < x_1$

The point source is within the segment $b - c$ while the point sink is within the segment $a - b$. This case is still similar to that discussed by Stommel *et al.* (1958), nevertheless there is a substantial modification. The only possible solution is shown in Fig. 5.2. The flow, with volume flux Q_0, starts from the source at (x_1, D) and moves southward along the geostrophic contour ℓ_0

$$q(x,y)|_{\ell_0} \; = \; q_0 \; \equiv \; \frac{f_N}{H - h(x_1)},$$

until it reaches the southern boundary at point f' $(x_{1*}, 0)$ with

$$\frac{f_S}{H - h(x_{1*})} \; = \; q_0.$$

At f', this flow splits into two parts with volume fluxes Q_1 and Q_2

$$Q_0 \; = \; Q_1 \; + \; Q_2. \tag{3.2}$$

Within the southern equivalent western boundary layer, one branch with volume flux Q_1 flows eastward to point g $(L/2 - x_0 + x_c, 0)$. The other branch with volume flux Q_2 flows westward along the southern boundary all the way to point j $(L/2 + x_0, 0)$. Afterwards, the Q_1 branch flows northward along the geostrophic contour ℓ_1

$$q(x,y)|_{\ell_1} \; = \; q_1 \; \equiv \; \frac{f_N}{H - h_0},$$

until it reaches the northern boundary at point c $(L/2, D)$. Then, it flows eastward along the northern boundary until it reaches point d' $(L - x_2, D)$. Within segments $f' - g$ and $c - d'$, the Q_1 branch flows within the equivalent western boundary layers in order to cross the geostrophic contours. The Q_2 branch does the same within the segment $f - f'$. From point j, the Q_2 branch flows northward along the geostrophic contour ℓ_2

$$q(x,y)|_{\ell_2} \; = \; q_2 \; \equiv \; \frac{f_S}{H},$$

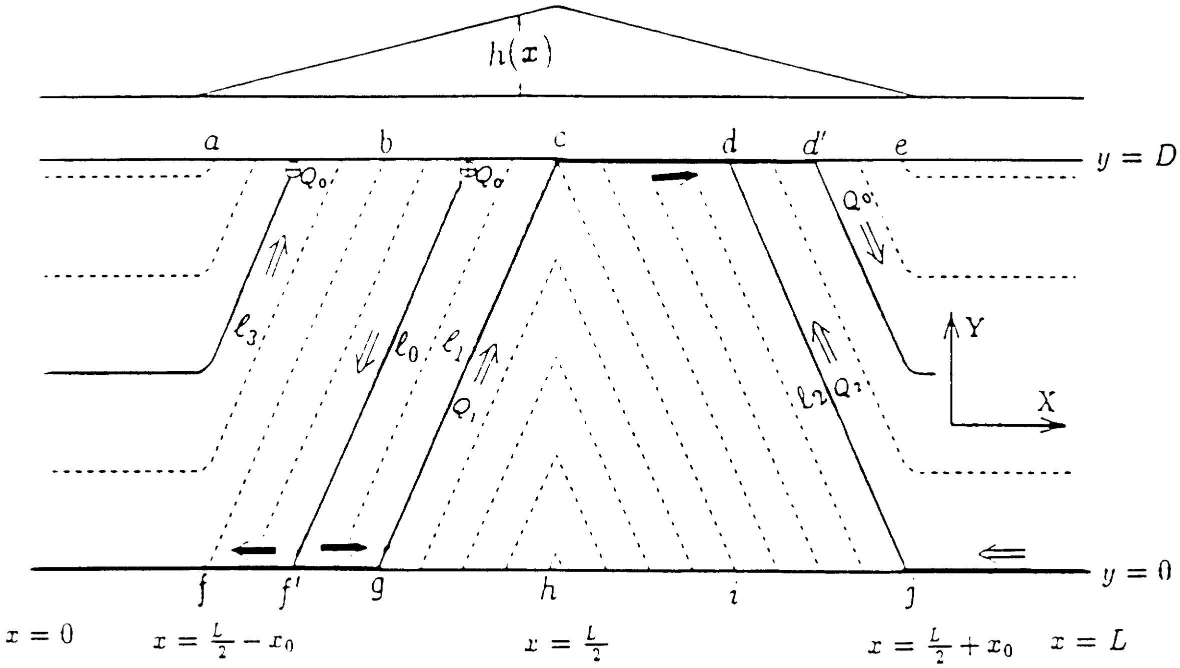

Figure 5.2: Similar to Fig. 5.1 but for *Case II*.

until it reaches point d $(L/2 + x_c, D)$, where it meets the Q_1 branch. Then, it turns eastward and flows along the northern boundary until it reaches point d'. From d', all the fluid from the source joins and flows along the geostrophic contour ℓ_3

$$q(x,y)|_{\ell_3} \;=\; q_3 \;\equiv\; \frac{f_N}{H - h(x_2)},$$

until it reaches the point sink at (x_2, D).

To determine Q_1 and Q_2, we need another equation besides (3.2). The periodicity of $\zeta(x,y)$ around the channel requires that

$$\Delta\zeta_0 \;+\; \Delta\zeta_1 \;+\; \Delta\zeta_2 \;=\; 0,$$

where $\Delta\zeta_j$ $(j \;=\; 0,1,2)$ is the difference of the surface dynamic topography across the corresponding geostrophic contours. The relation between the volume transport along a geostrophic contour and the corresponding surface topography difference across the geostrophic contour satisfies

$$Q_j \;=\; \frac{g}{q_j}\Delta\zeta_j \qquad j = 0,1,2.$$

With this relation, the above periodicity yields

$$Q_0 q_0 \;-\; Q_1 q_1 \;-\; Q_2 q_2 \;=\; 0. \tag{3.3}$$

Using (3.2) and (3.3) one can determine the volume fluxes of the two branches

$$\begin{aligned} Q_1 &= \frac{H - h_0}{H - h(x_1)} \cdot \frac{h(x_1) - h_c}{h_0 - h_c} Q_0, \\ Q_2 &= \frac{H - h_c}{H - h(x_1)} \cdot \frac{h_0 - h(x_1)}{h_0 - h_c} Q_0, \end{aligned}$$

noting $h(x_1) > h_c$ in the supercritical state. Again it is easy to verify that there is no net cross-channel volume flux, and (2.7) is satisfied. Unlike *Case I*, there are now both net eastward and westward zonal volume transports from the point source to the point sink. The eastward volume flux from the source to the sink is Q_1, while that of the westward one is Q_2. The relative strength of these two branches is determined only by the position of the source. As $x_1 \to L/2 - x_c$, *i.e.*, $h(x_1) \to h_c$, $Q_1 \to 0$, and the Q_1 branch disappears. This essentially degenerates to *Case I*. On the other hand, as $x_1 \to L/2$, *i.e.*, $h(x_1) \to h_0$, $Q_1 \to Q_0$ and $Q_2 \to 0$, ℓ_0 coalesces with ℓ_1 and both Q_1 and Q_2 branches disappear. In this limit, the fluid flows directly from the source to $(L - x_2, D)$, and then from there it flows along ℓ_3 all the way to the sink. Between these two extremes, the flow from the source always branches upon reaching the southern equivalent western boundary because of the two requirements, the periodicity of $\zeta(x, y)$ around the channel and no net cross-channel geostrophic volume transport. The other significant difference between *Case I* and *II* is that now the flow reaches the southern boundary, and cross $q-$contour flow occurs within both the northern and the southern equivalent western boundaries.

Case III: $L/2 - x_c < x_2 < x_1$

Both the point source and point sink are within segment $b - c$. This case is also similar to the case discussed by Stommel *et al.* (1958); nevertheless, there is again a substantial modification. With this forcing pattern, the only possible solution is shown in Fig. 5.3. The flow starts from the source at (x_1, D) and flows along the geostrophic contour ℓ_{10}

$$q(x,y)|_{\ell_{10}} \;=\; q_{10} \;\equiv\; \frac{f_N}{H - h(x_1)},$$

until it reaches the southern boundary at point g' $(x_{1*}, 0)$ with x_{1*} satisfying

$$\frac{f_S}{H - h(x_{1*})} \;=\; q_{10}.$$

It then splits into two parts. One branch with volume flux Q_1 flows eastward until it reaches point g $(L/2 - x_0 + x_c, 0)$. Afterwards, this Q_1 branch flows northward along the geostrophic contour ℓ_1

$$q(x,y)|_{\ell_1} \;=\; q_1 \;\equiv\; \frac{f_N}{H - h_0}.$$

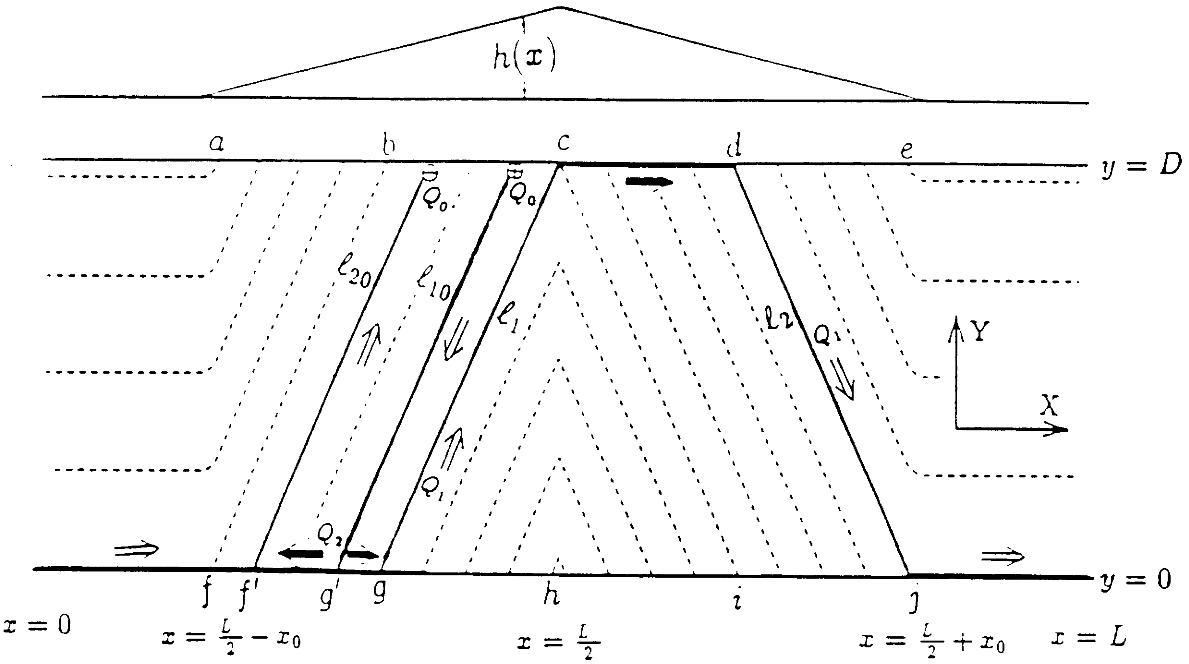

Figure 5.3: Similar to Fig. 5.1 but for *Case III*.

Upon reaching the northern boundary at point c, it flows eastward within the northern equivalent western boundary layer until point d $(L/2+x_c, D)$. Then, this Q_1 branch flows southward along the geostrophic contour ℓ_2

$$q(x,y)|_{\ell_2} = q_2 \equiv \frac{f_S}{H},$$

until it reaches the southern boundary at point j $(L/2+x_0, 0)$. After that, it flows westward all the way to point f $(L/2-x_0, 0)$. Within the southern equivalent western boundary layer, this Q_1 branch crosses geostrophic contours until it reaches point f' $(x_{2*}, 0)$ with x_{2*} satisfying

$$\frac{f_S}{H-h(x_{2*})} = q_{20} \equiv \frac{f_N}{H-h(x_2)}.$$

The other branch with volume flux Q_2 flows westward from the branching point at g' until f'. Here, the two branches join together and flow along the geostrophic contour ℓ_{20}

$$q(x,y)|_{\ell_{20}} = q_{20},$$

all the way to the point sink at (x_2, D).

To determine Q_1 and Q_2, we can use the mass balance (2.7) and the periodicity of the surface dynamic topography. Suppose we define the differences of the dynamic surface topography across geostrophic contours ℓ_{20}, ℓ_{10}, ℓ_1 and ℓ_2 as $\Delta\zeta_{20}$, $\Delta\zeta_{10}$, $\Delta\zeta_1$ and $\Delta\zeta_2$, respectively. Then, the periodicity of surface dynamic topography gives

$$\Delta\zeta_2 + \Delta\zeta_1 + \Delta\zeta_{20} + \Delta\zeta_{10} = 0, \tag{3.4}$$

while the mass balance (2.7) gives another equation

$$\Delta\zeta_2/q_2 + \Delta\zeta_1/q_1 = 0. \tag{3.5}$$

Solving (3.4) and (3.5) gives us

$$\begin{aligned} Q_1 &= \frac{(H-h_c)(H-h_0)}{(H-h(x_1))(H-h(x_2))} \cdot \frac{h(x_1)-h(x_2)}{h_0-h_c} Q_0, \\ Q_2 &= Q_0 - Q_1. \end{aligned}$$

Overall, the circulation shown in Fig. 5.3 is rather similar to that shown in Fig. 5.2. But unlike *Case II*, as $x_1 \rightarrow L/2$, although geostrophic contour ℓ_{10} overlaps ℓ_1, the branching does not disappear and still occurs at point c.

The three cases above are all forced by a pair of point source and sink located at the northern equivalent eastern boundary. If the pair of point source and sink is located at the southern equivalent eastern boundary, both the discussion and solution will be quite similar. In the discussions above, a supercritical ridge is assumed. In the supercritical state, as we discussed at the beginning of this section, point b divides the northern equivalent eastern boundary $a-c$ into two dynamically different segments $a-b$ and $b-c$. Similarly, point i divides the southern equivalent eastern boundary $h-j$ into two dynamically different segments $h-i$ and $i-j$. In the subcritical state, however, the regions between lines $f-b$ and $g-c$, $c-i$ and $d-j$, within which $q-$contours directly connect the two lateral boundaries, disappear. In this case, both *Cases II* and *III* degenerate to *Case I*. We readily see that in *Case I*, supercriticality of the ridge height, $h_0 > h_c$, is not necessary in the inviscid limit. Another common feature of the above three cases is that there is no through-channel recirculation, which results in the question: what will happen if the point source and sink are placed at different sides of the channel? This leads to the following section, which discusses the simplest case among those forced by a point source and sink placed at different sides of the channel.

5.4 Flow driven by a point source and a point sink placed at different sides of the channel

In the preceding section, flow driven by a pair of point source and sink both placed at the northern boundary are discussed. The common feature of the circulations is that there is no through-channel recirculation. Now let us look at the case forced by

$$Q(x,y) \;=\; -Q_0\delta(x-L/2-x_0)\delta(y) \;+\; Q_0\delta(x-L/2-x_0)\delta(y-D). \qquad (4.1)$$

In the absence of any bottom topographic features, there cannot be any net geostrophic volume transport across the channel in the inviscid limit. Thus, any net geostrophic mass flux from the source at the southern boundary to the sink at the northern boundary has to be associated with some bottom topographic features. The discussions for the previous three cases in the preceding section, where the flow from the source to the sink is geostrophic except along the two equivalent western boundaries, show that geostrophic flow can cross the channel along a blocked geostrophic contour, such as ℓ_1 and ℓ_2 in Fig. 5.2 and Fig. 5.3, which connects the two lateral boundaries. Nevertheless, in both *Case II* and *Case III*, there is no net meridional geostrophic volume transport because both the source and sink are placed at the northern boundary. Now let us see what happens when the point source and sink are placed at different sides of the channel.

Away from the point source and sink, there is no buoyancy forcing. Thus, any flow has to be along the $q-$contours, while any cross $q-$contour flow has to be within the two equivalent western boundary layers. In Fig. 5.4, the flow with volume flux Q_1 starts from the source at $(L/2 + x_0, 0)$ and moves northward along geostrophic contour ℓ_1,

$$q|_{\ell_1} = q_1 \equiv \frac{fs}{H},$$

which and its like will be called critical geostrophic contours hereafter in this section. Q_1 and $\Delta\zeta_1$, the jump of $\zeta(x, y)$ across ℓ_1, satisfy

$$Q_1 = \frac{g\Delta\zeta_1}{q_1}.$$

Upon reaching the northern boundary at point d, it splits into two branches. One branch with volume flux Q_0 flows along segment $d - e$ eastward within the northern equivalent western boundary layer until it reaches the sink at point e $(L/2+x_0, D)$. It is quite obvious that if $Q_1 = Q_0$, then the condition that $\zeta(x, y)$ be periodic around the channel is violated. Thus, another branch with volume flux Q_2 flows westward along segment $c - d$ until it arrives at point c $(L/2, D)$. Then, this branch flows southward along geostrophic contour

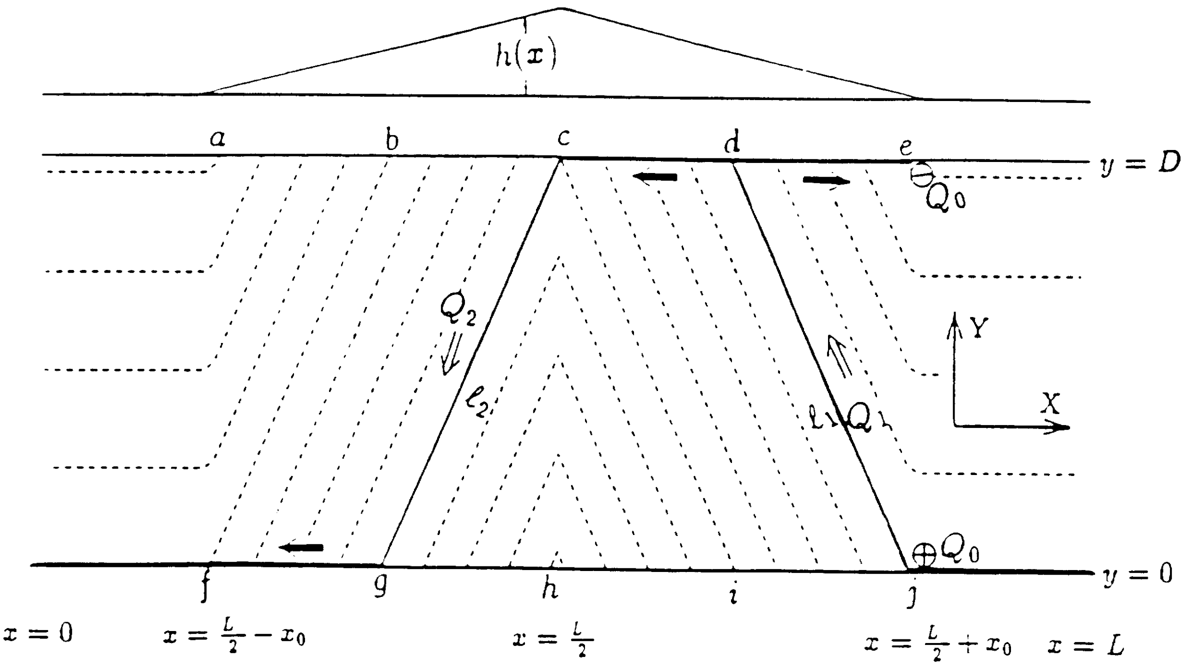

Figure 5.4: Similar to Fig. 5.1 but for the case driven by a pair of point source and sink with source (sink) at the southern (northern) boundary of the channel.

ℓ_2

$$q|_{\ell_2} = q_2 \equiv \frac{f_N}{H - h_0},$$

until it reaches the southern boundary at point g. Afterwards, it flows along the southern boundary and recirculates back to the source at $(L/2 + x_0, 0)$. Q_2 and $\Delta\zeta_2$, the jump of $\zeta(x, y)$ across ℓ_2, satisfy

$$Q_2 = \frac{g\Delta\zeta_2}{q_2}.$$

Along segment $f - g$ at the southern boundary the branch with volume flux Q_2 crosses the $q-$contours within the southern equivalent western boundary layer. Unlike the previous three cases where there is only divergent flow directly from source to sink, the buoyancy-driven circulation here consists of *two parts*, the divergent part and the rotational part. The first part flows directly from the point source to the point sink, always with volume flux Q_0 regardless of model parameters. The second part is the through-channel recirculation part with volume flux Q_2, which depends critically upon the model parameters.

To determine Q_1 and Q_2, both the periodicity of $\zeta(x, y)$ around the channel and the mass balance (2.7) have to be used. The periodicity of $\zeta(x, y)$ around the channel requires that

$$q_1 Q_1 + q_2 Q_2 = 0.$$

The conservation of volume flux gives

$$Q_1 + Q_2 = Q_0.$$

The solution is that along ℓ_1 the northward geostrophic volume flux is

$$Q_1 = \frac{H - h_c}{h_0 - h_c} Q_0, \tag{4.2}$$

while the geostrophic volume transport along ℓ_2 is

$$Q_2 = -\frac{H - h_0}{h_0 - h_c} Q_0. \tag{4.3}$$

It is obvious from these two equations that if $Q_0 > 0$, *i.e.*, we have a source at $(L/2+x_0,0)$ and a sink at $(L/2+x_0,D)$, along ℓ_1 the fluid flows northward, and the recirculation is westward. If we have a sink at $(L/2x_0,0)$, the fluid flows southward along ℓ_1, and the recirculation is eastward. In either case, we have

$$|Q_1| = |Q_2| + |Q_0|$$

With (4.2) and (4.3) we can introduce a recirculation index

$$R_c \equiv |Q_2/Q_0| = \frac{H-h_0}{h_0-h_c}. \tag{4.4}$$

This index depends only upon the model parameters, but is independent of the source/sink. The condition for the recirculating part to be equal to or stronger than the direct source to the sink flow is

$$R_c \geq 1,$$

i.e.

$$h_0 \leq h_0^* = \left(1 - \frac{f_N}{2f_S}\right)H, \tag{4.5}$$

noting that the supercriticality requires that

$$h_0 > (1 - \frac{f_N}{f_S})H.$$

For even higher ridge with $h_0 > h_0^*$, the source to sink flow is stronger than the recirculating part. Fig. 5.5 shows R_c versus h_0/H. It is not surprising to see that as

$$h_0 \to H,$$

we have

$$Q_1 \to Q_0,$$
$$Q_2 \to 0.$$

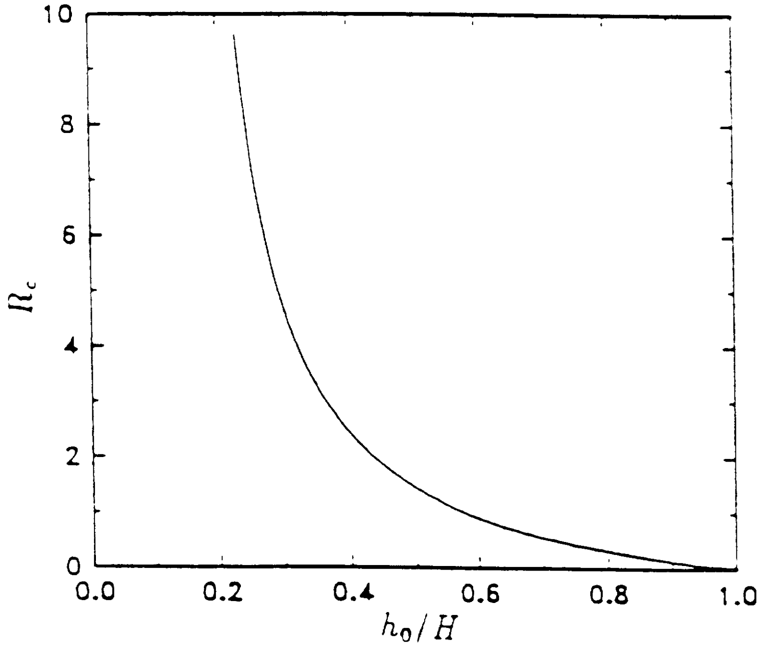

Figure 5.5: The recirculation index R_c versus h_0/H with $D = 1800km$ and $\theta_0 = 60°S$.

So, for a very high ridge extending almost to the surface, the recirculation is very weak, and the buoyancy-driven flow is predominantly from source to sink. In the limit with $h_0 \to H$, the buoyancy-driven circulation in the channel converges to that in a corresponding closed basin. On the other hand, as

$$h_0 \;\to\; h_c,$$

we have

$$Q_2 \;\to\; \infty.$$

Thus, the buoyancy forcing leads to a massive westward through-channel recirculation.

This discussion readily shows us that a ridge with a subcritical or even a critical height cannot support a net cross-channel geostrophic volume flux. To support a net cross-channel geostrophic volume transport, a ridge with a supercritical height is both necessary and sufficient as well. The ultimate reason is that in our linear $\beta-$plane channel model, away from the the point source/sink, cross-geostrophic-contour flow is possible only within the two equivalent western boundary layers. In the case with a subcritical ridge, there are non-blocked geostrophic contours, which separate the southern boundary from the northern boundary. Any flow from the southern boundary to the northern boundary or vice versa would have to cross these unblocked geostrophic contours, which is not allowed in the interior away from the two equivalent western boundaries. In the presence of a supercritical ridge, however, these closed geostrophic contours disappear, and the southern and northern boundaries are connected by geostrophic contours. Thus, any cross geostrophic contour flow is possible within either the southern or the northern equivalent western boundary. Another point worth noting is that, as clearly shown in Fig. 5.4, the net cross-channel geostrophic volume flux is the net sum of the northward flow along ℓ_1 and the southward flow along ℓ_2. The cross-channel geostrophic flow is not uniformly distributed around the channel.

Overall, this circulation pattern has some similarity to that in an annulus channel discussed by Hide (1968). In both cases, the circulation consists of two parts: the direct source to sink flow and a through-channel recirculation. Nevertheless, there are fundamental differences. First, in our case here, the cross-channel flow is geostrophic with the support of the sufficiently high ridge; while in the latter, the cross-channel flow is completely ageostrophic because a flat bottom was used. Second, in our case, the through-channel recirculation is critically determined by the ridge height and it flows as a loop of currents having a vanishingly small thickness; while in the latter, the through-channel recirculation is critically determined by the frictional process and it flows uniformly in the channel except near the boundaries.

The case discussed in this section and the three cases discussed in the preceding section are driven by a point source and a point sink, yet there is a fundamental difference between them. In the case discussed in this section, a ridge with a supercritical height is necessary, while in *Cases I*, *II* and *III*, supercriticality of the ridge height is not necessary. Second, as is required by mass balance, there is net cross-channel geostrophic volume flux in the case discussed in this section, while in the cases discussed in the preceding section there is no such cross-channel geostrophic volume flux. Third, in the case discussed in this section, the point source and sink drives a through-channel recirculation around the channel, in addition to the flow from the source to sink just like that in *Cases I*, *II* and *III*. In accordance with the discussions of Chapter 2, a ridge with a supercritical height poses a potential vorticity resistance, defined here in the model formulation of planetary geostrophy as

$$P_c = q_1 - q_2 \tag{4.6}$$

on the buoyancy-driven through-channel recirculation. In terms of this potential vorticity resistance, the through-channel recirculation is

$$Q_2 = \frac{q_1 Q_0}{P_c}. \tag{4.7}$$

Correspondingly, the recirculation index is

$$R_c = \frac{q_1}{P_c}. \tag{4.8}$$

Thus, the position of the source and the topography together determine the recirculation via q_1 and the potential vorticity resistance, for a given Q_0.

The results obtained for the simple ridge can be readily extended to topography with an arbitrary shape so long as all geostrophic contours are blocked. It is not difficult to see that the presence of any additional ridges with subcritical heights does not change the result. On the other hand, the presence of topographic features with supercritical heights will change the recirculations. Suppose there is a series of ridges with positive potential vorticity resistance $\{P_{cj}\}$, $(j = 1, \cdots, J)$, the buoyancy forcing is still in the form of (4.1). Then, the volume transport of the recirculation driven by the point source and point sink forcing is still in the form of (4.7). But the total potential vorticity resistance, P_c, is now

$$P_c = \sum_{j=1}^{J} P_{cj}.$$

5.5 Abyssal circulations driven by point source/sinks and a uniform sink at the surface

In the preceding sections we have discussed the abyssal circulation driven by point source and sink only. It is meant to demonstrate the dynamic role of a supercritical ridge. Following Stommel *et al.* (1958), in this section we choose the buoyancy forcing as a uniform sink at the upper surface and a point source and sink at each side of the channel to model crudely the Weddell Sea bottom water formation and the net deep water exchange between the circumpolar ocean and the rest of the world ocean. The buoyancy forcing is assumed to be

$$Q(x,y) = w_s - Q_1\delta(x - L/2 - x_0)\delta(y) - Q_2\delta(x - L/2 - x_0)\delta(y - D), \tag{5.1}$$

with

$$w_s = \frac{Q_1 + Q_2}{LD}.$$

Without losing generality, the northern equivalent eastern boundary along segment $a - c$ in Fig. 5.6 is used as a reference level for the free surface

$$\zeta|_{y=D} = 0 \qquad \text{for} \qquad L/2 - x_0 \le x \le L/2; \tag{5.2}$$

while at the southern equivalent eastern boundary along segment $h - j$

$$\zeta|_{y=0} = \zeta_0, \qquad \text{for} \qquad L/2 \le x \le L/2 + x_0, \tag{5.3}$$

where ζ_0 is a constant and will be determined by the mass balance (2.7). Noting the structure of the geostrophic contours, we divide the channel into subdomains A, B, C, D and E, shown in Fig. 5.6 for the convenience of characteristic integration.

To solve the potential vorticity equation (2.5), let us introduce a characteristic variable s such that

$$\frac{dx}{ds} = \frac{\partial q}{\partial y}, \tag{5.4}$$

$$\frac{dy}{ds} = -\frac{\partial q}{\partial x}. \tag{5.5}$$

Thus, the geostrophic contours serve as the characteristics and the governing equation is then converted to

$$\frac{d\zeta}{ds} = \frac{q^2}{g} w_s. \tag{5.6}$$

For different regions, we have different initial conditions.

In region A, the initial conditions for the characteristic equations are

$$\begin{aligned} x|_{s=0} &= x_s, \\ y|_{s=0} &= D, \\ \zeta|_{s=0} &= 0. \end{aligned}$$

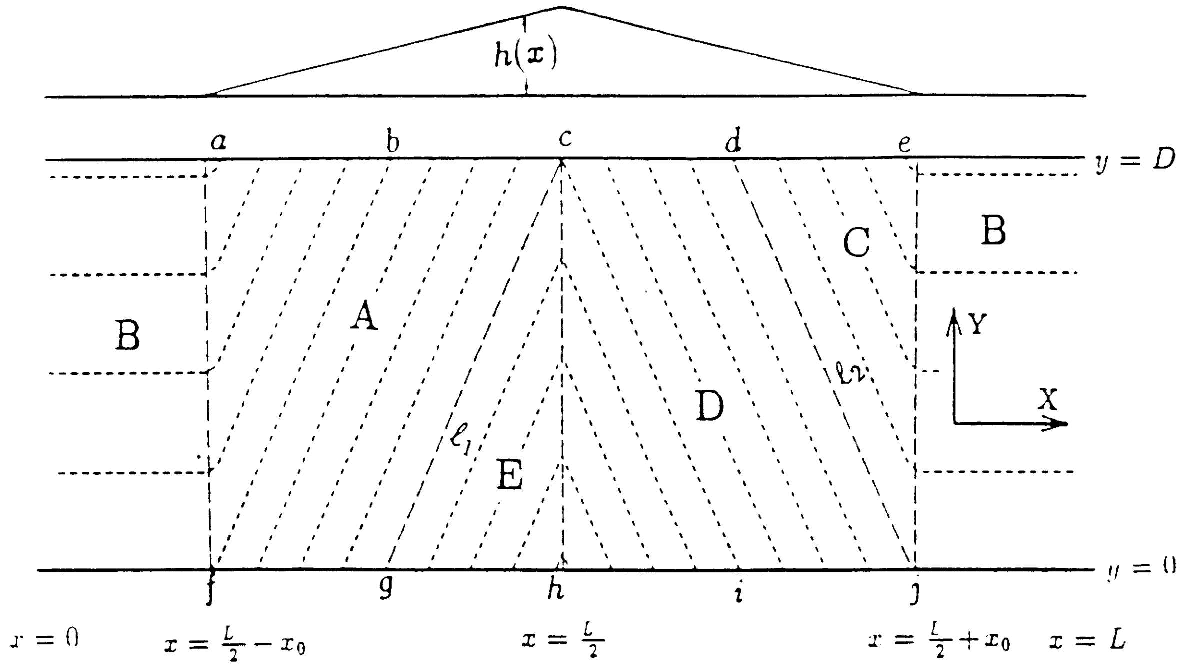

Figure 5.6: Schematic view of the model domain. On top is the profile of the ridge. Short dashed lines are the geostrophic contours, while long and heavy dashed lines are the boundaries of the various subdomains.

Integrating (5.4), (5.5) and (5.6), we have

$$\begin{aligned}\frac{f}{H-h(x)} &= \frac{f_N}{H-h(x_s)},\\ s &= \frac{f_N^2 - f^2}{2\alpha\beta q^2},\\ \zeta &= -\frac{f^2 - f_N^2}{2\alpha\beta g}w_s,\end{aligned}$$

with $\alpha \equiv h_0/x_0$. Along segment $f-g$ an equivalent western boundary layer is needed to close the circulation.

In region B except the north and south boundaries, the governing equation becomes

$$\frac{\partial\zeta}{\partial x} = \frac{f^2}{gH\beta}w_s,$$

with the boundary condition

$$\zeta|_{x=L/2-x_0} = -\frac{f^2 - f_N^2}{2\alpha\beta g}w_s.$$

The solution is

$$\begin{aligned}\zeta &= \frac{f^2}{gH\beta}w_s(x-L/2+x_0) - \frac{f^2 - f_N^2}{2\alpha\beta g}w_s \quad \text{for } 0 \le x \le L/2-x_0;\\ \zeta &= \frac{f^2}{gH\beta}w_s(x-3L/2+x_0) - \frac{f^2 - f_N^2}{2\alpha\beta g}w_s \quad \text{for } L/2+x_0 \le x \le L,\end{aligned}$$

and a boundary layer at each side of the channel is needed to close the circulation.

In region C, the initial conditions for the characteristic equations are

$$\begin{aligned}x|_{s=0} &= L/2+x_0,\\ y|_{s=0} &= y_s,\\ \zeta|_{s=0} &= \frac{f^2(y_s)}{gH\beta}w_s(2x_0-L) - \frac{f^2(y_s) - f_N^2}{2\alpha\beta g}w_s.\end{aligned}$$

Integrating equations (5.4), (5.5) and (5.6), we have

$$\begin{aligned}\frac{f}{H-h(x)} &= \frac{f(y_s)}{H},\\ s &= \frac{f^2 - f(y_s)^2}{2\alpha\beta q^2},\\ \zeta &= -\frac{2H^2q^2 - f^2 - f_N^2}{2\alpha\beta g}w_s - \frac{H^2q^2w_s}{gH\beta}\Delta L,\end{aligned}$$

where $\Delta L = L - 2x_0$. Along segment $d - e$ an equivalent western boundary layer is needed to close the circulation.

In region D, the initial conditions for the characteristic equations are

$$\begin{aligned} x|_{s=0} &= x_s, \\ y|_{s=0} &= 0, \\ \zeta|_{s=0} &= \zeta_0. \end{aligned}$$

Integrating equations (5.4), (5.5) and (5.6), we have

$$\begin{aligned} \frac{f}{H - h(x)} &= \frac{f_S}{H - h(x_s)}, \\ s &= \frac{f^2 - f_S^2}{2\alpha\beta q^2}, \\ \zeta &= \zeta_0 + \frac{f^2 - f_S^2}{2\alpha\beta g} w_s. \end{aligned}$$

Along segment $d - c$ an equivalent western boundary layer is needed to close the circulation.

In region E, the initial conditions for the characteristic equations are

$$\begin{aligned} x|_{s=0} &= L/2, \\ y|_{s=0} &= y_s, \\ \zeta|_{s=0} &= \zeta_0 + \frac{f(y_s)^2 - f_S^2}{2\alpha\beta g}. \end{aligned}$$

Integrating equations (5.4), (5.5) and (5.6), we have

$$\begin{aligned} \frac{f}{H - h(x)} &= \frac{f(y_s)}{H - h_0}, \\ s &= -\frac{f^2 - f(y_s)^2}{2\alpha\beta q^2}, \\ \zeta &= \zeta_0 - \frac{f^2 + f_S^2 - 2(H - h_0)^2 q^2}{2\alpha\beta g} w_s. \end{aligned}$$

Along segment $g - h$ an equivalent dynamic western boundary layer is needed to close the circulation.

Similar to the wind-driven circulation discussed in Chapter 2, flows in both regions A and D are purely zonal and discontinuities arise at the boundaries, ℓ_1 and ℓ_2, between regions A and E and regions C and D, respectively, and the explanation is similar. Across the boundary, ℓ_1, between regions A and E, the discontinuity is

$$\Delta\zeta|_{\ell_1} = \zeta_0 - \frac{f_S^2 - f_N^2}{2\alpha\beta g} w_s. \tag{5.7}$$

And across the boundary, ℓ_2, between regions D and C, the discontinuity is

$$\Delta\zeta|_{\ell_2} = -\zeta_0 - \frac{f_S^2 - f_N^2}{2\alpha\beta g} w_s - \frac{f_S^2 \Delta L}{gH\beta} w_s. \tag{5.8}$$

In addition, there are various boundary layers along both the southern and northern boundaries, which are needed to close the circulation.

With the solution above, we can compute the meridional volume flux across a latitude circle between any sections $x = x_1$ and $x = x_2$, defined as

$$T(y) = \int_{x_1}^{x_2} (H - h) v dx.$$

In regions A and D, the flow is purely zonal, thus there is no meridional flux

$$T_A(y) = T_D(y) = 0.$$

In region B, the meridional volume flux is

$$T_B = \frac{f}{\beta} \Delta L w_s,$$

which is always southward for $w_s > 0$. In region C, the meridional volume flux is

$$T_C = -\frac{2(f - f_S)}{\beta} \Delta L w_s - \frac{2(f - f_S)}{\alpha\beta} H w_s,$$

which is again always southward. In region E, the meridional volume flux is

$$T_E = \frac{2(f - f_N)}{\alpha\beta} (H - h_0) w_s,$$

which is also southward. So, the only places the flow goes northward are along ℓ_1 and ℓ_2. The northward volume flux along ℓ_1 is

$$T_{\ell_1} = -\frac{f_S^2 - f_N^2}{2\alpha\beta f_N}(H - h_0)w_s + g\zeta_0\frac{H - h_0}{f_N}, \tag{5.9}$$

which could be northward or southward, depending upon ζ_0. The northward volume flux along ℓ_2 is

$$T_{\ell_2} = -\frac{f_S^2 - f_N^2}{2\alpha\beta f_S}Hw_s - g\zeta_0\frac{H}{f_S} - \frac{f_S}{\beta}\Delta L w_s.$$

Then, the total volume flux across any latitude is

$$T_0 = -w_s yL + (Q_1 + Q_2)R^{(0)} + g\zeta_0\left(\frac{H - h_0}{f_N} - \frac{H}{f_S}\right), \tag{5.10}$$

with

$$R^{(0)} = \frac{x_0}{L}\left[1 - \frac{h_c}{2h_0}\cdot\frac{\Delta h_c}{H - h_c}\right].$$

The mass balance (2.7) requires that

$$T_0 = -w_s yL + Q_1.$$

Using (5.10), one determines the unknown constant ζ_0

$$\zeta_0 = -\frac{f_N}{g\Delta h_c}\left[Q_1 - (Q_1 + Q_2)R^{(0)}\right], \tag{5.11}$$

which is critically determined by the supercriticality, Δh_c, of the ridge height.

It is readily seen that if $w_s = 0$, *i.e.*, $Q_1 + Q_2 = 0$, the solution reduces to the case discussed in section 4. In the general case with $Q_1 + Q_2 \neq 0$, the volume transport of the internal jet along ℓ_1 is

$$T_{\ell_1} = -\frac{H - h_0}{\Delta h_c}\left[Q_1 - (Q_1 + Q_2)\frac{x_0}{L}(1 + \frac{\Delta h_c}{h_0})\right],$$

noting (5.9) and (5.11). This internal current could disappear should the model parameters satisfy

$$\frac{Q_1}{Q_1 + Q_2} = \frac{x_0}{L}(1 + \frac{\Delta h_c}{h_0}).$$

Otherwise, there is always an internal jet along the geostrophic contour ℓ_1, similar to that sketched some 35 years ago by Stommel (1958). The direction, however, could be either southward if

$$\frac{Q_1}{Q_1+Q_2} > \frac{x_0}{L}(1+\frac{\Delta h_c}{h_0}),$$

or northward otherwise. Thus, for a narrow ridge with a very small x_0, the internal jet flows southward. Obviously, if $Q_1 = 0$, the internal jet always flows northward just like that sketched by Stommel (1958, his Fig. 5.2).

The volume transport of the internal jet along ℓ_2 is

$$T_{\ell_2} = \frac{H}{h_c}(1-2x_0/L)(Q_1+Q_2) + \frac{H-h_c}{\Delta h_c}\left[Q_1-(Q_1+Q_2)\frac{x_0}{L}\frac{h_c}{h_0}\frac{H-h_0}{H-h_c}\right].$$

Generally, this internal current flows northward. Fig. 5.7 shows one example of the surface dynamic topography, $\zeta(x,y)$. In this case, the internal current along ℓ_1 flows southward, while that along ℓ_2 flows northward.

Noting (5.9) and $\zeta|_D$, the zonal volume transport at $x = L/2$ is

$$T_0 = \frac{x_0}{L}\cdot\frac{h_c}{h_0}\cdot\frac{H-h_0}{H-h_c}(Q_1+Q_2) + \frac{g\zeta_0}{f_N}(H-h_0).$$

Noticing the case discussed in section 4, the second term essentially represents the total volume flux of the net through-channel recirculation driven by the buoyancy forcing, *i.e.*,

$$T_{re} = \frac{g\zeta_0}{f_N}(H-h_0) = -\frac{H-h_0}{\Delta h_c}\left[Q_1-(Q_1+Q_2)R^{(0)}\right], \qquad (5.12)$$

critically determined by Δh_c, the supercriticality of the ridge height. This through-channel recirculation could either be westward or eastward. If

$$\frac{Q_1}{Q_1+Q_2} < R^{(0)},$$

it flows eastward; otherwise it flows westward. As

$$h_0 \longrightarrow h_c,$$

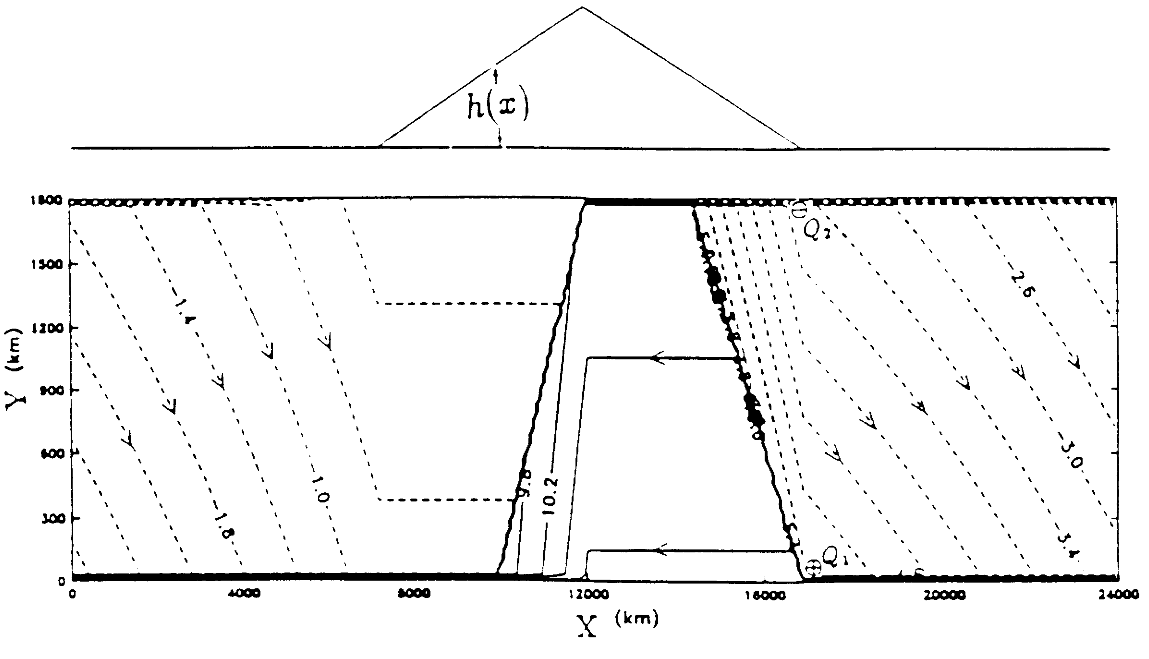

Figure 5.7: The surface dynamic topography (cm) for the case with $Q_1 = 5Sv$ and $Q_2 = -1Sv$, $D = 1800km$, $L = 24000km$, $h_0 = 1km$, $H = 3500m$, $x_0 = 4800km$ and $\theta_0 = 60°S$. Dashed (solid) lines represent the negative (positive) dynamic topography.

we have

$$T_{re} \;\rightarrow \pm\infty.$$

So for a ridge with a height close to the critical, the volume transport of the through-channel recirculation could be massive. On the other hand, as

$$h_0 \rightarrow H,$$

we have

$$T_{re} \;\rightarrow 0,$$

which approaches that in a corresponding closed basin! It is readily seen that if $Q_1 \;=\; 0$, the deep water formation at the northern boundary always drives an eastward through-channel recirculation. Generally, for a narrow ridge with $\frac{x_0}{L} \ll 1$, and $Q_1 \neq 0$, we have

$$T_{re} \;\sim\; -\frac{H - h_0}{\Delta h_c} Q_1 \;+\; o\left(\frac{x_0}{L}\right)(Q_1 + Q_2).$$

Correspondingly, the recirculation index

$$R_c \;\equiv\; |T_{re}/Q_1| \;\sim\; \frac{H - h_0}{\Delta h_c} \;+\; o\left(\frac{x_0}{L}\right),$$

which is rather similar to (4.4) for a case driven by a pair of point source and sink. So for a narrow ridge, bottom water formation in the southern boundary always drives a westward recirculation.

The discussions above show us that in this linear model, the buoyancy-driven flow can be divided into five different parts, as is shown in Fig. 5.7 for a chosen set of model parameters. The first one is the direct flow with a volume flux of $1Sv$ from the source to the sink along ℓ_2, noting Fig. 5.6. The second part with a volume flux of $4Sv$ from the point source at $(L/2 + x_0, 0)$ is carried by the horizontal flow and is lost through the uniform sink prescribed at the upper surface. The third part is the Sverdrupian gyre located on regions A, B and C, with a volume flux roughly as

$$T_{Sv} \;=\; \frac{f w_s (L - 2x_0)}{\beta} \;\approx 15Sv,$$

for the parameters chosen as those listed in Fig. 5.7. The part of the Sverdrupian gyre over region A is returned via the internal current along ℓ_1. The other two parts, similar to those in the wind-driven circulation discussed in Chapter 2, are two recirculations, which together make up the total through-channel flow with a volume flux roughly at $18Sv$. The major recirculation appears as a loop of currents. It flows along the southern boundary from point g to j, along the two $q-$contours ℓ_1 and ℓ_2 and $c-d$, noting Fig. 5.6. The minor one coalesces with the major one except over region D, where it flows as a purely westward flow. The Sverdrupian gyre is singly connected while the through-channel recirculations are multiply connected. The Sverdrupian gyre and the through-channel recirculations are rotational circulations.

Fig. 5.8 shows T_{re}/Q_1 (a), T_{ℓ_2}/Q_1 (b) and T_{ℓ_1}/Q_1 (c) for a case with $h_0 = 1000m$. First of all, the through-channel recirculation shown in (a), is always westward and the volume transport can be much larger than the bottom water formation rate at the southern boundary for a narrow ridge. Even if the ridge extends throughout the whole channel, the through-channel recirculation is still stronger than the bottom water formation at the southern boundary. Second, the flow along ℓ_2, shown in (b), is always northward and the volume transport is much stronger than the bottom water formation at the southern boundary, especially for a narrow ridge. Clearly, the ratio T_{ℓ_2}/Q_1 is usually much larger than the corresponding one in SA's model. This part roughly combines the volume of the five circulations discussed above. Third, the flow along ℓ_1, shown in (c), is generally southward except in special cases with very wide ridges and assisted by deep water formation at the northern boundary of the channel. The volume transport is again generally much stronger than the bottom water formation at the southern boundary. For a model circumpolar ocean, we estimate that $T_{\ell_1} \sim -25Sv$, $T_{\ell_2} \sim 50Sv$ and $T_{re} \sim -25Sv$ for a narrow ridge with $x_0 = 1200km$ and $h_0 = 1000m$ in a homogeneous model with $H = 3500m$, $Q_1 = 5Sv$ and $Q_2 = -1Sv$. All of them are much stronger than the bottom water formation at the southern boundary.

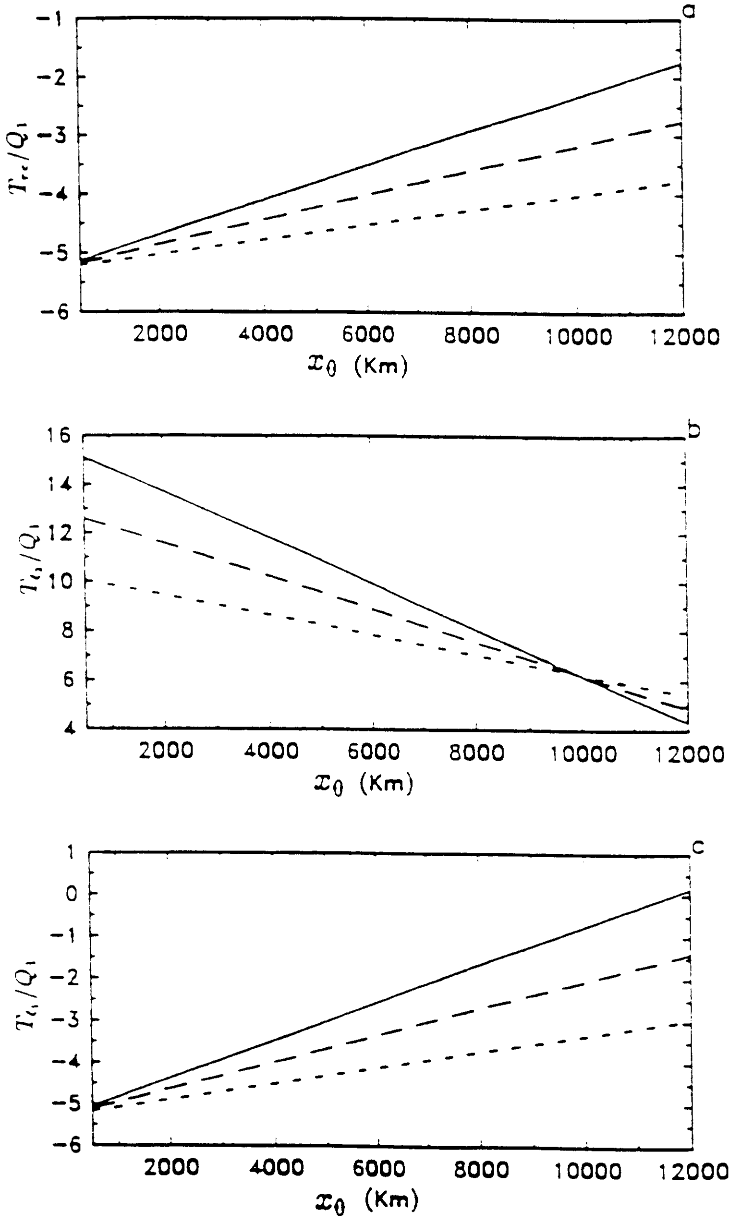

Figure 5.8: (a) T_{re}/Q_1 versus the width of the ridge. (b) T_{ℓ_2}/Q_1 versus the width of the ridge; (c) T_{ℓ_1}/Q_1 versus the width of the ridge. In all three plots, $Q_1 = 5Sv$, the solid, long and short dashed lines show the cases with $Q_2 = 2Sv$, $0Sv$ and $-2Sv$, respectively. The other model parameters are $h_0 = 1km$, $H = 3500m$, $f_S = -2\omega sin70°$, $\beta = 2\omega cos60°/a$, $L = 24000km$, $D = 1800km$.

The discussion above presumably has a very significant implication for Antarctic Bottom Water formation. The topographic feature around Drake Passage is indeed very narrow compared to the length of the circumpolar ocean. Thus, the discussions above imply that a small amount of AABW formation could drive a substantial amount of westward through-channel recirculation which is against that due to the wind stress discussed in Chapter 2. Were it not for the wind stress, we might have observed a westward flow at the Drake Passage. The observed flow at the Drake Passage is thus the sum of the through-channel recirculating flow due to the wind stress and that due to the buoyancy forcing. On the other hand, given the above estimation, the bottom water formation around the Antarctic continent is unlikely to play a major role in the momentum balance of the Antarctic Circumpolar Current as Barcilon (1966) originally thought.

5.6 Coupling the abyssal circulation in the circumpolar basin with that in the rest of the global ocean

In both Stommel's (1958) and Kuo & Veronis's (1973) schematic models of the abyssal circulation of the world oceans, the dynamic detail in the circumpolar ocean is not clear, although the circulation in the three closed basins is depicted by SA's model. In the preceding sections we have discussed the abyssal circulation in a rather idealized and isolated circumpolar basin. It is quite straightforward to couple this model circumpolar abyssal circulation with the abyssal circulation within other basins. Now let us construct a schematic picture of the global abyssal circulations in rather idealized world oceans, shown in Fig. 5.9. Suppose the deep water formation in the northern North Atlantic is Q_1 and that in the Weddell Sea is Q_2, the areas of the Atlantic, Pacific, Indian and the circumpolar oceans are S_a, S_p, S_i and S_c, respectively. The widths of the Atlantic, Pacific and Indian Oceans are L_a, L_p and L_i, respectively. In the spirit of SA, the uniform upwelling is

$$w_s = \frac{Q_1 + Q_2}{S_a + S_p + S_i + S_c}. \tag{6.1}$$

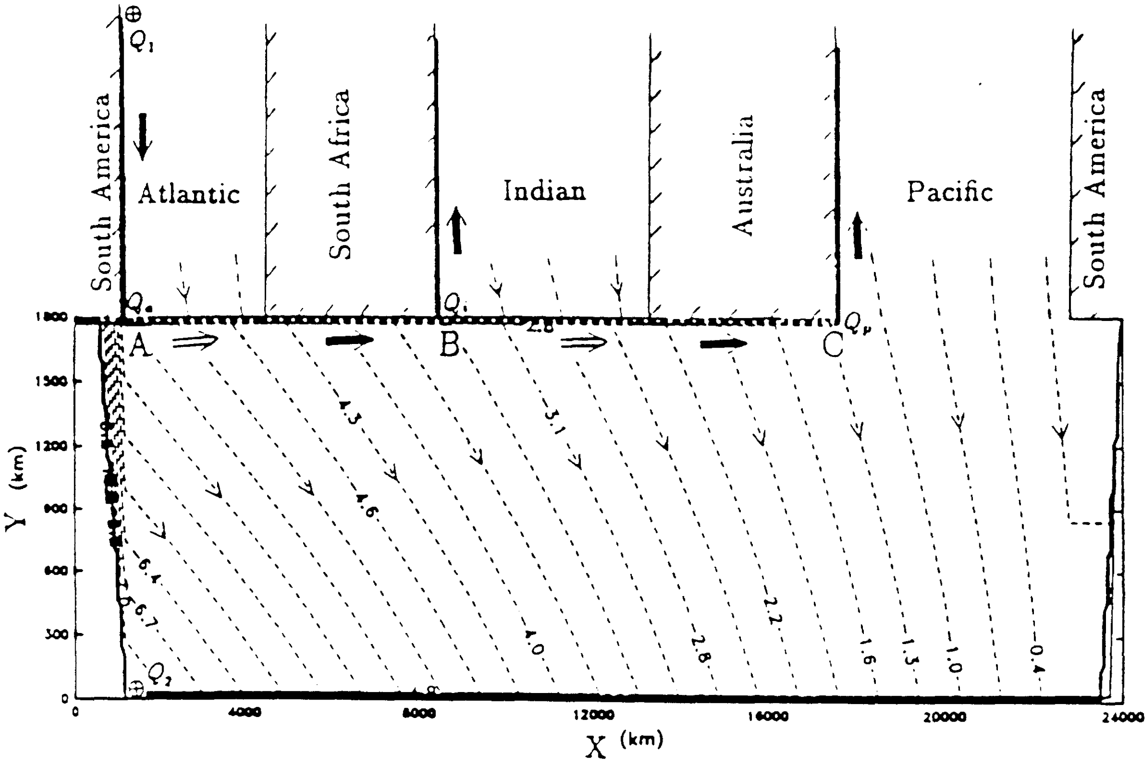

Figure 5.9: A schematic picture of the abyssal circulation in a circumpolar basin coupled with the other three major ocean basins.

Suppose that the ridge around Drake Passage is in the supercritical range. The interior planetary abyssal circulations in the three closed basins are still in the Sverdrupian regime, as were discussed by SA and Stommel (1958), while the circulation in the circumpolar ocean is the same as that discussed in the preceding section, except along its northern boundary. Thus, the linear potential vorticity balance yields

$$v = \frac{f}{\beta} w_s, \tag{6.2}$$

which is true everywhere in the global ocean basin away from topographic features and western boundary layers. From the SA model, we have three regular western boundary currents in each of the three closed ocean basins. At the northern boundary of the circumpolar basin, the volume fluxes of these three western boundary currents are

$$Q_a = Q_1 - \frac{f_N}{\beta} L_a w_s - S_a w_s, \tag{6.3}$$

$$Q_p = \frac{f_N}{\beta} L_p w_s + S_p w_s, \tag{6.4}$$

$$Q_i = \frac{f_N}{\beta} L_i w_s + S_i w_s. \tag{6.5}$$

We can view the three western boundary currents as one source (the Atlantic) and two sinks (the Pacific and Indian) for the circumpolar ocean. Then, where does the water of the deep western boundary currents for the Pacific and Indian Oceans come from? Due to the continuity of the Sverdrup balance in the ocean interior across the northern boundary of the circumpolar ocean, a northern boundary current starting from the southern boundary of South America across the model Atlantic and Indian basins as internal currents in the inviscid limit satisfies the potential vorticity balance. It only changes along the southern boundaries of the African and Australian continents. This narrow current along the northern boundary of the circumpolar ocean is needed to feed the deep western boundary currents for the Pacific and Indian Oceans. Different from that in the preceding section, the northern boundary current terminates at the western boundary of the Pacific Ocean. The schematic picture of the abyssal circulation in the model ocean is shown in Fig. 5.9.

The most prominent features of this schematic abyssal circulation are the internal boundary current along the geostrophic contours ℓ_1, ℓ_2 (see Fig. 5.6), the Sverdrupian gyre circulation downstream of the ridge, and the northern boundary current noting Fig. 5.6. The last one is consistent with the results from primitive equation models such as those of Toggweiler (personal communication) and Semtner & Chervin (1988). Their models suggest that there is an intense eastward flow starting from about the southern tip of South America, in the latitudes to the south of Africa and Australia. Due to the presence of frictional processes and transient meso-scale processes, the current in the numerical model appears to be rather wide. This northern boundary current also appeared in the schematic picture of inter-ocean water exchange discussed by Gordon (1986). The bottom water formed at the southern boundary immediately downstream of the ridge flows northward along ℓ_2 as an internal boundary current. Upon reaching the northern boundary, it splits into two parts. One part flows eastward to join the deep water from the North Atlantic at A, the eastern tip of the South American continent. The other branch flows westward along the northern boundary, then along ℓ_1 and the southern boundary. It recirculates back to the source region. The relative strength of these two branches depends critically upon the topographic parameters as discussed in the preceding section.

East of the South American continent, the bottom water from the two sources joins and flows eastward as an internal boundary current along the geostrophic contour $q = f_N/H$. While keeping its volume flux, this current is joined by water from the interior South Atlantic as the southward Sverdrupian flow but loses the same amount of water which flows southward into the circumpolar basin, as part of the southward flowing branch of the Sverdrupian gyre circulation in the circumpolar ocean. At the southern boundary of the South African continent, the current appears as a boundary current. It loses some water, due to the southward flowing Sverdrupian flow in the circumpolar basin. Upon reaching B, the eastern tip of the African continent, this eastward current branches into two parts. One part with volume flux Q_i flows northward as the deep western boundary current of the Indian Ocean. The other branch continues eastward along $y = D$. Across the

Indian Ocean, it does the same as when it crosses the South Atlantic. The only difference is that it entrains the Indian Ocean interior water to its north. As it flows eastward along the southern boundary of Australia, it does the same as along the southern boundary of the African continent. But upon reaching C, the eastern tip of Australia, it does not branch and flows northward as the deep western boundary current of the Pacific Ocean. Unlike those in both the South Atlantic and Indian Oceans, there is no mid-ocean internal boundary current within the South Pacific basin.

With the discussion in the appendix about the influence of bottom friction, this simple deep circulation scheme in the inviscid limit suggests to us that in the presence of mixing, the water masses of both the southward branch of the abyssal Sverdrupian gyre circulation in the circumpolar basin and the deep western boundary currents of the Indian and Pacific Oceans are quite complicated. In this barotropic model, the water mass of the deep western boundary current in the Indian Ocean is a mixture of water from both sources and from the interior South Atlantic and circumpolar ocean. In the Pacific, it is the combination of water from both sources and from the interior South Atlantic, Indian and circumpolar oceans. The water mass of the southward flowing branch of the abyssal Sverdrupian gyre circulation changes eastward. Flowing from the longitudes of both the South Atlantic and South Africa, it is a mixture of the deep water from the two sources and the interior South Atlantic. Flowing from the longitudes of both the Indian Ocean and Australia, it is the mixture of the deep waters from the two sources and the interior South Atlantic and Indian Ocean. Flowing from the longitudes of the Pacific, however, it consists purely of interior South Pacific water.

5.7 Discussion and conclusion

The classical SA model in a closed basin is applied to a circumpolar basin in the presence of sufficiently high ridges. The planetary geostrophy is assumed in the interior of the

β–plane channel. We begin with abyssal circulations driven by a point source and sink. In the first three cases with the forcing at the same side of the channel, there is neither net cross-channel geostrophic volume transport nor through-channel flow, although the flow passages are quite complicated compared with the similar case in a closed basin discussed by Stommel *et al.* (1958). For these three cases, actually, supercriticality of the ridge height is not necessary in the discussion. In the case with the point source and sink placed at different sides of the channel, supercriticality of the ridge height is both sufficient and necessary in order to support a net geostrophic volume flux across the channel. In this case, besides the divergent flow from the point source to the point sink, a through-channel recirculation is generated, which is a rotational flow. Its volume flux is critically controlled by the potential vorticity resistance, *i.e.*, the supercriticality of the ridge height. This is very similar to the wind-driven circulation. In this sense, the buoyancy forcing is very similar to the wind forcing. Near the critical state, this recirculation can be very strong compared with the source to sink flow. Only for a sufficiently high ridge will the recirculation be smaller than the source to sink flow. The recirculation is westward (eastward) for a case with a source (sink) at the southern boundary. As the ridge height extends to the surface of the water, the volume transport of the through-channel recirculation vanishes, *i.e.*, the circulation pattern converges to that in a corresponding closed basin.

Then, in the spirit of SA, we consider a model of the circumpolar abyssal circulation driven by a uniform sink prescribed at the surface and two point sources at each side of the channel immediately downstream of the ridge. The one at the southern boundary presumably mimics the bottom water formation in the Weddell Sea. On the other hand, the one at the northern boundary presumably represents the net deep water exchange between the circumpolar ocean and the rest of the world oceans. In the case with a ridge of a supercritical height which crudely simulates the dynamic effect of the topography around Drake Passage, the classical SA model in a closed basin applies with significant modifications. *First*, the interior southward Sverdrupian flow is returned northward via an internal boundary current along a critical geostrophic contour over the ridge, rather than through some equivalent western boundary current such as that in the SA model. This demonstrates the importance of the supercriticality of the ridge height. In the case with a supercritical ridge, there are geostrophic contours which run from the southern boundary to the northern boundary over the ridge. So, although a strong internal jet across $q-$contours is prevented by potential vorticity conservation, strong along $q-$contour flow is allowed. As the model demonstrates, the $q-$contours connecting the two boundaries provide the flow passages for the return of the interior basin predominantly southward Sverdrupian flow. *Second*, besides the interior singly connected Sverdrupian gyre circulation like that in the SA model, there is a through-channel recirculation, which is multi-connected. Its direction depends upon the model parameters. And its magnitude depends critically upon the supercriticality of the ridge height, in a way similar to that in the wind-driven circulation.

In our linear homogeneous model, the volume transports of both the internal boundary current and the through-channel recirculation could be much higher than the bottom water formation rate at the southern boundary of the channel, while in the classical SA model, the largest ratio of the deep western boundary current versus the deep water formation is 2. Only for a sufficiently high ridge will the volume transport of the through-channel recirculation be weaker than the bottom water formation rate at the southern boundary. For a narrow ridge such as that around Drake Passage, the through-channel recirculation will always flow westward with bottom water formation, such as the Weddell Sea bottom water formation, at the southern boundary. As the ridge extends to the whole water column, the buoyancy-driven circulation approaches that in a corresponding closed basin. This simple model suggests that the Antarctic Bottom Water formation in the Weddell Sea could drive a substantial westward through-channel flow, which could have been observed were it not for the wind-driven eastward through-channel flow. The observed eastward flow is thus the sum of these two flows, which suggests that the purely wind-driven through-channel volume transport at Drake Passage could be substantially higher than what is observed now. On the other hand, because the buoyancy-driven through-channel flow is substantially weaker than the wind-driven one, the AABW formation does not play a first order role in the overall momentum balance of the Antarctic Circumpolar Current. This indicates that only the topographic form drag discussed in Chapter 2 plays a vital role in the overall momentum balance of the ACC.

Then, assuming that the height of the ridge around the Drake Passage is within the supercritical range, the abyssal circulation in the circumpolar basin is coupled with those in the rest of the world oceans in a highly idealized model. The coupling does not affect the circulation pattern obtained from the isolated case except the circulation along the northern boundary of the circumpolar ocean. The most prominent feature is the eastward boundary current along the northern boundary of the circumpolar ocean, through which all ocean basins in the Southern Ocean are connected. This current entrains interior water from both the South Atlantic and Indian Oceans as it flows eastward. It loses water to the deep western boundary currents of the Indian and Pacific Oceans and the southward flowing branch of the abyssal Sverdrupian gyre circulation in the circumpolar basin. This current terminates at the western boundary of the South Pacific. The model shows us that the deep western boundary current of the Indian Ocean is composed of waters from the two sources and the interior South Atlantic Ocean, while that of the Pacific Ocean is from the two sources and the interior South Atlantic and Indian Oceans. The water mass of the southward flowing branch of the recirculation consists of waters from the two sources and the South Atlantic, Indian and South Pacific interiors.

In this chapter we have demonstrated the critical importance of a supercritical ridge in the buoyancy-driven circulation in a $\beta-$plane channel. First, all geostrophic contours in the channel are blocked by the lateral boundaries, just like those in a closed basin, albeit in a different form. Second, the two lateral boundaries are connected by some blocked geostrophic contours, while in the case with a subcritical ridge, the two lateral boundaries are separated by the nonblocked geostrophic contours. In the realistic circumpolar ocean, both topographic features and buoyancy forcing are much more complicated. And the model discussed here is not intended to be a realistic description of the deep-ocean circulation in the Southern Ocean. The most notable simplification is the barotropic assumption. It does not allow any layered deep flow, which happens most spectacularly in the South Atlantic where AABW flows northward beneath the southward flowing North Atlantic Deep Water. Nevertheless, the circulation scheme obtained is dynamically consistent although the model is extremely idealized. We believe two conclusions from the model have important implications for the realistic Southern Ocean. First, the model suggests that the AABW could drive a substantial amount of westward flow which could balance some part of the eastward flow driven by the wind stress, but it does not play a zeroth order role. Second, along the northern boundary of the circumpolar ocean, there is a strong, narrow current which connects all the oceanic basins in the Southern Ocean. It is part of the buoyancy-driven global conveyor belt as discussed by Gordon (1986). In the next chapter we will show that wind stress could also drive a strong inter-basin water mass exchange among the different basins in the Southern Ocean.

Appendix

The influence of a small finite bottom friction

In *Case I* of section 3, the discussion is carried out in the inviscid limit. In that case, the only places where cross $q-$contour flow is allowed are the two equivalent western boundary layers. In the presence of a finite albeit weak bottom friction, however, cross $q-$contour flow can be induced by the weak bottom friction through the entire flow passage, although it could be very weak away from the two equivalent western boundary layers. In the discussion on the wind-driven circulation by Wang (1993a), it was shown that because of the long route of the internal current, even a weak friction could have a profound effect on the circulation, and the circulation in the presence of a weak and finite friction could be substantially different from that obtained in the inviscid limit. Now let us look at how a weak and finite bottom friction could affect the circulation scheme of *Case I*. The discussion for other cases is similar. In the presence of bottom friction, the linear governing equation away from the point source/sink is

$$J\left(\zeta, \beta y + \frac{f_0}{H} h\right) = -\kappa \nabla^2 \zeta, \tag{A.1}$$

where κ is the bottom frictional coefficient. q is further linearized to $(\beta y + \frac{f_0}{H} h)/H$ for the sake of algebraic simplicity, because the following discussion is a scale analysis only. In the inviscid limit, the thickness of the internal current emanating from the point source to the point sink is vanishingly small. In the presence of a finite bottom friction, however, this thickness will grow from the source to the northern equivalent western boundary layer shown in Fig. 5.1 in light of the discussion by Wang (1993a). From the discussion there, by the time the internal current along ℓ_2 reaches the northern boundary again, its characteristic thickness grows to

$$\delta \sim \sqrt{\delta_S (L - 2x_0)} + 2\sqrt{\delta' L'}, \tag{A.2}$$

where $\delta_S = \kappa/\beta$ is the Stommel boundary layer thickness, $\delta' = \kappa/\sqrt{\beta^2 + \alpha^2}$ is the modified Stommel boundary layer thickness, $\alpha = |f_0| h_0 / H x_0$, and

$$L' = \sqrt{(x_1 - L/2 + x_0)^2 + D^2 h(x_1)^2 / h_c^2}$$

is the length of the jet over the ridge emanating from the source. The distance between ℓ_1 and ℓ_2 is

$$\delta_0 = \frac{h_c x_0}{\sqrt{D^2 h_0^2 + h_c^2 x_0^2}} (x_1 - x_2). \tag{A.3}$$

The condition that $\delta \sim \delta_0$ is

$$\kappa \sim \kappa_0 = \delta_0 \left[\sqrt{(L - 2x_0)/\beta} + 2\sqrt{L'/\sqrt{\beta^2 + \alpha^2}} \right]^{-1}. \tag{A.4}$$

So, if κ is small enough such that $\kappa \ll \kappa_0$, then the characteristic thickness of the current along ℓ_1 and ℓ_2 is much less than the distance between them and the cross q−contour flow occurs predominantly within the northern equivalent western boundary layer. In this case, the circulation pattern shown in Fig. 5.1 will be affected very little by the presence of the bottom friction and the buoyancy-driven circulation is essentially in the inviscid limit. On the other hand, if $\kappa \sim \kappa_0$ or even larger, then the presence of the bottom friction will have a fundamental influence on the circulation pattern shown in Fig. 5.1. In that case, because $\delta \geq \delta_0$, the cross q−contour flow has occurred before the current along ℓ_2 reaches the northern equivalent western boundary. In this case, the buoyancy-driven circulation is essentially diffusive and is fundamentally different from that in the inviscid limit shown in Fig. 5.1.

Chapter 6

How is the northward surface Ekman drift out of the circumpolar ocean returned?

6.1 Introduction.

In Chapters 2, 3 and 4, the wind-driven circulation in a $\beta-$plane channel is discussed from the viewpoint of momentum balance in quasi-geostrophic models. In considering the momentum balance, there is no communication between the circulations in the circumpolar ocean and those in the subtropical basins. In this chapter, we want to look at the wind-driven circulation in the $\beta-$plane channel from the viewpoint of mass balance. The question we want to address is how the northward surface Ekamn drift in the circumpolar zone, which is clearly present in the FRAM model simulation as shown by Saunders & Thompson (1993), is returned.

So far, most of the discussions of water masses have been primarily concentrated on those below the surface Ekman layer, to name a few examples, Worthington (1981) and Warren (1981) from an observational point of view and Cox (1989) from a numerical point of view. Much attention has been paid to the North Atlantic Deep Water and Antarctic Bottom Water formation and those various associated deep western boundary current transports. Little attention has been paid to the question associated with the surface Ekman flux. From an observational point of view, Wunsch and his co-workers, e.g., Wunsch & Grant (1982) and Wunsch (1984), included the surface Ekman flux in their inverse calculation. Thus the surface Ekman flux is involved in the overall general circulation of the ocean. From the theoretical point of view, Pedlosky (1967) and Csanady (1986) discussed a simple model of the circulation associated with the surface Ekman drift in a closed basin. Based on the model used, the circulation scheme is quite simple. As Csanady (1986) demonstrated, the surface Ekman layer picks up water from the subpolar gyre and drops it in the subtropical gyre. To close the circulation, there is a northward flow within the western boundary layer across the inter-gyre boundary from the subtropical gyre to the subpolar gyre along the western boundary. In this process, the western boundary plays a vital role to close the circulation.

In the latitudes of the circumpolar ocean, roughly between $56°S$ and $62°S$, there is no meridional boundary to support the western boundary layer current, a vital part in the Csanady model (1986). The surface Ekman drift present regardless of any geometry is about $30Sv$ as suggested by the recent data set compiled by Trenberth *et al.* (1990). It is northward and out of the circumpolar ocean. This volume flux is even larger than the North Atlantic Deep Water formation, and much larger than the Antarctic Bottom Water formation. How this amount of water is returned to the circumpolar ocean is of great interest to understand the overall large scale circulation in the Southern Ocean. In the numerical study carried out by Toggweiler & Samuels (1992), they tied this northward surface Ekman flux to the North Atlantic Deep Water formation. They argued that due to the fact that there are no north-south continental barriers, there can be no net meridional geostrophic flow across the latitude band of Drake Passage in the upper layer. Net meridional geostrophic flow is only possible at depths below the sill connecting South America and Antarctica. They argued that it is this deep southward flow that upwells and compensates for the water loss due to the Ekman sucking to the surface Ekman layer in the circumpolar ocean.

In the source-sink-driven circulation discussed in Chapter 5, it was shown that in the presence of a sufficiently high ridge, geostrophic flow in a $\beta-$plane channel can support a net meridional volume flux. Therefore, there is no geostrophic constraint in the circumpolar zone in the barotropic model. In the wind-driven circulation discussed in Chapters 2, 3 and 4, a quasi-geostrophic and depth integrated form of the circulation is discussed. As Stommel (1955) pointed out, this powerful technique of dealing solely with the vertical integral of the horizontal velocity often hides important details, notably the marked difference between the wind drift in a surface Ekman layer and the geostrophic regime below. It is the purpose of this chapter to see what happens if we partition the flow in the Southern Ocean into the surface Ekman layer and a geostrophic flow in the lower layer. As we will see, through this way a very simple plausible explanation for the circulation associated with the surface Ekman drift leaving the circumpolar ocean emerges. What is more interesting is that unlike that in the Q-G model discussed in Chapters 2, 3 and 4, circulations in the Southern Ocean are connected by this wind-driven surface Ekman drift. This presumably can lead to a strong inter-basin water mass exchange among the different oceanic basins in the Southern Ocean as discussed by Gordon (1986).

Consider two layers of homogeneous fluid. The upper layer with infinitesimal thickness is the surface Ekman layer which carries all the Ekman flux. Below this surface Ekman layer is a layer of homogeneous water extending to the bottom. The model domains are shown in Figs. 6.1 and 6.2. The length and width of the circumpolar ocean are L and D, respectively. The meridional width of the subtropical ocean is also assumed to be D. For algebraic simplicity of the discussions in sections to follow, the wind stress (τ_x, τ_y) is chosen to be in the form of

$$\tau_x = \tau_0 \frac{f}{f_0} \left(1 - cos\frac{\pi y}{D}\right), \qquad \tau_y = 0. \tag{1.1}$$

f is the Coriolis parameter, f_0 is the mean. In the circumpolar area, meridional structure of the wind stress chosen above looks somewhat similar to that shown in Fig. 1.3. At each latitude, this wind stress drives a zonally uniform northward Ekman flux in the surface

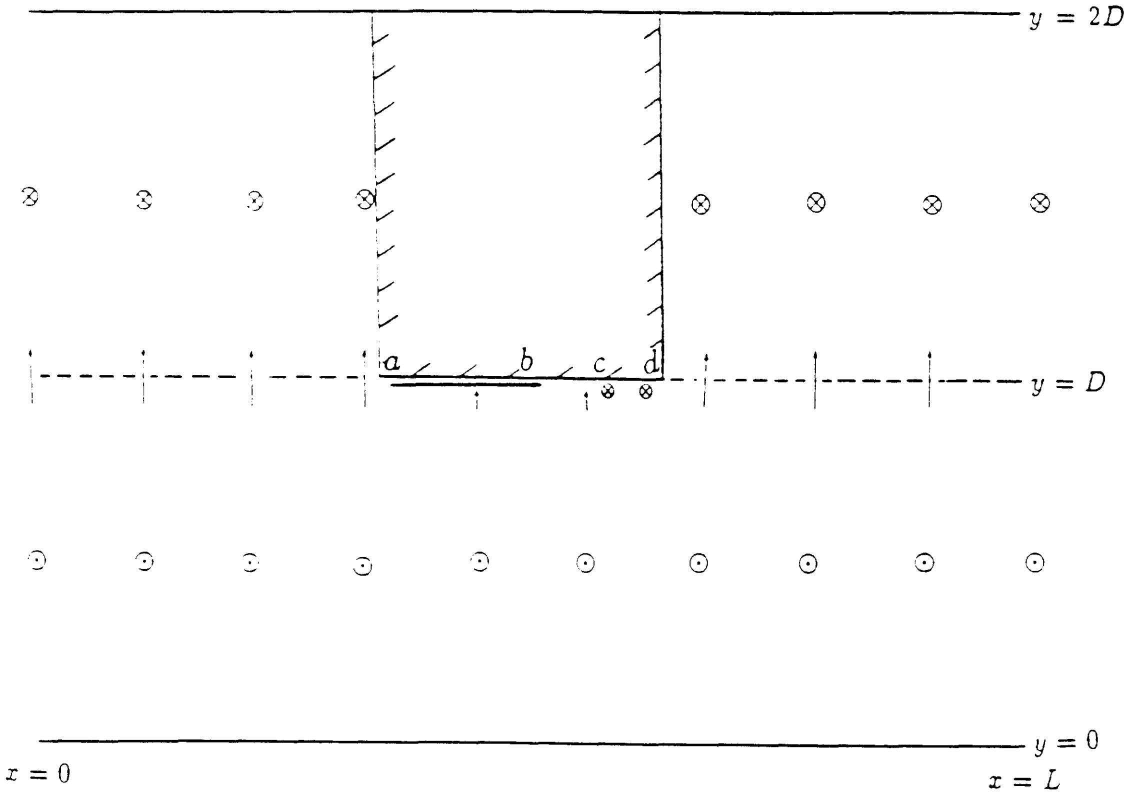

Figure 6.1: Schematic view of the circulations in the surface Ekman layer. Thin solid arrows represent the Ekman drift. Heavy solid arrow represents a boundary layer current along the southern coast of the South American continent. Cross within a circle represents downwelling Ekman pumping, while dot within a circle upwelling Ekman pumping.

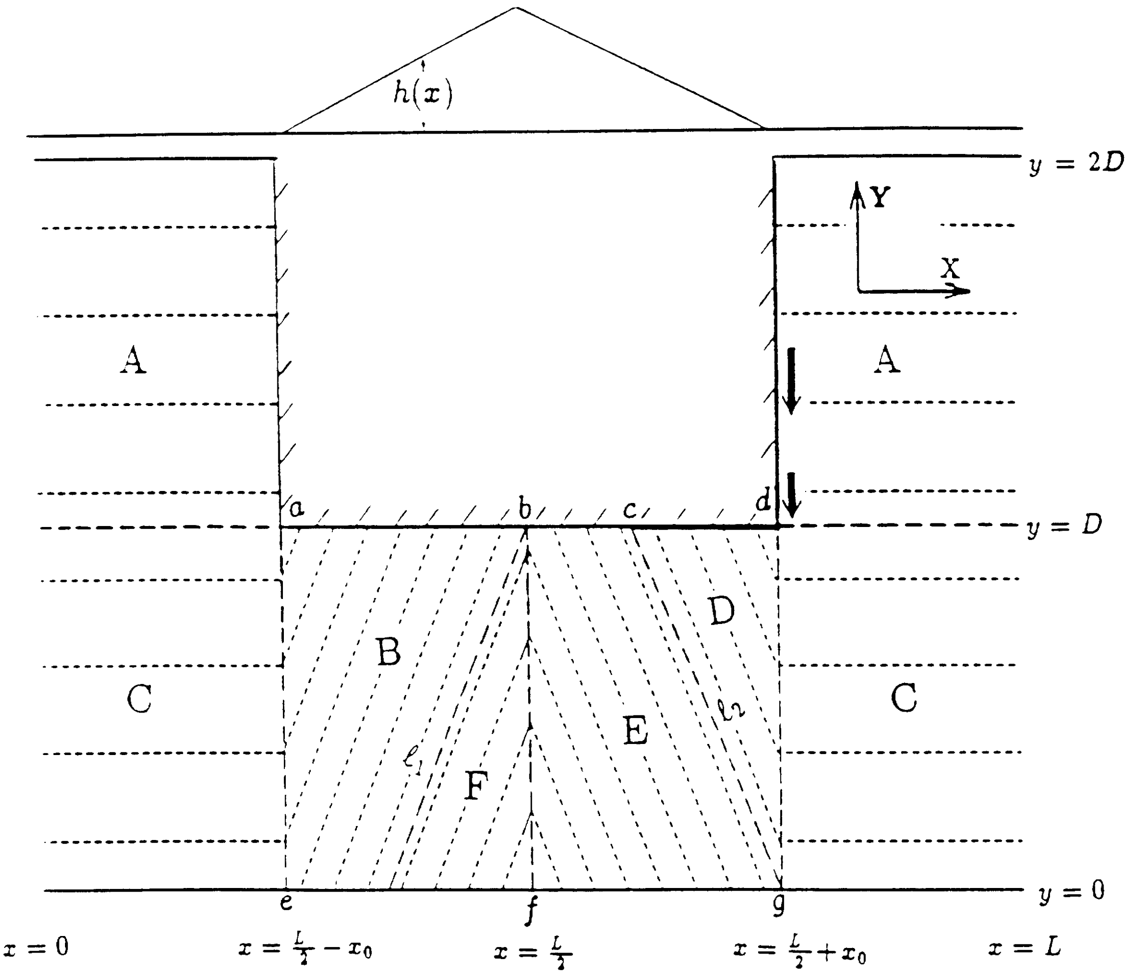

Figure 6.2: Schematic view of the model domain in the supercritical state. Dashed lines are the geostrophic contours, heavy dashed ones are the boundaries of the subdomains of A, B, C, D, E and F. On top is the profile of the ridge. Heavy solid lines are the various regular or equivalent western boundary currents needed to close the circulations.

Ekman layer with volume flux

$$T_{Ekman} = -\frac{\tau_0 L}{\rho_0 f_0}\left(1 - cos\frac{\pi y}{D}\right), \qquad (1.2)$$

where ρ_0 is the mean water density. At the northern boundary of the circumpolar ocean, one has

$$T_{Ekman}|_{y=D} = -2\frac{\tau_0 L}{\rho_0 f_0} \approx 28Sv$$

for $\rho_0 = 1.03 \times 10^3 kg/m^3$, $\tau_0 = 0.08N/m^2$, $L = 2.4 \times 10^7$ and $f_0 = 1.3 \times 10^{-4}s^{-1}$, which is comparable to that obtained by Trenberth *et al.* (1990) from the wind stress data. Through this Ekman flux, the surface Ekman layer in the circumpolar area with $0 \le y \le D$ loses water to the subtropical area with $D \le y \le 2D$. Then, how is this water compensated in the Ekman layer? To balance the water mass in the Ekman layer, in the subtropical area the Ekman layer pumps water down to the homogeneous layer below at the rate of

$$w_e = w_0 sin\frac{\pi y}{D}, \qquad (1.3)$$

where $w_0 = -\pi\tau_0/\rho_0 f_0 D$. w_e just compensates for the water gained across the northern boundary of the circumpolar ocean due to the northward surface Ekman flux. In the circumpolar area, the Ekman layer sucks water from the homogeneous layer of water below at the rate of w_e, which just compensates the water loss in the Ekman layer through the northern boundary of the circumpolar ocean. Through the Ekman downwelling, the lower layer in the subtropical area gains water, while the circumpolar area loeses water. This raises several questions for the mass balance in the lower layer. For the subtropical area, there should be ways to get rid of the amount of water from the Ekman layer, while for the circumpolar area, there are two questions. First, it has to get the same amount of water from somewhere. Second, there should be a net southward mass flux

$$T_{lower} = \frac{\tau_0 L}{\rho_0 f_0}\left(1 - cos\frac{\pi y}{D}\right), \qquad (1.4)$$

across each latitude of the circumpolar ocean to supply the water lost to the surface Ekman layer in the interior circumpolar ocean. In light of the discussions by Csanady (1986), the simplest possible explanation to the question for the subtropical area and the first question for the circumpolar area is quite straightforward. The amount of water gained in the subtropical area flows southward as a western boundary current across the inter-gyre boundary at $y = D$ to the circumpolar ocean, represented by the heavy arrow in Fig. 6.2. This is because the northward Ekman flux downwells in the subtropical gyres from the surface Ekman layer to the homogeneous layer below and is carried westward into the western boundary layer, and this water has to return to the circumpolar area where it will be picked up by the Ekman layer through the Ekman sucking. It is the second question concerning the circumpolar ocean that needs to be closely examined. The fundamental issue is that in the presence of bottom topography will geostrophic flow in a $\beta-$plane channel support a net southward volume flux in the form of (1.4)? Furthermore, in the case with multiple basins such as the Southern Ocean, what is the circulation associated with the surface Ekman drift?

6.2 The linear homogeneous model

To answer the questions raised in the preceding section, planetary geostrophy is assumed here. Away from boundary layers, with conventional notations, the linear momentum equations are

$$-fv = -g\frac{\partial \zeta}{\partial x}, \tag{2.1}$$

$$fu = -g\frac{\partial \zeta}{\partial y}, \tag{2.2}$$

where ζ is the deviation of the free surface of the lower layer from the mean. This homogeneous layer of water below the surface Ekman layer is forced above by the Ekman pumping, w_e, as required by mass balance. The linear mass conservation equation is

$$\frac{\partial (H-h)u}{\partial x} + \frac{\partial (H-h)v}{\partial y} = -w_e(y), \tag{2.3}$$

where H and h represent the mean water depth and the bottom topography, respectively. For simplicity as we did in the preceding chapters, we again choose the bottom topography

$h(x,y)$ as

$$h(x,y) \;=\; \begin{cases} h_0(1-|\frac{L/2-x}{x_0}|) & \text{if } |L/2-x| \;\le\; x_0; \\ 0 & \text{otherwise,} \end{cases} \tag{2.4}$$

where x_0 is the half width of the ridge. Isolated topographic features are of no interest to us here. (2.1), (2.2) and (2.3) lead to the following linear potential vorticity equation

$$J(\zeta,q) \;=\; \frac{q^2}{g}w_e, \tag{2.5}$$

where q is the linear potential vorticity defined as

$$q \;=\; \frac{f}{H-h}. \tag{2.6}$$

Similar to the linear Q-G model, in this linear planetary geostrophic model, potential vorticity of each fluid particle is solely determined by its position, and $q = \mathit{constant}$ defines the geostrophic contours of this linear model. The mass conservation (2.3) requires a southward mass transport by the geostrophic flow

$$\overline{(H-h)v}^{x} \;=\; T_{lower}/L, \tag{2.7}$$

at each latitude in the circumpolar area with $0 < y < D$, where

$$\overline{Z}^{x} \;\equiv\; \frac{1}{L}\int_0^L Z dx.$$

This southward volume flux exactly balances the northward surface Ekman flux and feeds the Ekman sucking in the interior circumpolar ocean, thus maintaining the mass balance in the lower layer and Ekman layer as well. In the absence of any bottom topographic features, it is quite clear from (2.1) that one always has

$$\overline{v}^{x} \;=\; 0,$$

in this linear model because of the periodicity for $\zeta(x,y)$. In this case, geostrophic flow in the lower layer can not support any net meridional volume transport in the circumpolar area. Any net meridional volume transport there has to be carried out through other physical processes, such as the surface and bottom Ekman boundary layers discussed by Hide (1968). Thus, the assumption of a two-layer fluid with Ekman layer on top of an inviscid fluid is invalid. In the presence of bottom topography, however, even though one still has $\overline{v}^x = 0$, but $\overline{(H-h)v}^x$ may not necessarily be zero, *i.e.*, geostrophic flow in the circumpolar ocean may be able to support a net meridional volume flux as is demonstrated in Chapter 5.

So long as we can see from (2.5), the discussion in terms of the geostrophic contours in Chapter 5 for the source-sink-driven flow holds equally well here for the Ekman pumping-driven flow. So in this chapter, we will follow the same approach developed there. For the source-sink driven flow, in the case with a very low ridge there is no solution in the inviscid limit. In the case with a sufficiently high ridge, however, there is a solution in the inviscid limit. In the absence of any topographic features, the geostrophic contours $q = constant$ are straight zonal lines and close themselves. So the two lateral boundaries are separated by these geostrophic contours. In the presence of a ridge in the form of (2.4), however, some of the geostrophic contours will strike either the southern or northern boundary. Nevertheless, for a ridge with $h_0 < h_c$, all of the geostrophic contours

$$q = \frac{f_S + \beta y_0}{H},$$

with $0 \leq y_0 < DH(h_c - h_0)/h_c(H - h_0)$ will strike neither the southern nor the northern boundary, they close themselves. $f_S = f|_{y=0}$ and h_c is defined as

$$h_c = -\frac{\beta D}{f_S} H.$$

In this case, the southern and northern boundaries of the circumpolar ocean are still separated by those unblocked geostrophic contours. Free solutions exist along these unblocked geostrophic contours in the inviscid limit. In this case, net meridional volume flux across these unblocked geostrophic contours has to be carried out by other physical process, such as the bottom Ekman flow discussed by Hide (1968). For a ridge with $h_0 > h_c$, however, all geostrophic contours in the channel are blocked by the lateral boundaries, and the southern and northern boundaries of the circumpolar ocean are connected by some geostrophic contours. Fig. 6.2 shows such an example, where ℓ_1 and ℓ_2 are two geostrophic contours connecting the two lateral boundaries of the circumpolar ocean. In this case, any movement in the channel has to be externally forced. Correspondingly, h_c is defined as the critical height, and the case with $h_0 > (<) h_c$ will be called the supercritical (subcritical) state. With discussion similar to that of the wind-driven circulation discussed in Chapter 2, segments $a-b$ (see Fig. 6.2) along the northern boundary and $f-g$ along the southern boundary are the two equivalent eastern boundaries. On the other hand, segments $b-d$ along the northern boundary and $e-f$ along the southern boundary are the two equivalent western boundaries. This is true regardless of the ridge height. In the subtropical gyre area, the conventional Sverdrupian dynamics applies, and $\zeta(x,y)$ has to be prescribed along the equivalent eastern boundaries. Without losing any generality, we can set the boundary condition along the western coast of the meridional barrier in the subtropical region and the northern equivalent eastern boundary $a-b$ as

$$\zeta(x,D)|_{a-b} \;=\; 0.$$

The boundary condition along the southern equivalent eastern boundary $f-g$ as

$$\zeta(x,0)|_{f-g} \;=\; \zeta_0.$$

This boundary condition can not be set arbitrarily and has to be determined through the mass balance (2.7). Thus, we have completed the model for the interior geostrophic regime. In the next section we will use this model to find the solution for the interior geostrophic regime and discuss the model circulation in the supercritical state. One will see that both the method and the solution are rather similar to the source-sink-driven circulation and correspond rather well with the wind-driven circulation in the parallel quasi-geostrophic models discussed in Chapter 2.

6.3 The circulation in the case with a single subtropical oceanic basin

To solve the potential vorticity equation (2.5), let us introduce a characteristic variable s such that

$$\frac{dx}{ds} = \frac{\partial q}{\partial y}, \tag{3.1}$$

$$\frac{dy}{ds} = -\frac{\partial q}{\partial x}. \tag{3.2}$$

The geostrophic contours serve as the characteristics and the governing equation is then converted to

$$\frac{d\zeta}{ds} = \frac{q^2}{g} w_e, \tag{3.3}$$

away from the equivalent western boundaries. For the convenience of characteristic integration, the model domain has been divided into subdomains A, B, C, D, E, F. For different regions, we have different initial conditions. The only difference between this model and that discussed in Chapter 5 is that here w_e is a function of y.

In region A, the conventional Sverdrupian dynamics applies. The governing equation (2.5) reduces to

$$\frac{\partial \zeta}{\partial x} = \frac{f^2}{gH\beta} w_0 sin\frac{\pi y}{D},$$

with the eastern boundary condition

$$\zeta|_{x=L/2-x_0} = 0.$$

The solution is

$$\begin{aligned} \zeta|_A &= \frac{f^2}{gH\beta} w_0 (x - L/2 + x_0) sin\frac{\pi y}{D} \quad \text{for } 0 \le x \le L/2 - x_0, \\ &= \frac{f^2}{gH\beta} w_0 (x - 3L/2 + x_0) sin\frac{\pi y}{D} \quad for \ \ L/2 + x_0 \le x \le L. \end{aligned}$$

In region B, the initial conditions for the characteristic equations are

$$\begin{aligned} x|_{s=0} &= x_s, \\ y|_{s=0} &= D, \\ \zeta|_{s=0} &= 0. \end{aligned}$$

Integrating (3.1), (3.2) and (3.3), we have

$$\begin{aligned} \frac{f}{H-h(x)} &= \frac{f_N}{H-h(x_s)}, \\ s &= -\frac{f^2-f_N^2}{2\alpha\beta q^2}, \\ \zeta|_B &= W_0\left(\frac{f}{\varepsilon}cos\frac{\pi y}{D} - \frac{1}{\varepsilon^2}sin\frac{\pi y}{D} + \frac{f_N}{\varepsilon}\right), \end{aligned}$$

with $f_N = f|_{y=D}$, $\alpha \equiv h_0/x_0$, $\varepsilon = \pi/\beta D$ and $W_0 = w_0/\alpha\beta g$. Along segment $e-f$ an equivalent western boundary layer is needed to close the circulation.

In region C, the governing equation becomes

$$\frac{\partial\zeta}{\partial x} = \frac{f^2}{gH\beta}w_0 sin\frac{\pi y}{D},$$

with the boundary condition

$$\zeta|_{x=L/2-x_0} = W_0\left(\frac{f}{\varepsilon}cos\frac{\pi y}{D} - \frac{1}{\varepsilon^2}sin\frac{\pi y}{D} + \frac{f_N}{\varepsilon}\right).$$

The solution is

$$\begin{aligned} \zeta|_C &= \frac{f^2}{gH\beta}w_0(x-L/2+x_0)sin\frac{\pi y}{D} + W_0\left(\frac{f}{\varepsilon}cos\frac{\pi y}{D} - \frac{1}{\varepsilon^2}sin\frac{\pi y}{D} + \frac{f_N}{\varepsilon}\right) \\ &\qquad for \quad 0 \le x \le L/2-x_0; \\ &= \frac{f^2}{gH\beta}w_0(x-3L/2+x_0)sin\frac{\pi y}{D} + W_0\left(\frac{f}{\varepsilon}cos\frac{\pi y}{D} - \frac{1}{\varepsilon^2}sin\frac{\pi y}{D} + \frac{f_N}{\varepsilon}\right) \\ &\qquad for \quad L/2+x_0 \le x \le L. \end{aligned}$$

In region D, the initial conditions for the characteristic equations are

$$x|_{s=0} = L/2+x_0,$$

$$
\begin{aligned}
y|_{s=0} &= y_s, \\
\zeta|_{s=0} &= -\frac{f(y_s)^2}{gH\beta} w_0 \Delta L sin \frac{\pi y_s}{D} + \\
W_0 &\left[\frac{f(y_s)}{\varepsilon} cos \frac{\pi y_s}{D} - \frac{1}{\varepsilon^2} sin \frac{\pi y_s}{D} + \frac{f_N}{\varepsilon} \right]
\end{aligned}
$$

where $\Delta L = L - 2x_0$. Integrating equations (3.1), (3.2) and (3.3), one has

$$
\begin{aligned}
\frac{f}{H - h(x)} &= \frac{f(y_s)}{H}, \\
s &= \frac{f^2 - f(y_s)^2}{2\alpha\beta q^2},
\end{aligned}
$$

$$
\begin{aligned}
\zeta|_D = & -W_0 \left[\frac{f}{\varepsilon} cos \frac{\pi y}{D} - \frac{1}{\varepsilon^2} sin \frac{\pi y}{D} - \frac{Hq}{\varepsilon} cos \varepsilon (Hq - f_S) + \frac{1}{\varepsilon^2} sin \varepsilon (Hq - f_S) \right] - \\
& \frac{(Hq)^2}{gH\beta} w_0 \Delta L sin \varepsilon (Hq - f_S) + W_0 \left[\frac{Hq}{\varepsilon} cos \varepsilon (Hq - f_S) - \frac{1}{\varepsilon^2} sin \varepsilon (Hq - f_S) + \frac{f_N}{\varepsilon} \right].
\end{aligned}
$$

Along segment $c-d$ an equivalent western boundary layer is needed to close the circulation.

In region E, the initial conditions for the characteristic equations are

$$
\begin{aligned}
x|_{s=0} &= x_s, \\
y|_{s=0} &= 0, \\
\zeta|_{s=0} &= \zeta_0.
\end{aligned}
$$

Integrating equations (3.1), (3.2) and (3.3), we have

$$
\begin{aligned}
\frac{f}{H - h(x)} &= \frac{f_S}{H - h(x_s)}, \\
s &= \frac{f^2 - f_S^2}{2\alpha\beta q^2}, \\
\zeta|_E &= \zeta_0 - W_0 \left(\frac{f}{\varepsilon} cos \frac{\pi y}{D} - \frac{1}{\varepsilon^2} sin \frac{\pi y}{D} - \frac{f_S}{\varepsilon} \right).
\end{aligned}
$$

Along segment $b-c$ an equivalent western boundary layer is needed to close the circulation.

In region F, the initial conditions for the characteristic equations are

$$
x|_{s=0} = L/2,
$$

$$y|_{s=0} = y_s,$$

$$\zeta|_{s=0} = \zeta_0 - W_0\left[\frac{f(y_s)}{\varepsilon}cos\frac{\pi y_s}{D} - \frac{1}{\varepsilon^2}sin\frac{\pi y_s}{D} - \frac{f_S}{\varepsilon}\right].$$

Integrating equations (3.1), (3.2) and (3.3), we have

$$\frac{f}{H-h(x)} = \frac{f(y_s)}{H-h_0},$$

$$s = -\frac{f^2 - f(y_s)^2}{2\alpha\beta q^2},$$

$$\zeta|_F = \zeta_0 + W_0\left(\frac{f}{\varepsilon}cos\frac{\pi y}{D} - \frac{1}{\varepsilon^2}sin\frac{\pi y}{D}\right) -$$

$$\left\{\frac{(H-h_0)q}{\varepsilon}cos\varepsilon\left[(H-h_0)q - f_S\right] - \frac{1}{\varepsilon^2}sin\varepsilon\left[(H-h_0)q - f_S\right]\right\} -$$

$$W_0\left\{\frac{(H-h_0)q}{\varepsilon}cos\varepsilon\left[(H-h_0)q - f_S\right] - \frac{1}{\varepsilon^2}sin\varepsilon\left[(H-h_0)q - f_S\right] - \frac{f_S}{\varepsilon}\right\}.$$

Along segment $e - f$ an equivalent dynamic western boundary layer is needed to close the circulation.

Similar to the source-sink-driven circulation, flows in both regions B and E, are purely zonal and discontinuities of the surface elevation arise at the boundaries, ℓ_1 and ℓ_2 between regions B and F and regions D and E, respectively. Discontinuity also arises at the southern boundary. The explanation is similar. Across the boundary between B and F, ℓ_1, the discontinuity is

$$\Delta\zeta|_{\ell_1} = \zeta_0 + W_0\frac{f_S + f_N}{\varepsilon}. \tag{3.4}$$

And across the boundary between D and E, ℓ_2, the discontinuity is

$$\Delta\zeta|_{\ell_2} = -\zeta_0 + W_0\frac{f_S + f_N}{\varepsilon}. \tag{3.5}$$

Across the southern boundary, the discontinuity is

$$\Delta\zeta|_{y=0} = -\zeta_0 + W_0\frac{f_S + f_N}{\varepsilon}, \tag{3.6}$$

because

$$\zeta|_{y=0^+} = \zeta_0, \quad for \quad 0 \le x < L/2 - x_0 \quad and \quad L/2 + x - 0 \le x \le L,$$

noting $\zeta|_{f-g} = \zeta_0$. These discontinuities represent internal currents of the model similar to those discussed in Chapter 2. In addition, equivalent western boundary layers along both segments $e - f$ and $b - d$ are needed to close the circulation.

With the above solution, one can compute the meridional geostrophic volume flux across a latitude circle in the circumpolar area between any $x = x_1$ and $x = x_2$, defined as

$$T(y) = \int_{x_1}^{x_2} (H - h) v dx.$$

In both regions B and E, the flow is purely zonal, and there is no meridional flux

$$T_B = T_E = 0.$$

In region C, the meridional geostrophic volume flux is

$$T_C = \frac{w_0 \Delta L}{\beta} f sin \frac{\pi y}{D},$$

which is always southward, and reaches its maximum at the middle of the circumpolar ocean. In region D, the meridional geostrophic volume flux is

$$T_D = -\frac{w_0 \Delta L}{\beta} f sin \frac{\pi y}{D} - \left(\frac{w_0 \Delta L}{\beta \varepsilon} + 2 \frac{g H W_0}{\varepsilon} \right) \left(1 - cos \frac{\pi y}{D} \right),$$

which generally flows southward. In region F, the meridional geostrophic volume flux is

$$T_F = 2 \frac{g(H - h_0) W_0}{\varepsilon} \left(1 - cos \frac{\pi y}{D} \right) - 4 \frac{g(H - h_0) W_0}{\varepsilon},$$

which always flows southward. Along ℓ_1, the geostrophic volume flux is

$$T_{\ell_1} = \frac{g(H - h_0)}{f_N} \left(\zeta_0 + W_0 \frac{f_N + f_S}{\varepsilon} \right), \tag{3.7}$$

which may or may not flow southward depending upon ζ_0. However, along ℓ_2, the geostrophic volume flux is

$$T_{\ell_2} = \frac{g H}{f_S} \left(-\zeta_0 + W_0 \frac{f_N + f_S}{\varepsilon} \right), \tag{3.8}$$

which again may or may not flow southward depending upon ζ_0. With the calculation above, the total meridional geostrophic volume flux in the interior circumpolar ocean is

$$T_{total} = \frac{\tau_0 L}{\rho_0 f_0}\left(1 - cos\frac{\pi y}{D}\right) - \frac{g\Delta h_c}{f_N}\zeta_0 - \frac{\tau_0 x_0}{\rho_0 f_0}\left[1 - \frac{h_c \Delta h_c}{2h_0(H - h_c)}\right]. \tag{3.9}$$

The mass conservation requires that the northward surface Ekman flux should be counterbalanced by the same amount of southward geostrophic volume flux in the lower layer, which gives

$$T_{total} = T_{lower}.$$

Thus, ζ_0 can be determined as

$$\zeta_0 = -\frac{f_N}{g\Delta h_c}\cdot\frac{2x_0\tau_0}{g\rho_0 f_0}\left[1 - \frac{h_c \Delta h_c}{2h_0(H - h_c)}\right], \tag{3.10}$$

which is critically determined by the supercriticality, Δh_c, of the ridge height, and is always negative noting $h_c\Delta h_c < 2h_0(H - h_c)$. Not surprisingly, in the quasi-geostrophic limit with $\beta D \ll |f_0|$ and $h_0 \ll H$, $g\zeta_0/f_0 \to \psi_0$ of the wind-driven circulation discussed in Chapter 2.

With ζ_0 determined, the geostrophic volume flux of the internal current along ℓ_1 is

$$T_{\ell_1} = -\frac{H - h_0}{\Delta h_c}\cdot\frac{2\tau_0 x_0}{\rho_0 f_0}\left(1 + \frac{\Delta h_c}{h_0}\right),$$

noting (3.7) and (3.10). This internal current always flows northward. The geostrophic volume flux of the internal jet along ℓ_2 is

$$T_{\ell_2} = \frac{H - h_0}{\Delta h_c}\cdot\frac{2\tau_0 x_0}{\rho_0 f_0}\left(1 - \frac{\Delta h_c}{h_0}\right),$$

noting (3.8) and (3.10). This internal current always flows southward. This corresponds rather well with the wind-driven circulation in the Q-G model discussed in Chapter 2.

Now let us look where the southward geostrophic volume flux in the lower layer comes from. Near the northern boundary, *i.e.*, $y \to D$, the meridional geostrophic volume fluxes in both regions C and F are vanishingly small, *i.e.*,

$$T_C,\ T_F \to 0.$$

In region D, the meridional geostrophic volume flux is

$$T_D \rightarrow -2\frac{\tau_0 L}{\rho_0|f_0|} - 4\frac{\tau_0 x_0}{\rho_0|f_0|}\left(\frac{H-h_0}{h_0}\right),$$

and

$$T_{\ell_1+\ell_2} = T_{\ell_1} + T_{\ell_2} = 4\frac{\tau_0 x_0}{\rho_0|f_0|}\left(\frac{H-h_0}{h_0}\right).$$

Therefore, near the northern boundary of the circumpolar ocean, northward flow occurs along ℓ_1, while southward flow occurs both along ℓ_2 and within region D. Furthermore, the source region for these southward flows is the equivalent western boundary at segment $c-d$ along the northern boundary of the circumpolar ocean, as is clearly shown in Fig. 6.3. This requires compensating water either from the subtropical gyre to the north or from the Ekman layer above.

With the solution $\zeta|_A$ for the subtropical gyre, one can compute the *net* westward volume flux into the western boundary layer of the subtropical gyre with $D \leq y \leq 2D$ as

$$T_W \equiv \int_D^{2D} Hu|_{x=L/2+x_0}dy = -2\frac{\tau_0(L-2x_0)}{\rho_0|f_0|}.$$

This amount of water crosses the inter-gyre boundary at $y = D$ in the same way as that in a closed basin discussed by Csanady (1986) to the equivalent western boundary layer at segment $c-d$ of the circumpolar ocean along the west coast of the meridional barrier. This water from the western boundary layer of the subtropical gyre, however, does not account for all the southward volume flux in the circumpolar ocean. Along segment $a-d$, the northward surface Ekman flow with volume flux

$$T_* = \frac{4\tau_0 x_0}{\rho_0|f_0|}$$

impinges the southern boundary of the meridional barrier (the cross-hatched area in Fig. 6.3). In the discussion here it is assumed that $x_0 \ll L$. So

$$T_* \ll T_W.$$

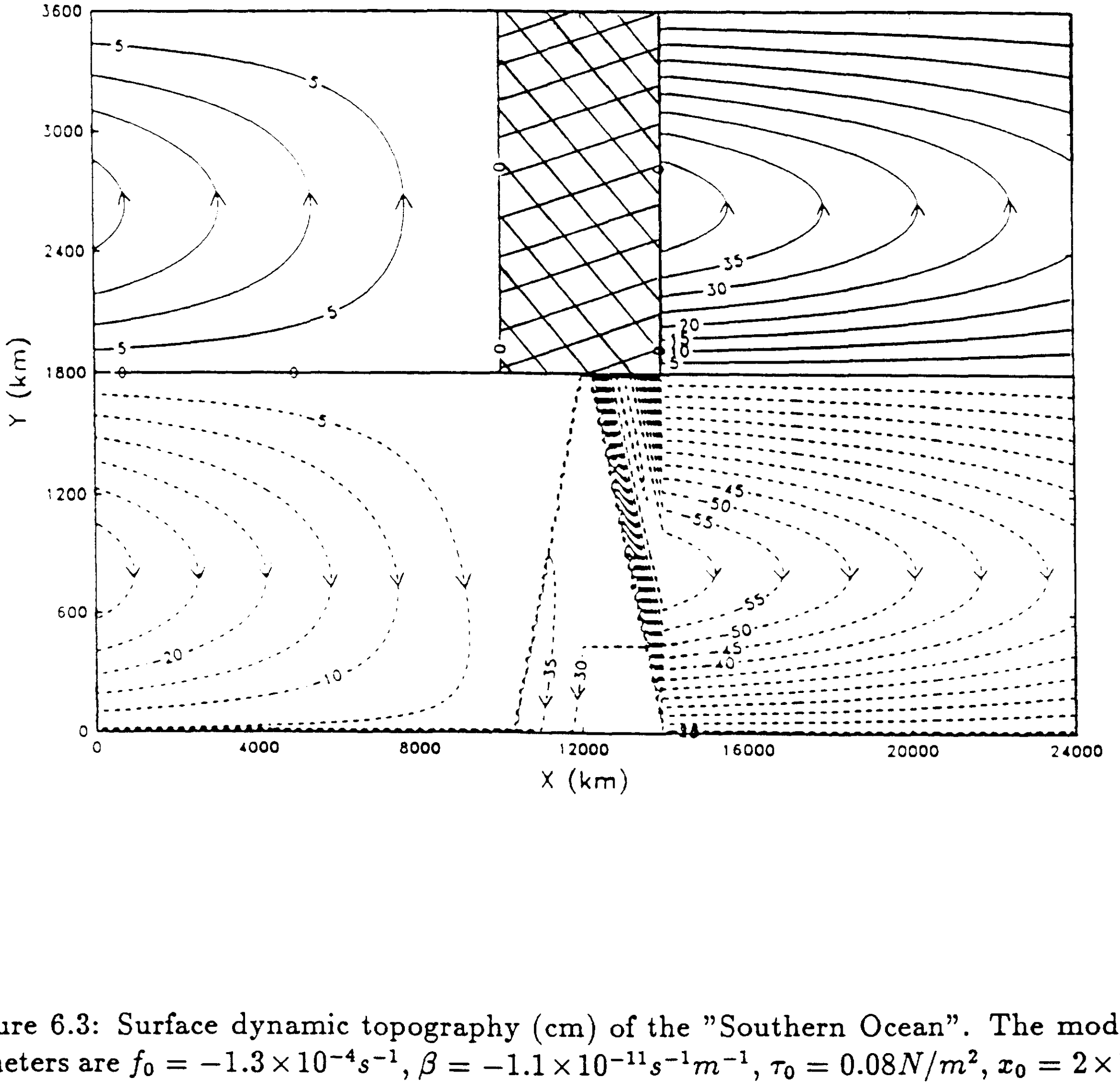

Figure 6.3: Surface dynamic topography (cm) of the "Southern Ocean". The model parameters are $f_0 = -1.3\times10^{-4}s^{-1}$, $\beta = -1.1\times10^{-11}s^{-1}m^{-1}$, $\tau_0 = 0.08N/m^2$, $x_0 = 2\times10^6m$, $L = 2.4\times10^7m$ and $D = 1.8\times10^6m$. Cross-hatched area is the meridional barrier in the subtropical area. Dashed (solid) lines represent the negative (positive) dynamic topography.

The flow impinging segment $a - c$ moves eastward along the southern boundary of the meridional barrier in the surface layer in a way similar to that discussed by Pedlosky (1968) to within segment $c - d$ and sink to the lower layer there in a way similar to that discussed by Hide (1968) to compensate for the total southward volume flux of the circumpolar ocean. Due to the fact that the detail dynamics of the flow along $a - d$ within the surface Ekman layer and that along the lateral boundary in the lower layer are not explicitly included in the model, the above circulation scheme resulting from the Ekman flow impinging upon segment $a - d$ is rather schematic. The discussion about the detailed dynamics is very much involved and tedious, and beyond the scope of this paper. Nevertheless, the volume flux associated with this circulation is much weaker than that returned from the subtropical gyre, *i.e.*, $T_* \ll T_W$ with the assumption $x_0 \ll L$. Thus we complete the source water with volume flux of T_{lower} for the southward flow from the segment $c - d$ along the northern boundary of the circumpolar ocean.

With the discussion above, we have completed the wind-driven meridional cell, called Deacon Cell, *e.g.*, Bryan (1991), in this simple homogeneous two-layer model. As we have seen through the discussion above, this meridional cell is fundamentally three dimensional and nonhomogeneous in the layer below the surface Ekman layer, although it is often project into a two-dimensional meridional plane as Gill & Bryan (1971) did for example. In the surface Ekman layer, *i.e.*, the surface branch of the cell, fluid particle moves northward according to the Ekman layer dynamics. This surface branch is vanishingly thin in the inviscid limit, but the fluid movement is rather uniform except along the segment $a - d$. The sinking branch is in the subtropical area, while the rising branch is the circumpolar zone. Both the sinking and rising are carried out by the Ekman pumping. This three branches of the cell are governed by the Ekman layer dynamics. The lower branch in this two-layer model formulation is much more complicated. The downwelling water from the Ekman layer in the subtropical area is carried northward and westward by the subtropical Sverdrupian gyre to the corresponding western boundary. This water is then carried southward by the western boundary layer current to segment $c - d$, see Fig. 6.2. It is then further carried southward by the Sverdrupian gyre circulation in circumpolar zone to feed the Ekman sucking. Thus, the lower branch of the Deacon Cell is governed by both Sverdrupian and western boundary layer dynamics. Therefore, the dynamics governing the so-called Deacon Cell is quite different for different part.

Noting (3.7) and $\zeta|_E$, the zonal volume transport at $x = L/2$ is

$$T_0 = \frac{2\tau_0 x_0}{\rho_0|f_0|} \cdot \frac{H - h_0}{\Delta h_c}.$$

Because the flow within the circumpolar ocean is divergent, the zonal volume flux at different longitudes is different. This presumably suggests that the volume transport of the Antarctic Circumpolar Current measured at different locations is different, although the transport measured at Drake Passage is often quoted as the transport of the ACC. Nevertheless, the difference, so far as the linear model discussed here is concerned, is no more than the surface Ekman flux. We will define T_0 roughly as the net through-channel transport driven by the surface Ekman pumping, anyway. Not surprisingly, in the quasi-geostrophic approximation with $h_0 \ll H$, this transport approaches the through-channel transport in the corresponding quasi-geostrophic model discussed in Chapter 2. Although the discussion carried out for the quasi-geostrophic model only applies for a low ridge, the discussion here applies for any ridge so long as it is in the supercritical range. Quite intuitively, as $h_0 \rightarrow H$,

$$T_0 \rightarrow 0.$$

For a narrow ridge with $x_0 \ll L$, the interior basin is occupied chiefly by the Sverdrupian gyre circulation, as is shown in Fig. 6.3. The volume transport of this Sverdrupian gyre is roughly

$$T_{Sv} = -\frac{\pi\tau_0(L - 2x_0)}{\beta\rho_0 D}.$$

Both these transports are forced by the surface Ekman pumping. To measure these transports against the total water sucked from the lower layer to the surface Ekman layer, two parameters, R_0 and R_{Sv},

$$R_0 = \frac{x_0}{L} \cdot \frac{H - h_0}{h_0 - h_c}, \quad (3.11)$$

$$R_{Sv} = \frac{\pi}{2} \cdot \frac{|f_0|}{\beta D} \cdot \frac{L - 2x_0}{L}, \quad (3.12)$$

are introduced. R_{Sv} is independent of the ridge height so long as it is supercritical, and one has

$$R_{Sv} \sim \frac{\pi}{2} \cdot \frac{|f_0|}{\beta D},$$

for a narrow ridge. It is purely determined by the ridge width. R_0 depends upon the ridge height. There are two interesting limits. In one extreme, as $h_0 \to h_c$

$$R_0 \rightarrow \infty.$$

While in the other extreme, as $h_0 \to H$

$$R_0 \rightarrow 0.$$

Fig. 6.4 shows R_0 versus h_0, and we have

$$R_0 \begin{pmatrix} > \\ = \\ < \end{pmatrix} 1 \quad \text{if} \quad h_0 \begin{pmatrix} < \\ = \\ > \end{pmatrix} \frac{h_c + Hx_0/L}{1 + x_0/L}.$$

Thus, the through-channel transport could be either stronger or weaker than the total surface Ekman sucking depending upon both the ridge height and width. And in this homogeneous model, R_0 is rather sensitive to the ridge height, h_0.

6.4 Implications for inter-basin water mass exchange in the Southern Ocean

In the preceding section, the subtropical area consists of a single ocean basin for simplicity of discussion. The subtropical area of the realistic Southern Ocean, on the other hand,

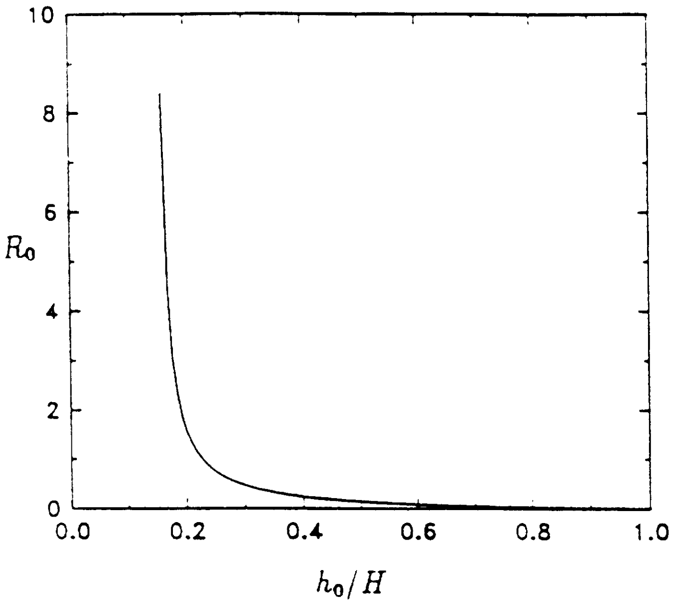

Figure 6.4: R_0 versus h_0/H. The model parameters are similar to those in Fig. 6.3 except that $x_0 = 1.2 \times 10^6 m$.

consists of three ocean basins in the subtropical area. They are the South Atlantic, Indian Ocean and South Pacific, which are partially separated by South American, African and the Australian continents. A schematic view of the subtropical area is shown in Fig. 6.5. In the case with a single ocean basin in the subtropical area, all the Ekman flux carried northward into the subtropical area downwells into the subtropical gyre and is carried westward into the single western boundary layer. Then, a western boundary layer current carries this amount of water southward across the inter-gyre boundary into the northern equivalent western boundary layer of the circumpolar ocean. In the presence of multiple north-south barriers, such as South American, African and the Australian continents, the situation is much more complicated. For simplicity, it is assumed that each ocean basin has the same width, W, and each continent has the same width, w, too, and $w \ll W$. The southern boundary of each continent is assumed all at $y = D$. Furthermore, in the circumpolar ocean there are no topographic features other than the supercritical bottom ridge in the form of (2.4) which connects South America and Antarctic. The remaining model parameters are same as those in the preceding sections.

In each subtropical ocean basin, across its boundary with the circumpolar ocean, there is a northward inflow in the surface Ekman layer to the subtropical area with volume flux

$$T_{oE} \;=\; 2\frac{\tau_0 W}{\rho_0 |f_0|}. \tag{4.1}$$

In each subtropical ocean basin, this same amount of water is pumped down into the subtropical gyre and carried westward by the subtropical gyre to the corresponding western boundary layer. The northward Ekman flow impinging upon the southern boundary of South America with volume flux

$$T_{oe} \;=\; 2\frac{\tau_0 w}{\rho_0 |f_0|} \tag{4.2}$$

does the same as that discussed in the preceding section. Those northward Ekman flows impinging upon the southern boundaries of the other two continents sink to the lower layer in a way similar to that discussed by Hide (1968). Again, the circulation associated with Ekman flux impinging upon the southern boundary of the three meridional barriers is not explicitly depicted by the model used here. Nevertheless, $T_{oe} \ll T_{oE}$ assuming $w \ll W$. Supposing the ridge connecting South America and Antarctica is supercritical, then the discussion in the preceding section about the circulation in the circumpolar ocean applies here regardless of whatever happens in the subtropical area in the linear model used here. To maintain mass balance in each ocean basin gives rise to two questions. First, how does the water lost in the circumpolar interior due to the Ekman sucking get compensated? Second, how does each ocean basin in the subtropical region export the amount of water brought in by the surface Ekman drift?

The answer to the first question is the same as that discussed in the preceding section. The equivalent western boundary layer along the southern boundary of the South American continent serves as the source region to compensate for the water loss to the surface Ekman layer in the interior circumpolar ocean. Now the only remaining question is how the amount of water brought in by the surface Ekman drift in each subtropical basin can reach the equivalent western boundary layer along the southern boundary of the South American continent. For the South Atlantic ocean, the answer is quite straightforward given the discussion in the preceding section. The water with volume flux T_{oE} flows within the western boundary layer southward directly to the equivalent western boundary layer for the circumpolar ocean. Nevertheless, for the other two basins, the solution is not so straight forward. In the South Pacific, the inflow is carried westward into the western boundary layer by the subtropical gyre in the subtropical South Pacific. Then, a current with volume flux T_{oE} flows southward within the western boundary layer to point E, the southeast corner of the Australian continent. At point E, this current turns westward and flows westward along $y = D$ across the Indian Ocean to point C, the southeast corner of the African continent. It entrains the water that sank from the surface Ekman layer with volume flux T_{oe} between D and E. An eastward flow along $y = D$ across the South Pacific would intersect the east coast South America, which violates the condition of no flow intersecting an eastern boundary. Because there are no topographic features other than that connecting South America and Antarctica by model assumption, $y = D$ is a geostrophic contour in the linear model and any flow along it with a constant volume flux abides by the law of potential vorticity conservation in the inviscid limit. This flow pattern is quite similar to the cross-ocean internal current discussed in the source-sink-driven circulation in Chapter 5. In the Indian basin, the subtropical gyre there carries the inflow from the surface Ekman layer to the western boundary layer. Like the South Pacific, a current with volume flux T_{oE} flows southward within the western boundary layer to point C and joins the flow from the South Pacific. Then, it turns westward along $y = D$ all the way to the equivalent western boundary layer along the southern boundary of the South American continent. It entrains the water that sank from the surface Ekman layer with volume flux T_{oe} between B and C. After B, the volume flux of this current grows to

$$T_{westward} = 2T_{oE} + 2T_{oe}.$$

This completes the inter-basin water mass exchange driven by the surface Ekman drift, as is shown by the heavy and open arrows in Fig. 6.5 in the inviscid limit. The most significant characteristics for this flow pattern of inter-basin water mass exchange is the following. The water mass from the South Pacific to the equivalent western boundary layer along the southern boundary of the South American continent does not participate in the circulations of the subtropical gyre in either the South Atlantic or the Indian Ocean. In a similar way, the water mass from the Indian Ocean does not participate in the circulations of the subtropical gyre in the South Atlantic either.

In Fig. 6.5, the westward internal current from D to C and from B to A along $y = D$ is flanked by eastward flow on both sides under the assumption of inviscid limit. In the realistic oceans, frictions such as bottom friction and lateral diffusion, are present regardless of other physical processes. It may be small, but its effect may be profound as is demonstrated by Wang (1993a). In the presence of finite bottom friction, the internal current along $y = D$ will have finite width, and thus it will overlap and strongly interfere

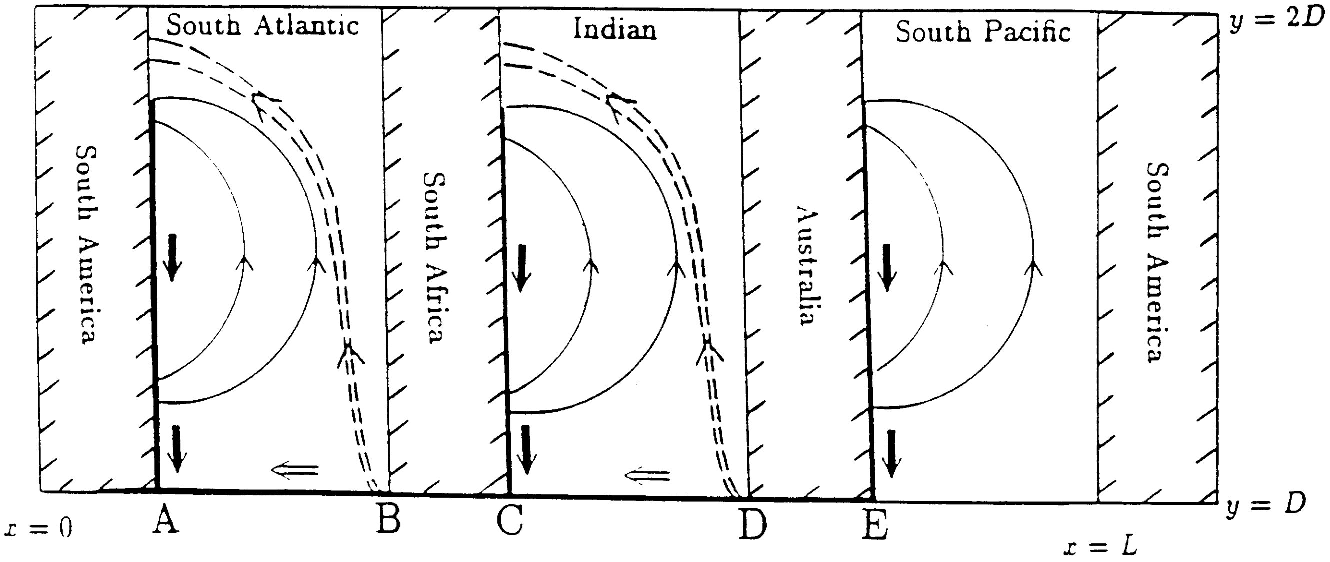

Figure 6.5: Schematic view of the circulation and inter-basin water exchange in the Southern Ocean. Thin solid lines represent the subtropical gyre circulations. Heavy solid arrows represent the western boundary layer currents associated with the inter-basin exchange driven by the wind stress. Open arrows represent the internal currents associated with the inter-basin exchange in the inviscid limit. The dashed arrows represent the revised inter-basin exchange in the presence of finite bottom friction.

with the eastward flow on both sides. The governing equation for the internal current along $y = D$ in the presence of bottom friction is approximately

$$\beta \frac{\partial \zeta}{\partial x} \approx -\kappa \frac{\partial^2 \zeta}{\partial y^2}, \tag{4.3}$$

where κ is the linear bottom frictional coefficient. Then, a scale analysis of this equation gives rise to the characteristic width of the internal current as

$$\delta_y = \sqrt{\delta W}, \tag{4.4}$$

where $\delta = \kappa/\beta$ is the Stommel boundary layer thickness. Thus, the characteristic westward zonal velocity of the internal jet is

$$U_{In} \sim -T_{oE}/H\delta_y,$$

in the Indian Ocean, noting $w \ll W$. In the South Atlantic we have

$$U_{SA} \sim -2T_{oE}/H\delta_y,$$

in the presence of bottom friction. The characteristic zonal velocity at $y = D$ of the subtropical gyre is

$$U_{sub} \sim \frac{\pi f_0 w_0 W}{H\beta D},$$

in either the South Atlantic or Indian Ocean, noting $\zeta|_A$ in the preceding section. Then, for a small bottom friction with $\delta \sim 15km$, one always has

$$U_{sub} + U_{SA} > 0, \tag{4.5}$$

for other model parameters chosen as $f_0 = -1.3 \times 10^{-4}s^{-1}$, $\beta = -1.1 \times 10^{-11}s^{-1}m^{-1}$ and $D = 1.8 \times 10^6 m$. Thus, as the result of interfering with either the subtropical gyre or the circumpolar circulation, the internal current can not flow along $y = D$ any more in the presence of a finite and small bottom friction. Instead, it will be entrained into and participates in the subtropical gyre and the circulations within the circumpolar basin.

If the southern ends of the South American, African and Australian continents are indeed at the same latitude $y = D$, the zero line of w_e, then the water from the internal current is about evenly partitioned into the subtropical basins and the circumpolar basin. In the realistic Southern Ocean, the South American continent extends much farther south than the other two continents. Furthermore, the southern ends of the African and Australian continents are much farther north than the local zero line of wind stress curl, see Nowlin & Klinck (1986). Taking this into account, the internal current would be completely within the subtropical gyres rather than at the boundary between the subtropical gyres and the circumpolar circulation. Thus, in the presence of a small but finite bottom friction, the internal current will only interfere with the subtropical gyre. As a result, it will be entrained by and participates only in the generally northward flowing subtropical gyre interior flow. The inter-basin water mass exchange in the open ocean will be fundamentally different from that shown in Fig. 6.5 for the inviscid limit. *Schematically*, the route for the inter-basin water exchange is shown as the dashed line in Fig. 6.5 for the case with a small yet finite bottom friction. The water from the South Pacific flows as the northeast branch of the subtropical gyre in the Indian basin, and is carried by the subtropical gyre to the western boundary layer. After that the same amount of water together with downwelling water from the surface Ekman layer into the subtropical gyre in the Indian Ocean flows southward as a western boundary current and around the southern boundary of the African continent into the South Atlantic. In the South Atlantic, the circulation in the subtropical basin similar to that in the Indian Ocean happens, only that the inflow from the southeast corner is about twice as strong as that in the Indian Ocean. This might be one possible reason why the inflow from the Indian Ocean to the South Atlantic is so visible from the observation such as shown by Gordon (1986). Comparing to the simpler case discussed in the preceding section, the structure of the Deacon cell is quite similar except in the subtropical region, where the flow structure associated with the cell is more complicated. It is now governed by Sverdrupian, western boundary layer and internal boundary layer dynamics.

6.5 Discussion and conclusion

In this chapter the dynamic role of a supercritical ridge in the mass balance associated with the surface northward Ekman drift in the Southern Ocean is discussed in a linear homogeneous model. In the quasi-geostrophic formation of the wind-driven circulation in a $\beta-$plane channel discussed in Chapter 2, a vertically integrated form of the circulation is discussed. This technique of dealing solely with the vertical integral of the horizontal velocity often hides the marked difference between the wind drift in the thin surface Ekman layer and the geostrophic regime below. In this chapter, the circulation is split into the thin surface Ekman layer and lower homogeneous layer. This leads to the question as to what is the circulation associated with the surface Ekman drift, which is present regardless of the model geometry. In the surface Ekman layer, water is sucked up from the circumpolar region and flows northward across the inter-gyre boundary between the circumpolar ocean and the subtropical gyre. In the subtropical area, water from the circumpolar area is pumped down to the subtropical gyre in the lower layer. Due to the circulation associated with the surface Ekman flow, the subtropical area in the lower layer has a net gain of water while the circumpolar area in the lower layer has a net loss of the same amount of water. Then, there must be a southward flow from the subtropical area across the inter-gyre boundary into the circumpolar zone. In the linear model discussed, it was proposed that this cross-gyre flow occurs as a regular western boundary layer current. This water mass from the subtropical area, however, has to be carried southward across the latitudes of the circumpolar region. It requires that there should be a net southward geostrophic volume flux even though there are no meridional barriers.

In a $\beta-$plane channel without any topographic features, any meridional flow in the latitudes of the circumpolar ocean has to be associated with ageostrophic processes. In the presence of a sufficiently high ridge, however, geostrophic flow can support a net meridional volume flux. Associated with the southward volume flux required by mass balance is an eastward flowing loop of currents, which are similar to those discussed in a quasi-geostrophic model. So in the case with a supercritical ridge connecting the Antarctic and the meridional barrier in the subtropical region, the northward flowing surface Ekman drift out of the circumpolar zone returns to the southern boundary of the barrier as a western boundary layer current in the lower layer. From the southern boundary of the meridional barrier, this water mass from the subtropical gyre is carried southward by the Sverdrupian gyre circulation in the circumpolar ocean and sucked up by the surface Ekman layer. The most important characteristics of this flow pattern is that in the lower layer all the return flow to the interior circumpolar ocean starts from the eastern part of the southern boundary of the meridional barrier to the north of the circumpolar ocean. This discussion essentially completes the three dimensional structure for the so-called Deacon Cell first founded by Gill & Bryan (1971) in a numerical model in a rather simple homogeneous two-layer model. The surface branch, which has vanishingly thin thickness, and the sinking and the rising branches are all governed by the Ekman layer dynamics. The lower branch, which dynamically is very nonhomogeneous, is governed both boundary and Sverdrupian dynamics. This cell is fundamentally three dimensional system.

This circulation associated with the surface Ekman drift has a very significant implication for the inter-basin water mass exchange among the subtropical basins in the Southern Ocean. It has generally been thought that inter-basin water mass exchange is closely associated with the global thermohaline circulation, such as in the studies of Gordon (1986) and Rintoul (1988). It is demonstrated that the circulations associated with the surface Ekman drift, however, can also induce a strong inter-basin water mass exchange. The chief reason is that all the return flow to the interior circumpolar ocean starts from the eastern part of the southern boundary of South America, so long as the present simple model is concerned. Therefore, the model, albeit being linear and homogeneous for the water below the surface Ekman layer, essentially suggests that the wind stress can also drive a strong inter-basin water exchange in the Southern Ocean. Thus, the observed inter-basin exchange might not be necessarily associated only with the thermohaline circulation.

Another way in which the wind stress can drive an inter-basin water mass exchange purely due to the geometry of the Southern Ocean and the various land areas was discussed by de Ruijter & Boudra (1985). All these add up to the complexity of identifying the cause for the inter-basin water mass exchange. If we project the meridional circulation associated with the surface Ekman drift, albeit being depicted just in a two-layer model, into a meridional plane, one would get the so-called Deacon cell as discussed by England (1992) in a GCM experiment.

The discussion in this chapter is carried out in rather simple models, notably the simple geometry and bottom topography, linear and homogeneous assumption for the water below the thin surface Ekman layer and a solid northern boundary. This last assumption essentially excludes the possibility of returning the water mass from the South Pacific and Indian Oceans to the South Atlantic by other means. Gordon (1986) pointed out that the inflow from the South Pacific to the Indian Oceans is mostly, if not all, to the north rather than to the south of the Australian continent. Nevertheless, the essential significance of the supercritical ridge connecting South America and the Antarctica and the inter-basin water mass exchange associated with the surface Ekman drift is believed to be relevant to the large scale circulations in the Southern Ocean. The discussion in this chapter is purely dynamic. It is not difficult to see that in the realistic Southern Ocean, associated with this inter-ocean water mass exchange is a very complicated three dimensional structure of various tracer fields.

Chapter 7

Discussion and conclusion

7.1 Summary of the thesis

In this thesis, the dynamic role of bottom topography in both momentum and mass balances in a $\beta-$plane channel is systematically studied in both homogeneous and layered models in the presence of either wind stress (Chapters 2, 3, 4 and 6) or buoyancy forcing (Chapter 5). In these studies, the structure of the geostrophic contour plays a fundamental role. Accordingly, the bottom topography is classified into two categories. In the first one, all geostrophic contours are blocked by lateral boundaries, while in the second category, not all or none of the geostrophic contours in the channel are blocked by the lateral boundaries. Chapters 2 and 3 address the question of how topographic form drag is generated in a $\beta-$plane channel in a homogeneous model. Chapter 4 addresses the questions of what is the effect of stratification on the bottom topographic form-drag generation and how is the interfacial form drag generated. These three chapters mainly discussed the dynamic role that bottom topography plays in the momentum balance. Chapters 5 and 6 address the question of whether geostrophic flow in a $\beta-$plane channel can support a net cross-channel volume flux. These two chapters mainly discuss the dynamic role bottom topography plays in the mass balance. As shown in Chapters 2 and 6 these two questions are essentially one question but looked at from different angles.

First, wind-driven circulation in the inviscid limit is discussed in a linear barotropic channel model in the presence of a bottom ridge. There is a critical height of the ridge, above which all geostrophic contours in the channel are blocked. In the subcritical case, the Sverdrupian balance does not apply and there is no solution in the inviscid limit. In the supercritical case, however, the Sverdrupian balance applies and an explicit form for the wind-driven circulation and especially the zonal transport in the channel is obtained, which clearly demonstrates what model parameters determine the zonal through-channel transport.

In the case with a uniform wind stress, the transport in the $\beta-$plane channel is independent of the width of the ridge, linearly proportional to the wind stress and the length of the channel, while inversely linearly proportional to the ridge height. In the $f-$plane with $\beta = 0$, the transport is even independent of the width of the channel. In the case with a nonuniform wind stress $\tau_x = \tau_0(1 - cos\pi y/D)$, the Sverdrupian flow driven by the vorticity input always induces a form drag against the mean wind stress. Now, the transport depends on the width of the ridge but not on the length of the channel.

The model clearly demonstrates how the topographic form-drag is generated in a linear barotropic model, which is fundamentally different from the nonlinear Rossby wave drag generation. In this linear model, the presence of a supercritically high ridge is essential to the form-drag generation in the inviscid limit. In the supercritical case, form-drag is generated regardless of the flow direction. In addition, the model demonstrates that most of the potential vorticity dissipation occurs at the northern boundary where the ridge is located.

The results from the homogeneous channel model in Chapter 2 are extended to a model whose geometry consists of a zonal channel and two partial meridional barriers along each boundary at the same longitude. Both the model transport and especially the model circulation are significantly affected by the presence of the two meridional barriers.

There is a critical height of the ridge between the two partial meridional barriers, above which all geostrophic contours in the channel are blocked.

In the subcritical state, the Sverdrupian balance does not apply and there is no solution in the inviscid limit. In the supercritical state, however, an explicit form for the through-channel transport is obtained in the inviscid limit. In the case with a uniform wind stress, the transport is independent of the width of either the ridge or the channel, and is linearly proportional to the wind stress and the length of the channel, while inversely linearly proportional to the ridge height. In the case with a nonuniform wind stress $\tau_x = \tau_0(1 - cos\frac{\pi}{D}y)$, the relation between the transport and model parameters is more complicated. It is related to the width of both the ridge and the channel, and the lengths of the two partial meridional barriers, besides those like the case with a uniform wind stress forcing. The presence of the northern barrier always leads to a decrease in the transport. The presence of the southern barrier, however, increases the transport for a narrow ridge.

The model again demonstrates the importance of the topographic form drag generation via the Sverdrupian flow forced by the wind stress curl. In terms of the circulation structure, the presence of a southern barrier has a far more profound influence than that of a northern one. The northern barrier only has a localized influence on the circulation pattern over the ridge, while the southern barrier has a global influence in the channel. In addition, the model demonstrates that most of the potential vorticity dissipation occurs around the northern barrier.

Chapters 2 and 3 address the question regarding the role of bottom topography in the momentum balance in a homogeneous model. In Chapter 4 the same question is addressed in a layer model. By assuming that potential vorticity in all sub-surface layers is homogenized, a multi-layer Q-G model of large scale wind-driven circulation in a $\beta-$plane channel is constructed. The circulation is made up of a baroclinic part and a barotropic part. The barotropic part is the same as that in a corresponding barotropic model discussed in Chapter 2. The wind stress only determines the barotropic component, while the baroclinic part is not directly related to the wind stress. The potential vorticity homogenization in each subsurface layer and lateral boundary conditions together determine the baroclinic component. The presence of the stratification does not affect the topographic form drag generation discussed in the corresponding barotropic model. The interfacial form drag is generated by the stationary perturbations. Corresponding to the circulation, the zonal through-channel transport associated with the barotropic circulation is determined by the wind stress and bottom topography. The other part associated with the baroclinic circulation, however, is not directly related to the wind stress; it is determined by the background stratification. The presence of stratification increases the zonal transport.

Chapters 2, 3 and 4 demonstrate the importance of a supercritical ridge in the form drag, both bottom and interfacial, generation and thus the momentum balance. The same question is looked at from a different angle in Chapters 5 and 6. It is rather easy to see that in a $\beta-$plane channel with a flat bottom, geostrophic flow can not carry any net cross-channel volume flux. The question is whether geostrophic flow can carry a net cross-channel volume flux in the presence of bottom topography. We begin with the source-sink-driven circulation. In Chapter 5, a simple barotropic model of abyssal circulation in a circumpolar ocean basin is constructed. In the presence of a sufficiently high ridge, the classical Stommel & Arons theory applies here with very substantial modifications. In the case with a point source at one side of the channel and a point sink at the other side of the channel, there is a through-channel recirculating flow in addition to the flow from the source to the sink. The volume flux of this recirculating flow is critically determined by the supercriticality of the ridge height. In the case with uniform sink and point sources and sinks, the circulation is essentially in the Stommel & Arons sense with one major novelty. That is, a through-channel recirculating flow is generated. Both its strength and direction depend critically upon the model parameters. This suggests that the Antarctic Bottom Water formation could drive a substantial amount of westward flow which counterbalances the wind-driven eastward flow. Lastly, a schematic picture of the abyssal circulation in a rather idealized Southern Ocean is obtained. The most significant feature is the narrow current along the northern boundary of the circumpolar basin, which feeds the deep western boundary currents of the Indian Ocean and Pacific Ocean. It serves to connect all the oceanic basins in the Southern Ocean.

What is the fate of the northward surface Ekman transport out of the circumpolar ocean? This question is discussed in a two-layer model with an infinitesimal surface Ekman layer on top of a homogeneous layer of water in a rather idealized Southern Ocean basin. First, the case with a single subtropical ocean basin is discussed. In the case with a sufficiently high ridge connecting the Antarctic and the meridional barrier, an explicit solution is found. The surface Ekman layer sucks water from the lower layer in the circumpolar basin. This same amount of water flows northward as the surface Ekman drift, and downwells to the lower layer in the subtropical gyre, where it is carried to the western boundary layer. From the western boundary layer of the subtropical gyre, the same amount of water flows southward as a western boundary current across the inter-gyre boundary between the circumpolar ocean and the subtropical gyre along the west coast to the southern boundary of the meridional barrier. From there, the amount of water is carried southward by the Sverdrupian flow and feeds the water loss to the surface Ekman layer due to the Ekman sucking in the interior circumpolar ocean. Then, the case with multiple subtropical ocean basins such as the Southern Ocean is discussed. It is demonstrated that the surface Ekman drift drives a strong inter-basin water mass exchange.

7.2 What have we learnt?

The first question one would like to ask about this thesis is what have we learnt. The most important thing we have learnt from the thesis is the fundamental role a topographic feature of the first category plays in determining both the wind-driven and source-sink-driven circulations in a β−plane channel. It boils down to one central question which can be looked at from two different angles. From the viewpoint of momentum balance in the channel, the question is how bottom topographic form drag is generated. From the point of view of mass balance in the channel, the question is whether geostrophic flow in a β−plane channel can carry net cross-channel volume transport.

From the viewpoint of momentum balance, it is demonstrated that the supercriticality of the ridge used in discussions throughout the thesis is essential in the process of bottom topographic and interfacial form-drag generation. It appears that the form drag can be generated through two different physical processes. The first one is by the barotropic zonal through-channel recirculating flow. In this process, the zonal transport and the supercriticality of the ridge height determines the bottom form-drag generation. In the second process, the wind stress curl determines the form-drag generation so long as the ridge is in the supercritical range. The presence of stratification appears to have no direct influence on the bottom topographic form-drag generation. In the layered model, however, another question arises as to how the momentum input at the surface gets down to the bottom. It is demonstrated that the stationary eddies resulting from the Sverdrupian gyre circulation together with the baroclinic flow over bottom ridge carried out the momentum downward transport.

From the viewpoint of water mass balance in the channel, it is shown that in the presence of a supercritical ridge, geostrophic flow *can* carry net cross-channel volume transport. In the wind-driven circulation, associated with westerly wind stress is a strong northward Ekman drift throughout the channel in the surface Ekman layer. This northward flow is supplied by the geostrophic flow regime below which carries a net southward cross-channel volume flux.

So far as the circulation structure is concerned, only in the supercritical state can we find an explicit solution in the inviscid limit. In the homogeneous model, the wind-driven circulation consists of the Sverdrupian gyre circulation and the through-channel recirculation flow. The source-sink-driven circulation is similar. In the stratified model, the wind-driven circulation consists of two parts. The first part is the barotropic circulation which is same as the corresponding barotropic model. The second part is the baroclinic part which is anticyclonic circulation over the ridge superimposed upon a uniform baroclinic flow. The barotropic circulation is determined by the wind stress forcing. The baroclinic circulation, however, is not directly related to the wind stress forcing. This presumably implies that the wind stress variability can only drive a similar response in the barotropic circulation and its associated zonal transport and that there is no response in the baroclinic circulation and its associated zonal transport. This seems to be consistent with the currently available measurements about the time variability in the circumpolar area.

Apparently the model used in the discussions throughout this thesis is rather idealized, particularly with respect to the bottom topographic ridge and coastline shape. Nevertheless, the methodology employed here can be extended to fairly general bottom topography and coastline. Despite the many simplifications discussed throughout thesis, some results from the model are believed to be robust regardless of the model assumption. *First*, geostrophic contour blocking plays an essential role in both homogeneous and stratified oceans in terms of generating bottom topographic and interfacial form drag and of supporting a net cross-channel geostrophic volume flux. This clearly singles out the fundamental importance of the topographic features around Drake Passage in determining the overall dynamics of both the wind-driven and source-sink-driven circulation in the Southern Ocean, thus the global ocean circulation. Were there no topography around Drake Passage or if the distance between the Antarctic and South America were much larger, both the wind and buoyancy-driven circulations in the Southern Ocean and thus the global ocean would be completely different from what exists today. *Second*, the physical process associated with the bottom topographic form-drag generation is closely relevant to the momentum balance in the circumpolar ocean, especially the importance of the wind stress curl driven circulations, which puts a high quality demand on the wind stress measurement in order to properly constrain the transport of the Antarctic Circumpolar Current. *Third*, the circulation driven by the wind stress curl plays a fundamental role in the momentum downward transport process, and stationary eddies rather than transient eddies play a dominant role in this process. Nevertheless, those transient eddies would presumably tend to homogenize the potential vorticity in all subsurface layer, thus leave all potential vorticity gradient trapped near the upper surface. *Fourth*, the thermohaline circulation, which presumably determines the background stratification, plays a significant role in determining the transport of the ACC. Unfortunately I am unable to address the source-sink-driven thermohaline circulation in a similar way as I do the wind-driven circulation. The discussion here, however, does suggest that to *really* understand what determines that transport of ACC one has to understand the thermohaline circulation first. *Fifth*, the wind stress through the surface Ekman drift drives a strong inter-ocean exchange among the different basins in the Southern Ocean which has been generally thought to be driven primarily by the source-sink forcing.

7.3 Future work

Although we have made significant progress in terms of our theoretical understanding of the large scale circulation in the Southern Oceans, much more work is needed to deepen our understanding. From a theoretical point of view, the most important issue is the buoyancy-driven circulation in the Southern Ocean, which presumably sets the background stratification for the wind-driven circulation. Bottom topography is again expected to play an important role in determining the thermohaline circulation. One of the most significant feature in the circumpolar ocean is the multiple frontal structures, why are there multiple fronts and what determines the position of these fronts. From the standpoint of observational studies there are several issues need to be resolved. The first one is related to the downward momentum transport or meridional heat flux. I believe that most of the downward momentum transport is due to the large scale stationary eddies, and we should be able to infer some of this information from currently available data base. The second issue is the volume flux, heat and fresh water fluxes associated with both the wind and buoyancy driven inter-ocean exchange among the different basins in the Southern Ocean. This inter-ocean exchange is the key part of the global "conveyer belt", which is of fundamental importance to the understanding of the global climate of decadal or longer time scale.

REFERENCES

Baker, D.J., Jr. 1982: A note on Sverdrup balance in the southern ocean. *J. Mar. Res.*, 40, *Suppl.*, 21-26.

Barcilon, V., 1966: On the influence of the peripheral Antarctic water discharge on the dynamics of the circumpolar current. *J. Mar. Res.*, 24, 269-275.

Barcilon, V., 1967: On the motion due to sources and sinks distributed along the vertical boundary of a rotating fluid. *J. Fluid Mech.*, 27, 551-560.

Bryan, K., 1991: Ocean circulation models. Pp265-286, in *Strategies for future climate research*, ed: Latif, M. Max-Planck Institut fur Meteorologie, Hamburg. 387pp.

Bryan, K., and M. Cox, 1972: The circulation of the world ocean: A numerical study. Part I: A homogeneous model. *J. Phys. Oceanogr.*, 2, 319-335.

Bryden, H. and R.D. Pillsbury, 1977: Variability of deep flow in Drake Passage from year-long current measurements. *J. Phys. Oceanogr.*, 7, 803-810

Bryden, H.L. and R.A. Heath, 1985: Energetic eddies at the northern edge of the Antarctic Circumpolar Current in the southwest Pacific. *Prog. Oceanogr.*, 14, 65-87.

Cessi, P., and J. Pedlosky, 1986: On the role of topography and in the ocean circulation. *J. Mar. Res.*, 44(3), 445-471.

Charney, J.G., 1955: The Gulf Stream as an inertial boundary current. *Proc. Nat. Acad. Sci.*, 41, 731-740.

Chelton, D.B., 1982: Statistical reliability and the seasonal cycle: Comments on the "bottom pressure measurements across the Antarctic Circumpolar Current and their relation to wind". *Deep-Sea Res.*, 29, 1381-1388.

Cox, M.D., 1989: An idealized model of the world ocean. Part I: The global-Scale water masses. *J. Phys. Oceanogr.*, 19, 1730-1752.

Csanady, G.T., 1986: Cross-gyre transport. *J. Phys. Oceanogr.*, 16, 1703-1711.

Davey, M.K., 1980: A quasi-linear theory for rotating flow over topography. Part I. Steady $\beta-$plane channel. *J. Fluid Mech.*, 99, 267-292.

Deacon G.E.R., 1984: The Antarctic Circumpolar Ocean. 180pp., Cambridge University Press, New York.

Dewar, W.K., 1987: Planetary shock waves. *J. Phys. Oceanogr.*, 17, 470-482.

de Ruijter, W.P.M. and D.B. Boudra, 1985: The wind-driven circulation in the South Atlantic-Indian Ocean, I, Numerical experiments in a one-layer model. *Deep-Sea Res.*, 32, 557-574.

England, M.H., 1992: On the formation of Antarctic Intermediate and Bottom Water in ocean general circulation models. *J. Phys. Oceanogr.*, 22, 918-926.

Fandry, C. and R.D. Pillsbury, 1979: On the estimation of absolute geostrophic volume transport applied to the Antarctic Circumpolar Current. *J. Phys. Oceanogr.*, 9(3), 449-455

Foster, L.A., 1972: Current measurements in the Drake Passage, M.S. thesis, 61 pp., Dalhousie Univ., Halifax, N.S., Canada.

The FRAM Group, 1991: An eddy-resolving model of the Southern Ocean. *Eos, Transactions AGU*, 72, 174-175.

Gill, A.E., 1968: A linear model of the Antarctic Circumpolar Current. *J. Fluid Mech.*, 32, 465-488.

Gill, A.E., and K. Bryan, 1971: Effects of geometry on the circulation of a three-dimensional Southern Hemisphere ocean model. *Deep-Sea Res.*, 18, 685-721.

Gordon, A.L., H.W. Taylor and D.T. Georgi, 1977: Antarctic oceanographic zonation, In *Polar Oceans, Proceedings of the Polar Ocean Conference*, edited by M.J, Dunbar, pp. 45-76, Arctic Institute of North America, Calgary, Alberta, Canada.

Gordon, A.L., E. Molinelli and T. Baker, 1978: Large-scale relative dynamic topography of the Southern Ocean. *J. Geophys. Res.*, 83, 3023-3032.

Gordon, A.L., E. Molinelli and T. Baker, 1982: *Southern Ocean Atlas*, 11 pp., 233 plates, Columbia Univ. Press, New York.

Gordon, A.L., 1986: Interocean exchange of thermocline water. *J. Geophys. Res.*, 91, 5037-5046.

Hautala, S.L., and S.C. Riser, 1989: A simple model of abyssal circulation, including the effect of wind, buoyancy and topography. *J. Phys. Oceanogr.*, 19, 596-611.

Haynes, P.H., 1985: Wind gyres in a circumpolar oceans. *J. Phys. Oceanogr.*, 15, 670-683.

Hidaka, K. and M. Tsuchiya, 1953: On the Antarctic Circumpolar Current. *J. Mar. Res.*, 12, 214-222.

Hide, R., 1968: On source-sink flows in a rotating fluid. *J. Fluid Mech.*, 32, 737-764.

Hoffman, E.E., 1985: The large-scale horizontal structure of the Antarctic Circumpolar Current from FGGE drifters. *J. Geophys. Res.*, 90, 7087-7097.

Huang, R.X., 1991: The three-dimensional structure of wind-driven gyres, ventilation and subduction. *Rev. Geophys.* 29 (2)

Johnson, E.R., 1977: Stratified Taylor columns on a $\beta-$plane. *Geophysical and Astrophysical Fluid Dynamics*, 9, 159-177.

Johnson, G.C. and H.L. Bryden, 1989: On the size of the Antarctic Circumpolar Current. *Deep-Sea Res.*, 36, 39-53.

Johnson, J.A. and R.B. Hill, 1975: A three-dimensional model of the southern ocean with bottom topography. *Deep Sea Res.*, 22, 1157-1181.

Kamenkovich, V.M., 1962: Towards a theory of the Antarctic Circumpolar Current (in Russian), *Tr. Inst. Okeanol. im. P.P. Shirshova, Akad. Nauk. SSSR*, 56.

Kawase, M., 1987: Establishment of deep ocean circulation driven by deep-water production. *J. Phys. Oceanogr.*, 17, 2294-2317.

Klinck, J.M., 1991: Vorticity dynamics of seasonal variation of the Antarctic Circumpolar Current from a modeling study. *J. Phys. Oceanogr.*, 21, 1515-1533.

Kuo, H.H. and G. Veronis, 1973: The use of oxygen as a test for an abyssal circulation model. *Deep-Sea Res.*, 20, 871-888.

Lindzen, R.S., 1993: Baroclinic neutrality and the tropopause, *J. Atmos. Sci.*, 50, 8, 1148-1151.

Luyten, J., J. Pedlosky and H. Stommel, 1983: The ventilated thermocline. *J. Phys. Oceanogr.*, 13, 292-309.

Marshall, J., D. Olbers, H. Ross and D. Wolf-Gladrow, 1993: Potential vorticity constraints on the dynamics and hydrography of the Southern Ocean. *J. Phys. Oceanogr.*, 23, 409-425.

McCartney, M.S., 1975: Inertial Taylor columns on a $\beta-$plane. *J. Fluid Mech.*, 68, 71-95.

McWilliams, J.C. and J.H.S. Chow, 1981: Equilibrium geostrophic turbulence, I: A reference solution in a $\beta-$plane channel. *J. Phys. Oceanogr.*, 11, 921-949.

McWilliams, J.C., W.R. Holland and J.H.S. Chow, 1978: A description of numerical antarctic circumpolar currents. *Dyn. Atmos. Oceans*, 2, 213-291.

Meinardus, W., 1923: Ergebnisse der Seefahrt des Gauss. *Dtsch. Sudpol. Exped.* 1901-1903, 3, 531.

Munk, W.H., 1950: On the wind-driven ocean circulation. *J. Meteor.*, 7, 79-93.

Munk, W.H. and E. Palmen, 1951: Note on the dynamics of the Antarctic Circumpolar Current. *Tellus*, 3, 53-55.

Nowlin, W.D., Jr., T. Whitworth III, and R.D. Pillsbury, 1977: Structure and transport of the Antarctic Circumpolar Current at Drake Passage from short-term measurements, *J. Phys. Oceanogr.*, 7(6), 788-802.

Nowlin, W.D. and M. Clifford, 1982: The kinematic and thermohaline zonation of the Antarctic Circumpolar Current at Drake Passage. *J. Mar. Res.*, 40, *Suppl.*, 481-507.

Nowlin, W.D., Jr. and J.M. Klinck, 1986: The physics of the Antarctic Circumpolar Current. *Rev. Geophys.*, 24(3), 469-491.

Olbers, D. and C. Wubber, 1993: The role of wind and buoyancy forcing of the Antarctic Circumpolar Ocean. Manuscript.

Orsi, A.H., W.D. Nowlin and T. Whitworth III, 1992: On the circulation and stratification of the Weddell Gyre. *Deep-Sea Res.*, 40, 169-203.

Pedlosky, J., 1968: An overlooked aspect of the wind-driven ocean circulation. *J. Fluid Mech.*, 32, 809-821.

Pedlosky, J., 1987: *Geophysical Fluid Dynamics.* 2nd edition. Springer-Verlag, 710pp.

Reid, J.L. and W.D. Nowlin, Jr., 1971: Transport of water through the Drake Passage. *Deep-Sea Res.*, 18, 51-64.

Rhines, P.B., 1983: Lectures in geophysical fluid dynamics. *Fluid Dynamics in Geophysical and Astrophysics*, N. Lebowitz, Ed., Amer. Math. Soc., 3-59.

Rhines, P.B. and W.R. Holland, 1979: A theoretical discussion of eddy-driven mean flows. *Dyn. Atmos. Oceans.*, 3, 285-325.

Rhines, P.B. and W.R. Young, 1982a: A theory of the wind-driven circulation. I. Mid-ocean gyres. *J. Mar. Res.*, 40, 849-872.

Rhines, P.B. and W.R. Young, 1982b: Homogenization of potential vorticity in planetary gyres. em J. Fluid Mech., 122, 347-367.

Rhines, P.B., 1989: Deep planetary circulation and topography: simple models of mid-ocean flows. *J. Phys. Oceanogr.*, 19, 1449-1470.

Rintoul, S.R., 1988: Mass, heat and nutrient fluxes in the Atlantic Ocean determined by inverse methods. Ph.D thesis, Massachusetts Institute of Technology and Woods Hole Oceanographic Institution Joint Program.

Rooth, C., H. Stommel and G. Veronis, 1978: On motion in steady layered geostrophic models. *J. Oceanogr. Soc. Japan*, 34, 265-267.

Saunders, P.M., and S.R. Thompson, 1993: Transport, heat, and fresh water fluxes within a diagnostic numerical model (FRAM). *J. Phys. Oceanogr.*, 23, 452-464.

Schulman, E.E., 1970: The Antarctic Circumpolar Current, paper presented at Summer Computer Simulation Conference, Natl. Sci. Found., Denver, Colo., June 1970.

Semtner, A.J., and R.M. Chervin, 1988: A simulation of the global ocean circulation with resolved eddies. *J. Geophys. Res.*, 93, 15,502-15,522.

Smith, N.R. and C.B. Fandry, 1978: Combined effects of wind stress and topography in a two-layer model of the Southern Ocean. *Deep-Sea Res.*, 25, 371-390.

Stommel, H., 1948: The westward intensification of wind-driven ocean currents. *Trans. Amer. Geophys. Union*, 99, 202-206.

Stommel, H., 1955: *The Gulf Stream: A Physical and Dynamical Description*, 2nd ed. University of California Press, Berkeley, and Cambridge University Press, London, 248pp

Stommel, H., 1957: A survey of ocean current theory. *Deep-Sea Res.*, 4, 149-184.

Stommel, H., 1958: The abyssal circulation. *Deep-Sea Res.*, 5, 80-82.

Stommel, H., and A.B. Arons, 1960a: On the abyssal circulation of the world ocean—I. Stationary planetary flow patterns on a sphere. *Deep-Sea Res.*, 6, 140-154.

Stommel, H., and A.B. Arons, 1960b: On the abyssal circulation of the world ocean—II. An idealized model of the circulation pattern and amplitude in oceanic basins. *Deep-Sea Res.*, 6, 217-233.

Stommel, H., A.B. Arons and A.J. Faller, 1958: Some examples of stationary planetary flow patterns in bounded basins. *Tellus*, 10, 179-187.

Straub, D.N. and P.B., Rhines, 1990: Effects of large scale topography on abyssal circulations. *J. Mar. Res.*, 48, 223-253.

Sverdrup, H.U., 1947: Wind-driven currents in a baroclinic ocean; with application to the equatorial currents of the eastern Pacific. *Proc. Nat. Acad. Sci.*, 33, 318-326.

Swallow, J.C., and L.V. Worthington, 1957: Measurements of deep currents in the western North Atlantic. *Nature* 179, 1183-1184.

Toggweiler, J.R. and B. Samuels, 1992: Is the magnitude of the deep outflow from the Atlantic Ocean actually governed by Southern Hemisphere winds? In *The Global Carbon Cycle*, M. Heimann, ed., NATO ASI Series, Springer-Verlag, Berlin.

Treguier, A.M. and J.C. McWilliams, 1990: Topographic influences on wind-driven, stratified flow in a β-plane channel: an idealized model for the Antarctic Circumpolar Current. *J. Phys. Oceanogr.*, 20, 321-343.

Trenberth, K.E, W.G. Large and J.G. Olson, 1990: The mean annual cycle in global ocean wind stress. *J. Phys. Oceanogr.*, 20, 1742-1760.

Wang, L., 1993a: Numerical studies on the wind-driven circulation in a $\beta-$plane channel with application to the Antarctic Circumpolar Current. *Manuscript.*

Wang, L., 1993b: Flow over topography in a $\beta-$plane channel. *Manuscript.*

Warren, B.A., 1981: Deep circulation of the World Ocean. *Evolution of Physical Oceanography, Scientific Surveys in Honor of Henry Stommel*, B.A. Warren and C. Wunsch, Eds., MIT Press, 6-41.

Warren, B.A., 1990: Suppression of deep oxygen concentrations by Drake Passage. *Deep-Sea Res*, 37A, 1899-1907.

Wearn, R.B., Jr. and D.J. Baker, Jr., 1980: Bottom pressure measurements across the Antarctic Circumpolar Current and their relation to wind. *Deep Sea Res.*, 27(11), 875-888.

Whitworth, T., III, W.D. Nowlin, Jr. and S.J. Worley, 1982: The net transport of the Antarctic Circumpolar Current through Drake Passage. *J. Phys. Oceanogr.*, 12, 960-971.

Whitworth, T., III and R.G. Peterson, 1985: The volume transport of the Antarctic Circumpolar Current from three-year bottom pressure measurements. *J. Phys. Oceanogr.*, 15(6), 810-816.

Wolff, J.O., E. Maier-Reimer and D.J. Olbers, 1991: Wind-driven flow over topography in a zonal $\beta-$plane channel: A Q-G model of the Antarctic Circumpolar Current. *J. Phys. Oceanogr.*, 21, 236-364.

Wolf-Gladrow, D., A. Hense, F. Kruse, J. Schroter and D. Olbers, 1991: A quasi-geostrophic eddy-resolving model of the Antarctic Circumpolar Current. In preparation.

Worthington, L.V., 1981: The water masses of the world oceans: some results of a fine-scale census. *Evolution of Physical Oceanography—Scientific Surveys in Honor of Henry Stommel*, B.A. Warren and C. Wunsch, Eds., MIT Press, 42-78.

Wright, D.G., and A.J. Willmott, 1992: Buoyancy-driven abyssal circulation in a circumpolar ocean. *J. Phys. Oceanogr.*, 22, 139-154.

Wyrtki, K., 1960: The Antarctic Circumpolar Current and the Antarctic Polar Front. *Dtsch. Hydrogr.Z*, 3, 153-173.

Wunsch, C., 1984: An eclectic Atlantic Ocean circulation model. Part I: The meridional flux of heat. *J. Phys. Oceanogr.*, 14, 1712-1733.

Wunsch, C. and B. Grant, 1982: Towards the general circulation of the North Atlantic Ocean. *Progress in Oceanography*, Vol. 11, Pergamon, 1-59.

Young, W.R. and P.B. Rhines, 1982: A theory of the wind-driven circulation. II. Gyres with western boundary layers. *J. Mar. Res.*, 40, 849-872.